METHOD FOR THE FLIGHT PATH OPTIMIZATION OF THE ELECTRIC-POWERED RECONFIGURABLE ROTOR (EPR^2) VTOL CONCEPT

A Dissertation
Presented to
The Academic Faculty

by

David Rancourt

In Partial Fulfillment
of the Requirements for the Degree
Doctor of Philosophy in the
School of Aerospace Engineering

Georgia Institute of Technology
December 2016

METHOD FOR THE FLIGHT PATH OPTIMIZATION OF THE ELECTRIC-POWERED RECONFIGURABLE ROTOR (EPR^2) VTOL CONCEPT

Approved by:

Professor Dimitri N. Mavris,
Committee Chair
School of Aerospace Engineering
Georgia Institute of Technology

Professor Dewey H. Hodges
School of Aerospace Engineering
Georgia Institute of Technology

Professor Brian German
School of Aerospace Engineering
Georgia Institute of Technology

Dr. Thomas L. Thompson
Chief Engineer, Aeromechanics Division
U.S. Army Aviation Engineering Directorate

Professor Marilyn Smith
School of Aerospace Engineering
Georgia Institute of Technology

Dr. Keith Bergeron
Senior Research Aerospace Engineer
U.S. Army Natick Soldier RDEC

Date Approved: 7 October 2016

To Émilie and Jules Rancourt,

May this work inspire you to achieve greater goals than what you think is possible.

ACKNOWLEDGEMENTS

This dissertation marks the end of a long journey as a graduate student at Georgia Tech. I would like to highlight the contributions of numerous people who were there to support me both on the good and bad days.

First, I would like to thank my advisor, Dr. Dimitri Mavris who was the first to believe in me even before I applied to join the ranks of ASDL. Thanks "Doc" for the support and encouragement throughout those five years. I would definitely not be the same researcher today if it was not for your teachings.

Second, the novel helicopter concept presented in this thesis, the *Electric-Powered Reconfigurable Rotor VTOL Concept* (EPR^2), would not have existed without the brainstorming and initial studies by Etienne Demers Bouchard. Let this work motivate you to pursue your research in this field.

I would also like to thank other colleagues at ASDL with whom I had the pleasure to work with: Alek Gavrilovski, Sayan Ghosh, Jason Corman, Adam Siegel, Steven Berguin, and others. Great ideas always originate from hallway discussions, brainstorming on a white board or at other unexpected occasions. Thanks for those years of productive scientific discoveries, and I am sure our paths will cross in the future.

My years in the lab would not have been the same without the "French Canadian Mafia," who made my journey much more enjoyable through motorcycle rides and amazing cookouts. Although we love "poutine," those five years in the south contributed to the discovery of a new type of gastronomy.

Finally, to my close family, thank you for the support. It has been a rough ride, but I cannot be more proud of this achievement. Émilie and Jules, when you grow up, I hope you will understand why your father had to work so hard at night.

TABLE OF CONTENTS

LIST OF TABLES

LIST OF FIGURES

SUMMARY

Vertical Takeoff and Landing aircraft (VTOL) have been essential to our society since their introduction in the mid-1940s. Today, helicopters are extensively used for military and civilian applications such as search and rescue, police surveillance, oil rig servicing, and cargo transport over short distances.

Although helicopters have seen a continuous improvement in performance over the last decades, they still fall short of fixed-wing aircraft in terms of fuel burn. Their limited range is the consequence of the low equivalent lift-to-drag ratio (L/D) in cruise and high empty weight fraction. Also, given the large number of moving parts and the higher level of vibration, helicopters incur a higher maintenance cost.

Recently, Demers Bouchard and Rancourt developed an advanced VTOL concept using three tethered fixed-wing aircraft: the *Electric-Powered Reconfigurable Rotor* (EPR^2) VTOL Concept. This concept takes advantage of the scale-free characteristics of electric motors and their high power density. The rotor is considered "reconfigurable" since the quasi-circular flight path of the unmanned aerial vehicle (UAV) can be adapted as a function of the flight condition. The features of this concept can enable performance enhancement never seen before compared to conventional helicopters.

Initial studies of this concept, performed in 2014 and 2015, showed that a payload of one metric ton could be lifted with 60 kWe in hover. However, the capability to evaluate the performance throughout the flight regime was not available. The main research objective of this thesis was to develop a multidisciplinary model for the analysis and performance optimization of the EPR^2 VTOL Concept in hover and with positive flight speed. The novel methodology, based on a two-level of fidelity

environment, was used to answer the overarching research question: *How can the flexibility in the tethered aircraft flight path of the EPR^2 VTOL Concept be used to minimize the power required to fly throughout the flight envelope?*

Four main contributions are highlighted in this dissertation. First, this work details the development of a multifidelity and multidisciplinary method for the flight path optimization of electric-powered, tethered aircraft. The method detailed in this work is based on a prescribed flight path obtained from a minimal set of parameters $\boldsymbol{P}$. This approach removes any feedback loop, and therefore, is ideal for a design space exploration. The lower fidelity environment was used to explore the design space and perform direct optimization while the higher fidelity environment is mainly used for analysis. The test cases in this work use the Makani's *Wing 7* tethered UAV, initially developed for wind energy harvesting. It was shown that for a total fuselage mass of 800 kg, the power requirement is as low as 42 kWe. At a travel speed of 20 m/s, the power requirement increases to 62 kWe and reaches 95 kWe at 27.5 m/s. The absolute maximum takeoff weight of the whole system was estimated at 1,835 kg, with an estimated total empty weight of only 400 kg. This leads to an impressive empty weight ratio of 22%. The maximum hovering time could be as high as 150 hours (no payload), or 24 hours with a 900 kg payload if powered by jet fuel.

Second, a rigid tether model for the flight path optimization of tethered aircraft was developed. As an alternative to the full dynamic tether model for the design space exploration phase, a kinematic model was developed to evaluate the approximate tether forces. This model uses the same aerodynamic modeling method than the higher fidelity dynamic model, except that it assumes that the tethers are rigid. The computational time was shown to be on the order of seconds, compared to $\approx$ 20 minutes for the complete dynamic problem with a minimal difference in the accuracy of the results.

Third, an improvement to the calculation of the aerodynamic forces on tether

segments was developed to minimize the number of required tether segments for this application. An analytical approach was used to demonstrate the benefits of this method versus the standard approach used in the recent literature.

Finally, this dissertation details the development of a wake consolidation model for application to fixed-wing aircraft aerodynamics and its integration in a custom-designed free-vortex wake model. This model bridges the gap between conventional helicopter aerodynamic methods and fixed-wing aircraft methods. It considers, the wake interaction between the aircraft and the effect of control surface deflection on the loads and wake. To the author's knowledge, this complete aerodynamic model, which captures all the relevant physics required to analyze tethered aircraft, is novel and provides a strong foundation for future studies.

CHAPTER I

MOTIVATION

"If a man is in need of rescue, an airplane can come in and throw flowers on him and that's just about all. But a direct lift aircraft could come in and save his life." Igor Sikorsky

The interest for vertical flight in the 20$^{\text{th}}$ century was strongly motivated by the ability of helicopters to operate on unprepared terrain with minimal runway size. Today, helicopters or vertical takeoff and landing (VTOL) aircraft are extensively used for military [110] and civilian applications [99, 25, 71], such as search and rescue, police surveillance, oil rig servicing, and cargo transport over short distances. Although conventional helicopters fulfill the need of specific markets, their performance is limited for extended hover flight time, and long cruise distances, as described in Section 1.1.

1.1 Limitations of Conventional Helicopters

Helicopters operate in a very complex aerodynamic and structural environment as summarized by Leishman [99] in Figure 1. As a consequence, conventional helicopter configurations have the following limitations:

- **Limited airspeed** – In flight with positive airspeed, a part of the rotor is operated with an increase in relative airspeed (advancing side), while the other half of the rotor sees a reduction in relative airspeed (retreating side). In the latter case, a part of the rotor blade operates in a "reverse flow region" where the freestream originates from the trailing edge. On the advancing side, the high airspeed near the rotor tip can lead to shock waves which cause a reduction in

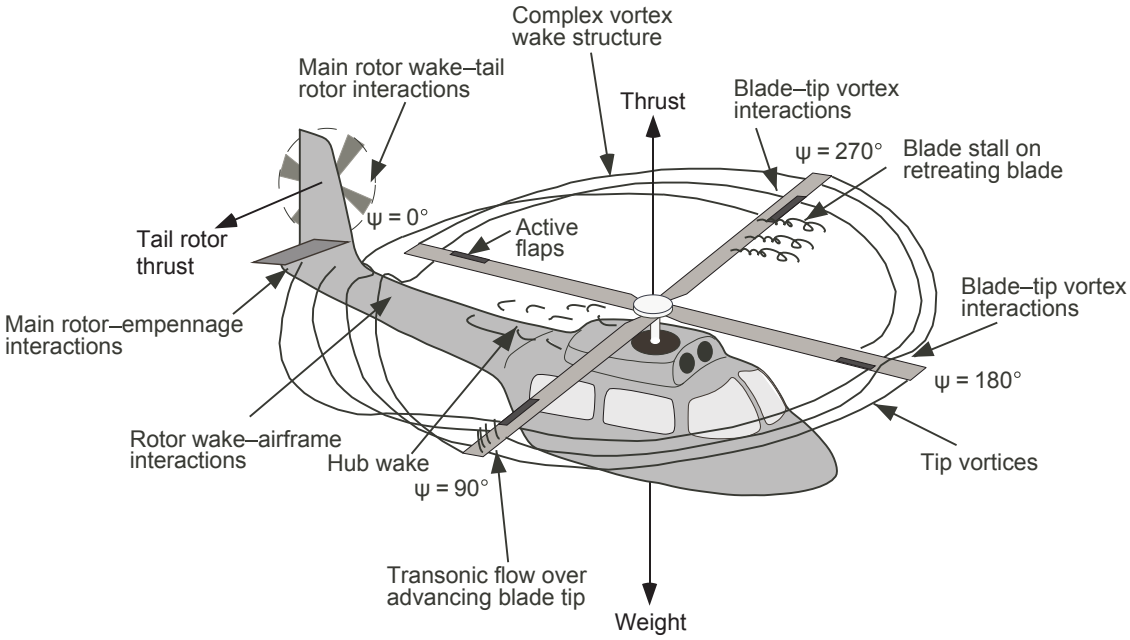

Figure 1: Complex Operating Environment of Rotorcraft [99]
(Image Courtesy of J. G. Leishman and Cambridge University Press, reprinted with permission)

efficiency and high noise levels. The cyclic variation in velocity, combined with the requirement that the blades must generate approximately the same lift, can lead to stall, which also reduces the aerodynamic efficiency in forward flight. The parasitic drag of the fuselage (including the rotor hub) also contributes to the high power requirement of helicopters at high speed [99, 128, 143].

- **Limited range** – The equivalent lift-to-drag ratio (L/D) of a helicopter in flight is at best on the order of 5 [128], which is comparable to the performance of a fighter airplane at Mach 1.15 [133]. Commercial transport aircraft have a maximum L/D on the order of 17 [133]. Such low efficiency, combined a high empty weight fraction, limits the range of conventional helicopters to a few hundred miles only.

- **Limited payload in low air density operation** – The power required to take off and land in low air density usually limits the payload that can be

carried. Moreover, the low air density reduces the power available for air-breathing engines, limiting even more the capability to hover, especially out of ground effect (OGE) conditions.

- **High maintenance** – Due to the complex operating environment with high levels of vibration and complex mechanical systems, the maintenance-to-flight time ratio of conventional helicopters is higher than airplanes, based on a study by Gajetti and Maggiore [59]. In return, the reliability is also affected by the high number of rotating parts (swashplate, gearboxes, blades, etc).

- **Cost** – The operating cost of helicopters is much greater than airplanes with the same payload capability due to fuel and high maintenance cost. A high acquisition cost is related to the mechanical complexity of such vehicles and to the low number of units sold per year. As an example, the Bell 206 L4 [17] has an estimated average cost per hour (direct cost of operations per hour) of $435 USD, from which $280 USD are for airframe, powerplant inspection, and parts. An airplane with the equivalent payload capacity and speed, such as the Cessna 182, has a direct cost of operation per hour of less than $100 USD.

In order to remove the constraining limitations of helicopters, especially the need to fly faster [81], numerous advanced VTOL concepts were developed since the 1950s. Two approaches are used: to adapt conventional fixed-wing aircraft for vertical take-off, or enhance the performance of rotary-wing aircraft with additional technology. Appendix A summarizes the two approaches with examples. Novel rotary-wing aircraft architectures, such as coaxial rotors or compound helicopters are more efficient than conventional helicopters at high airspeed, but do not show improvement in hover. For extended hover or low airspeed operation with very heavy payload, there is still a need for a novel VTOL concept.

1.2 Future Needs for Heavy VTOL Concept to Carry Payloads

In 1996, a project named "On the Need and Feasibility of a Very Heavy Lift Helicopter (VHLH) in Support of the Army's Force XXI Operations Concept" was initiated [64]. The objective was to generate advanced helicopter concepts to fulfill the need to carry heavy military equipment such as Future Combat vehicles (FCV) over long distances in areas with limited access. General Robert Scales once said: "We can conceive of a Future Combat Vehicle (FCV) of about 30-40 tons, [...]. So conjure me up an aerial lift vehicle that can transport such a load: -tactically, over 200-300 miles -a great speed - 150-250 mph - with stealth -capable of flying at a very low level [...] Such a machine is the essential ingredient to our Army After Next Operational concept."[64] The ability to transport combat vehicles over a variety of terrains is necessary for the success of such missions.

The Future Transport Rotorcraft (FTR) program was intended to develop a vehicle to lift a 20-ton combat vehicle on a hot day with VTOL capability. The sizing mission was a 500 km radius with VTOL initial takeoff. Upgrading current large helicopters (such as the CH-53) with new engines would allow only a payload of approximately 12-15 tons [63].

In order to fulfill these goals, Bell Helicopter proposed a tilt-rotor configuration with four rotors. The payload capability, 12.5 tons, fell short of the goals, with a range of 610 miles at over 300 mph. Carter Aviation Technologies proposed a compound helicopter concept that could carry 22.5 tons at 450 mph and 30,000 ft. The rotorcraft could take off, hover and land like a helicopter. At higher speed, the lift is provided by high aspect ratio wings on the side of the fuselage [64].

The need for VHLH was highlighted by Ardema [13] in a NASA-sponsored study on vehicle concepts and technology requirements for buoyant heavy-lift systems. Table 1 highlights the useful load requirements for heavy lift helicopters for civilian

Table 1: Principal heavy-lift airship markets. Adapted from [13].

Market area	Useful loads (tons)	Number of vehicles required
Logging	25-75	> 1000
Unloading cargo in congested ports	16-80	200
High-voltage transmission tower erection	13-25	10
Support of remote drill-rig installations	25-150	15

applications that cannot be fulfilled with current helicopter technology. This report also highlights the need for airships with a payload capacity of 180-800 tons. However, this study concluded that only lighter-than-air vehicles could fulfill this need.

For civil applications, VHLH are also used as aerial cranes or sky cranes. Use of those vehicles have been seen in the logging industry, and in the construction of towers and bridges around the world since the 1960s. The S-64 Skycrane shown in Figure 2 is one of the most widely used aircraft to perform these tasks, with a payload capacity of 20,000 lbs, a range of 200 nm at a cruise speed of 91 kts [56]. Although that vehicle is still in use today, there is a need for much larger helicopter concepts for both civilian and military applications, with lower fuel burn in hover and reduced maintenance cost.

In 2007, a report by the Defence Science Board Task Force for the Department of Defense [20] reiterated the need for VTOL concepts with both rotary and fixed-wing technologies. Moreover, due to the increase in weight and size of vehicles in today's Future Combat System (FCS), this report highlighted the need to develop a VTOL airlift fleet (or adapt the current fleet) to be able to carry the extra payload without reducing the range. Storage of those new concepts should also be considered for sea-basing capability.

Figure 2: S-64E in flight, one of the most popular sky crane in use today. The unusual fuselage shape allows larger payload to be carried.

1.3 Electric Propulsion in Aircraft Design

With the stringent NASA goals to reduce the fuel burn of aircraft in the next decades [83], numerous new aircraft concepts have been proposed with novel propulsion systems. One enabler is the use of electric propulsion, which has seen a recent increase in interest by researchers due to its numerous advantages, especially for small to medium size aircraft. The improvement in battery capacity and a highly coupled aerodynamic and propulsion integration have opened up the design space for such vehicles. A short overview of the benefits, drawbacks and current research on electric powered airplanes is required to understand how such technology can be applied efficiently on VTOL concepts. This review is not meant to cover all the electric airplane concepts, but an overview of the considerations to take into account in the design of electric powered aircraft. Since the energy density of batteries is much lower than hydrocarbon-based fuel, it is expected that electric propulsion should be coupled with high-speed turboelectric generators to supply the electricity to the system.

The advantages of electric propulsion over conventional internal combustion engines and gas turbines are significant. The readers should refer to the work of Moore

[114, 113, 116], Patterson [126], Fredericks [57] and Demers Bouchard [44] for a detailed description of the advantages and drawbacks of electric motors for aerospace applications.

- **Low emissions** – The use of electric propulsion can alleviate the pollution problem near airports if a fully electrical configuration is used. Otherwise, a better control of the emission can be achieved with a hybrid configuration.

- **Wide range of operating rpm with a high efficiency** – Compared to internal combustion engines and gas turbines, electric motors maintain a high efficiency over a wide range of rpm, allowing the use of simpler fixed pitch propeller over a wide variety of flight velocities [22, 21]. Moreover, the efficiency can be from three to four times higher than conventional internal combustion engines [116].

- **Reduced vibrations** – The vibrations generated by an electric motor are much smaller compared to internal combustion engines, or similar to gas turbines.

- **High power-to-weight ratio** – Recent electric motor designs developed for aviation have shown power densities of 2.17 hp/lb in continuous operation, and over 3.30 hp/lb for a transient 15 second operation [85]. The ability to use electric motors over their rated power for a short period of time increases the safety margin in case of an emergency or can enhance performance during more demanding operations. Cryogenic motor designs have shown steady-state power densities of 3.6 hp/lb [109] and 4.6 hp/lb [108]. With power densities up to 3.3 times the value of gas turbines [66, 86], the use of electric motors in aviation can revolutionize how aircraft design is performed. However, although the technology is mature for motors up to 200 kW, the design of lightweight megawatt-size motors remains a challenge [66, 65]. Commercially available and off-the-shelf electric motors are now available for electric aircraft [52] with power

densities that can reach 6 hp/lb for a few minutes (transient operation) and 2.5 hp/lb for continuous operations.

- **Reduced maintenance** – The required maintenance time and cost are reduced for electric motors compared to internal combustion engines due to the lower number of moving parts, no extensive use of oil for lubrication, and reduced complexity of cooling systems

- **Increased reliability** – The reliability of electric motors used in primary propulsion systems of aircraft is expected to be greater than conventional engines due to the lower vibration and reduced number of parts.

Moore [116] summarized a set of five misconceptions about the design of electric propulsion systems. The first and most important misconception is that "The design of electric aircraft is no different than existing aircraft." Many of the current electric propulsion designs are based on a retrofit installation, where an electric motor replaces the existing conventional engine. Examples of retrofit installations can be seen in Green Flight Challenge [98]. However, such designs do not take advantage of the scale-free characteristics of electric motors, where the efficiency is not dependent on the motor size nor its nominal power. As shown by Moore [116], scale independence results in electric integration approaches with a high number of motors.

The integration of electric propulsion into aircraft involves far greater freedom for the designer and for the operation of the vehicle as well. Multidisciplinary coupling and synergistic integration with aerodynamics, flaps, acoustics, control, balance, and aeroelasticity is required to fully take advantage of electric propulsion. Initial studies have shown that vehicle-level benefits are only possible if the propulsion system is considered as a part of the entire aircraft system [126]. The required capabilities for such a coupled integration were highlighted by Patterson [125], which include the consideration for propeller/wing interaction. One example of a highly integrated

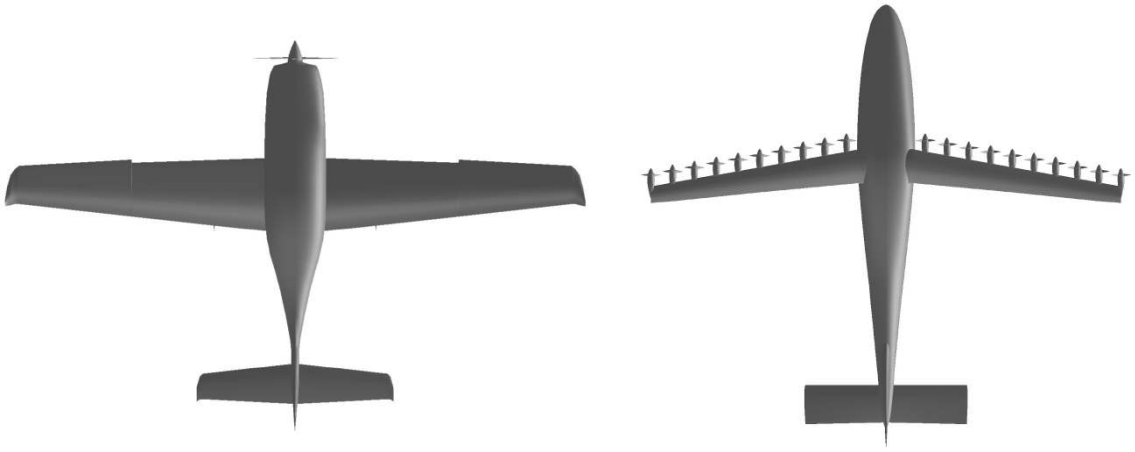

Figure 3: Comparison of the Cirrus SR22 with the LEAPTech aircraft [150].

design is the NASA LEAPTech (Leading Edge Asynchronous Propellers Technology) aircraft [150], shown in Figure 3. The aircraft on the left represents a top-view of a Cirrus SR22 with a conventional propulsion system, while the aircraft on the right is an aircraft with similar performance equipped with the LEAPTech technology. Supported by numerical simulations, this concept should increase the lift-to-drag ratio (L/D) in cruise and reduce the noise. Since the technology shows promising benefits for general aviation aircraft, NASA designed this airplane as the X-57 Maxwell [119].

In summary, the use of electric motors in aircraft design increases the design freedom. Salient characteristics of electric motors, such as the high efficiency over a wide range of rpm, allow the use of fixed pitch propeller over a wider variety of velocities without sacrificing performance. However, new aircraft concepts and highly integrated multidisciplinary design optimization are required to fully take advantage of this breakthrough technology. The next section reviews the use of electric propulsion for VTOL concepts.

1.4 Integration of Electric Propulsion into VTOL Concepts

The simplest approach to integrate electric propulsion in a VTOL concept is to replace the current engine with an electric motor of approximately the same power

Figure 4: Sikorsky Firefly all-electric helicopter concept. This prototype shows similarity with a conventional helicopter as the main engine was directly replaced with an electric motor of the same power curve [144].

curve. Such replacement reduces the development time, as shown by Durkee [50] and Sikorsky [144]. In the latter case, a 190 hp electric motor designed to "mimic power profiles of the legacy motor" was used. The maximum flight time was between five and ten minutes per charge. Figure 4 shows the similarity of the prototype with a conventional helicopter.

In order to take advantage of electric motors, NASA and Piasecki Aircraft Corp. developed in 1997 a heavy lift VTOL electromotive propulsion concept. On-blade electrically powered counter-rotating propellers were used to spin the main rotor, which eliminate the main rotor torque and improved lift efficiency. The use of electric motors and propeller on the main rotor was expected to increase the reliability through redundancy. The vehicle was designed to carry 25,000 lbs.

Using the property of scalability of electric motors, an approach is taken by E-Volo to use 18 direct drive electric motors to provide VTOL capabilities with a cruise speed of 50 kts for 20 minutes [53]. A hybrid power pack is under development to increase

Figure 5: E-Volo all-electric helicopter concept. Eighteen motors and propellers are used to generate the required lift to transport two people at 50 kts [53].

the endurance. The use of numerous propellers and motors increases the reliability of the system in case of a motor failure. Figure 5 shows the unusual arrangement of the motors in this all-electric aircraft concept.

The NASA Puffin [113] is a single-seater, tailsitting concept developed for high-speed, short flights. Designed to carry a 200 lbs person at a speed of 120 mph over 50 miles (with a 200 Wh/kg battery specific power density), this vehicle could reach over 250 mph using transient operation of the motors. A power of 60 hp is required to hover, but approximately 20 hp is required in cruise.

A novel autonomous concept for a single passenger has been proposed by Ehang [51] with eight direct drive electric motors and fixed pitch propellers. The use of multiple electric motors is a technology enabler by providing additional control and by reducing weight.

Three concepts of electric tilt-rotors were developed and tested in the last several years: the GL-10 Greased Lightning [120, 57, 137], the Joby S2 [151, 115], and the AgustaWesland Project Zero [4, 74]. The G-10 Greased Lightning is powered by ten electric motors with folding propellers mounted on a tilting wing for the hover phase.

Figure 6: Joby S2 VTOL concept. 12 tilting motors are used to provide lift in hover, while two tip-mounted motors are used to provide thrust in cruise [151].

A hybrid powertrain increases the expected endurance to up to 24 hours. The Joby S2 adopts a similar multirotor configuration, except that it uses tilt-rotors instead of a tilt-wing. Figure 6 shows a rendering of the S2 concept in vertical takeoff phase. In 2013, AgustaWesland unveiled their all-electric VTOL concept, the Project Zero, which first flew in 2013. It uses a twin tilting ducted fan concept embedded into a triangular wing planform as shown in Figure 7.

In summary, electric VTOL concepts mainly use the thrust generated by propellers to provide the lifting capability. Since the disk area remains relatively small, especially for tilt-rotor configurations, the power requirement in hover is not minimized.

1.5 Electric-Powered Reconfigurable Rotor VTOL Concept

In 2015, Demers Bouchard and Rancourt [44] proposed a new heavy-lift VTOL concept that uses electric propulsion, the *Electric-Powered Reconfigurable Rotor* (EPR^2) VTOL Concept. This section provides a detailed description of the concept, preliminary results and a set of observations. The main objective of this concept is to allow extended hovering capability while maintaining the ability to perform relatively

Figure 7: AgustaWesland Project Zero all-electric VTOL concept. The lift is generated with two ducted fans embedded in the wing during hover [4]. Both fans rotate during forward flight.

high-speed flight during cruise with a reduced power requirement.

1.5.1 Concept

The EPR^2 VTOL Concept provides a new way to lift payloads or carry passengers using tethered fixed-wing aircraft. Three or more unmanned electric airplanes are used to generate the lift by flying along a quasi-circular path above the fuselage. In order to reduce the weight of the airplanes, the source of energy is located in the fuselage, and the electrical power is transmitted through conductors embedded in the tether. The source of energy can either be batteries, a high power density electric generator [132, 127], or a hybrid powertrain. Figure 8 illustrates the concept in the hover flight mode.

The possibility to perform vertical pickup and delivery of payloads using long tethers towed by fixed-wing airplanes has been proposed as early as 1931 by Beauford [28]. A single airplane lowers a long tether and maintains a circular flight path.

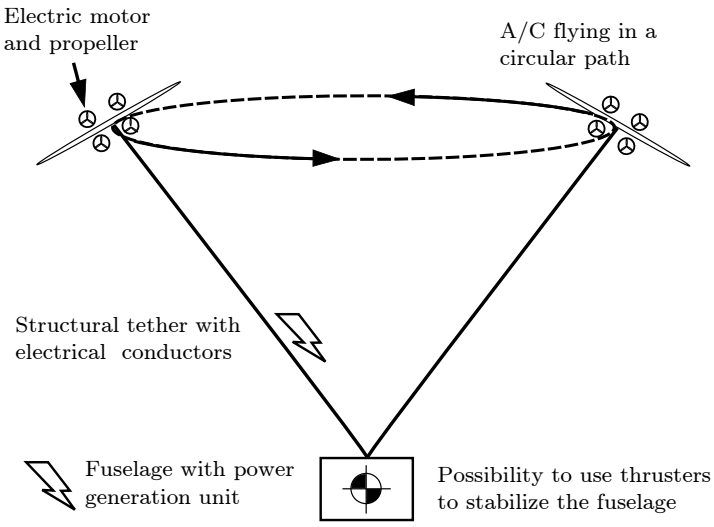

Figure 8: Schematic view of the *Electric-Powered Reconfigurable Rotor* VTOL Concept during the hover phase with the aircraft flying along a circular path [44].

Under specific flight conditions, the tip of the tether becomes the apex of an inverted cone, allowing loading and unloading a payload from an airborne aircraft. A similar method was proposed in the late 1930s by Smith [147] with the additional claim that the tether could be reeled in from both the aircraft and the payload. The technique was demonstrated by a missionary pilot, who used this technique to deliver small payloads in remote regions in South America. The early techniques assumed the use of a single aircraft with a long tether. This technique was also seen as a potential means to replace a variety of airdrop techniques used by the U.S. Air Force [49].

Between 1940 and 2012, eight patents [11, 7, 8, 39, 167, 60, 43, 124] covering different aspects of this technique were issued. Figure 9 illustrates the salient characteristics of a subset of those patents. The main motivation behind the concept of using fixed-wing aircraft to lift payloads in the 1940s was to achieve a higher payload lift capability than rotary wing aircraft, which were in their early days of development. The interest for a VTOL concept using tethered aircraft is not limited to a

few individuals. Large corporations such as Lockheed Martin [167] and Northrop Grumman [43] have also shown interest in this concept.

The actual use of such a system to lift *heavy* payloads has not been reported. As shown in Section 2.1, very few studies actually attempted to evaluate the performance of such complex system throughout the flight envelope.

Recent advances in control methods of unmanned aerial vehicles (UAVs) in the last decade could provide a part of the solution to improve the performance of the concept and remove the need for a runway for the manned aircraft to take off and land. Founded in 2006 and now under Google X, Makani specializes in the development of airborne wind turbines based on the concept of a tethered airplane with onboard electric generators. The single UAV takes off vertically from the ground station by using electric power provided through conductors in the tether. The aircraft are built using lightweight carbon materials and since no energy storage is kept onboard the aircraft (batteries), a thrust-to-weight ratio well above one can easily be achieved. Once the vehicle reaches its operating altitude and the tether is slightly under tension, the aircraft initiates a circular flight trajectory, similar to the tip of a wind turbine blade. Power is extracted using the same propellers and motors used in the takeoff phase. If the wind velocity reduces below some threshold, the aircraft returns to the ground station. Figure 10a shows the aircraft during the takeoff phase and Figure 10b illustrates the typical flight path during the power generation phase. Since a complete autonomous flight has been proven by Makani, the technology readiness level (TRL) of the control methods throughout the flight envelope is relatively high.

The proposed concept by Demers Bouchard and Rancourt [44] reuses a similar technology to the one developed and demonstrated by Makani for load lifting purposes. Three or more aircraft are tethered to a fuselage that includes the useful load and the energy source. The flight can be divided into three phases: takeoff/landing, hover or low-speed flight, and high-speed flight, as shown in Figure 11. The tether

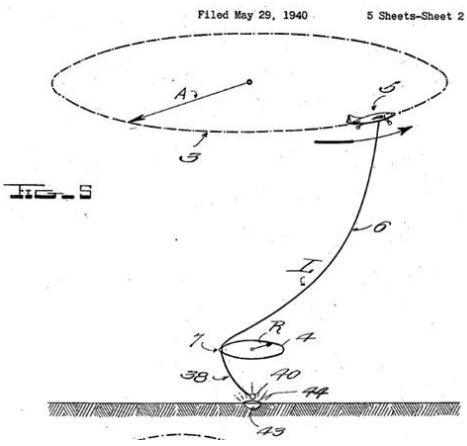

Anderson 1942

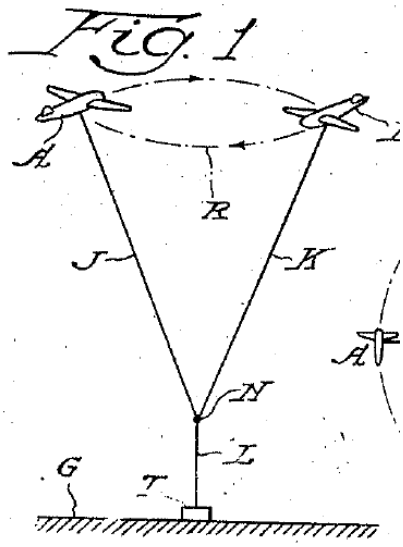

Alaburne 1942

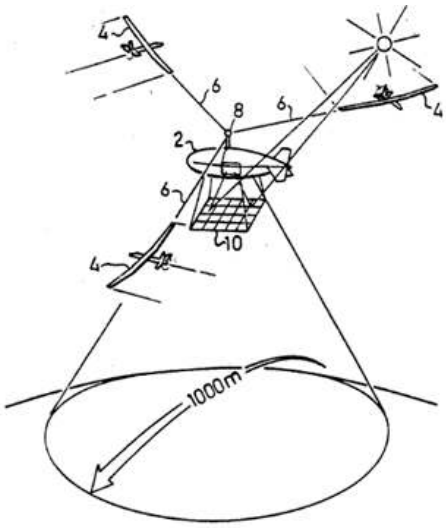

Gamzon 1991

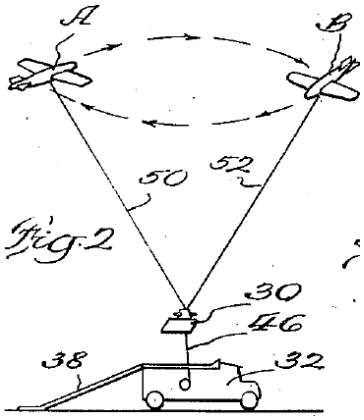

Alaburne 1945

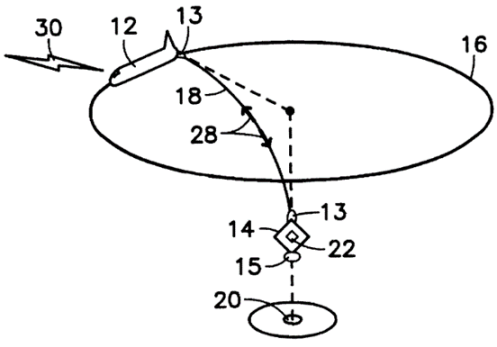

Jacobs 1998

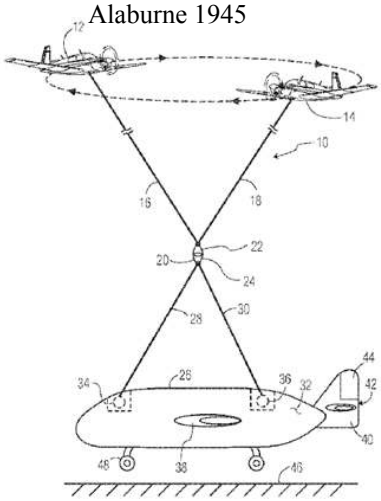

Olson 2012

Figure 9: Overview of a few patents about VTOL concepts using tethered aircraft

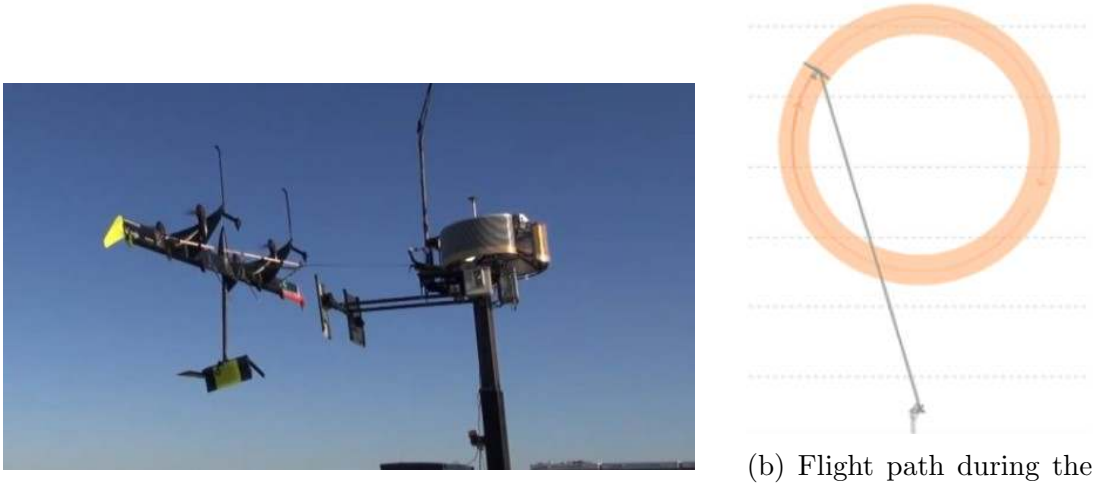

(a) Aircraft during takeoff

(b) Flight path during the power generation phase

Figure 10: Overview of the Makani airborne wind energy concept [106]

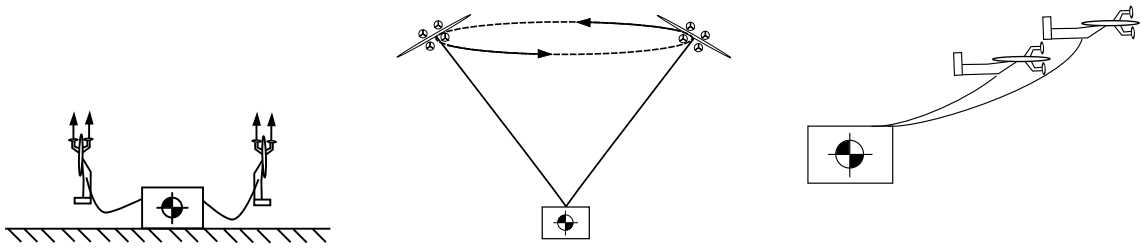

(a) Takeoff/landing

(b) Hover/low-speed flight

(c) High-speed flight

Figure 11: Notional representation of the three flight phases of the proposed concept [44]

length can be adjusted using a hoist located on the fuselage.

Prior to the flight, the aircraft are attached to the fuselage in a vertical position. The aircraft take off while the fuselage remains on the ground. The use of lightweight aircraft without onboard energy storage is a key enabler to allow a thrust-to-weight ratio greater than unity. Once the aircraft reaches the prescribed altitude, the aircraft transition to a circular flight path to generate a much higher lift than the thrust generated by the propellers. The aircraft are controlled individually using conventional control surfaces and differential thrust. A slight deviation from the circular flight path or changing the phase between the aircraft could allow slow flight velocity in any direction. For high-speed flight, the aircraft can be arranged in formation flight

and the tether length adjusted to optimize the overall performance of the system. Finally, landing is performed in the reverse order.

1.5.2 Initial Studies

Two conceptual studies on the concept were performed in the Aerospace Systems Design Laboratory (Georgia Institute of Technology). First, Demers Bouchard and Rancourt evaluated the overall power requirement for specific parts of the flight envelope. The following flight phases were investigated: takeoff of the aircraft, hover phase (with no wind velocity) and forward flight. Details on the modeling assumptions can be found in [44].

A first test case assumed that two *Wing 7* aircraft developed by Makani Power were used. Detailed specifications can be found in [6, 106]. Each aircraft is rated for over 20 kW continuous power, weighs 60 kg, measures 8 m in span, and is powered by four electric motors with fixed-pitch propellers/turbines. The objective of the study was to optimize the flight condition (flight speed, radius, tether length) to minimize the power required to lift a given fuselage weight. It must be highlighted that the fuselage weight includes the fuselage structure, power source, and useful load. Figure 12 presents an estimation of the hover power requirement as a function of the fuselage weight with the power breakdown.

Given that the two aircraft are designed for 40 kW, the maximum payload that can be lifted based on the previous definition is 770 kg. By summing the weight of both aircraft with the tether weight, the empty weight of the rotor system is only 150 kg. The extremely low power requirement is the result of the low disk loading in the order of 0.75 kg/m^2 at maximum gross weight.

Figure 12 also shows the power breakdown during the hover phase. At the rated power, less than 50% of the power loss originates from the induced drag, while 20% is the result of the wing parasitic drag. However, a high uncertainty on the aerodynamic

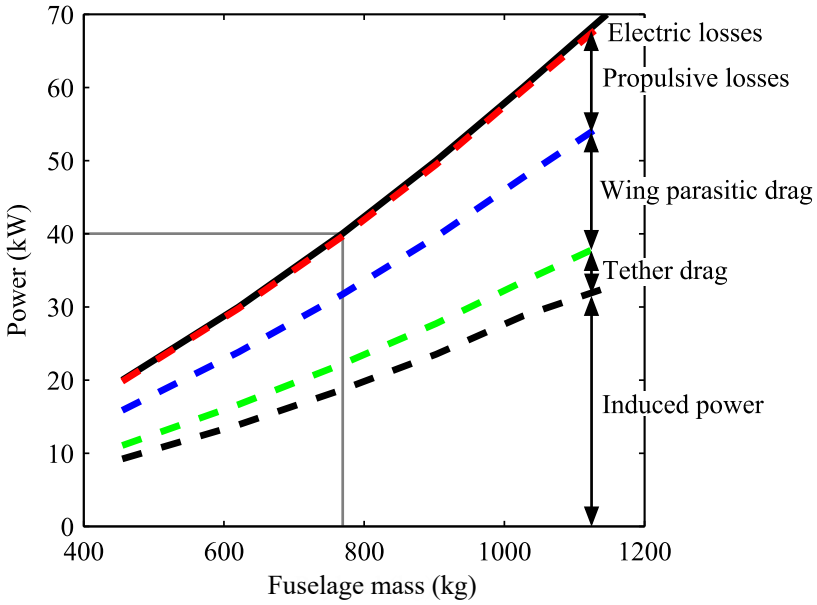

Figure 12: Power requirement as a function of payload for two Makani's *Wing 7* aircraft.

modeling of the system is associated with the use of the blade element momentum theory (BEMT) with tip and root loss model in such a flight condition. The current method is also unable to evaluate the performance of the system in slow flight when the UAVs must still fly along a quasi-circular flight path.

A second test case using the same modeling techniques was performed on the much larger 600 kW aircraft also under development by Makani Power. Each aircraft has a span of 28 m and weighs slightly over 1,000 kg. With this configuration, the system could lift a payload of 18,700 kg at maximum power, close to the 20,000 kg payload capacity of the *Mil Mi-26* [84]. As a comparison, this conventional helicopter is powered by two 8,500 kW turboshaft engines[1].

A second study was recently completed by Cormier and Rancourt [37, 38] to analyze the power requirement in the high-speed flight configuration by taking into

[1]Note that the power of the engines does not directly translate to the power in hover

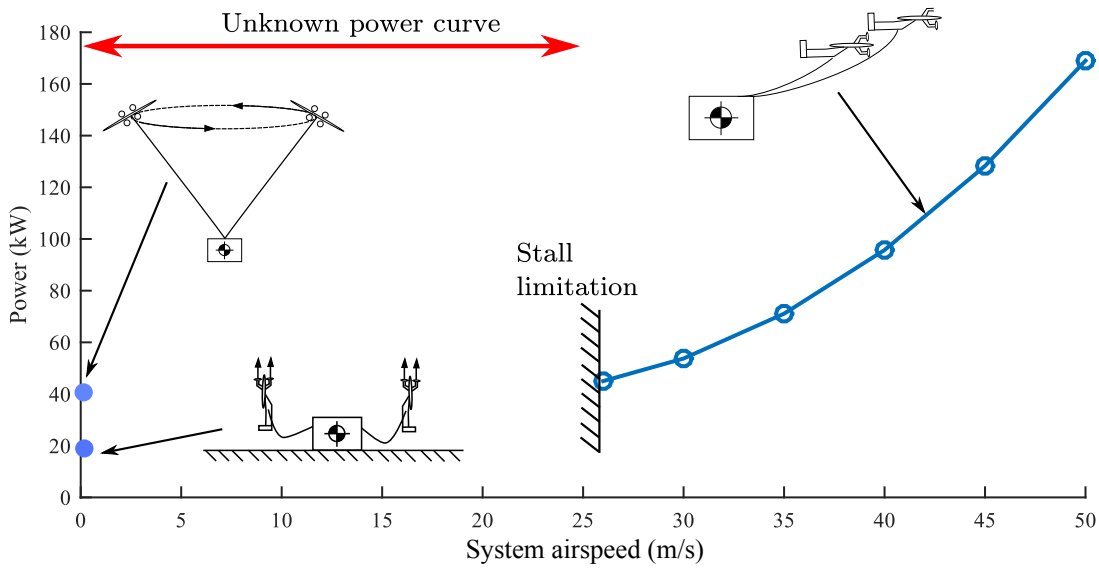

Figure 13: Power requirement across the flight speed based on the initial studies by Demers Bouchard, Cormier, and Rancourt [37, 44]. Between the hover phase and the forward flight phase, the power requirement is unknown since no model is currently available. This study assumed that only two aircraft were used.

account the aerodynamic interaction between the two fixed-wing aircraft. The objective was to minimize the power required to fly given a fuselage mass, a distance between the aircraft with respect to the tether length and aircraft attitude. Control surface deflections were also evaluated to maintain the aircraft attitude. The power requirement for the takeoff, hover and forward flight modes from the two studies were combined in Figure 13 for a fixed fuselage mass of 770 kg, and two Makani's *Wing 7* aircraft.

The simulations to evaluate the power required during the three flight phases were obtained through a multidisciplinary analysis environment. For the takeoff phase, a readily available and validated code was used to predict the power required to overcome the tether and aircraft weight. In forward flight, a vortex-lattice method predicted the aerodynamic forces with the wake interaction. Both of those codes were validated through numerous studies for these applications. In the hover phase, since the aircraft bank angle is not zero, an assumption of the blade-element momentum

theory used to predict the aerodynamics had to be violated. The authors assumed that the theory was still valid given the small bank angle. However, between the hover phase and the high-speed flight phase, the power requirement as a function of the airspeed is unknown. A high coupling between the aerodynamics and dynamics of the aircraft is expected since the vehicles should continuously change their attitude to respond to the varying local true airspeed. A complex flight path might be required to alleviate the payload dynamic response or to minimize the power requirement.

1.6 Summary

This first chapter showed the need for VTOL concepts with greater lift capabilities while maintaining a long range and high-speed capability. Numerous concepts were developed and tested in the last 40 years to fulfill this need, both using fixed-wing aircraft augmented with VTOL capabilities or advanced rotary-wing concepts. However, most advanced VTOL concepts are developed for high-speed flight and therefore lack efficiency during the hover phase and for extended operation at low velocity. Moreover, the noise generated in hover and maintenance cost for both conventional and advanced VTOL concepts still remain a challenge. A review of electric propulsion has shown that the design of electric aircraft *cannot* be performed using old paradigms. Electric motors are scalable, have an efficiency in the order of 90%, and have a power density greater than modern gas turbines. The concept proposed by Demers Bouchard and Rancourt, the *Electric-Powered Reconfigurable Rotor* (EPR^2) VTOL Concept could provide a solution. Electric-powered tethered aircraft replace the main rotor of the helicopter and the fuselage contains the power source.

Although the two initial studies were limited in scope and fidelity, they showed promising results for this concept. A low disk loading under 1 kg/m^2 enables a low power consumption in hover, which could allow extended use of the system in this flight phase or when operating at high altitude. The vertical takeoff phase is

possible since the energy source is located in the fuselage to reduce the UAV weight. Fixed pitch propellers can be used due to the wide range of operability of the electric motors without the use of gearboxes. A much larger design freedom is available to optimize the operation of this system, such as the trajectory of the aircraft, the power distribution between the aircraft and the tether length.

However, these studies did not evaluate how the system would behave at low airspeed while the aircraft must still execute quasi-circular flight paths. The complexity to evaluate this particular flight phase is increased since a high coupling between multiple disciplines is expected.

The focus of this research is to develop a methodology to evaluate and optimize the performance of tethered aircraft in circular or quasi-circular patterns, both from a dynamic and aerodynamic perspective at various flight conditions. Thus, the power requirements throughout the flight envelope for the EPR^2 VTOL concept could be obtained. Then, a proper assessment of the technology would be possible.

The remainder of this research thesis is organized as follows:

- *Chapter 2* presents a literature review of the different modeling techniques for helicopter rotors, fixed-wind aircraft and tethers and their applicability to the current problem.
- *Chapter 3* presents the research objective, research questions and hypotheses.
- *Chapter 4* details the modeling and simulation environment.
- *Chapter 5* provides results for specific test cases that uses Makani's *Wing 7* aircraft under various flight conditions.

CHAPTER II

BACKGROUND AND LITERATURE REVIEW

The second part of Chapter 1 introduced the *Electric-Powered Reconfigurable Rotor* VTOL Concept. This system uses tethered fixed-wing aircraft instead of a conventional rotor to provide lift. First, this chapter presents an overview of the tether modeling techniques with an emphasis on tethering a payload behind fixed-wing aircraft. Since the EPR^2 VTOL Concept is a hybrid between a fixed-wing aircraft and a helicopter, a literature review of the aerodynamic modeling techniques is presented for both fixed-wing aircraft and conventional rotary wing helicopters with various levels of fidelity. It will be shown that conventional methods cannot be applied to this concept.

2.1 Modeling of Tethered Systems

Recent dynamic tether models are mainly based on the finite element method and the equivalent lumped mass method because of their large flexibility. Hansen and Crist [70] from the Air Force Academy studied the steady-state shape of a tether towed by an aircraft in a quasi-circular flight path. An analysis of the SNOWBIRD communication system was performed. The model was based on a finite element approach, where the tether was discretized with 10 elements. The analysis focused on long tethers (4,000 ft and 8,000 ft) with end masses between 25 lbs and 100 lbs with the objective to optimize the flight path to minimize the vertical "yo-yo" effect associated with crosswind flight conditions. The highest verticality was obtained with long cables with a variable altitude circular orbit with moderate drogue weight.

Winglet [168] developed a non-linear finite segment dynamic model of a cable or a chain. The discretized masses are connected by a series of links with ball-and-socket

joints. The equations of motion are derived using Lagrange's form of d'Alembert's principle, for a total of $3N + 3$ degrees of freedom, where N is the number of tether segments. Finally, the set of equations is integrated using a fourth order Runge-Kutta method. Huston and Winglet [82] validated the model with analytical and experimental data.

The equilibrium and stability of a whirling cable was studied by Russell in his Ph.D. dissertation [138]. The results of his discretized tether modeling approach showed good agreement with experimental results. In the following years, Russell studied the whirling rod-mass system [140] with the United States Air Force Academy. The rod was assumed to be inextensible and massless. A mass was attached at the tip. Stability of the equilibrium was determined using the perturbed equations of motion. The addition of viscous drag also affected the stability of this simple system. In 1977, he published the results of a study on the equilibrium and stability of a circularly towed cable subject to aerodynamic drag and assuming an elastic cable [139]. The model also used a finite-element approach and a Newton-Raphson procedure to solve the set of algebraic equations. The results showed multivalued solutions for specific rotational frequency and tow radius as shown later by Zhu [173].

Leonard [102] examined the difference between the finite element (FEM) and lumped parameters methods (LPM) for the analysis of oceanic cables under hydrodynamic load conditions. It was shown that these two discretized approaches are both accurate if proper attention is paid to defining the boundary conditions and the degree of discretization.

The dynamic modeling of towed aircraft saw an increased interest in the 1990s. Cochran [34] developed a dynamic model of a small flight vehicle being towed by a larger aircraft. A lumped mass model was used for the tether and a six degree-of-freedom (DOF) model was used for the towed vehicle. Using a similar approach, Henderson [72] developed a model to capture the dynamic behavior of an airborne

target towed by a tug aircraft via a cable. It was shown that active control of the towed vehicle is required for sufficient stability.

The interest of the dynamic modeling of long trailing-wire antenna was still present in the 1990s for military application as shown by Clifton in his dissertation [32]. A dynamic model of this system was developed to evaluate the concept of controlling the wire's steady-state shape and oscillation due to wind gradient. A classic vibrating chain with free/fixed boundary conditions was superimposed upon the wire's steady state shape and tension distribution with the assumption of an inextensible cable. It was shown that if the tow plane orbit radius is modulated according to the wind gradient, 50% or better reduction in the oscillations can be achieved, and a controllable drogue at the end of the wire was also effective in tailoring the steady-state shape of the wire. For a tether of 20,290 ft towed at 156 kts and at an altitude of 18,325 ft, the prediction on the tether tip height differed by approximately 8% between the model and experimental results [33].

Although the prediction of the trajectory of a payload (given the trajectory of the tow plane) is of interest, the inverse problem is usually more relevant. Murray [118] proposed an approach to optimize the trajectory of the tow plane given a target motion of the payload using differential flatness. With the property that the system is differentially flat, the trajectory of the tow plane can be obtained by integrating the position of the tether from the payload to the aircraft. The model used a discretized tether approach with 20 inextensible elements. Murray was one of the first to show that the aircraft flight path must be tilted (varying altitude) to minimize the motion of the tether if a crosswind is present, and in some cases, the target trajectory cannot be obtained due to limitations of the tow plane performance.

The tether length between the tug vehicle and the payload can be varied to adapt to specific operating conditions. Kamman [92] modeled the variation in tether length by having a variable length link near the towing or anchoring vessel. A similar

approach was adopted by Frost and Costello [58] to model the dynamic behavior of a tethered-connected ammunition system. In this case, the tether was modeled by a series of particles (point mass) each connected by a spring and damper in parallel.

Between 2006 and 2010, Williams made significant contributions in the field of tether dynamics modeling. Lumped mass models were used to discretize the cable, with approximately 10 to 20 elements. In 2006, Williams and Trivailo [164] studied the dynamics of a cable-supported sliding payload deployment mechanism from a circling aircraft. The same authors analyzed the trajectory of a single long tether towed by an aircraft in a circular path in the presence of a cross-wind [160]. As shown previously by Murray [118], flying in an eccentric orbit contributes to offset some of the lateral and downwind drift in the presence of moderate wind strengths. Williams, Lapthorne and Trivailo validated the discretized tether model with viscoelastic elements with experimental data [162].

Williams was the second researcher to explicitly consider the limitations of the aircraft performance in the dynamic tether study after the early study by Wilson from the Lockheed-Georgia Company [167]. In a two-part paper, Williams and Trivailo [165, 166] studied the dynamics of a circularly towed tether with a special consideration for the aircraft performance limitation. A point-mass model was used to derive the equations of motion of the tug-vehicle. The maximum thrust available and lift coefficient were considered to avoid unfeasible solutions. A limited aerodynamic model was used based on aircraft performance [9]. Part 1 focused on the stability and equilibrium of the solution. As per the previous research on the topic, practical towing solutions that achieve a small motion of a towed body can be achieved using a long tether. It was shown that it is possible to achieve a cable tip motion of 1.5 m using a light aircraft towing a 3 km long cable. Part 2 studied the transitional dynamics from straight flight to circular flight and the inverse motion. The prescribed flight path was discretized using Chebyshev polynomials as the basis functions for the variation

of the radius. If a fast motion of the aircraft is performed during the transition, the tether can develop slack and a longitudinal wave is developed. This study highlighted the importance of tether dynamics during the transition for long tethers. It must be noted that as conventional aircraft were considered for this study, only simple flight parameters were varied to simplify the pilot task.

In a later study, Williams and Ockels [163] extended the concept to multiple fixed-wing aircraft as initially proposed by Alabrune [8, 7] and then studied by Wilson for a two-aircraft configuration [167]. This configuration allows greater control of the payload position and a wider choice of aircraft speed and lift coefficient. It is shown that this configuration is superior to a single-cable system as the "almost" symmetrical cable tension forces acting on the payloads cause the payload to remain at the center of the circle in the equilibrium configuration. With a well-planned transition from hover to forward flight, the motion of the payload is very smooth with very little oscillation of the payload position. Figure 14 shows the aircraft, tether and payload trajectory during a transition from hover to forward flight with a two-aircraft configuration. However, it is unknown if such motion is acceptable if the payload is replaced by a fuselage with passengers.

Williams also studied the effect of a random wind of approximately 5 m/s on the payload motion. Figure 15 shows that the payload moves by up to 50 m if no control system exists on the payload. The sensitivity to wind is largely due to the use of long tethers required to maintain the conventional fixed-wing aircraft within their performance limits. It must be noted that this work focused mainly on the tether and payload dynamics more than the performance optimization of the concept. Only simple aircraft motions could be tested as manned aircraft were considered for the study.

Extensive research by Sgarioto [142] was aimed at improving the optimal control of aerial tethers for remote delivery and capture of payloads using a single fixed-wing

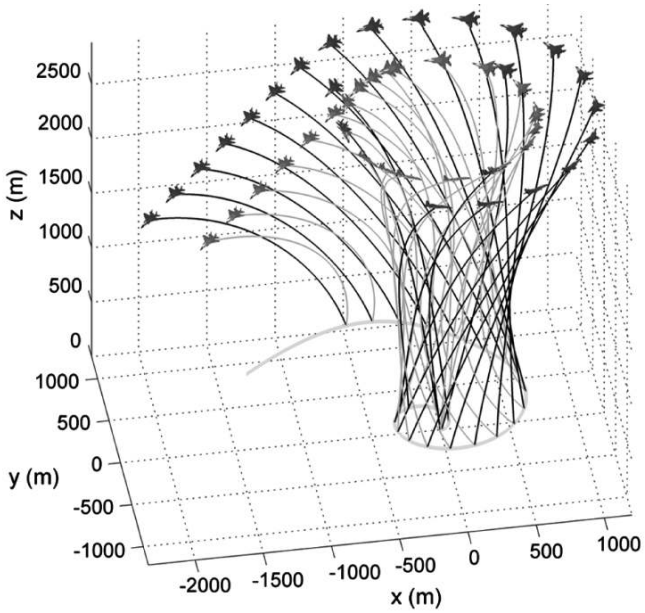

Figure 14: Two-aircraft configuration during a transition from a circular flight path to a linear flight path [163]

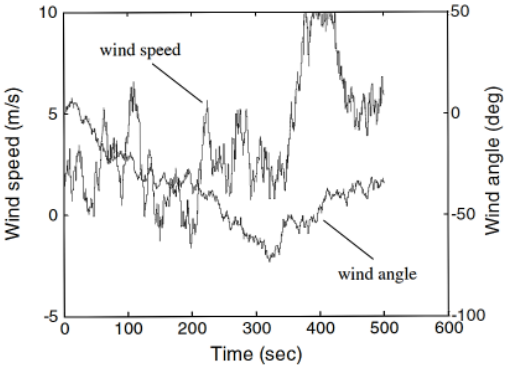

(a) Random wind model

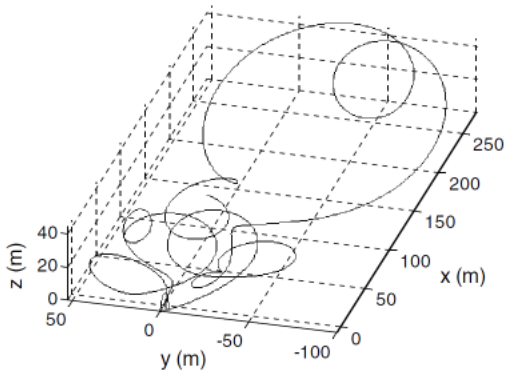

(b) Payload trajectory under random wind

Figure 15: Effect of a random wind on the payload trajectory in hover [163]. It is shown that the payload moves within a radius of 50 m.

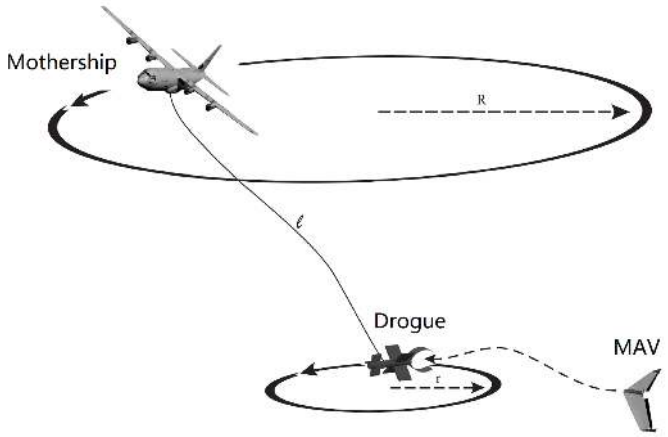

Figure 16: Tethered drogue behind a mothership for MAV recovery [152]

aircraft, as initially proposed in the early 1930s. A lumped parameter approach is used to model the tether which concentrates the distributed forces to discrete point mass elements, articulated by frictionless hinges.

The analysis in steady-state of tether/payload systems in a circular motion was also studied by Kolla [95] using a commercially available finite element method (FEM) software package ADAMS©. Physical experiments on a 58-inch tethers were used to validate the model and to demonstrate the jumps between the responses for specific flight conditions. Gottimukkala [67] studied the minimum damping required to ensure that only a single steady-state solution exists. Numerical continuation and bifurcation analysis were used. The stability analysis used the Galerkin's method to provide the linearized vibration equation.

The concept of using a fixed-wing aircraft in a circular path with a long tether has been studied by Sun to perform airborne recovery of micro air vehicles (MAV) [153, 152, 154]. A mothership transitions to a circular orbit that places a drogue in a stable and slower orbit that is tracked by the MAV. Figure 16 illustrates the concept.

Sun optimized the trajectory of the mothership to achieve a prescribed trajectory of the towed drogue using differential flatness as shown by Murray [118]. An elastic discretized model of the tether was used. In his dissertation, Sun evaluated different

strategies to place and stabilize the flight path of the drogue in the presence of wind. Gauss's Principle and Newton's second law were used to derive the equations of motion for inelastic and elastic cables, respectively. Flight test results were used to validate the mathematical model and the number of tether elements required for convergence.

In summary, the most popular approach to model tethers is the use of discretized elements since it increases the flexibility of the models. Most studies focussed on the dynamics of tethered payload with long tethers motivated by the used of conventional fixed-wing aircraft, which differs significantly from the architecture of the *Electric-Powered Reconfigurable Rotor* VTOL Concept.

2.2 Aerodynamic Modeling of Rotary Wing and Fixed-Wing Aircraft

The objective of this section is to describe the main methods for the aerodynamic modeling of rotary-wing and fixed-wing aircraft in subsonic flight. An emphasis is given on methods that are available for conceptual studies and design space exploration early in the design process. A short description of each method is provided and examples of design studies are provided. Traditional fixed-wing aircraft design methods are presented first, followed by rotary-wing design methods. It will be shown that the methods used in previous studies to evaluate the aerodynamic performance of aircraft flying in a circular path have a low level of fidelity compared to the tether dynamic models.

2.2.1 Fixed-Wing Aircraft Aerodynamics

Methods to evaluate the aerodynamic performance vary with level of fidelity and computational cost. In this section, the most popular methods for conceptual sizing of fixed-wing aircraft are detailed. Computational Fluid Dynamics (CFD) is not covered since it is seldom used early in the conceptual design, especially for design

space exploration, due to the high computational cost.

2.2.1.1 Prandtl's Lifting Line

The lifting line theory was developed independently by Frederick W. Lanchester [97] in 1907 and by Ludwig Prandtl in 1918 after working with Max Munk and Albert Betz. This method is still in use today for preliminary calculations of finite wing aerodynamics [10]. The main advantage of this method over its approximation is the capacity to analyze wing planform geometry and control surface deflection on the aircraft aerodynamics. Prandtl's lifting line represents the basis of numerous other advanced methods and is also still in use for the near-field helicopter aerodynamics, as will be shown in Section 2.2.2.

The low computational cost to solve the Prandtl lifting line makes this method practical for conceptual studies where there is a need to consider the effect of control surfaces, the wing planform geometry and wing twist under the assumptions of inviscid fluid at low Mach numbers. However, this method assumes that the trailing wake is straight and extends to infinity. Therefore, this method does not consider vortex interaction nor the curved wake in the case of a non-linear flight path. The exclusive use of this method for the evaluation of the aerodynamics of aircraft flying in circular paths can introduce errors if the turn radius is small compared to the wingspan of the vehicles and cannot consider the wake interaction over multiple rotor revolutions.

Bangash [15] analyzed the aerodynamics of formation flight and the influence of the configuration. The aerodynamics of the leading aircraft was evaluated using the lifting line theory. Far behind the leading aircraft, it was assumed that the vortex sheet rolls up into two tip vortices for the analysis of the aerodynamics of the trailing aircraft.

A more suitable method for wings with sweep under asymmetrical flow conditions is the extended lifting-line method, also referred as the Weissinger method [156]. This

method uses collocation points where the flow tangency must be satisfied. These points are located at the three-quarter chord location while the bound vortex is located at the quarter chord. This method provides relatively good results for the spanwise lift distribution, rolling moment, and induced drag for wings with sweep. This method corresponds to the numerical panel method with one chordwise element.

One popular approach that is extensively used is the approximation of Prandtl's lifting line as shown by Anderson for the performance analysis of fixed-wing aircraft [9]. The total drag component is the sum of numerous terms that are typically combined into an induced drag component C_{D_i} from the three-dimensionnal effects and another component C_{D_0}. This last term, the viscous drag, must be evaluated from other methods than the lifting line since the assumption of irrotational flow implies that $C_{D_0} = 0$.

The lift-dependent term is typically evaluated with Equation 1 where e is the Oswald efficiency factor and $\mathcal{AR}$ is the wing aspect ratio. This term can be evaluated using the lifting line theory to take into account a non-elliptical lift distribution. Typical values for e range from 0.85 to 1 [133, 9].

$$C_{D_i} = \frac{C_L^2}{\pi e \mathcal{AR}} \tag{1}$$

There are numerous uses for these approximate methods based on the lifting line theory for the performance analysis of airplanes flying in a circular path. The initial study by Demers Bouchard and Rancourt [44] compared both the approximate methods from the lifting line and the blade element momentum theory (BEMT). Williams [165] used these methods to constrain the prescribed trajectory of the aircraft within their performance limit, such as by imposing a maximum lift coefficient, $C_{L_{\max}}$, of 1.1. A constraint on the maximum power available was enforced. Sgarioto [142] also applied a maximum lift coefficient to the aircraft.

This method has also been used extensively in the design of airborne wind turbines

based on aircraft flying in a circular or "8-shaped" flight path. Figiano [55] studied control methods to maximize the power harvested from tethered flexible wings. The aerodynamic model of the flexible wing uses a non-linear function of the lift and drag coefficient as a function of the angle of attack. Those models do not consider the variation in velocity as a function of wingspan nor unsteady effects.

In a survey paper about airborne wind energy by the same author [54], it is shown that this approach is commonly used to evaluate the aerodynamic efficiency of airborne wind turbines. The same conclusion can be extracted from a review article by Ahmed in 2012 on flexible kites to harvest wind energy [5].

Zanon [172] compared the performance of single and dual tethered aircraft flying in circular paths to harvest energy based on the concept by Makani Power. The aerodynamic models neglected the variation of the lift as a function of span, the unsteady effects, and the wake interaction. A simple model proposed by Damon Vander Lind, the lead engineer at Makani Power (see Chapter 28 of [6]), is based on the approximate method highlighted in this section. Experimental results validated the models. However, it must be noted that the inflow at the rotor for a wind turbine compared to a helicopter differs significantly.

Williams [6, 161] also contributed to the field of airborne wind turbines by studying the efficiency and control methods of flexible kites to harvest power. Both studies assumed a simple aerodynamic model similar to a point mass approach.

In summary, the use of an approximate method based on Prandtl's lifting line is commonly used in conceptual design of fixed wing aircraft and airborne wind turbines. It was shown that the method was also used for conceptual design study of circling aircraft to lift payloads. However, it is unclear how valid this approach is for the design of fixed-wing aircraft flying in a circular path since the wake interaction and the variation in wind velocity across the span are not considered. Moreover, the change in induced drag associated with the rapid motion of the vehicle or control

surface deflection cannot be captured.

2.2.1.2 Vortex-Lattice and Panel Methods

The application of numerical techniques allows the treatment of more realistic geometries while taking advantage of the increase in computational power. Two general methods are described: the vortex lattice method and the more general panel methods. Both methods are described to provide an overview of the limitations and capabilities of those methods. The reader should refer to Katz and Plotkin [93], Anderson [10], Bertin [18] and Hess [73] for an overview of those numerical methods. Also, the readers should refer to the work of Margason [107] for a comparison of commercial surface panel methods: HESS, VSAERO, QUADPAN, MCAERO and PAN AIR codes, the last two codes being of higher order.

Both classes of method attempts to solve the Laplace equation, which is a simplification of the more general Navier-Stokes equation under the assumption that the flow is inviscid and incompressible. The sum of the solutions to the Laplace's equation is also a solution to the equation. This property, the principle of superposition, is the basis of vortex-lattice and panel methods. First, the more general class of panel methods is described which are essentially an extension of the vortex-lattice method through the introduction of the thickness of the lifting surface [169].

The surface is discretized in quadrilateral panels lying on the surface of the body. A finite set of control points, equal to the number of singularity parameters, is selected at which the boundary conditions are imposed. Typical singularities are sources, doublets or vortices. For each control point, the velocities induced at the control point by the singularities associated with each of the panels of the configuration are summed, resulting in a set of algebraic equations. Figure 17 shows a representation of an airplane flow field by panel methods.

Vortex-lattice methods are suited for the numerical investigation of complex lifting

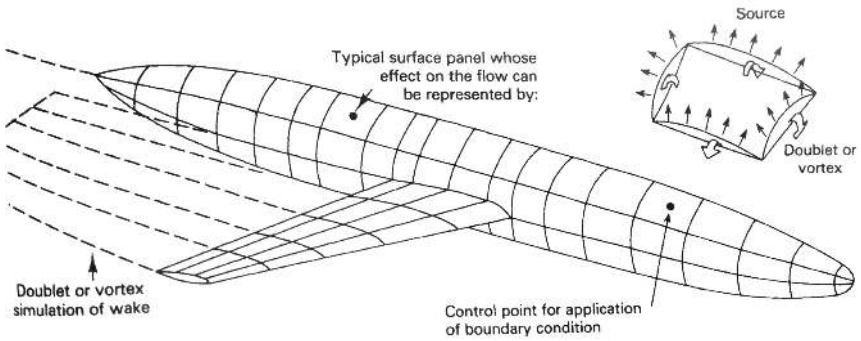

Figure 17: Representation of an airplane flowfield by panel methods [18].

surface geometries, in which classical formulations ignore thickness. Vortex lattice methods were first formulated in the late 1930s. The widespread adoption of the method was seen in the early 1960s with the development of computers. Vortex-lattice methods are more efficient than panel methods due to the lower number of singularities [23] but they fail at capturing the effect of the wing thickness.

The vortex-lattice methods (VLM) are based on a discretization of the lifting surface into quadrilateral panels. One of the salient differences between the general panel methods and the VLM are the singularities; the latter uses vortices only. Figure 18 shows a notional vortex lattice system on a finite wing and the schematic of a single horseshoe vortex with its control point. The set of algebraic equations is then solved to obtain the individual vortex strength. Finally, the lift is calculated using the pressure distribution or by the Kutta-Joukowski theorem. The drag can be estimated using numerous approaches, such as the energy in the Trefftz plane or the vorticity at the trailing edge [23].

The traditional VLM assumes that the wing wake remains flat and aligned with the freestream or along another axis as defined by the user, such as the aircraft reference axis. The traditional VLM is applicable only to a low camber airfoil. The low computational cost of this method makes it practical for conceptual design, as shown by the popularity of the well-known code AVL by Drela and Tornado by Merlin [111]. As an example, Smooth [148] used AVL to evaluate the lift and drag of kites

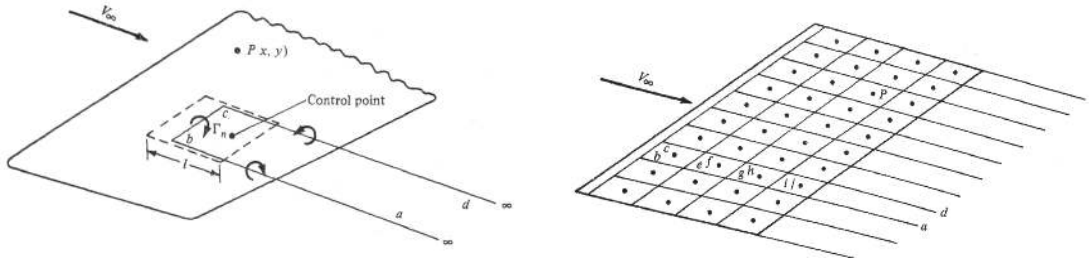

(a) Single horseshoe vortex (b) Vortex lattice system

Figure 18: Representation of the vortex lattice method [10] based on horseshoe vortices.

to study the performance and stability of tethered platforms.

A derivative of the VLM, the unsteady lifting-surface solution by vortex ring elements is described in detail in [93]. In this approach, the wing's bound circulation and the vortex wake are modeled by vortex ring elements. As per the traditional VLM, the velocity induced by the vortex rings is solved using the boundary condition at the collocation points. The intensity of the vortex rings is fixed once they leave the lifting surface. This method captures the effect of the shed vortices on the lift and drag. This method was used by Fritz [103] for the analysis of flapping wing aircraft and by Reichert [134] for the analysis and optimization of flapping birds. Wang [155] studied the aerodynamics of formation flight using the unsteady VLM with a force-free wake model. Mook [112] applied with success the unsteady VLM to high angle of attack delta wings.

In order to take advantage of the simplicity of the lifting line but keep the ability to model more complex geometries, the multiple lifting lines model was developed by Horstmann in 1986 (original publication in German: [79]). The panel elements have a parabolic circulation in the spanwise direction, with a continuous magnitude and slope between the elements. The shed vorticity is a sheet with a continuous spanwise vorticity distribution of first order. Traditional force-free VLM must use a solid core model to desingularize the velocity near the core of the vortex. Bramesfeld [23, 24] developed a force-free vortex wake model based on an extension of the multiple lifting

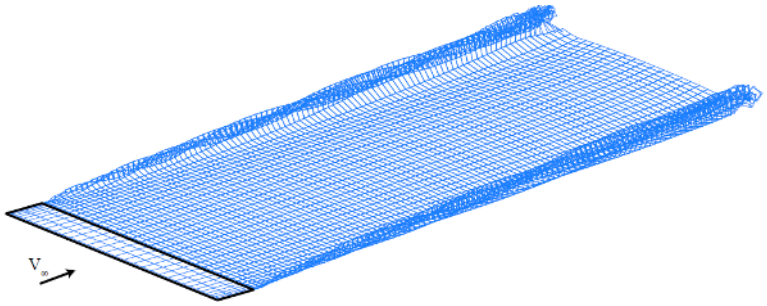

Figure 19: Vortex sheet roll-up in the wake [125] modeled using the Distributed Vorticity Elements (DVE) approach. The rectangular wing has an aspect ratio of 7 and an angle of attack of 4°. Convergence on lift and drag occurs after approximately 100 timesteps.

lines method.

This higher order method can handle unsteady flow, along with a force-free or prescribed wake geometry. The primary advantage is the fact that no singularities occur if the flow is steady and the trailing vortices are defined with a continuous sheet instead of discrete vortices with an infinite velocity at the core. However, the computational cost for each panel is higher than traditional first order VLM. Since 2006, this method has been applied to single wings, multiple wings in formation flight, wind turbine analysis, and to propeller-wing interaction [125].

Among the numerous variants of VLM and panel methods, a significant difference in computational cost is observed between force-free and prescribed wake models. In theory, a free shear layer in the wake cannot support any forces after it is shed from the trailing edge, and therefore, it must be displaced by the local flow field. This phenomenon can easily be seen by observing the roll-up of the vortex sheet near the tip, as computed by Patterson [125] for a rectangular wing at 4° angle of attack as shown in Figure 19.

In a fixed-wake model, it is assumed that the wake shape is prescribed, either along the direction of the free stream velocity or a reference plane [93]. Although there can be a reduction in the accuracy of the predicted drag coefficient, the lesser computation effort is significant. A free-wake model (force-free wake) requires $\mathcal{O}\left(N_S + N_W\right)^2$

evaluation of the induced velocities at each timestep, where N_S is the number of elements in the wake and N_W the number of elements on the lifting surface. On the other hand. prescribed wake models only require $\mathcal{O}\left(N_S^2 + N_S \cdot N_W\right)$ function evaluation. Given that the wake must be modeled for a considerable number of timesteps as shown in Figure 19, prescribed-wake panel methods can be orders of magnitude faster than free-wake models.

For a conventional fixed-wing airplane in a cruise condition at low angle of attack, the gain in accuracy is relatively small compared to the increase in computational cost to use a force-free wake model. However, as shown by Bramesfeld [23], the difference in the drag prediction is significant in the case where the wake between two vehicles can interact, such as during formation flight.

Bangash [15] studied the aerodynamic efficiency of formation flight using a hybrid approach. The aerodynamics of the leading aircraft was modeled using a lifting line method and only the two tip vortices were propagated in the wake with a Lamb-Oseen core model. The aerodynamics of the trailing aircraft was modeled using a panel method with a prescribed wake model, but considered the induced velocity from the tip vortices of the leading aircraft.

The analysis of formation flight is quite an interesting challenge as it attemps to capture the strength and location of the tip vortices of the leading aircraft while keeping the computational manageable. Also, the aerodynamics of fixed-wing aircraft flying along a circular path shows similarity to formation flight over long distances. Ning [121] studied the aerodynamic performance of extended formation flight with a streamwise spacing over 10 spans. The method used a vortex decay model (Holzäpfel model) with a wake roll-up method based on the theories developed by Betz. It was shown that the atmospheric stability affects the efficiency of formation flight due to the large distance between the vehicles.

2.2.2 Aerodynamic Modeling of Rotary-Wing Aircraft

As summarized in Figure 1, helicopter rotor aerodynamics differs significantly from fixed-wing aircraft aerodynamics. In hover, the flow can be assumed axisymmetrical, allowing use of low-cost methods to support conceptual design studies. On the other hand, the evaluation of the forward flight performance is much more challenging. The flow is inherently three-dimensional with unsteady effects, transonic flow conditions near the blade tip on the advancing side, and regions with reverse flow near the blade root on the retreating side. Although helicopter aerodynamic theory benefited greatly from the increase in computational power [88], it still remains an expensive process. This section highlights the analytical and numerical methods to evaluate the aerodynamics of rotary-wing aircraft during the conceptual design phase.

2.2.2.1 Momentum Theory

The simplest approach to evaluate the power required to hover for a rotary-wing aircraft is to evaluate the momentum that must be imparted to the flow through the rotor disk and then estimate the power required. This approach was pioneered by Rankine and Froude for the design of marine propellers and then used by Glauert for the design of aircraft propellers [14]. The method was then applied to the design of helicopter rotors in hover and climb.

The method is valid under the assumption of irrotational, incompressible and steady flow. It is also assumed that the flow through the rotor plane is one-dimensional, and therefore, of uniform velocity with no swirl.

The power required to hover out of ground effect given a thrust requirement T is [99]

$$P = \overbrace{T \cdot \underbrace{\sqrt{\frac{T}{2\rho A}}}_{v_i}}^{P_i} \cdot \frac{1}{FM} \tag{2}$$

where v_i is the induced velocity at the rotor plane, P_i is the minimum theoretical induced power, ρ is the air density, $A = \pi \cdot R^2$ is the disk area covered by the rotor, and FM is the figure of merit. Additional losses from a non-uniform inflow and parasitic losses on the blades are accounted by the latter term. For most modern helicopter rotors, FM ranges between 0.7 and 0.8 [36]. In other words, for a given rotor diameter, even with a perfect rotor it would not be possible to reduce significantly the power required in hover since most of the losses come from the induced flow.

This method cannot be used for blade design and is valid only at the limit where the number of blades becomes large. This method represents the basics of the blade element momentum theory (BEMT).

2.2.2.2 Blade Element Theory and Blade Element Momentum Theory

In order to incorporate the blade geometry in the prediction of the power required of propellers, the blade element theory was developed by Drzewiecki [99]. The blade element theory (BET) forms the basis of most comprehensive helicopter codes since it provides estimates of the radial and azimuthal distributions of the blade aerodynamic loading on the rotor. The main assumption is that each slice of the blades at a fixed radial location behaves independently, but three-dimensional effects such as tip losses can be considered.

At each spanwise location on the blade, the lift, drag and pitching moment coefficients of the airfoil sections are obtained through a table look-up approach or analytical methods given the local angle of attack. Let dr be the infinitesimal span of a blade section at radius r, the rotor thrust coefficient increment dC_T can be approximated by:

$$dC_T = \frac{1}{2} \underbrace{\left(\frac{N_b c}{\pi R} \right)}_{\sigma} C_l(\alpha) \, r^2 dr \tag{3}$$

where $C_l(\alpha)$ is the airfoil lift coefficient, N_b is the number of blades, c the local blade chord, and σ the local rotor solidity. The local lift coefficient is a function of the

local angle of attack α, which in return is also a function of the induced inflow. The blade element momentum theory (BEMT) was first proposed in the mid-1940's as a hybrid method to relate the momentum theory and the blade element theory. The incremental thrust provided by the blade section (Eq. 3) is equated to the incremental thrust evaluated from the momentum theory applied to the same annulus. Then, it is possible to solve the induced inflow in hover v_i or its normalized value λ_i. [1]

$$dC_T = 4\lambda_i^2 r dr \tag{4}$$

This method was shown to be accurate within a few percent for the prediction of the power required to hover especially for low solidity rotors [99]. Moore [113] used this approach to size the propeller of the Puffin in hover. The BEMT with a tip and root loss model was used to predict the power required in hover in the initial study by Demers Bouchard and Rancourt [44]. However, since the BEMT cannot capture the effect of the aircraft bank angle on the aerodynamic efficiency, the accuracy of this method is limited for specific flight conditions.

The evaluation of the blade loads in forward flight is much more involved than in hover since the axisymmetrical condition does not hold. The blade loads are a function of the azimuthal position. The main challenge remains the evaluation of the inflow velocity through the rotor plane. Numerous methods were developed over the last 80 years, as reviewed by Chen [27]. Glauert initially proposed a simple model to extend the momentum theory to forward flight, where the uniform inflow model would consider the advance ratio, μ,

$$\lambda_{\text{TPP}} = \underbrace{\mu \tan \alpha_{TPP}}_{\text{Normal flow}} + \underbrace{\frac{C_T}{2\sqrt{\mu^2 + \lambda_{TPP}^2}}}_{\text{Induced inflow}} \tag{5}$$

where α_{TPP} is the tilt of the rotor tip path plane with respect to the freestream and λ_{TPP} is the normalized velocity through the rotor plane. The advance ratio is defined

[1] The general BEMT can also be derived including a positive climb rate, but is limited to the hover case in the present formulation.

as the ratio of the flight speed to the blade tip speed. Although this model can be used early in the design process to provide a rough estimate of the power requirements in forward flight, it assumes that the whole rotor disk contributes to generate lift, and that the blades remain approximately in the same plane (small coning angle). Analytical expressions of the thrust and power required can be obtained with this simple inflow model.

The effect of the individual tip vortices tend to produce a highly nonuniform inflow over the rotor disk in forward flight. Non-uniform inflow models can represent the basic effects of the inflow resulting from the rotor wake. Those models are usually derived from a mix of experimental results and advanced wake theories. The reader should refer to Chen [27, 99] for a complete list of models. In most cases, the inflow models can only be applied to conventional rotor configurations which limit their use in the current problem. Given an induced inflow, one can estimate the power required by the rotor through the blade element theory and unsteady aerodynamic theories and the concept of azimuthal averaging.

A simplified approach to evaluate the power required in forward flight can be derived from an energy approach, where the power required comes from the induced inflow, blade parasitic drag, fuselage drag, climb rate, and tail rotor. Figure 20 shows the power requirement as a function of the airspeed for a conventional helicopter. It is shown that most of the power requirement in hover is for the induced flow to generate the lift, while at high forward flight, the fuselage drag (parasitic) contributes to most of the power requirements. It must be noted that conventional helicopter fuselage has a drag coefficient that can reach up to an order of magnitude higher than an airplane fuselage due to the landing gear, rotor hub, and separation in the tail section [99].

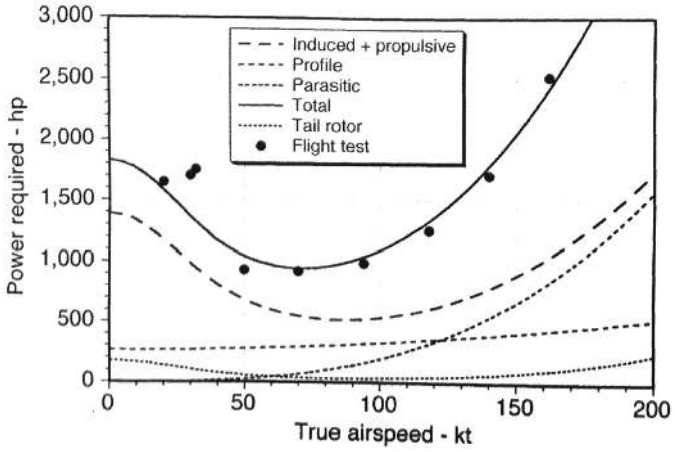

Figure 20: Distribution of the power required for a 16,000 lbs conventional helicopter at 1,585 m with $\kappa = 1.15$, $f = 2.137\text{m}^2$, $C_{d_0} = 0.008$ [99]

2.2.2.3 Advanced Wake Models Approach

The blade element method (BET) was shown to be an effective method to evaluate the forces on a helicopter rotor in hover and forward flight, as long as an accurate inflow could be provided. Such a model acts as a surrogate model of the actual inflow caused by the far field wake. For unconventional configurations or more detailed calculations, the inflow must be derived directly from the wake. This section introduces the basic concepts behind prescribed and free-wake models to analyze conventional helicopters. The reader should refer to Leishman [99, 101], Conlisk [35, 36], and Okulov [123] for a review of the wake models and implementation.

The general approach is to separate the aerodynamic modeling in two categories: the near-field and the far-field. The near-field models use methods such as the lifting line, panel methods, and table look-up to evaluate the loads on the blades with the additional effect of the induced velocity from the far-field. The far-field model evaluates the induced velocity from the strong tip vortex, root vortex, and shed vortices. Figure 21 summarizes the most common wake models.

First, the left-hand side of Figure 21 shows a few examples of inflow models, which can only be applied to conventional rotor types as they require a prior knowledge

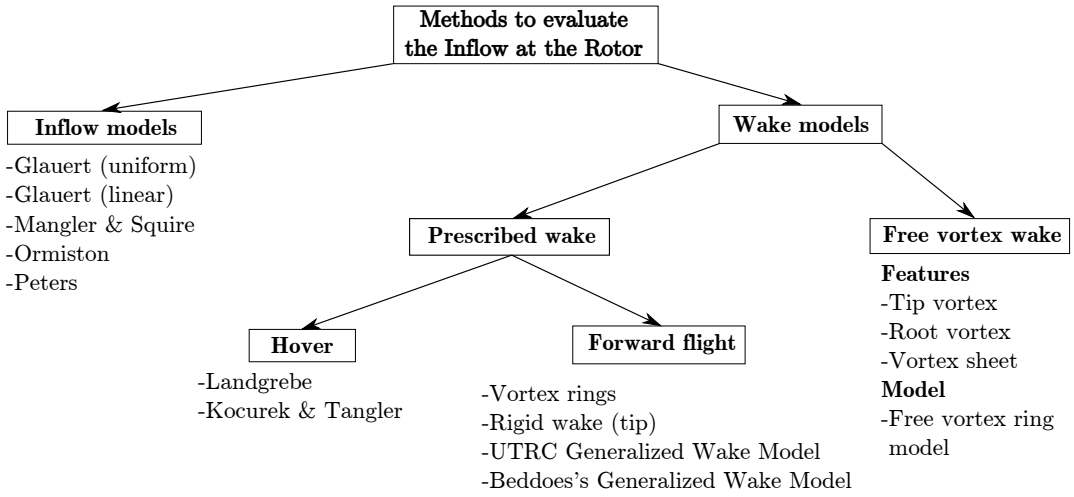

Figure 21: Overview of the methods to evaluate the inflow at the rotor plane. The inflow can be evaluated using two distinc categories: inflow models and wake models

of the wake parameters. The wake models can be separated into two categories: prescribed wake and free vortex wake. In both cases, the concept of a wake model is to evaluate the inflow at the rotor (or anywhere in the flow) given the shape of the wake and the use of the Biot-Savart law. Prescribed wake models assume that the wake shape is known as a function of a few parameters. For example, the Landgrebe model (only applicable in hover) assumes that the wake is constituted of a tip vortex, a vortex sheet, and a root vortex. The motion of those features was evaluated using the results of approximately 70 subscale helicopter configurations [99] to generate empirical relationships.

Prescribed wake models are also used in forward flight, such as the simple vortex ring model. In this approach, a stack of vortex rings (or vortex tube) is used to approximate the trailed wake vorticity from the rotor. The main advantage is that an analytic solution exists for the induced velocity given this prescribed wake shape. The ring position can be determined simply based on the momentum theory.

Free vortex wake models are much more general, but their computational cost is much higher since the induced flow by the wake itself contributes to the shape change

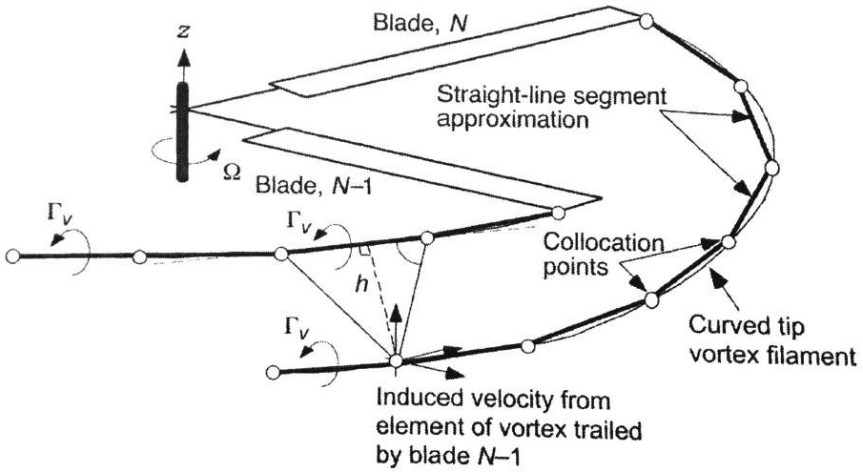

Figure 22: Notional representation of a free vortex wake model [99]. A straight-line approximation of the vortices is made and each vortex segment creates an induced velocity on all the other vortex segments, changing the shape of the wake as a function of time.

of the wake as shown in Figure 22. Those models solve for the vortex strengths and the rotor wake geometry, and therefore, do not need detailed physical experiments. Moreover, since those models are much more general and do not rely on empirical relationships, they can be applied to unconventional configurations. The accuracy and computational cost of free vortex wake models also depend on the features to be modeled. Since helicopter wakes are mainly driven by the strong tip vortex, numerous models only consider this element [101] with a desingularized core model. The reader should refer to Leishman [100] for more details. The most common core models are the Rankine vortex model, the Scully model, the Lamb-Oseen vortex model, and the Vatistas model.

Numerous examples are available in the literature about the use of free vortex wake models, and slight variants can be seen in their implementation depending on their application. Griffiths [68] studied the dual-rotor interference in the presence of ground effect using a free vortex wake model. A Lamb-Oseen model was used to desingularize the core and to consider the effect of viscosity. The far-wake model assumed only the presence of the strong tip vortex. The near-wake aerodynamics was

evaluated using the Weissinger model with 25 spanwise segments. The circulation in the near wake was carried over 10 degrees prior to being converted to the single tip vortex.

The evaluation of the blade loads and aerodynamic performance of propellers has also been analyzed with free wake models where the whole vortex sheet was trailed from the near field to the far field. Bramesfeld [23, 24] analyzed the aerodynamics of a helicopter rotor in hover as well as the aerodynamics of formation flight using a force-free high-order panel method. Although the method proved to be accurate, the computational cost was very high due to the number of function evaluations required to evaluate the induced velocity at every control point in the wake, at every time step.

Recently, Robertson and Reichert from Aerovelo [135] developed a novel approach to analyze the aerodynamics of helicopters in hover under the influence of ground effect. A vortex ring is emitted once per rotor revolution at numerous spanwise locations. The rings are convected in the flow at each time step. The downwash velocity induced on every axisymmetric ring is shown to be much more efficient than if the rings were discretized into linear segments. This model was used for the aerodynamic design of the Atlas Human-Powered Helicopter, which won the American Helicopter Society Sikorsky Prize in June 2013.

2.3 Observations and Summary

Extensive studies on the dynamic response of long tethers with and without payload were performed since the early 1970s. The main motivation was the need to create an improved method to pick-up payloads in remote locations and for long distance communication with very low frequency (VLF) radios using a single fixed-wing aircraft. Most research on the topic focused on the maximization of the verticality of the tip of the tether (payload) and the evaluation of the stability of the system.

One major limitation was to only consider conventional fixed-wing aircraft instead of much more maneuverable unmanned aerial vehicles (UAVs), such as proposed in the concept developed by Demers Bouchard and Rancourt. The use of conventional aircraft does not provide a truly VTOL system; the aircraft must still take off and land on a conventional runway since they are limited in their thrust-to-weight ratio. The maneuvers that can be performed by UAVs can be more complex with higher load factors, making the same task more difficult or impractical by pilots. Therefore, previous studies have not performed a detailed exploration of the various flight paths necessary to increase the efficiency, defined here as the power requirement to lift a given payload. Since the power source of the system is located in the fuselage, the fixed-wing UAVs weight is reduced, which increases their maneuverability. Finally, due to the size of the conventional aircraft used in the studies, only very long tether configurations were studied. Therefore, the consideration for unmanned fixed-wing aircraft increases significantly the variety of flight paths that each aircraft can perform in order to minimize the power required to lift a given payload.

All the studies of aircraft flying in a circular path, such as the one by Williams on multi-aircraft configuration [163], used a very low fidelity aerodynamic model based on the approximation of the lifting line theory (refer to Section 2.2.1 for more details). This model assumes no wake interaction between the aircraft, and thus, is valid if the spacing between the vehicle is large with a large flight path radius. In that case, the free stream velocity can be assumed uniform across the wing span. In the proposed concept, since the tether contains electrical conductors, it is expected that the optimal tether length might be shorter given the increase in weight and electrical losses. Therefore, wake interaction is expected to be present, or at least, should be evaluated. Moreover, the use of approximations of the lifting line cannot capture the effect of control deflection on the induced drag nor the effect of variable free stream velocity across the wing span. In maneuvers with rapid changes in the bank angle,

the change in the lift distribution and the associated losses should be captured.

A review of the conceptual methods to evaluate fixed-wing and rotary wing aerodynamic was presented. For rotary-wing aircraft, the induced power in hover contributes to more than 75% of the losses, while the rest such as the tip losses and parasitic drag contributes to approximately 25%. Therefore, conceptual design methods for helicopters focus on evaluating the losses in the inflow through inflow models or wake models with various levels of fidelity.

For fixed-wing aircraft, the induced (tip losses) and parasitic drag contribute to most of the losses, while there are no losses associated with the induced flow like a helicopter since it is assumed that the flight path is linear with the Prandtl lifting line. Advanced panel methods can capture non-linear flight path wake but such analysis was seldom performed due to the computational cost.

The *Electric-Powered Reconfigurable Rotor* VTOL Concept is a hybrid between a helicopter and fixed-wing aircraft with rapid control deflections, high variation in the velocity and bank angle as a function of the azimuthal position. Simple aerodynamics methods developed for helicopters or airplanes cannot be used for this concept. In hover, in the limit in which the diameter of the circular flight path is very large compared to the wingspan and that the wake completely dissipates within a very short distance behind each airplane, a fixed-wing approach could possibly be used as illustrated in Figure 23. On the other hand, if the annulus is almost a full disk such as a conventional helicopter, well known rotary-wing aerodynamic analysis methods could be used if the bank angle of the vehicles can be neglected. In between, there is a lack of understanding of how the analysis can be performed, especially in the presence of crosswind and variable aircraft bank angles. Therefore, there is a need to develop a novel method that can balance the computational cost while still capture the relevant physic phenomena.

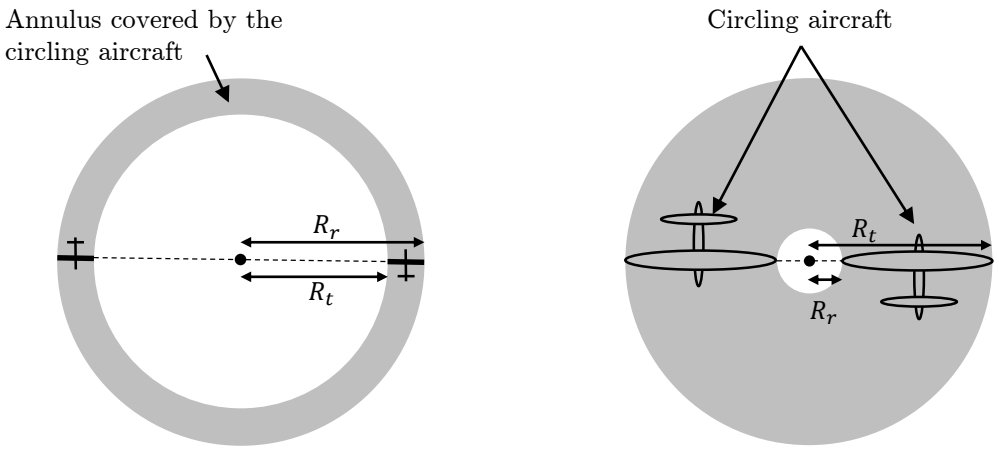

(a) Large diameter circular flight path (b) Small diameter circular flight path

Figure 23: Notional comparison of two configurations, one with a very low disk loading, large diameter circular flight path and one with a high disk loading with a small diameter circular flight path.

CHAPTER III

PROBLEM FORMULATION

3.1 Research Objective

Given the performance potential of this advanced helicopter concept and the lack of modeling capabilities to understand how to maximize the efficiency of the highly coupled system, the main research objective is:

Research Objective

Develop the method and models needed to evaluate and optimize the power requirement of the *Electric-Powered Reconfigurable Rotor* (EPR^2) VTOL Concept characterized by tethered aircraft flying along a quasi-circular and periodic flight path.

From the main objective, the following sub-objectives are derived:

- Improve the understanding of the aerodynamics of aircraft flying in a circular or quasi-circular flight path.
- Quantify the effect of the dynamic behavior of the tether for the EPR^2 VTOL concept.
- Retrieve the power curve of this helicopter concept for the optimal flight condition as a function of the flight speed.
- Evaluate what gap still exists in assessing the capability of this technology in order to guide future research investment.

The next section details the research questions to be answered, motivated by the global research objective.

3.2 Research Questions

Conventional helicopters have six main control degrees of freedom: cyclic (2), collective, tail rotor pitch, and two pseudo-controls (tilt and bank of the vehicle) provided that the rotor speed is constant. For a given flight condition, such as forward flight at a constant speed, there is only one setting of the controls (trim) that can be used to maintain that flight condition. For example, vertical motion is obtained by increasing the main rotor collective. More complex motions, such as a translation of the vehicle is obtained first with a tilt of the hub plane (initiated with a cyclic control input) and then with the tilt or pitch of the whole vehicle. Therefore, no optimization can be performed on how to trim the vehicle.

The reconfigurable rotor VTOL concept shows a much larger number of control degrees of freedom since a large number of flight paths can lead to the same airspeed of the system. Therefore, the first and overarching research question is:

Research Question 1

How can the flexibility in the tethered aircraft flight path of the EPR^2 VTOL Concept be used to minimize the power required to fly throughout the flight envelope?

The use of circular flight paths can be seen as the most obvious choice based on the paradigm of conventional helicopter rotors. Previous research on tethered payload towed by circling aircraft also used this approach given the simplicity to fly such flight path by manned aircraft. However, in the present case, much more advanced flight path trajectories can be exploited to reduce the power required as a function of the

flight speed. The following sections will expand on this research question with a focus on different flight phases.

3.2.1 Hover Phase

As shown in Equation 2, the induced power decreases with an increase in rotor disk area. Given that two or more aircraft have a fixed geometry, the rotor disk area can be increased by maximizing the turn radius of the aircraft, as shown in Figure 23. However, the benefits of the reduction in induced drag must overcome the increase in tether drag and losses associated with the increase in the bank angle.

Research Question 2

What is the most efficient flight path for each aircraft of the *Electric-Powered Reconfigurable Rotor* VTOL Concept to minimize the power required to fly in hover?

Since an increase in the disk area should reduce the induced power, it is expected that an increase in the constant-radius turn should be beneficial. Figure 24a shows two side views of the flight path and Figure 24b shows the disk area for a circular flight path in hover.

Another viable alternative is to fly the aircraft along non-circular flight paths to reduce the effect of the wake interaction, increase the apparent disk area and minimize the risk of vortex ring state (VRS) condition in descent. Figure 25a shows two side views of the flight path and Figure 25b shows the disk area for an hypotrochoid ("spirograph shape") flight path in hover as seen from above. This flight path is smooth, while covers a greater disk area than a circular flight path. The x and y axes define a plane perpendicular to the gravity, which is aligned along the negative z axis.

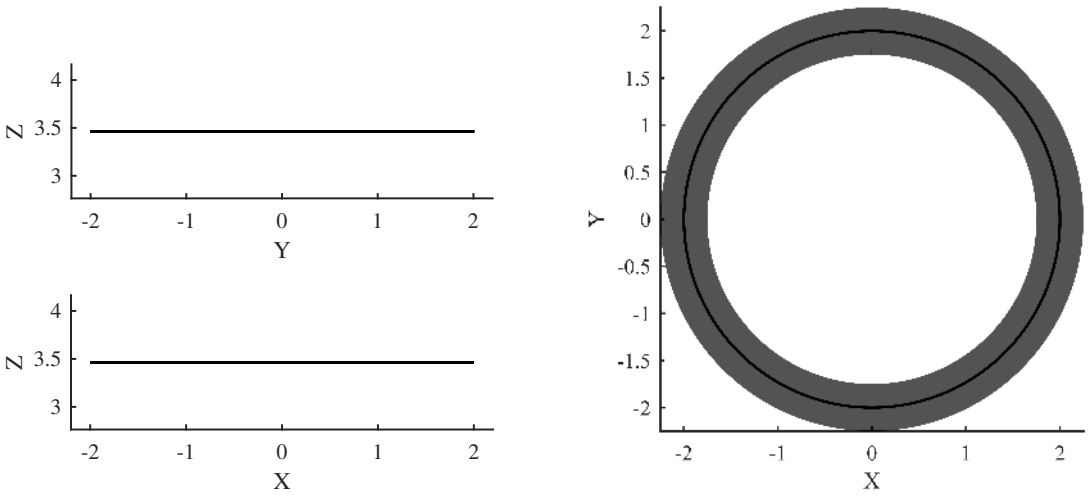

(a) Two side views of the aircraft flight path (b) Top view of the flight path and disk area

Figure 24: Flight path and disk area over 5 revolutions for a circular flight path in hover. The disk area is shown in dark gray and the aircraft flight path in a solid black line. Tether length: 4 units, flight path radius: 1.5 units.

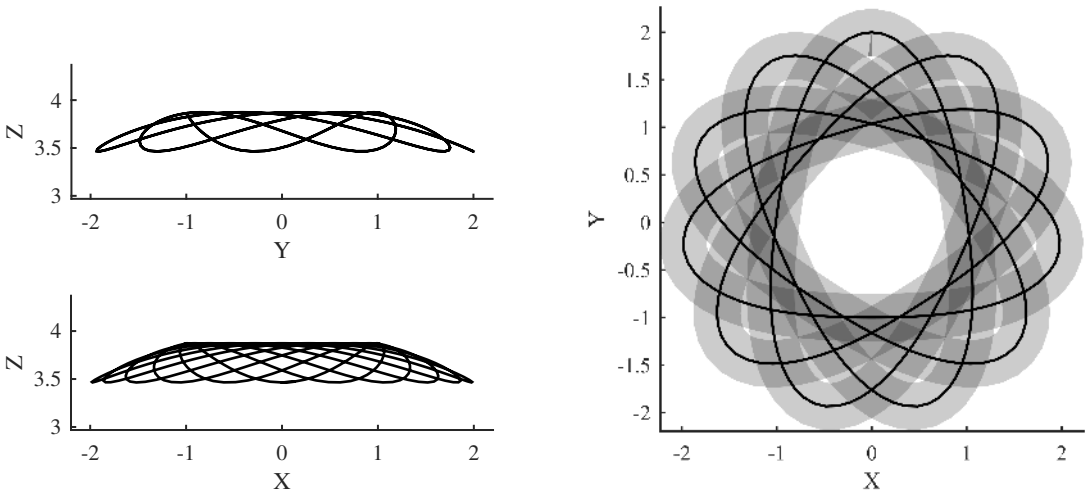

(a) Two side views of the aircraft flight path (b) Top view of the flight path and disk area

Figure 25: Flight path and disk area over 5 revolutions for an elliptical flight path with an offset every revolution (hypotrochoid) in hover. The disk area is shown in gray where the intensity represents the frequency at which the aircraft flies over this region. The aircraft flight path (center) is depicted by a solid black line. Tether length: 4 units, semi-major axis: 2 units, semi-minor axis: 1 unit, offset of 20% every revolution.

The hypothesis to Research Question 2 is:

Hypothesis to RQ 2

A non-circular and periodic flight path with a continuous phase offset can reduce the induced power and therefore the power required to hover assuming the dynamic behavior of the tether and the aircraft do not increase significantly the losses.

There are numerous losses to be considered. First, the dynamic motion of the tether will most likely create cyclic loads to be supported by the fixed-wing aircraft. Second, the proposed flight path requires continuous control inputs by the UAVs, which increases the trim drag. Third, the variation in lift and lift distribution will create unsteady aerodynamics, which will increase the system power requirement. Fourth, the change in potential energy must be compensated by a cyclic variation in the power requirement for each aircraft. The methods developed in this thesis to analyze the coupled system are able to consider those loss mechanisms.

3.2.2 Forward Flight with Periodic Aircraft Motion

As shown in Figure 1, conventional helicopters have a very complex flowfield due to the asymmetrical flow conditions on the advancing and retreating sides. The reverse flow region and the true airspeed on the advancing side increase the noise level and reduce the efficiency of the blade. As a result, conventional helicopters are limited to advance ratios on the order of $\mu = 0.3$.

The EPR^2 VTOL Concept allows the lift on the aircraft to vary as a function of the azimuthal position since an independent control of the aircraft is possible. Moreover, the angular velocity can vary as a function of the azimuthal position and the free stream velocity to maximize the efficiency of the system. The change from

a circular flight path to a non-circular flight path also changes the lift requirement of each aircraft as a function of their position. As an example, if the aircraft on the advancing side passes near vertical of the payload, the lift requirement increases compared to the other UAVs. In such case, a reduced relative airspeed would not be detrimental on the retreating side since the stall speed of the UAV is reduced. Given the high flexibility of this advanced helicopter concept and the inefficiency of conventional helicopters in high-speed flight, the third research question is:

Research Question 3

In forward flight, what flight path should be used to minimize the impact of the forward velocity on the tethered aircraft (advancing and retreating side), and thus, improve the efficiency?

The hypothesis to Research Question 3 is:

Hypothesis to RQ 3

A non-circular flight path with a non-center payload with load transfer between the tethered aircraft will mitigate the consequences of the reduction of the relative airspeed on the retreating side, and therefore reduce the power requirement compared to a conventional circular flight path.

The next chapter presents the models and the method developed for the analysis of the EPR^2 VTOL concept.

CHAPTER IV

DEVELOPMENT OF THE METHOD AND MODELS

4.1 Introduction

This chapter details the method developed to analyze and optimize the flight path of the tethered UAVs to reduce the power requirement. The objective of the new method is to be able to calculate the power requirement of tethered aircraft as a function of the system airspeed (airspeed that the whole system moves); the equivalent of the power curve for a conventional helicopter.

In a nutshell, the developed methodology is based on an inverse simulation approach to decouple the system and obtain only a feed-forward of information to minimize the computational time. The aircraft flight path is prescribed through a set of flight path variables, and the aerodynamic and dynamic simulations allow to extract the thrust requirement. Then, a propulsion model is used to evaluate the electrical power required from the power source.

In order to reduce the computational time of the whole methodology, a multifidelity approach is developed. It allows for global design space exploration using a lower fidelity set of models and then focuses on the regions of interest using the more accurate (and expensive) higher fidelity approach. This chapter presents the design structure matrix for both the lower and higher fidelity simulation environments.

This chapter first presents the physical breakdown of the system, the two design structure matrices, and introduces the various models developed. Then, each individual model is detailed and validated using both analytical and experimental results. Contributions of this work are clearly highlighted.

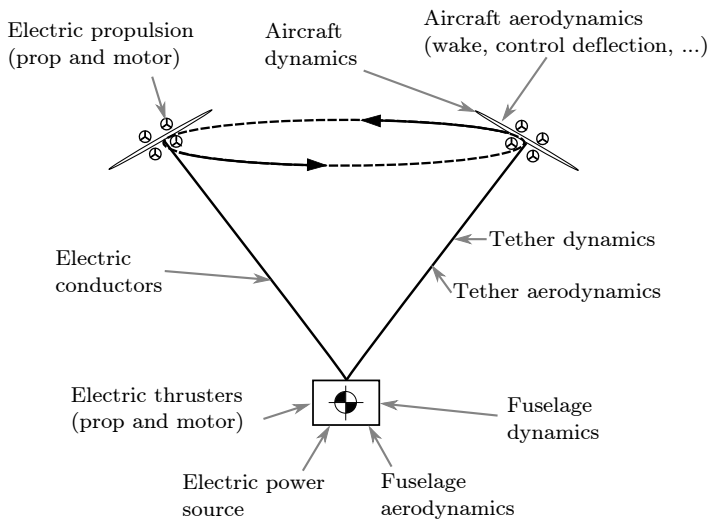

Figure 26: Overview of the models required for the electric-powered *Reconfigurable Rotor VTOL Concept*. This concept shows a high level of interaction between the subsystems.

4.2 Overall Methodology

4.2.1 Physical Breakdown

Figure 26 shows a physical breakdown of the EPR^2 VTOL concept, characterized by tethered aircraft powered by electricity provided by a power source in the fuselage. This chapter details the development of six models that are used to analyze the performance of tethered aircraft:

- Flight path parameterization of the tethered aircraft
- Tether and fuselage aerodynamics and dynamics model (Lower fidelity)
- Tether and fuselage aerodynamics and dynamics model (Higher fidelity)
- Coupled aircraft dynamics and lower fidelity aerodynamics model
- Higher fidelity aircraft aerodynamics model
- Propulsion and electrical system

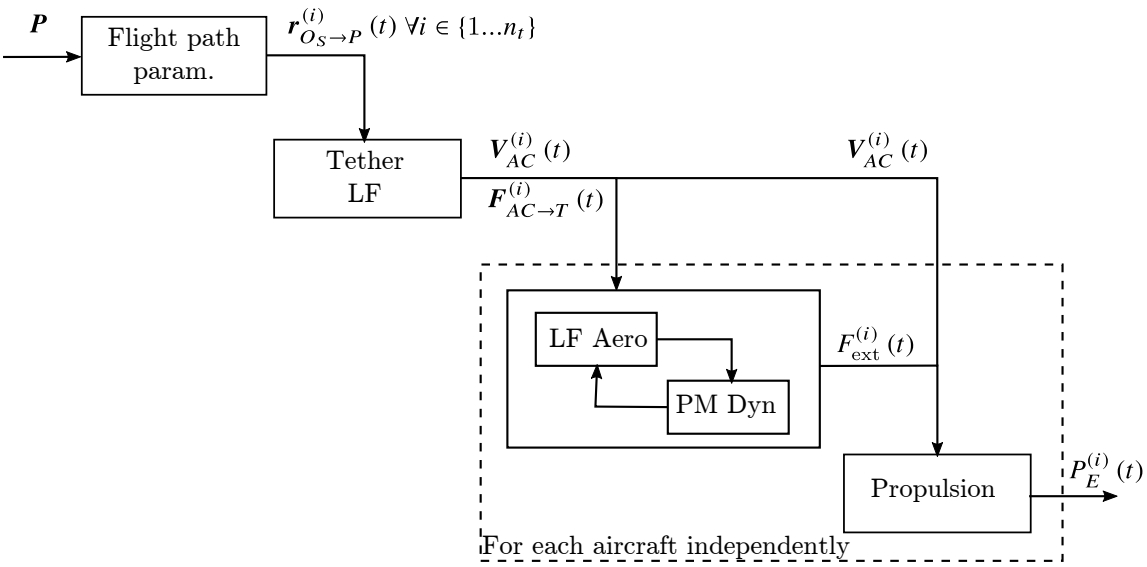

Figure 27: Design structure matrix of the low fidelity environment. (LF: Low fidelity, HF: High fidelity, PM: Point mass, dashed box: repeated process for each aircraft)

Before providing the details of each model, Section 4.2.2 presents the lower fidelity design structure matrix (DSM) and Section 4.2.3 details the higher fidelity design structure matrix (DSM). The introduction to the general architecture for both approaches should provide a better understanding of the requirements of each model.

4.2.2 Lower Fidelity Design Structure Matrix

The first modeling and simulation environment (M&SE) is used to explore the design space with minimal computational cost. It combines models that can provide sufficient information to discard unfavorable regions of the design space, using the set-based design approach.

Figure 27 presents the design structure matrix of the low fidelity modeling and simulation environment.

Let $\boldsymbol{P}$ be a small set of parameters that can describe the three-dimensional flight path of the tethered aircraft. The first model, *Flight path parameterization*, converts the parameters to an actual position vector for the $i^{\text{th}} \leq n_t$ aircraft with respect to

the system-carried frame, $\boldsymbol{r}_{O_S \to P_i}(t)$. Details about the reference frames are provided in Section 4.3.

Then the second model, *Coupled tether and fuselage aerodynamics and dynamics model, lower fidelity*, denoted "Tether LF", performs a dynamic simulation of the tether and fuselage given the prescribed aircraft trajectory. The metrics of interest are the relative velocity vector seen by each aircraft $\boldsymbol{V}_{AC}^{(i)}(t)$ and the force vector applied on each aircraft from the tether $\boldsymbol{F}_{AC \to T}^{(i)}(t)$.

A lower fidelity aerodynamic model combined wih a point-mass aircraft dynamic model are used to evaluate the thrust required $F_{\text{ext}}^{(i)}(t)$ as a function of time. Other metrics are also obtained, such as the lift coefficient and the aircraft attitude.

Finally, the *Propulsion and electric system model* is used to evaluate the electrical power required $P_E^{(i)}(t)$ as a function of time for each aircraft.

The first observation from this design structure matrix is the absence of feedback due to the inverse simulation approach adopted in this work. The second observation is that the aerodynamic analysis of each tethered aircraft is independent from the other aircraft.

The models presented in this design structure matrix are of relatively low cost, such that one simulation can be performed within seconds. The following section presents the higher fidelity modeling and simulation environment, which reuses several features of the lower fidelity M&SE.

4.2.3 Higher Fidelity Design Structure Matrix

The higher fidelity modeling and simulation environment is much more computationally intensive, but captures effects that have never been studied before for tethered aircraft, such as wake interaction. Figure 28 illustrates the flow of information in the high fidelity M&SE.

The first section of the higher fidelity M&SE design structure matrix is similar

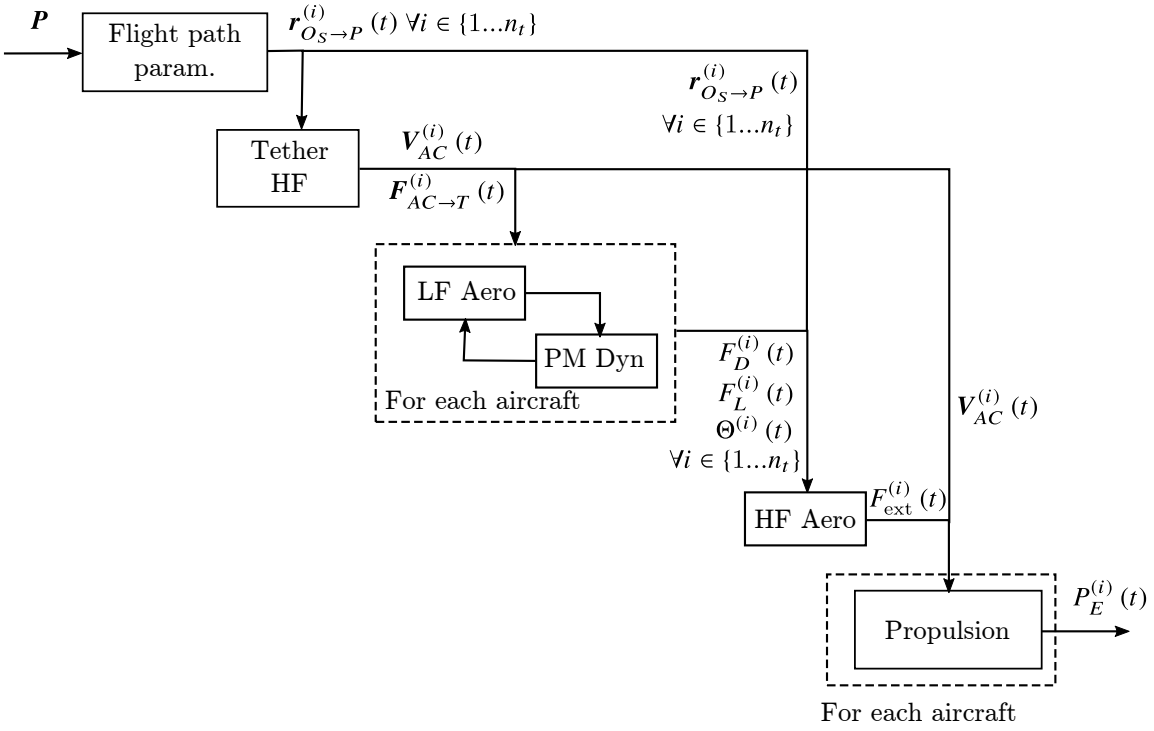

Figure 28: Design structure matrix of the higher fidelity environment

to the lower fidelity M&SE. A set of parameters $\boldsymbol{P}$ are used to define the periodic flight path of the aircraft, denoted $\boldsymbol{r}_{O_S\to P_i}(t)$. A higher fidelity dynamic tether model replaces the lower fidelity model, which captures the dynamic behavior, tether elasticity, and instabilities. As for the lower fidelity model, the metrics of interest are the relative velocity vector $\boldsymbol{V}_{AC}^{(i)}(t)$ and the force applied on each aircraft from the tether $\boldsymbol{F}_{AC\to T}^{(i)}(t)$.

The lower fidelity aerodynamic model and the point-mass dynamic model are used to approximate the aircraft attitude as a function of time, $\Theta^{(i)}(t)$, the target lift $F_L^{(i)}(t)$ and the resulting force from the tether aligned with the relative velocity, $F_D^{(i)}(t)$. This last variable does not include the drag terms; they are obtained from the higher fidelity aerodynamics model.

In contrast to the lower fidelity aerodynamics model, the higher fidelity model captures the wake interaction between the aircraft, considers vortex decay, control

surface deflection, and others. The increased complexity of this model translates into a significant increase in computational time, for simulation time reaching up to 1 hour on a personal computer (Intel i7-2600 CPU @ 3.4 GHz). One of the numerous interesting metrics of interest is the required thrust as a function of time, $F_{\text{ext}}^{(i)}(t)$, that is then used in the propulsion model to retrieve the power requirement.

The remaining of this chapter presents the individuals models and their validations.

4.3 Definition of the Reference Frames

A total of four reference frames are defined to analyze the kinematics of the periodic but non-circular flight path of the tethered aircraft:

- Earth-fixed reference frame E
- System-carried frame S
- Hub reference frame H
- Body (aircraft) frame - one per tethered aircraft B

4.3.1 Earth-Fixed Reference Frame

First, the Earth-fixed reference frame, denoted E, is fixed to the Earth surface. This reference frame is inertial since the Earth rotation and translation are neglected in the current work. Such an assumption can be made since the timescale of the analysis and the velocity involved are small relative to the size of the Earth. The Earth curvature is also neglected given the small traveled distance.

The origin of the reference frame, O_E is located on the surface of the Earth right below the system at the beginning of the simulation. A Cartesian coordinate system using the North-East-Down standard is attached to this reference frame.

4.3.2 System-Carried Reference Frame

The system-carried frame, denoted S, can be compared to the more conventional vehicle-carried frame defined in flight dynamics. This reference frame translates with the system but does not rotate with respect to the Earth-fixed reference frame.

The origin of this reference frame could be located at an arbitrary point on the EPR[2] since the system is comprised of numerous moving bodies. For practical reasons, the origin O_S is defined at the reference fuselage location. A Cartesian coordinate system with the conventional North-East-Down is also used with this reference frame.

4.3.3 Hub Reference Frame

Due to the complex aircraft flight path, an additional reference frame is required. The hub frame, denoted H, shows some similarity with the conventional hub plane as defined for helicopter rotors, except that it can also rotate about its z-axis. It will be detailed in Section 4.4.2 that this rotation is *not* used to defined the angular velocity of the UAVs about the payload. The origin of this reference frame, denoted O_H, coincides with the origin of system-carried frame O_S.

The hub frame is obtained through three rotations defined using Euler angles, θ_S, ϕ_S, and ψ_S as shown in Figure 29. The index $()_S$ is used to identify the System reference frame angles. The first rotation is $\theta_S + \pi$ rad about $\vec{j}_S$. The second rotation is ϕ_S about $\vec{i}_1$ The third rotation is ψ_S about $\vec{k}_2$.

The direction cosine matrix from the system-carried frame to the hub frame $[T_{S\to H}]$ is:

$$[T_{S\to H}] = L_3(\psi_S) \cdot L_1(\phi_S) \cdot L_2(\theta_S + \pi) \tag{6}$$

$$= \begin{bmatrix} c_\psi & s_\psi & 0 \\ -s_\psi & c_\psi & 0 \\ 0 & 0 & 1 \end{bmatrix} \cdot \begin{bmatrix} 1 & 0 & 0 \\ 0 & c_\phi & -s_\phi \\ 0 & s_\phi & c_\phi \end{bmatrix} \cdot \begin{bmatrix} c_\theta & 0 & s_\theta \\ 0 & 1 & 0 \\ -s_\theta & 0 & c_\theta \end{bmatrix} \tag{7}$$

where $c_x = \cos(x)$ and $s_x = \sin(x)$.

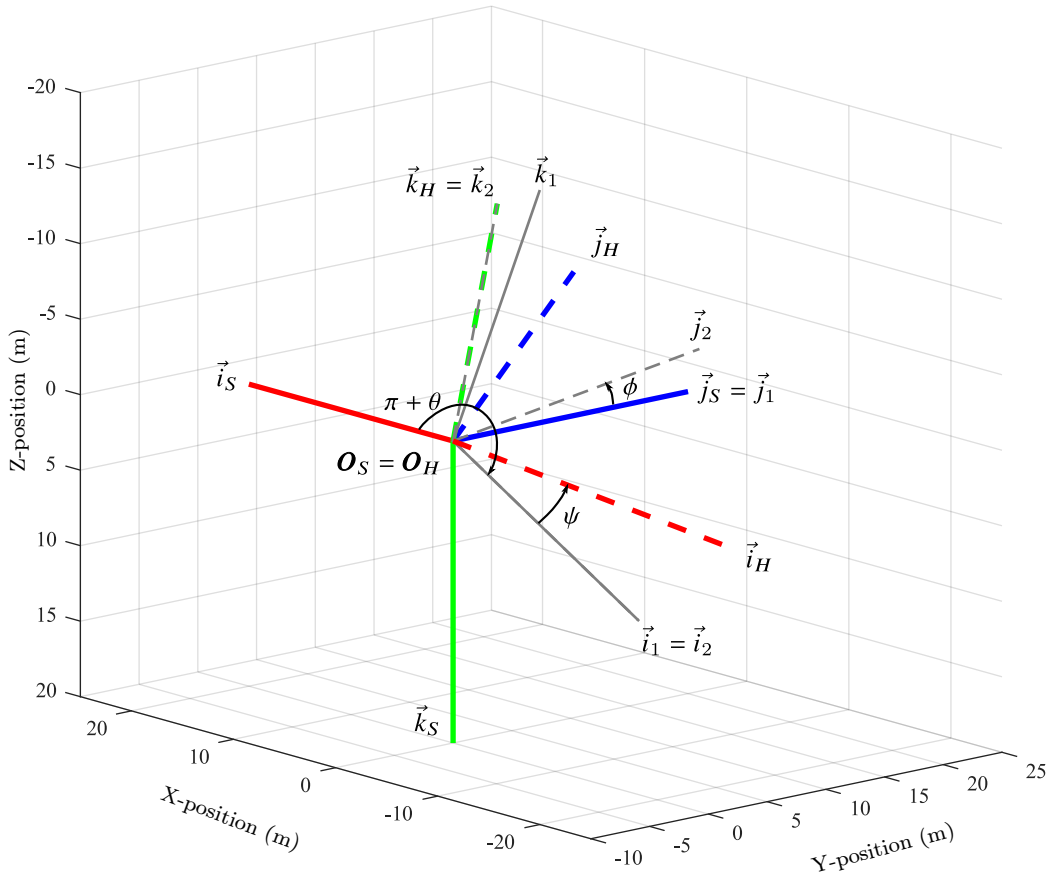

Figure 29: Definition of the angles between the system-carried frame S and the hub frame H. The hub frame is illustrated with colored dashed lines while the system-carried frame is shown with solid colored lines. The two intermediate frames are presented in gray.

Although the current implementation is flexible enough to allow for time-varying angles θ_S and ϕ_S, all the simulations are performed with a constant value of those variables. The angle ψ_S can vary with time to create an hypotrochoid flight path. The details about the approach to model the flight path is described in Section 4.4.2.

4.3.4 Body-Fixed Reference Frame

A body-fixed reference frame, denoted B_i is attached to each i^{th} aircraft at its center of gravity at $O_{B,i}$. A Cartesian coordinate system is used, where the x-axis points forward, y-axis towards the right wing, and z-axis points downward. As for the hub frame H, a set of Euler angles are used to define the attitude of the aircraft with respect to the system-carried frame S. The translation of the body reference frame with respect to the system-carried frame, denoted $\boldsymbol{r}_{O_H \to O_{B,i}}$, is driven by the tether tip position through the flight path parameterization. In the special case where the aircraft is modeled as a point mass, the tether tip location and the $O_{B,i}$ are coincident.

A more conventional approach using an $L_3(\psi_{B,i}) \to L_2(\theta_{B,i}) \to \cdot L_1(\phi_{B,i})$ rotation is used to convert to coordinates from the system-carried frame to the body reference frame B, where the index $()_{B,i}$ is used to denote the rotation definition for the i^{th} aircraft.

4.4 Flight Path Parametrization

4.4.1 Objective

The objective of the flight path parameterization model is to define the kinematics $(\boldsymbol{r}_{O_S \to P_i}(t))$ of the attachment point of the i^{th} tether to the unmanned aircraft with a minimal number of parameters $\boldsymbol{P}$, such that

$$\boldsymbol{P} \to \boldsymbol{r}_{O_S \to P_i}(t) \tag{8}$$

where $\boldsymbol{P}$ is a finite and small set of parameters. For conciseness, the i index will be omitted for the remaining of this section. The target parameters should allow the

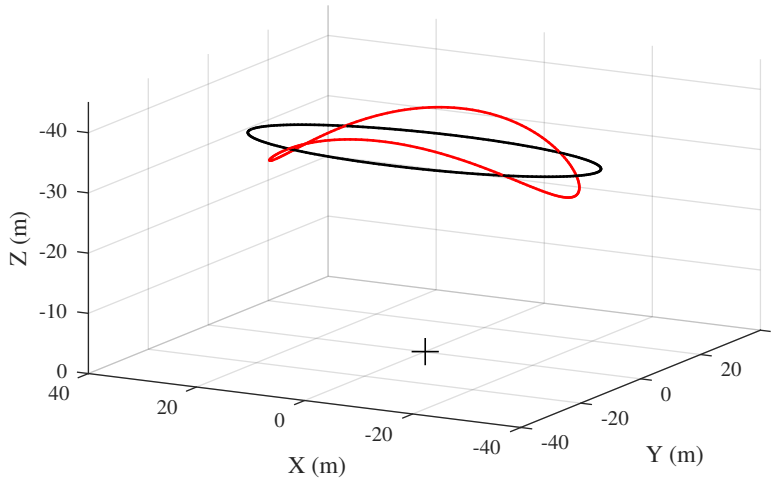

Figure 30: Effect of a constant tether length on a defined elliptical flight path. The black curve represents an elliptical flight path defined in the plane defined by $z = -35$ m. In order to maintain a constant tether length, the flight path has to be adapted, as shown by the red curve)

generation of unique and periodic flight paths with a decoupling between the critical parameters and include variations in the flight speed along the flight path. In order to illustrate this concept, a simple case is demonstrated, where it is desired to keep the distance between the target fuselage location and the aircraft constant. In other words, if tether elasticity is neglected, the fuselage would not move in space. In this example, the three coordinates required to define the flight path in three dimensions are coupled due to the tether length. Figure 30 illustrates the resulting flight path of one aircraft flying along a target elliptical flight path defined in 2D, with the height being derived for the tether length constraint.

The developed method to parametrize the periodic flight paths of tethered aircraft should meet the following characteristics:

- The parametrization method should allow for the definition of a flight path through parameters with decoupled effects, such that the design space (or the operating space) is approximately hypercubic.

- Each parameter should have a physical meaning that the user can relate to.

- Non-circular flight paths should be allowed with variable velocity.
- With minimal modification, the proposed method should also allow for flight path parametrization of non-periodic flight paths.

Section 4.4.2 presents the details of the parametrization method.

4.4.2 Parameters

The method presented in this section is based on the following parameters:

1. Baseline tether length
2. Baseline flight path in parametric representation
3. Height variation
4. Mean speed and variation in speed
5. Hub plane angles with respect to the system-carried frame

The next sections detail each category of parameters to fully define the tether tip kinematics.

The first parameter is the baseline tether length l_t. Since there is a desire to decouple the effect of the different parameters, the baseline tether length is used to create a flight path with a baseline distance from the fuselage reference point to the UAV constant to l_t, as shown in Equation 9,

$$l_t = |\boldsymbol{r}_{O_H \to P}| = |\boldsymbol{r}_{O_S \to P}| \tag{9}$$

where $\boldsymbol{r}_{O_S \to P}$ is the vector from the fuselage reference point to the tether tip.

Let $\boldsymbol{r}_{O_H \to P}$ be the position vector of the tether tip (on the UAVs) in the hub reference frame H. The position can be described using the measure numbers x, y, z such that

$$\boldsymbol{r}_{O_H \to P} = x\vec{i}_H + y\vec{j}_H + z\vec{k}_H \tag{10}$$

where $\left\{\vec{i}_H, \vec{j}_H, \vec{k}_H\right\}$ is a set of orthonormal vectors that define the coordinate system associated with the hub reference frame H, defined in Section 4.3.3. Let the three measure numbers be a function of a single parameter s, such that $x = x(s), y = y(s), z = z(s)$. Thus,

$$\boldsymbol{r}_{O_H \to P} = \boldsymbol{r}_{O_H \to P}(s) \tag{11}$$

which is a typical trajectory parametrization method. For an arbitrary and non-periodic flight path, the present parametrization method could be sufficient. For periodic flight paths with the desire to perform a design space exploration, the baseline flight path is constrained by the fixed tether length. Let d be the distance between the tether tip and the origin of the hub frame, located at the target payload location, as shown in Equation 12.

$$d = |\boldsymbol{r}_{O_H \to P}| \tag{12}$$

$$= \sqrt{x^2 + y^2 + z^2} \tag{13}$$

If the provided baseline flight path is in three dimensions, the measure numbers can be "corrected" to meet a constant distance with O_H. This transformation is enforced through Equation 14,

$$[x_1, y_1, z_1] = \frac{[x, y, z]}{d} \cdot l_t \tag{14}$$

where l_t is the reference tether length.

If the baseline flight path is provided on a plane (such as a circle, an ellipse or other geometric forms), the z measure number can be evaluated such that the norm is equal to the tether length by projecting the 2D shape on the sphere defined by tether length, as shown in Equation 15.

$$[x_1, y_1, z_1] = \left[x, y, \sqrt{l_t^2 - x^2 - y^2}\right] \tag{15}$$

In the current formulation, there is no limitation in the type of flight path that can be prescribed for the aircraft. However, for a design space exploration phase, it

is required to parametrize the flight path one step further to remove the dependency on s. Let the baseline flight path be an ellipse, defined by two normalized distance parameters, a and b, with $0 < a \leq 1$ and $0 < b \leq 1$. The flight path in two dimensions is defined by Equation 16

$$\frac{x^2}{a^2} + \frac{y^2}{b^2} = l_t^2 \tag{16}$$

or in parametric form

$$x\,(s) = l_t \cdot a \cdot \cos(u) \tag{17}$$

$$y\,(s) = l_t \cdot b \cdot \sin(u) \tag{18}$$

with $0 \leq u < 2\pi$ for one period.

In the limits, if $a = b = 0$, the position of the aircraft is still, right above the payload at a distance $z = l_t$. If $a = b = 1$, the flight path is a circle of radius l_t at $z = 0$.

For any ellipse defined using a and b, the reference measure numbers $x(u), y(u), z(u)$ are obtained. If desired, flight path types other than an ellipse could be developed, such as the Steiner inellipse, the Steiner ellipse, the multifocal ellipse, the superellipse, and others, by using the same approach shown in this section. In the limit, one could directly define a finite (and small) set of x,y coordinates, as a function of s and use a smooth interpolation method to obtained a continuous flight path.

At this point, there is no relationship between the flight speed and the flight path. The actual velocity is obtained through another parameter that relates u to time t, as explained later in this section.

Before the application of the height variation parameter, two transformations are required. Let s be the arc length long the flight path, while u is defined as the unique parameter for the ellipse. Let s_n be the normalized arc length for periodic flight path, such that $0 \leq s_n < 2\pi$. First, a transformation is required such that a unit variation in the path coordinate leads to a unit distance covered. Then the second

transformation is used to normalized the arc length.

Let $\vec{e}_T$ be a unit vector tangent to the flight path, defined as

$$\vec{e}_T = {}^{H}\frac{d\boldsymbol{r}_{O_H \to P}}{ds} \tag{19}$$

where s is the arc length. The upper-left H indicate an H-time derivative. Using the chain rule,

$$|\vec{e}_T| = \left| {}^{H}\frac{d\boldsymbol{r}_{O_H \to P}}{ds} \right| \tag{20}$$

$$= \left| {}^{H}\frac{d\boldsymbol{r}_{O_H \to P}}{du} \right| \cdot \frac{du}{ds} \tag{21}$$

$$= 1 \tag{22}$$

the transformation that relates s to u can be obtained. The result is shown in Equation 23.

$$\frac{ds}{du} = \left| {}^{H}\frac{d\boldsymbol{r}_{O_H \to P}}{ds} \right| \tag{23}$$

The flight path is now parametrized such that

$$\boldsymbol{r}_{O_H \to P} = \boldsymbol{r}_{O_H \to P}(s) \tag{24}$$

where $0 \leq s < L$, the total flight path length. The final linear transformation allows representation of the periodic flight path over a single period using a normalized path length s_n, so that $0 \leq s_n < 2\pi$ using Equation 25.

$$s_n = \frac{s \cdot 2\pi}{L} \tag{25}$$

The variation in height parameter Δh can be described as a variation of d, the distance between the UAVs and the reference point at the origin of the hub reference frame by some percentage of the tether length l_t. Fourier series, defined in Eqs. 26-29 where x is replaced by s_n, are used to vary the tether length.

$$f(x) = \frac{1}{2}a_0 + \sum_{n=1}^{\infty} a_n \cos(nx) + \sum_{n=1}^{\infty} b_n \sin(nx) \tag{26}$$

$$a_0 = \frac{1}{\pi}\int_{-\pi}^{\pi} f(x)\,dx \tag{27}$$

$$a_n = \frac{1}{\pi}\int_{-\pi}^{\pi} f(x)\cos(nx)\,dx \tag{28}$$

$$b_n = \frac{1}{\pi}\int_{-\pi}^{\pi} f(x)\sin(nx)\,dx \tag{29}$$

The result (depicted as $f(x)$ in Eq. 26) represents a deviation from the baseline target distance. First and second order terms are used to parameterize the variation of only a few percent of the target distance. The corrected measure numbers to take into account for the variation in height is obtained through Eq. 30,

$$[x_2, y_2, z_2] = [x_1, y_1, z_1] \cdot [1 + \Delta h(s_n)] \tag{30}$$

where $0 \leq s_n < 2\pi$.

Conventional helicopters have a constant main rotor angular velocity. Tethered aircraft above a fuselage do not have this requirement, which has the potential to reduce the mean power requirement of the overall system. In order to enforce a variation in velocity as a function of the position along the flight path, the following approach is developed.

First, another transformation is required, such that the normalized path length with variation in height ranges from 0 to 2π. Let s be the path coordinates and L be the periodic path length with consideration for the small variation in height from $\Delta h(s_n)$. The variation in height using the Fourier series expansion increases the total path length, and such increase must be accounted for in the speed calculation.

Let V_m be the target mean speed in the hub frame and t be the time. The speed along s is allowed to vary along the flight path using a Fourier series. Let V_1 be locally defined as the initial prescribed speed along s.

$$V_1(s) = \frac{V_m + V_{a1} \cdot V_m \cos(s) + V_{b1} \cdot V_m \sin(s)}{k} \tag{31}$$

The actual velocity along s is obtained by scaling the velocity presented in Equation 31 to make sure that the actual mean speed (as a function of time) is enforced, as shown in Equation 32.

$$V(s) = \frac{V_1(s(t))}{\frac{\int_{t=0}^{t=t_f} V_1(s(t))dt}{V_m}} \tag{32}$$

By using this approach, the mean speed is easily prescribed by the user. A Fourier series is an effective method to prescribe this variation since the fight path is periodic with $0 \leq s < 2\pi$.

The measure numbers $[x_2, y_2, z_2]$ used to define the flight trajectory are defined in the hub reference frame H. Two parameters are used to "tilt" the hub reference frame with respect to the system-carried reference frame. The reader should refer to section 4.3.3 for a review of the angle definitions.

First, the hub plane can be tilted backward, similar to the rotor blowback from a conventional helicopter, with $\theta_S > 0$. Second, the hub plane can be tilted to the left with a positive value of $\phi_S > 0$. Both parameters are fixed in time since the objective of this work is to analyze the system in a periodic state for a constant wind velocity (or constant system velocity). Those simplifications could be removed with minimal efforts, where θ_S and ϕ_S could become a function of time. Given that the two reference frames have the same origin, the distance between the tether tip and the payload reference point remains valid after a rotation. It will be shown in Section 4.5 that a lateral or longitudinal tilt of the hub plane can be used to transfer loads between the UAVs if the flight path defined in the hub frame was initially centered with respect to the reference payload location.

The last parameter to define the aircraft kinematics is the hub reference frame rotation about $\vec{k}_H$, which can be used to create an offset in position between every period of the flight path. In simple terms, this parameter can transform an elliptical flight path to approximately a hypotrochoid. The expected benefits of using this flight path parameter should be seen in hover, where the power requirement of the

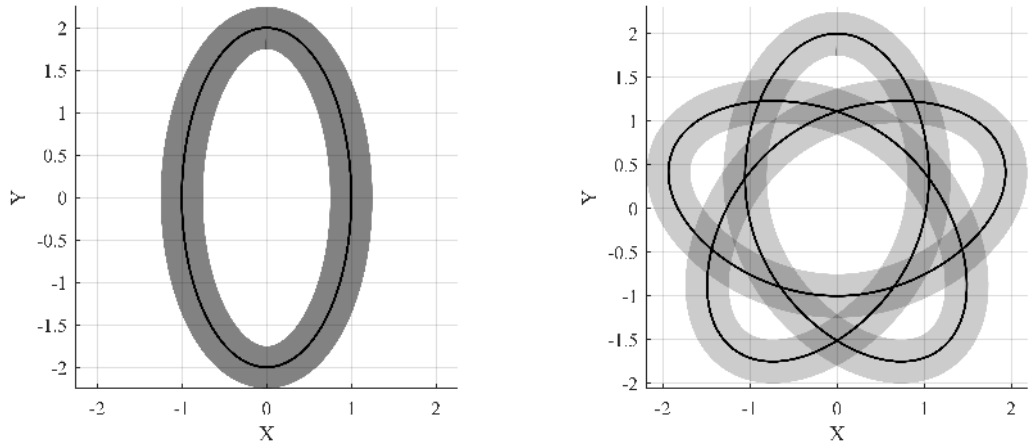

(a) Without hub frame rotation

(b) With hub frame rotation

Figure 31: Effect of the hub rotation on the area covered by an aircraft flying along an elliptical flight path. The swept area by the notional wing is depicted by the shaded area, while its level of darkness depicts the frequency at which the wing passes on the same region.

aircraft could be reduced if the total area covered by the aircraft over time is larger than if the aircraft would fly along the same flight path for every revolution. Figure 31 shows the effect of rotating the hub frame with respect to the system-carried frame for an elliptical flight path on the area covered by a single UAV. Since the velocity is defined with respect to the hub frame, if there is a rotation of H about $\vec{k}_H$, the velocity of the tethered aircraft with respect to the system-carried frame S will vary.

4.4.3 Position, Velocity, Acceleration

Let $[x_3(t), y_3(t), z_3(t)]$ be the measure numbers of the position of the tether tip P with respect to the system reference frame,

$$\boldsymbol{r}_{O_S \to P}(t) = x_3(t)\vec{i}_S + y_3(t)\vec{j}_S + z_3(t)\vec{k}_S \tag{33}$$

where the measure numbers are derived using the parameters described in the previous sections. The velocity can then be determined by taking a S-time derivative of the

vector position,

$$\boldsymbol{v}_{P/S} = {}^{S}\frac{d\boldsymbol{r}_{O_S \to P}(t)}{dt} \tag{34}$$

$$= \dot{x}_3(t)\vec{i}_S + \dot{y}_3(t)\vec{j}_S + \dot{z}_3(t)\vec{k}_S \tag{35}$$

since the unit vectors that define the coordinate systems are fixed in S. Finally, the acceleration of the aircraft in the system-carried frame is obtained by

$$\boldsymbol{a}_{P/S} = {}^{S}\frac{d\boldsymbol{v}_{S/P}(t)}{dt} \tag{36}$$

$$= \ddot{x}_3(t)\vec{i}_S + \ddot{y}_3(t)\vec{j}_S + \ddot{z}_3(t)\vec{k}_S \tag{37}$$

by similarity to the derivation of the velocity. It must be noted that since the system-carried frame may *not* be inertial due to some acceleration, corrections must be considered before directly applying Newton's law in the dynamic analysis of the tethers and UAVs. Verification cases of the flight path parameterization model are provided in Appendix C.

4.4.4 Summary

This section presented a method to parameterize the flight path of tethered aircraft flying along periodic and non-circular flight paths. The method has the advantage to decouple the effect of the parameters, such that the design space with feasible solutions is closer to a hypercube, thus improving the design space exploration.

A total of 12 parameters are used, but this number can increase as a function of the number of terms used in the Fourier series for the variation in height and perturbation of the velocity. In its simplified form, a periodic flight path is provided in the hub frame, in two dimensions. The altitude of the baseline aircraft flight path is determined based on the baseline tether length. Then, a deviation of the tether length and phase from the baseline is performed using Fourier series. Finally, three parameters are used to tilt and rotate the hub plane with respect to the system-carried frame. Each aircraft is given with its own flight path.

The method was validated using six test cases, for which analytical solutions were derived. It was shown that the numerical results are within engineering accuracy of the analytical solutions. Given a set of flight parameters, the position, velocity, and acceleration of the tether tips as a function of time are available. Those results are used both for the aircraft dynamics model and for the tether and payload dynamic model described in the following section.

4.5 Higher Fidelity Tether Dynamic Model

Section 4.4 presented an approach to create periodic aircraft flight paths from a small set of parameters. Moreover, with minimal modifications, this method can also be used to convert any prescribed flight path defined in two dimensions to a three-dimensional flight path with prescribed variations in the tether length. This section presents the *Higher Fidelity Tether and Fuselage Dynamics Model*, which uses the prescribed kinematics of the tether tip and evaluates the forces required on each tether tip to perform the trajectory. Those forces are then required for the analysis of the aircraft dynamics and thrust requirement.

The objectives of the model are as follow:

1. From the tether tip kinematics, determine the forces on the tether tip as a function of time, and the local wind velocity vector, both for transient maneuvers and periodic steady-state conditions.

2. Calculate the fuselage trajectory. This trajectory is not known a priori unless 3 tethers/aircraft are used and the tethers are rigid.

3. Determine the system stability and the effect of using a simple active control system to maintain the payload within reasonable motion.

4. Allow for design space exploration by maintaining a low computational cost.

In order to fulfill the last objective, a multifidelity approach is proposed to model the multiple tether and payload dynamics. The *lower fidelity* tether model assumes that the tethers are rigid rods. The *higher fidelity* model considers the tethers as a set of masses connected with springs and dampers. Although both models share similarities and provide relevant information on the performance of the system, the computational cost is more than two orders of magnitude different.

In a nutshell, the lower fidelity approach can provide a good estimate for tether drag, preliminary tether tension, and forces applied on the aircraft. Moreover, the lower fidelity tether model is used in the large-scale design space exploration, while the higher fidelity model provides insights on the need for active control methods to reduce the fuselage motion. The next section details the higher fidelity model and its validation and verification.

4.5.1 Introduction

The coupled tether and payload dynamics model is inspired by the work of Williams initially presented in [165] and reused without modifications on the method for numerous other studies by the same author [164, 166, 163, 162, 161, 159, 160]. The model is based on a lumped-mass representation. Modifications are developed to reduce the computational time as detailed in this section. Given the prescribed periodic aircraft kinematics ($\boldsymbol{r}_{O_S \to P_i}(t)$) the trajectory of the payload as a function of time is calculated, as well as all the tether segment states. From the latter, the tether tension can be derived. The forces that must be applied on the tether tip as a function of time are required for the aircraft dynamics and aerodynamics model. The details of the higher fidelity tether model are found in ref. [131].

Figure 32 presents the primary inputs and outputs of the higher fidelity tether dynamic model. The tether tip trajectory for each tether, $\boldsymbol{r}_{O_S \to P_i}(t)$ is an input to the model. The aircraft trajectory can be corrected slightly to take into account the

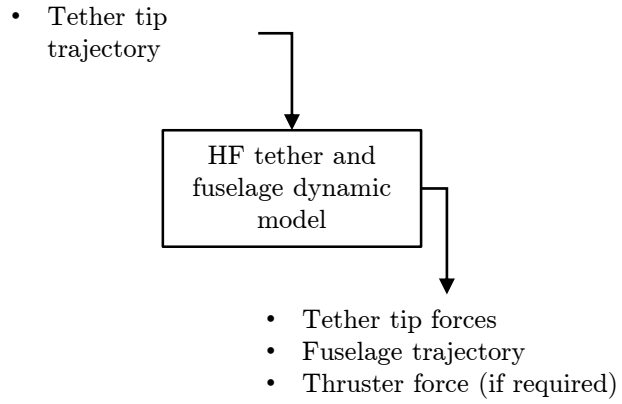

Figure 32: Primary inputs and outputs of the higher fidelity tether model

tether elasticity as will be demonstrated in Section 5.3.1.

The objective of the higher fidelity tether and payload model is to determine the tether tip forces that are applied to each aircraft given the prescribed flight path. Moreover, since the tethers are considered elastic, the payload location is not known a priori and must be found using a time-marching approach. The payload stability can be found by analyzing the payload trajectory over time. If required, the forces generated by thrusters on the payload can be evaluated to maintain the system stability. The energy required by the thrusters should be included in estimating the overall energy consumption of the system.

4.5.2 Theory

Let n_t be the number of tethers, with $1 \leq i \leq n_t$. In most applications and for the EPR^2 VTOL Concept, the number of aircraft is fixed to three. Each tether is discretized into n_s segments of undeformed length l_j^i, where $1 \leq j \leq n_s$ with $j = n_s$ being the tether segment attached to the payload. Let λ be the tether mass per unit length, which includes the electric conductors and the structural components. Then,

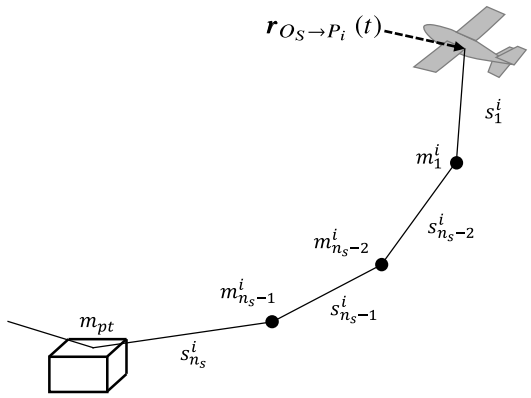

Figure 33: Tether segments

the lumped mass at node j and tether i is:

$$m_j^i = \begin{cases} \lambda \cdot \frac{l_j^i + l_{j+1}^i}{2} & \text{if } 1 \leq j < n_s \\ \lambda \cdot \frac{l_j^i}{2} & \text{if } j = n_s \end{cases} \tag{38}$$

The fuselage mass m_{pt} is comprised of the sum of the last tether segment weight $m_{n_s}^i$ and the actual fuselage weight m_p,

$$m_{p_t} = m_p + \sum_{i=1}^{n_t} \lambda \cdot \frac{l_{n_s}^i}{2} \tag{39}$$

Figure 33 shows how the tether is discretized. In order to simplify the notation, the tether index i is removed from this point and it is assumed that the process is repeated for each tether except noted otherwise.

The payload is assumed to be a point-mass, with only three degrees-of-freedom (translation). The tethers are all attached at the center of gravity of the payload. It is acknowledged that a full 6-DOF model would be required to capture the detailed payload trajectory, especially if the payload is a bluff body with strong unsteady aerodynamics. In the present model and study, the payload is assumed to be a streamlined body with an empennage (similar to an airplane without its wings), augmented with small thrusters and/or small lifting surfaces to better control its position.

The external forces applied on each discretized mass m_j are:

- Elastic forces, $\mathbf{F}_{\mathbf{e}j}$
- Damping forces, $\mathbf{F}_{\mathbf{d}j}$
- Aerodynamic forces, $\mathbf{F}_{\mathbf{a}j}$
- Gravitational forces, $\mathbf{F}_{\mathbf{g}j}$

Let the position of the j^{th} mass with respect to the system-carried frame S, $\boldsymbol{r}_{O_S \to m_j}$, be reduced to $\boldsymbol{r}_j$. Using the same approach, let the velocity of the j^{th} mass be reduced to $\dot{\boldsymbol{r}}_j$. Also, let ϵ_j be the strain of segment s_j defined as:

$$\epsilon_j = \frac{|\boldsymbol{r}_{j-1} - \boldsymbol{r}_j| - l_j}{l_j} \tag{40}$$

where l_j is the unstretched j^{th} segment length.

Let $\boldsymbol{r}_{\boldsymbol{n}j}$ be the normalized position vector from node j to $j-1$ as shown in Equation 41.

$$\boldsymbol{r}_{\boldsymbol{n}j} = \frac{\boldsymbol{r}_{j-1} - \boldsymbol{r}_j}{|\boldsymbol{r}_{j-1} - \boldsymbol{r}_j|} \tag{41}$$

The elastic forces $\mathbf{F}_{\mathbf{e}j}$ on element j are evaluated using Hooke's law (see Equation 42) with a parameter f_k to ensure that the elastic forces vanish if the tether becomes slack.

$$\boldsymbol{F}_{\boldsymbol{e}j} = k_e \cdot f_k(\epsilon_j) \cdot \boldsymbol{r}_{\boldsymbol{n}j} \tag{42}$$

where

$$f_k(\epsilon_j) = \begin{cases} 0 & \text{if} \quad \epsilon_j \leq 0 \\ \epsilon_j & \text{if} \quad \epsilon_j > 0 \end{cases} \tag{43}$$

The damping forces are evaluated assuming a linear viscous damper with a parameter $f_d(\epsilon_j)$ to ensure that the tether does not create any damping if the tether is

slack. Let $\dot{\epsilon}_j$ be the stretch rate of the tether segment j.

$$\dot{\epsilon}_j = \frac{(\dot{\boldsymbol{r}}_{j-1} - \dot{\boldsymbol{r}}_j) \cdot \boldsymbol{r}_{\boldsymbol{n}j}}{l_j} \tag{44}$$

The damping forces on node j from s_j are evaluated using Equation 45.

$$\boldsymbol{F}_{\boldsymbol{d}j} = k_d \cdot f_d(\epsilon_j) \cdot \dot{\epsilon}_j \cdot \boldsymbol{r}_{\boldsymbol{n}i} \tag{45}$$

where $f_d(\epsilon_j)$ is detailed in Equation 46.

$$f_d(\epsilon_j) = \begin{cases} 0 & \text{if} \quad \epsilon_j \leq 0 \\ 1 & \text{if} \quad \epsilon_j > 0 \end{cases} \tag{46}$$

The gravitational force on element j, $\boldsymbol{F}_{\boldsymbol{g}j}$, is the mass of the node mass multiplied by the gravity constant, with an orientation along the positive z-axis of the system-carried frame S. As for most problems of this type, the gravity field is assumed to be constant with altitude. It should be noted that Equation 48 is always valid since the system-carried frame does not rotate and that the curvature of the Earth is neglected.

$$\boldsymbol{F}_{\boldsymbol{g}_j} = m_j \cdot \boldsymbol{g} \tag{47}$$

$$= \left(0 \cdot \vec{i}_S\right) + \left(0 \cdot \vec{j}_S\right) + \left(m_j \cdot g \cdot \vec{k}_S\right) \tag{48}$$

The aerodynamic force $\mathbf{F}_{\mathbf{a}j}$ on the j^{th} mass is evaluated slightly differently than in the work of Williams [165]. The proposed method considers the velocity at the center of the segments instead of the velocity at the nodes, which increases significantly the accuracy given a fixed low number of tether segments. The aerodynamic forces are determined from the crossflow principle as detailed in [76] and physical experiments on the drag of a cylinder at various Mach numbers below the critical Reynolds number [104]. The crossflow principle equation used in this work was highlighted by Abkowitz [2] in his literature review of towed bodies as one of the most frequently

used approaches. For compactness, the tether index i is removed from the following equations. The lift and drag coefficients for a cylinder are given by:

$$C_{D,j} = C_{f,j} + C_{n,j} |\sin^3 \theta_j| \tag{49}$$

and

$$C_{L,j} = C_{n,j} \sin^2 \theta_j \cos \theta_j \tag{50}$$

Let $\boldsymbol{V}_j$ be the relative wind velocity at the *center* of the segment j and $\boldsymbol{W}_j$ be the normalized velocity, so that the norm of the velocity vector equals unity, $|\boldsymbol{W}_j| = 1$. The angle of attack of segment j, θ_j is evaluated from:

$$\theta_j = \arccos\left(\boldsymbol{W}_j \cdot \boldsymbol{r_{n}}_j\right) \tag{51}$$

The velocity parallel to segment j, $V_{p,j}$, and normal to the tether segment j, $V_{n,j}$, are obtained using Equations 52 and 53,

$$V_{p,j} = \boldsymbol{V}_j \cdot \boldsymbol{r_{n}}_j \tag{52}$$

$$V_{n,j} = \left|\boldsymbol{V}_j \times \mathbf{r_n}_j\right| \tag{53}$$

where $\boldsymbol{V}_j$ is obtained at the center of the segment. Using the results from Equations 52 and 53 and after conversion of $V_{p,j}$ and $V_{n,j}$ to Mach numbers, $M_{p,j}$ and $M_{n,j}$ respectively, the skin-friction and crossflow drag coefficients are obtained from Equations 54 and 55 from Cochran [34].

$$C_{f,j} = \begin{cases} 0.038 - 0.0425 M_{p,j} & \text{if} \quad M_{p,j} < 0.4 \\ 0.013 + 0.0395 \left(M_{p,j} - 0.85\right)^2 & \text{if} \quad M_{p,j} \geq 0.4 \end{cases} \tag{54}$$

$$C_{n,j} = 1.17 + \frac{M_{n,j}}{40} - \frac{M_{n,j}^2}{4} + \frac{5 M_{n,j}^2}{8} \tag{55}$$

Equation 55 is valid above a Reynolds number of approximately 100 [76, 157]. Therefore, any application of this equation for micro air vehicles would need a correction for low Reynolds number. This equation also does not consider the potential benefits

of operating the tether above the critical velocity, which could reduce the parasitic drag coefficient to a value as low as 0.4.

Finally, the lift and drag on each segment are evaluated as follows:

$$\mathbf{F_d}_j = \frac{1}{2}\rho_j C_{D,j} l_j d \left|\mathbf{V}_j\right|^2 \mathbf{e}_{D,j} \tag{56}$$

$$\mathbf{F_l}_j = \frac{1}{2}\rho_j C_{L,j} l_j d \left|\mathbf{V}_j\right|^2 \mathbf{e}_{L,j} \tag{57}$$

where d is the tether external diameter and the unit vectors oriented in the direction of the lift $\mathbf{e_L}_i$ and drag $\mathbf{e_D}_i$ are obtained from Equations 58 and 59.

$$\boldsymbol{e}_{D,j} = \boldsymbol{W}_j \tag{58}$$

$$\boldsymbol{e}_{L,j} = \frac{\left(\boldsymbol{W}_j \times \boldsymbol{r_n}_j\right) \times \boldsymbol{W}_j}{\left|\left(\boldsymbol{W}_j \times \boldsymbol{r_n}_j\right) \times \boldsymbol{W}_j\right|} \tag{59}$$

The sum of forces on each mass is then evaluated by distributing the aerodynamic forces from the center of the tether segments to the two nodes on each side as detailed in Equations 60 and 61,

$$\sum \boldsymbol{F}_j = \left(\boldsymbol{F_e}_j + \boldsymbol{F_d}_j\right) - \left(\boldsymbol{F_e}_{j+1} + \boldsymbol{F_d}_{j+1}\right) + \boldsymbol{F_g}_j + \frac{\boldsymbol{F_a}_j + \mathbf{F_a}_{j+1}}{2} \tag{60}$$

where

$$\mathbf{F_a}_j = \mathbf{F_d}_j + \mathbf{F_l}_j \tag{61}$$

The calculation of the aerodynamic forces for the payload itself assumes a streamlined fuselage with a conventional empennage similar to a blimp with only a drag term, as detailed by Khoury [94]. Let $\boldsymbol{V}_P$ be the relative wind velocity on the payload and $\mathbf{W}_P$ be its normalized value, then

$$\boldsymbol{F_D}_P = \frac{1}{2}\rho_P C_d A \left|\boldsymbol{V}_P\right|^2 \boldsymbol{W}_P \tag{62}$$

The payload node also receives 50% of the aerodynamic loads from the last element of each tether segment. An additional force $\boldsymbol{F_{th}}_P$ can be added to the point mass fuselage model from thrusters mounted on the fuselage. Those thrusters are assumed

to create a force through the center of mass (from the basic assumption of a point mass model). This force can be used to stabilize the fuselage in case of an unstable motion due to the tether elasticity.

The sum of forces that are applied on the payload is:

$$\sum \boldsymbol{F}_P = \boldsymbol{F}_{\boldsymbol{D}P} + \boldsymbol{F}_{\boldsymbol{g}_P} + \boldsymbol{F}_{\boldsymbol{th}P} + \sum_{i=1}^{n_t} \left(\boldsymbol{F}^{\,i}_{\boldsymbol{e}_{n_s}} + \boldsymbol{F}^{\,i}_{\boldsymbol{d}_{n_s}} + \frac{\boldsymbol{F}_{\boldsymbol{a}_{n_s}}}{2} \right) \tag{63}$$

where i is the index of each tether attached to the fuselage. In the extreme case where only one tether segment is used, 50% of the tether aerodynamic force is applied on the fuselage, and the other 50% is applied on the aircraft. This latter statement will be described in more detail in the aircraft dynamics section.

The equations of motion are then obtained using Newton's law. Since Cartesian coordinate systems are used for all the reference frames and that there is no rotation of the system-carried frame S, the sum of forces on the tether discretized masses equals

$$\sum \boldsymbol{F}_j = m_j \cdot \boldsymbol{a}_{m_j/E} \tag{64}$$

$$= m_j \cdot \left(\boldsymbol{a}_{m_j/S} + \boldsymbol{a}_{E/S} \right) \tag{65}$$

which is significantly simpler than if cylindrical coordinate systems are used.

The set of differential equations are solved using a state-space approach, for a total of $n_t \left(6n_s - 1\right) + 1$ states. To improve the convergence of the payload trajectory and forces as a function of time, the aircraft trajectory $\boldsymbol{r}_{O_S \to P_i}$, is slowly accelerated up to the desired periodic flight path. Once the forces and trajectory of the tether masses reach a periodic steady state, the desired metrics as a function of time are extracted.

One of the most important metrics to be extracted is the force that the tether tip imposes on the aircraft, namely $\boldsymbol{F}^{(i)}_{AC \to T}(t)$, for the i^{th} tether. This value is derived

from Equation 66.

$$\boldsymbol{F}^{(i)}_{AC\to T}(t) = -\left(\boldsymbol{F}_{\boldsymbol{e}1} + \boldsymbol{F}_{\boldsymbol{d}1}\right) + \frac{\boldsymbol{F}_{\boldsymbol{a}1}}{2} \tag{66}$$

The second metric of interest is the local wind velocity at the tether tip, $\boldsymbol{V}^{(i)}_{AC}(t)$. This value is reused for aerodynamics calculation of the tethered aircraft. Validation and verification cases are provided in Appendix C.

4.5.3 Improvement to the Aerodynamic Modeling of the Tether

Section 4.5.2 described the higher fidelity tether model, with one simple, but quite effective improvement over the previous work on tethered aircraft modeling. In most work, the aerodynamic forces are calculated at the discretized masses, while in the present work, the aerodynamic forces are calculated at the center of each tether segment, and transferred to the two masses on each side of the segment. Although this modification is small, it leads to a significant reduction in computational time through a reduction in the number of tether segments for the same accuracy, especially when the tether shape is nearly a straight line.

In order to demonstrate the benefits of this approach, two demonstrations are provided. First, a two-dimensional example with analytical solutions is provided, followed by a three-dimensional numerical example. Figure 34 illustrates the difference between the two approaches and a comparison with the theory for a two-dimensional tether with a linearly varying velocity between v_1 at $x = 0$ and zero at $x = L$;

If it is assumed that the tether drag coefficient C_d is constant and that the tether diameter is also a constant, the norm of the drag per unit length is simplified to,

$$F_D(x) = \frac{1}{2}\rho v^2 C_d d \tag{67}$$

$$= \frac{1}{2}\rho\left(v_1 - \frac{v_1 \cdot x}{L}\right)^2 C_d d \tag{68}$$

$$= \frac{1}{2}\rho C_d d v_1^2\left(1 - \frac{2x}{L} + \frac{x^2}{L^2}\right) \tag{69}$$

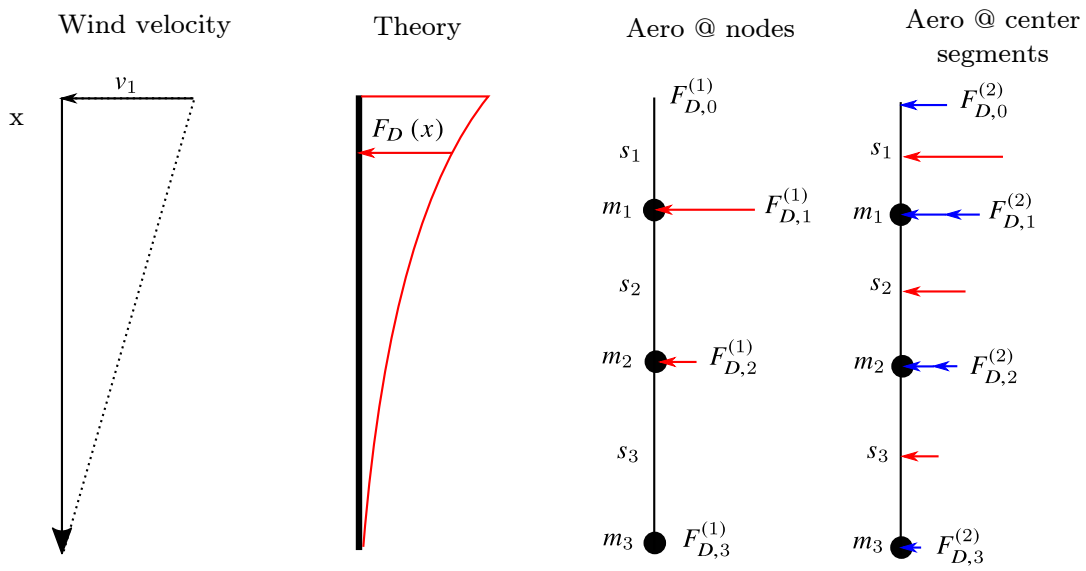

Figure 34: Effect of the location of the aerodynamic control point on the tether drag prediction. The first figure shows the velocity distribution for this example, from v_1 at $x = 0$ to 0 at $x = L$. The third figure shows the effect of evaluating the drag at the nodes, while the last figure illustrates the forces at the node (blue arrows) resulting from the evaluation of the drag at the center of the segments (red arrows).

where $0 \leq x \leq L$ and d is the tether drag, as shown in the second illustration in Figure 34. The total tether drag, locally denoted F_T, is the integral of Equation 67,

$$F_T = \int_0^L \frac{1}{2}\rho v_1^2 C_d d \cdot dx \tag{70}$$

$$= \left[\frac{1}{2}\rho C_d d v_1^2 \left(x - \frac{x^2}{L} + \frac{x^3}{3L^2}\right)\right]_0^L \tag{71}$$

$$= \frac{1}{6}\rho C_d d L v_1^2 \tag{72}$$

The centroid of the tether drag, locally denoted x_D, is evaluated using Equation 73.

$$x_D = \frac{\int_0^L F_D(x) \cdot x \cdot dx}{F_T} \tag{73}$$

$$= \frac{\int_0^L \frac{1}{2}\rho C_d d v_1^2 \left(x - \frac{2x^2}{L} + \frac{x^3}{L^2}\right)}{F_T} \tag{74}$$

$$= \frac{\frac{1}{24}\rho C_d d v_1^2 L^2}{F_T} \tag{75}$$

$$= \frac{L}{4} \tag{76}$$

The equivalent forces applied on the aircraft (at $x = 0$) and the payload (at $x = L$) are then found by solving for the sum of forces and sum of moments. The equivalent force at the aircraft, locally denoted $F_{eq,0}$ and the equivalent force at the payload, locally denoted $F_{eq,L}$ are,

$$F_{eq,x=0} = \frac{3}{4}F_T \tag{77}$$

$$= \frac{3}{24}\rho C_d d v_1^2 L \tag{78}$$

$$F_{eq,x=L} = \frac{1}{4}F_T \tag{79}$$

$$= \frac{1}{24}\rho C_d d L v_1^2 \tag{80}$$

which shows that 3/4 of the tether drag is transferred to the aircraft, and 1/4 is transferred to the payload. Since the tether cannot transfer loads other than tension (no bending moment is assumed), this force is the result of a slight tether curvature for which the projection of the tension is approximately equal to the forces shown in Equations 77 and 79. Figure 35 illustrates this concept.

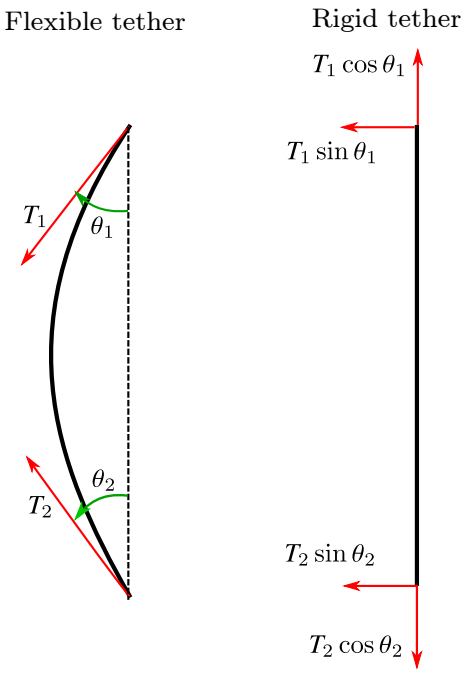

Figure 35: Difference on how lateral forces are transferred between a rigid and flexible tether

The forces at each node and the equivalent force at $x = 0$ and $x = L$ (assuming a rigid rod) for the two numerical methods presented in Figure 34 are evaluated. Let the force applied on each node be

$$F = \frac{1}{2}\rho C_d d L v_1^2 \cdot k \tag{81}$$

where k is detailed in Table 2 for each case.

Table 2 provides a short summary of the comparison of the predicted drag at each node and especially, the resulting forces at each tether tip for a model with three segments. The method proposed in this work, which evaluates the drag at the center of the segment, has an error of 5.6% in the prediction of the equivalent force at $x = 0$, $F_{eq,x=0}$, and 6% at $x = L$ compared to the analytical solution. The total drag prediction is only 2.8% less the analytical solution, for a discretization using only three tether segments.

The drag prediction using the velocity of the nodes lead (Option 1) shows a much higher error. The error on the total force prediction reaches 44%, and the same level

Table 2: Factor k to evaluate the localized drag force applied at each reference point

Variables	**Analytical**	**Aero @ node (1)**	**Aero @ center segment (2)**
$F_{D,0}$	–	0	0.116 (25/216)
$F_{D,1}$	–	0.148 (4/27)	0.157 (34/216)
$F_{D,2}$	–	0.037 (1/27)	0.046 (10/216)
$F_{D,3}$	–	0	0.005 (1/216)
$F_{eq,x=0}$	0.250 (1/4)	0.111 (1/9)	0.236 (153/648)
$F_{eq,x=L}$	0.083 (1/12)	0.074 (6/81)	0.088 (57/648)
F_T	0.333 (1/3)	0.185 (15/81)	0.324 (210/648)

of error is seen by the equivalent forces at the tips.

In summary, this analytical example demonstrates the benefits of evaluating the aerodynamic forces using the velocity evaluated at the center of each segment, applying the aerodynamic force at the center of the segment, and then transferring that force equally at both tips of each segment. It is understood that in the limit with a large number of nodes, both methods will return the same results. However, the computational cost will also increase accordingly.

The last demonstration on that topic uses the actual, 3D tether dynamics model. A circular flight path with a radius of 100 m is prescribed with a 300 m long tether towed at an angular velocity of 0.5 rad/s. The fuselage trajectory is constrained to remain at $x = y = 0$, but the altitude is free to vary. The tether diameter is constant at 5 mm, with a linear weight of 0.1 kg/m. Finally, the fuselage weight is fixed at 400 kg. The simulation is performed until a periodic steady state is reached, using both aerodynamic methods and by varying the number of tether segments. Figure 36 summarizes the results of this experiment.

As shown with the analytical model, the three-dimensional tether simulation reveals the increased accuracy of using the proposed method using the center of the segment. To complete the comparison, Figure 37 compares the total drag prediction

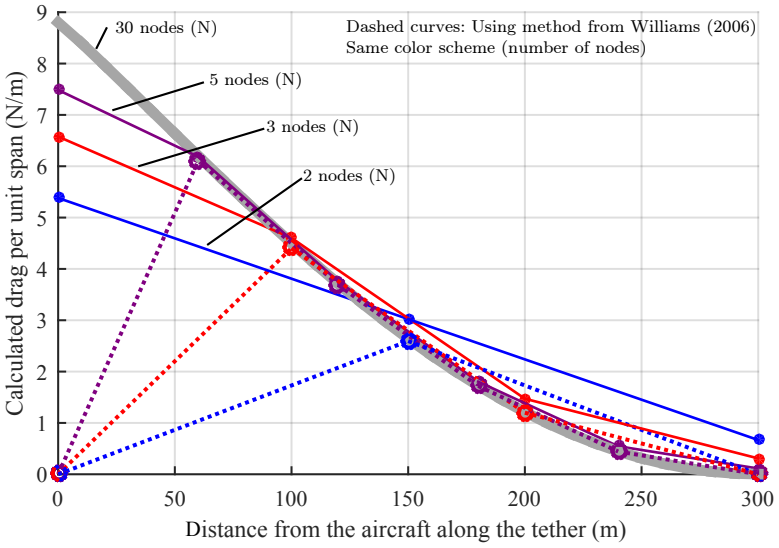

Figure 36: Drag per unit span as a function of distance for different numbers of tether segments. The solid curves connect the forces per unit span obtained for various number of elements. The dashed curves connect the forces per unit span with the aerodynamic method that used the nodes to evaluate the forces. The thick grey curve is considered the true value.

as a function of the number of tether segments for both methods.

As expected, *if* the tether remains in a relatively straight line, a coarse discretization can be sufficient to evaluate the tether losses with the novel method. The error in the drag is less than 1% with only 5 segments, while the other method requires more than 20 elements to reach the same level of accuracy.

4.5.4 Summary

The objective of the higher fidelity tether and payload dynamic model is to determine the payload trajectory and the tether forces applied to the aircraft. The aerodynamic, inertial, gravitational, and internal (elastic and damping) forces on the payload and tether are evaluated. A time-marching solution using a numerical integration method is used. The analysis of the payload motion over time reveals the stability of the system, which is significantly affected by the stiffness of long tethers.

Contributions were made on the method to obtain the aerodynamic forces on

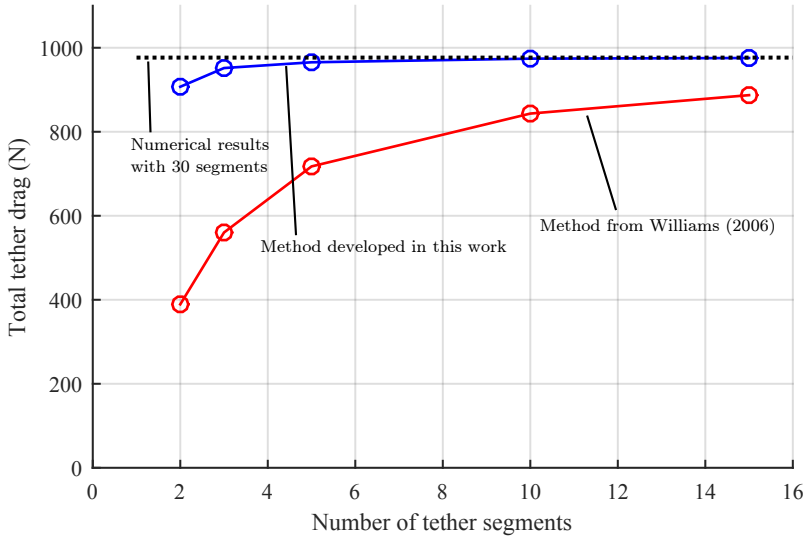

Figure 37: Tether drag prediction as a function of the number of tether segments for both aerodynamics methods. The blue curve represents the method that uses the center of the tether segment to evaluate the forces, while the red curve shows the method used by Williams [165]. The dashed line is considered the true value.

each tether element. Most numerical models consider the wind velocity at the node location instead of the center of the segment. For coarse tether discretization, such assumption can lead to a significant error on the tether drag prediction. The current implementation evaluates the tether aerodynamic force at the center of the segment and distributes this force equally among the nodes on each side.

In order to validate and verify the implementation of the model and each sub-component, four test cases were analyzed and detailed in Appendix C. A priority was given for cases with numerical solutions or experimental results. Only the results from the last test case were compared to numerical predictions to ensure that the complete model could reproduce the verticality property of long tethers while towed in a circle.

The computational cost of a full tether dynamic model increases rapidly with the number of tether segment and number of tethers. Since the periodic payload location is obtained only after the transient motion is damped, simulation times can reach more

than 30 minutes on a personal computer. A lower fidelity, and more computationally efficient tether model, is required to improve the process of exploring the design space.

4.6 Lower Fidelity Tether Model

Section 4.5 presented the theory and validations of a dynamic tether model. This model evaluates the payload motion and the tether forces that are applied to each aircraft, at the tether tips. However a dynamic model with discretized tether segments can quickly become expensive as the number of states required to model the system increases. Moreover, the damping force in the tether requires the time-marching solution to have very short timesteps to maintain the desired accuracy.

The number of tethers and aircraft is assumed to be three as shown in the EPR^2 VTOL Concept notional representations. Given a prescribed trajectory of three aircraft, most of the payload dynamics is only associated with the tether elasticity (except for radical aircraft motion which could cause the tethers to become slack). Three aircraft is the minimal number of aircraft for this statement to be true.

Numerical simulations with the higher fidelity tether model have shown that the tether remains relatively straight for most flight paths. This observation differs from the results by Williams, since much shorter tethers are used in the EPR^2 concept, and there is no requirement of verticality using a single tether. The following reasons explain this observation:

1. The fuselage mass is generally above one order of magnitude higher than the tether mass, reducing the tether dynamic motion to a minimum.

2. The tethers remain in tension throughout the motion.

3. The ratio of the tether drag and lift to the payload weight remains small.

The following hypothesis is made, and will be validated with this model:

Hypothesis

If the three tethers remain relatively straight with positive tension during the periodic flight path, then a lower fidelity tether model with a rigid representation of the tethers can provide first-order estimates of the required aircraft power and tether tension.

The assumptions and theory of the lower fidelity tether model are provided in the next section. It is important to note that this model is only valid if three tethered aircraft are used.

4.6.1 Theory

Let $\boldsymbol{r}_{O_S \to P_i}(t)$ be the position vector of the i^{th} tether tip (near the aircraft) in the system reference frame, with $i \in \{1, 2, 3\}$. Let L_i be the length of the i^{th} tether. The colinearity of the tether can be verified with Equation 82.

$$\nexists k : \boldsymbol{r}_{O_S \to P_i} = k \cdot \boldsymbol{r}_{O_S \to P_j} \quad \forall \quad i \neq j \tag{82}$$

If Equation 82 is respected, and the elliptical flight path parameters are bounded between zero and one, then there exist two possible payload locations given the aircraft positions if the tethers are modeled as rigid rods. For three aircraft flying along approximately a circular flight path, one possible solution is to have the fuselage *above* the three aircraft and the other solution is *below* the aircraft. The latter option should be considered.

The fuselage position $\boldsymbol{r}_{O_S \to f}$ given the prescribed aircraft position $\boldsymbol{r}_{O_S \to P_i}(t)$ is obtained by solving the set of three nonlinear equations as detailed below.

$$\begin{aligned} &\text{find} && \boldsymbol{r}_{O_S \to f} \\ &\text{subject to} && |\boldsymbol{r}_{f \to P_i}| = L_i \quad \forall \quad i \in \{1, 2, 3\} \end{aligned}$$

A numerical solver is used to solve for the fuselage position in the system-carried reference frame. Compared to the higher fidelity tether model, the lower fidelity model identifies the payload position only given the aircraft position, without any time dependence.

The fuselage velocity and acceleration are obtained by performing a numerical differentiation of the position as a function of time, as shown in Equations 83 and 84.

$$\boldsymbol{v}_{f/S} = {}^{S}\frac{d\boldsymbol{r}_{O_S \to f}(t)}{dt} \tag{83}$$

$$\boldsymbol{a}_{f/S} = {}^{S}\frac{d\boldsymbol{v}_{f/S}(t)}{dt} \tag{84}$$

If the standard set of flight parameters $\boldsymbol{P}$ are used, except the Δh terms, the payload position $\boldsymbol{r}_{O_S \to f}$ should always be the null vector. This result comes from the definition of the flight paths; they are defined to maintain a constant distance L_i with respect to the origin of the system-carried frame.

The aerodynamic modeling of the tethers is the same as for the higher fidelity tether model, except that the position of each tether segment is not obtained directly from the states, but from the fuselage and aircraft position at time t. For simplicity, let $\boldsymbol{r}_{O_S \to m_j^i}$ represent the nodes of the tether segments (where the masses were located in the higher fidelity model). Since the tether remains straight, the position of the n_s nodes for the i^{th} tether can be found from Equation 85.

$$\boldsymbol{r}_{O_S \to m_j^i} = \boldsymbol{r}_{O_S \to P_i} + \frac{j}{n_s}\left(\boldsymbol{r}_{O_S \to f} - \boldsymbol{r}_{O_S \to P_i}\right) \quad 0 \leq j \leq n_s \tag{85}$$

The velocity of the nodes is also evaluated using a numerical differentiation method. The aerodynamic forces are evaluated at the center of each tether segment using the same method. The reader should refer to Section 4.5.2 for more details on the aerodynamic model. The mass of the payload m_{p_t} is equal to m_p (the actual payload weight) because of the discretization method that considers the mass to be centered in the segments. Gravitational forces are considered for the payload as previously shown for

the high-fidelity model. The lower fidelity tether model can be summarized in four steps, of which the three first steps were described above.

1. Evaluate the aircraft kinematics (velocity, acceleration) at time t using the prescribed aircraft position.

2. Evaluate the fuselage (position, velocity, acceleration) at time t.

3. Evaluate the individual forces on the tether segments and the payload (aerodynamics, inertial, gravitational).

4. Solve for the tether forces on both ends of the tethers.

The last step consists in solving for the forces on the rigid tether (both tips) at each timestep. For this section only, let $\boldsymbol{F}_a^i$ be the force vector applied on the i^{th} tether, at location a, the attachment point between the tether and the aircraft. Using the same approach, let $\boldsymbol{F}_b^i$ be the force applied on the other end of the tether at the attachment point with the payload as shown in Figure 38. Each of those forces is comprised of three components (measure numbers) as detailed in Equation 86.

$$\boldsymbol{F}_a^{(i)} = \left(F_{a,x}^{(i)} \cdot \vec{i}_S\right) + \left(F_{a,y}^{(i)} \cdot \vec{j}_S\right) + \left(F_{a,k}^{(i)} \cdot \vec{k}_S\right) \tag{86}$$

An additional "pseudo-force", T_i is added, which represents a torque value along the tether. It will be shown that this value will always be zero, but this additional variable is required to have the same number of variables as the constraints.

For the three tethers, a total of 21 unknowns must be solved. Let the vector $\boldsymbol{X_i}$ be the vector of unknowns for tether i, and let $\boldsymbol{X}$ be the vector of all unknown:

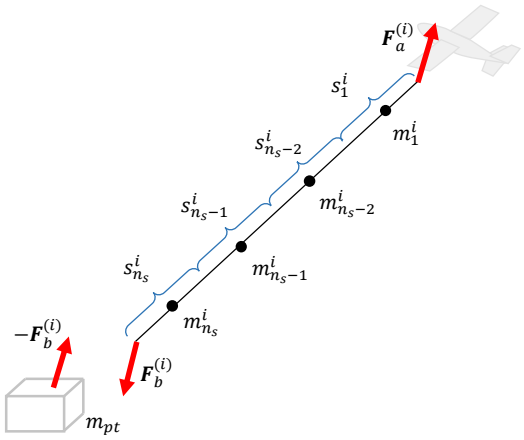

Figure 38: Tether discretization in the lower fidelity tether model. The individual masses are centered on the tether segments.

$$\boldsymbol{X_i} = \begin{bmatrix} F_{a,x}^{(i)} \\ F_{b,x}^{(i)} \\ F_{a,y}^{(i)} \\ F_{b,y}^{(i)} \\ F_{a,z}^{(i)} \\ F_{b,z}^{(i)} \\ T^{(i)} \end{bmatrix} \quad \forall \quad i \in \{1,2,3\} \tag{87}$$

$$\boldsymbol{X} = \begin{bmatrix} \boldsymbol{X_1} \\ \boldsymbol{X_2} \\ \boldsymbol{X_3} \end{bmatrix} \tag{88}$$

A set of 21 linear equations is constructed using the sum of forces and moments. First, the sum of forces on the payload must equal the mass times acceleration of the payload in the inertial reference frame,

$$-\boldsymbol{F}_b^{(1)} - \boldsymbol{F}_b^{(2)} - \boldsymbol{F}_b^{(3)} = m_{pt} \cdot \left(\boldsymbol{a}_{f/S} + \boldsymbol{a}_{S/E}\right) \tag{89}$$

resulting in the first three equations.

Then, the sum of forces and moments are derived for each tether. The sum of forces on each tether is simplified to,

$$\boldsymbol{F}_a^{(1)} + \boldsymbol{F}_b^{(1)} + \boldsymbol{F}_{\text{ext}}^{(1)} + \boldsymbol{F}_{\boldsymbol{D}P} = \sum_{j=1}^{n_s} m_j \cdot \left(\boldsymbol{a}_{m_j/S} + \boldsymbol{a}_{E/S}\right) \tag{90}$$

where $\boldsymbol{F}_{\text{ext}}^{(1)}$ is the sum of the aerodynamic forces applied on the tether and the right hand side is the acceleration of each element multiplied its mass.

Let $\boldsymbol{r}_{P_i \to m_j^i}$ be the position vector from the i^{th} aircraft to the tether mass j and $\boldsymbol{r}_{P_i \to f}$ be the position vector of the payload with respect to the i^{th} aircraft. The sum of moments about the tether tip near the aircraft is equal to the inertial reaction of each discretized tether elements.

$$\boldsymbol{r}_{P_i \to f} \times \boldsymbol{F}_b^{(i)} + \sum_{j=1}^{n_s} \left(\boldsymbol{r}_{P_i \to m_j^i} \times \boldsymbol{F}_{\text{ext},j}^{(1)}\right) + T_i \left(\frac{\boldsymbol{r}_{P_i \to f}}{|\boldsymbol{r}_{P_i \to f}|}\right) = \sum_{j=1}^{n_s} m_j \cdot \left(\boldsymbol{r}_{P_i \to m_j^i} \left[\boldsymbol{a}_{m_j/S} + \boldsymbol{a}_{E/S}\right]\right) \tag{91}$$

Equations 91, 90 and 89 are used to create a set of 21 linear equations to solve for the 21 unknowns. Since no torque can be applied on the tether, a sanity check consists in confirming that T_1, T_2, and T_3 are all zero. The tether tension is then evaluated by taking the average of the forces applied on each side of the tether, as shown in Equation 92,

$$F_T^{(i)} = \frac{\left|-\boldsymbol{F}_a^{(i)} + \boldsymbol{F}_b^{(i)}\right|}{2} \tag{92}$$

where $F_T^{(i)}$ is the mean tether tension.

4.6.2 Validation

This section describes two test cases that are used to compare the numerical predictions from the lower fidelity tether model to the higher fidelity, dynamic model. Those two experiments validate the hypothesis stated earlier in this section and the lower fidelity model.

Table 3: Salient results for the lower fidelity tether model, Test Case 1

Parameters	**LF model**	**HF model**	**error**
Tether tension (at the aircraft) (N)	4,413	4,376	0.84 %
Tether tension (at the payload) (N)	4,261	4,243	0.42 %
Mean tension (at the payload) (N)	4,337	4,310	0.63 %
Power required (kW)	32,212	32,282	0.53 %
Payload altitude (m, along $\vec{k}_S$)	0	4.98	–

4.6.2.1 Case 1: Circular Flight Path on a Calm Day

In Test Case 1, three aircraft fly along a circular flight path of 100 m radius with 120^o spacing between them at 50 m/s. As for the example shown in Section 4.5.3, the tether length is 300 m, with a diameter of 5 mm, and a linear mass of 0.1 kg/m. The tether elasticity is 2.356e5 N (The actual tether tension is found by multiplying this value by the tether strain). Finally, the fuselage mass is set to 1,200 kg. Table 3 presents the salient results for both the higher and lower fidelity tether models under the same conditions.

The tether tension is less than 1% different between the two approaches, although the lower fidelity model shows an improvement in the computational cost by more than two orders of magnitude compared to the high fidelity model. There are two reasons for this high accuracy.

1. *Simple flight path* – A circular flight path in hover results in a stationary fuselage without any oscillation once the transient phase is decayed.

2. *Small tether deflection* – The tether deflection remains small due to the high tether tension and relatively heavy fuselage compared to the tether weight and the tether drag. It represents the opposite from the verticality property of long tethers shown in Test Case 4, of the higher fidelity tether model.

To highlight the last item above, the tether deflection is plotted in Figure 39 as a function of the distance from the aircraft (unstretched). The deflection goes to zero

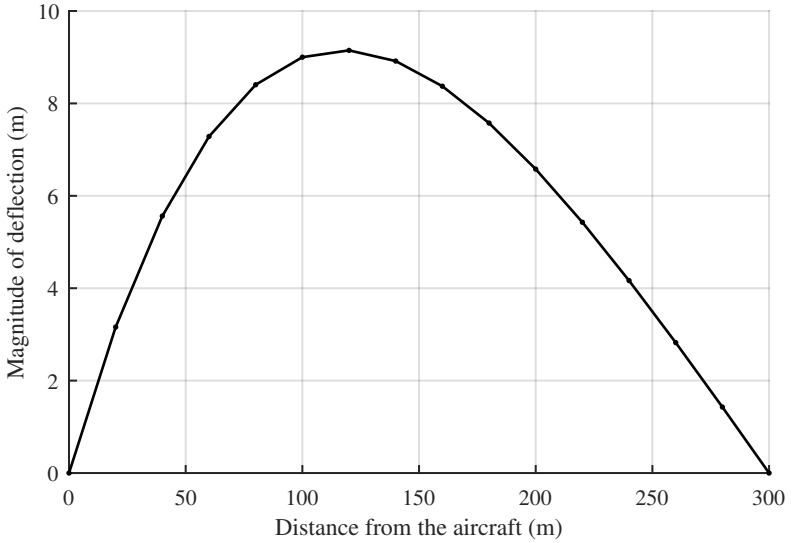

Figure 39: Tether deflection using the higher fidelity tether model for Test Case 1. The tether deflection is minimal compared to the tether length. (Payload mass: 1200 kg, flight path radius: 100 m, angular velocity: 0.5 rad/s, tether properties as described in the beginning of this section.

both at the payload and the aircraft, which is expected. The deflection is slightly more important in the upper section of the tether due to the higher relative airspeed created by the conical motion of the tether. The effect of the tether elasticity is shown in Table 3 with a positive payload altitude, meaning that the payload is almost 5 m below its target (or reference) location.

The final and most important result is the predicted power required to tow the tether. This power is evaluated with a dot product between the tether force at the aircraft and the freestream velocity seen at the aircraft. In this case, the only contribution to the power is the tether drag, since the tether tension and the inertial reaction of the tether elements are orthogonal to the relative velocity. The prediction using the lower fidelity model is less than 1 % different than the prediction from the higher fidelity tether model. In other words, the tether drag measured by both methods is equal, since the tether shape is "almost" a straight line, as approximated in the lower fidelity model.

In order to introduce the concept of tether multifidelity, the following example is detailed. If there was an objective to maintain the fuselage at a given location, one could have used the tether tension estimated using the lower fidelity model and adapted the flight path (increase the altitude by some distance), then evaluate the system's dynamics with the higher fidelity model. Although this example is trivial, it is much more relevant for advanced flight paths and in forward flight, as shown in the following test case.

4.6.2.2 Case 2: Circular Flight Path in Forward Flight

The second test case is similar to Test Case 1 detailed in Section 4.6.2.1 except that a 10 m/s wind coming from $\vec{i}_S$ is added to the simulation. Although this change may seem minimal, it adds periodic loads to the system and moves the fuselage away from its target location due to its drag. Both methods were used for the simulation. First, Figure 40 presents the fuselage trajectory during the 100 seconds simulation.

Numerous phenomena can be observed on Figure 40. First, the simulation shows strong variation in the position during the transient phase, and then the payload trajectory converges to an almost circular path. At the end of the simulation, the mean altitude is approximately 5 m under the reference point, shifted in the direction of the freestream by 4.5 m and shifted to the right by 2 m. This transient phase does not really affect the results in the present case since the interest is in the analysis of the periodic steady-state solution. However, a large computational cost is incurred for solution convergence during this phase.

Second, the quasi-circular payload motion is not centered; the payload is aft and to the right of the reference point as seen from the top. First, the payload is aft due to its relatively high drag, with $C_dA = 2$ m^2. The lateral motion results from the increased tether drag on the advancing side (when $y > 0$.) The resulting drag creates a curvature in the tether which has the effect of shortening the distance between the

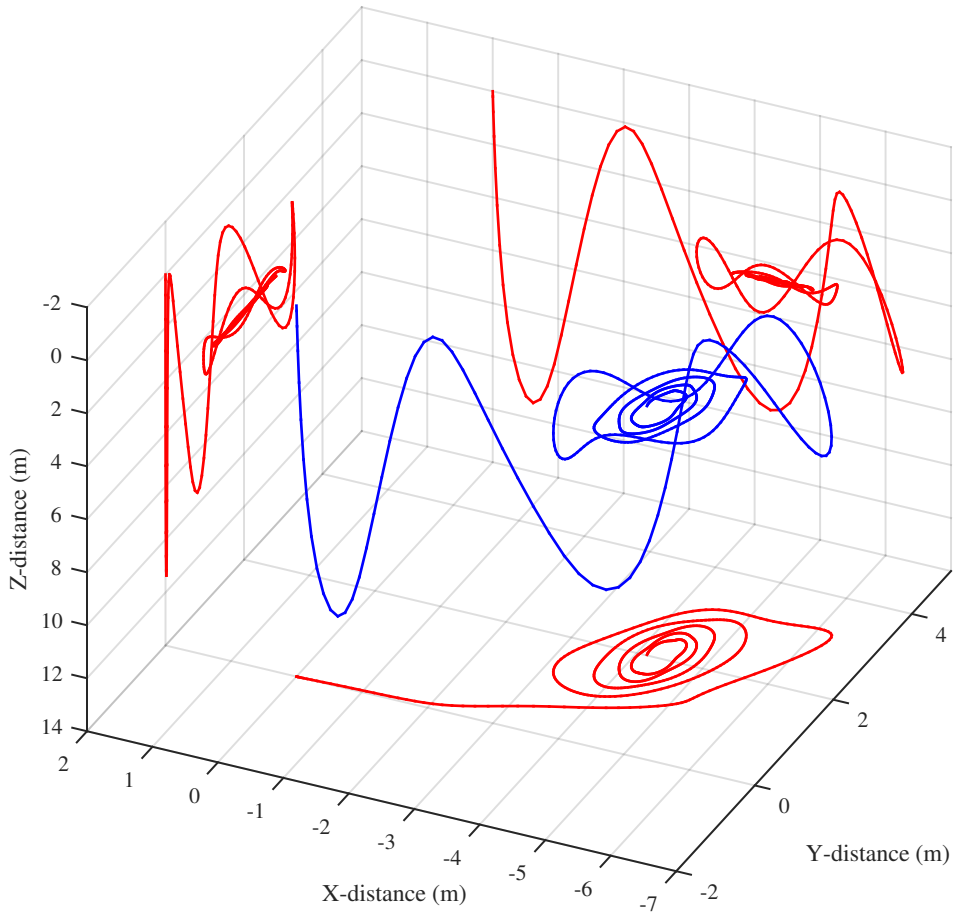

Figure 40: Test Case 2: Payload trajectory in three dimensions and the three projections (in red). The payload trajectory starts at coordinates (0,0,0).

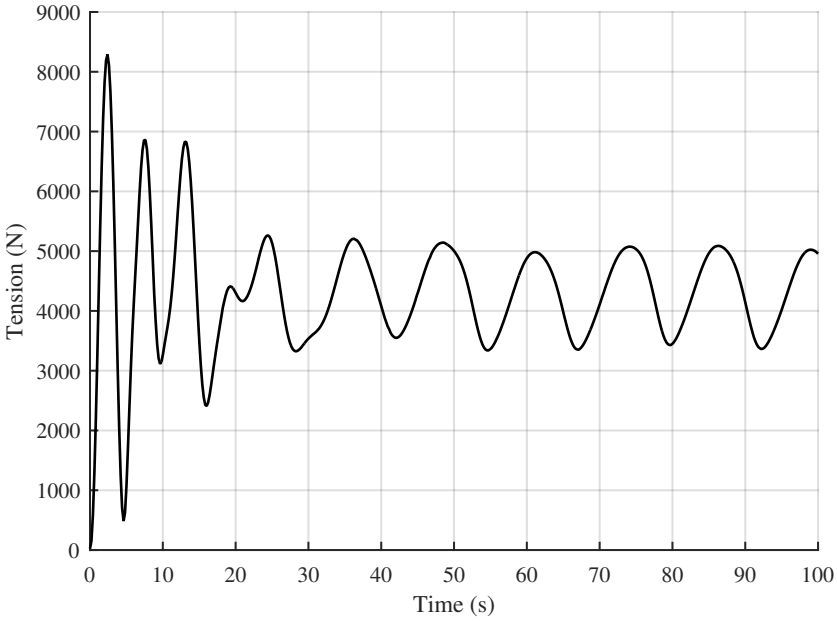

Figure 41: Test Case 2: Mean tether tension calculated with the higher fidelity model. The transient can clearly be seen during the first 40 seconds of the simulation. Then, the tension oscillates due to the presence of wind, between 3,300 N to 5,100 N.

payload and the aircraft.

Although there is no requirement to maintain the payload centered, it is desirable to remove any oscillatory motion during the periodic steady-state. Two methods can be used. The first consists in the addition of thrusters that can respond to the payload acceleration and create an additional force. The second is to slightly modify the aircraft trajectory to neutralize the payload motion and to cancel the effect of tether elasticity and curvature.

Figure 41 presents the mean tether tension as a function of time.

A motion of the system by only 10 m/s greatly affects the tether tension as a function of time, as shown in Figure 41. After the transient phase, a cyclic variation in the tension between 3,300 N to 5,100 N is observed. In Test Case 1, the tether tension was approximately 4,200 N or near the mean of the current test case. Figure 42 shows the power required to move the tether along the prescribed flight path.

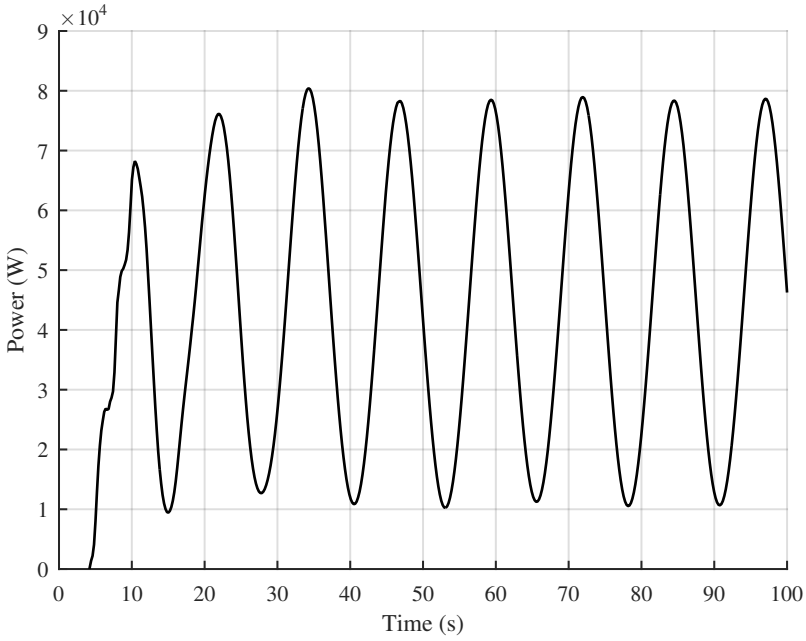

Figure 42: Test Case 2: Power required to rotate the tether, calculated with the higher fidelity tether model

Given the motion of the system, the power requirement is expected to vary significantly. First, the tether drag is not constant and second, the airspeed seen by the UAVs also varies, increasing on the advancing side. As a consequence, the power requirement for Test Case 2 is shown to vary from approximately 10 kW to as high as 80 kW. It should be noted that a negative power requirement could be possible if the tether tension is "pulling" the aircraft into the wind or a strong reduction in speed is required.

The same test case was analyzed using the lower fidelity tether model to compare the results. Since there is no transient behavior for the lower fidelity model, the results are compared with the higher fidelity model over the last complete period (around $t = 90$ s). First, the predicted mean tension in the tether as a function of time for one period is compared in Figure 43.

The first observation from Figure 43 is the capacity of the lower fidelity model to capture the increase in power requirement at time $t = 6$ sec. The tension prediction

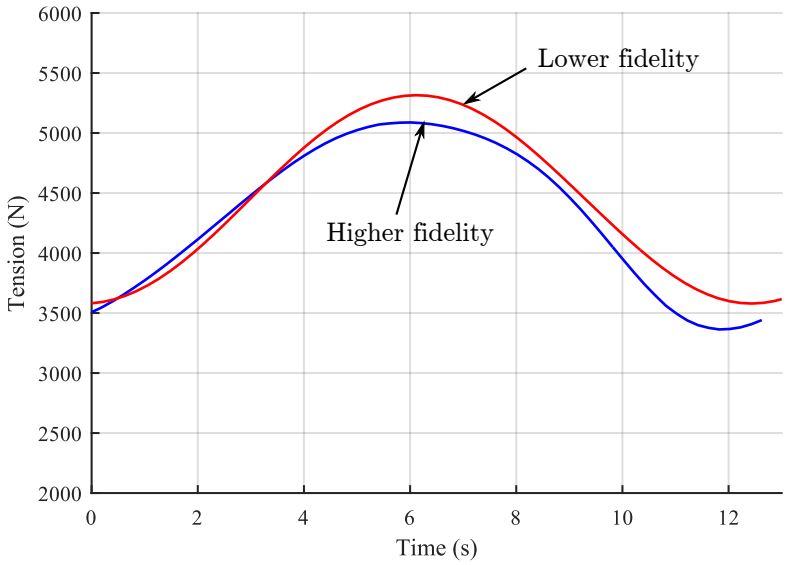

Figure 43: Test Case 2: Tether tension prediction for both the higher fidelity tether model (blue) and the lower fidelity model (red).

is within 10 % of the predictions from the higher fidelity model and provides valuable information on the system at minimal cost. Since the aerodynamic forces are much more important than in Test Case 1 due to the 10 m/s airspeed on the system, the tether deflection is expected to increase, especially on the advancing side. *The main cause of this discrepancy is the dynamic motion of the payload that is not compensated for in the lower fidelity model.* A complete demonstration of the compensation process is shown in Section 5.2. Figure 44 illustrates the tether deflection as a function of time and distance from the aircraft.

The tether deflection is the highest at $t \approx 2.2$ sec, or at $x = 0$ on the advancing side, for a value of 14 m. At this location, the relative velocity seen by the tether segment is maximum, since the relative velocity of the segments in the system-carried frame are added to system's motion. The deflection is reduced on the retreating side for the opposite reason. Even if the deflection is higher, the lower fidelity model still captures most of the main effects. In order to better capture the consequence of the discrepancy on the tether tension, Figure 45 details the power requirement to drag the tether for one period.

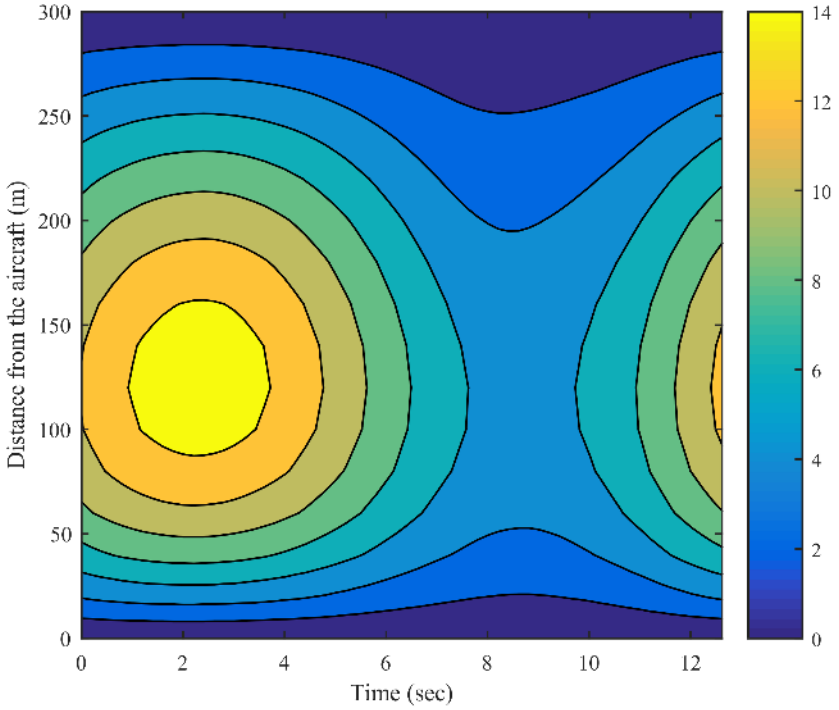

Figure 44: Test Case 2: Tether deflection (in meters) as a function of time and distance from the aircraft. The tether deflection is maximum on the advancing side, closer to the aircraft since the freestream velocity in higher due to the relative motion of the vehicle.

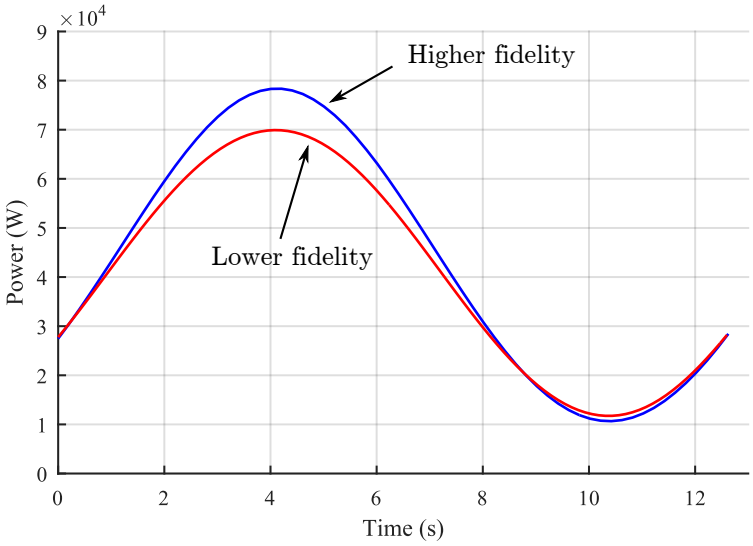

Figure 45: Test Case 2: Power requirement as a function of time. The lower fidelity is depicted with the red curve and the higher fidelity predictions are predicted with the blue curve.

The power prediction by the lower fidelity model is at most 11% less than the value calculated by the higher fidelity model. This discrepancy is the result of the error in tether tension between the models, caused by an undesirable payload motion.

4.6.3 Summary

This section described the lower fidelity tether and fuselage model. Given that three aircraft and tethers are used in the current system, the fuselage location can be found by solving a set of non-linear equations if the tethers are assumed rigid rods. Since the model is not a truly dynamic model, the timesteps can be much longer. Also, the tether forces, aircraft relative velocity, and power requirement can be obtained over only a single "rotor" revolution. This results in a model that is approximately two orders of magnitude faster.

Two test cases were used to demonstrate the validity of the model, in hover and in forward flight. A discrepancy of less than 11% between the two models was observed on the power requirement to drag the tether around the prescribed flight path, even in the presence of undesirable fuselage motion. With a major computational cost improvement over the higher fidelity model, the lower fidelity model can provide valuable information in a multifidelity architecture adapted for design space exploration.

4.7 Aircraft Dynamics Coupled with a Low Order Aerodynamic Model

The model described in the previous section returns the tether forces $\boldsymbol{F}^{(i)}_{AC\to T}(t)$ and the fuselage trajectory given a prescribed aircraft flight path $\boldsymbol{r}^{(i)}_{O_S\to P}(t)$. It should be noted that the superscript $^{(i)}$ denotes the i^{th} tether, and the notation $_{AC\to T}$ denotes the force applied on the aircraft from the tether. This section details the *aircraft dynamic model*. In a nutshell, given the aircraft prescribed trajectory and the forces applied to the aircraft from the tether, the objective is to evaluate the required external forces and moments as a function of time to perform the mission with consideration for the

inertial reaction of the UAVs.

The objective of the lower fidelity dynamic and aerodynamic model is to estimate the aircraft attitude and forces applied on the aircraft in the body reference frame B as a function of time with minimal computational time. The lower fidelity approach can be seen as a starting point for iterative, higher fidelity models.

The main assumptions of the dynamic model are:

- Point-mass aircraft model: No consideration of the angular momentum.
- Small angle approximation between the aircraft flight path (along with the relative velocity) and the aircraft longitudinal axis.
- The relative velocity is the result of the freestream velocity and the motion of the aircraft.

In the point-mass model, given the prescribed flight path $\boldsymbol{r}^{(i)}_{O_S \to P}(t)$, the required lift L and bank angle ϕ are derived using Equations 93 and 94.

$$m\frac{V^2}{r_1} = L\cos\phi - W\sin\theta + \boldsymbol{F}^{(i)}_{AC\to T}(t)\cdot\boldsymbol{e}_1 \tag{93}$$

$$m\frac{(V_\infty\cos\theta)^2}{r_2} = L\sin\phi + \boldsymbol{F}^{(i)}_{AC\to T}(t)\cdot\boldsymbol{e}_2 \tag{94}$$

where r_1 is the instantaneous radius along the curved flight path, and r_2 is the turn radius projected on a plane parallel to the flat earth. The last terms in Equations 93 and 94, ($\boldsymbol{e}_1$, $\boldsymbol{e}_2$), are unit vectors aligned with the direction in which the sum of forces is calculated.

Equations 95 and 96 are used to solve for an estimation of F_{ext}, defined as the thrust required minus the drag prediction,

$$F_{\text{ext}} = T - D \tag{95}$$

$$m\frac{dV}{dt} = F_{\text{ext}} - W\sin\theta + \boldsymbol{F}^{(i)}_{AC\to T}\cdot\boldsymbol{e}_3 \tag{96}$$

where the drag D is estimated using the approximation of the lifting line, and θ is the flight path angle, and $\boldsymbol{e}_3$ is a unit vector aligned with the local freestream velocity. Given the very low computational cost to obtain a crude estimation of the power requirement using the approximation of the lifting line theory, this method is coupled with the dynamic model. The estimated drag D is

$$D = \frac{1}{2}\rho \underbrace{\left\{ \frac{C_L^2}{\pi \text{Æ} e} + C_{D,0} \right\}}_{C_D} V^2 S \tag{97}$$

where Æ is the wing aspect ratio, e is the Oswald efficiency factor, and $C_{D,0}$ is the parasitic drag coefficient of the aircraft.

In summary, a set of coupled equations (93 - 97) are used to solve for the bank angle ϕ, the lift required L, and the external force required F_{ext}, defined as the thrust minus the drag. The approximation of the lifting line is systematically used to estimate the aircraft drag given the low computational. However, more advanced methods that consider varying wind velocity as a function of span and the wake interaction is required, as described in the next section.

The aircraft attitude, denoted $\boldsymbol{\Theta}^{(i)}(t)$ is fully defined from $\theta_{AC}^{(i)}, \phi_{AC}^{(i)}, \psi_{AC}^{(i)}$, where $\theta_{AC}^{(i)}$ and $\psi_{AC}^{(i)}$ are obtained from the tether model, since the aircraft is aligned with the relative velocity, and $\phi_{AC}^{(i)}$ is the bank angle obtained in this section.

4.8 Higher Fidelity Aerodynamic Modeling of Tethered Aircraft

4.8.1 Introduction

Sections 4.5 and 4.6 detailed the method used to extract the forces that the tethers apply on each aircraft, denoted $\boldsymbol{F}_{AC\to T}^{(i)}(t)$ for the i^{th} aircraft. Moreover, the relative wind velocity seen by each aircraft, denoted $\boldsymbol{V}_{AC}^{(i)}(t)$, assumes that this velocity is the result of the relative motion of the UAVs in the Earth-fixed reference frame. Then, those two results were used in the dynamic model to extract the required bank angle, lift, and the longitudinal force required, defined as the thrust required minus the drag.

The bank angle is determined by assuming that the minimum drag is obtained at zero sideslip angle of the aircraft. In practice, there are cases where this assumption breaks down, where the bank angle for zero sideslip in steady level flight is *not* vertical. For example, a twin engine aircraft with an engine failure must maintain a roll angle of a few degrees on the side of the operational engine to compensate for the side force created by the rudder and vertical stabilizer [61]. For very tight turn radii, where a lot of rudder deflection is required to coordinate the turn, such behavior can also be seen. The method presented in this chapter could be applied to converge on other loads than the target lift and rolling moment. There is no restriction to expand the method to other loads and control surfaces. In this work, it will be assumed that the optimal roll angle is obtained from the sum of forces applied on the mass-point such that no aerodynamic side loads are produced.

The first method used to evaluate the drag is based on the approximation of the lifting line theory, as shown in Equation 97, which has the advantage of being computationally affordable. However, the limitations on the applicability of this method to compute the actual drag of an aircraft in any flight conditions are significant. Other than the preliminary work by Demers Bouchard and Rancourt [44], all the studies on tethered aircraft only used the approximation of the lifting line method.

One of the most important parameters for power prediction of a for highly-loaded helicopter rotor is the induced velocity by its wake as shown in Section 2.2.1. For very lightly loaded "rotors," such as in the case of an aircraft flying along a circular flight path, there is no proof that neglecting the wake is a valid assumption.

This section presents the higher fidelity aerodynamic model that captures the relevant physics to analyze the aerodynamic performance of tethered aircraft along an arbitrary flight path. The model considers the following parameters, which are described in the next sections:

- Convergence of the forces and moments at each timestep through adjustment

of the control surface deflection and the angle of attack.

- Consideration of wake interaction between aircraft.
- Consideration of circulatory unsteady aerodynamics.
- Time decaying tip (and aileron) vortices over time.

The developed method is based on a second-order implementation of the lifting line to solve for the near wake on the wing. Other lifting surfaces could be added if desired. The far-wake model is built from vortex segments with a consolidation model that differs from the model implemented in CAMRAD, by Johnson [89, 87, 90] to be more general. Both free and prescribed wake models can be used. Finally, the induced velocity from the consolidated vortices is also evaluated differently to consider the roll-up process. Figure 46 illustrates the salient characteristics of the higher fidelity aerodynamics model.

The main characteristic of the approach to solve for the aircraft aerodynamics is the ability to solve for the control deflection and the angle of attack at each timestep. Moreover, the consolidation model reduces the computational time by more than one order of magnitude. The theory and its implementation are discussed in the next sections, and contributions are highlighted.

4.8.2 Lifting Surface Descriptions

Each lifting surface planform is fully defined by specifying the chord, twist, and leading edge coordinates in the body refererence frame. The control surfaces are defined between two sections by a ratio of control surface chord. Figure 47 shows a notional wing in the body reference frame.

Let P_1, P_2, P_3, and P_4 be the four vertices that define a vortex ring in the body reference frame, as shown in Figure 48. The position vector of the m^{th} vertex with respect to the origin of the body reference frame is denoted $\boldsymbol{r}_{O_B \to P_m}$ The bound vortex

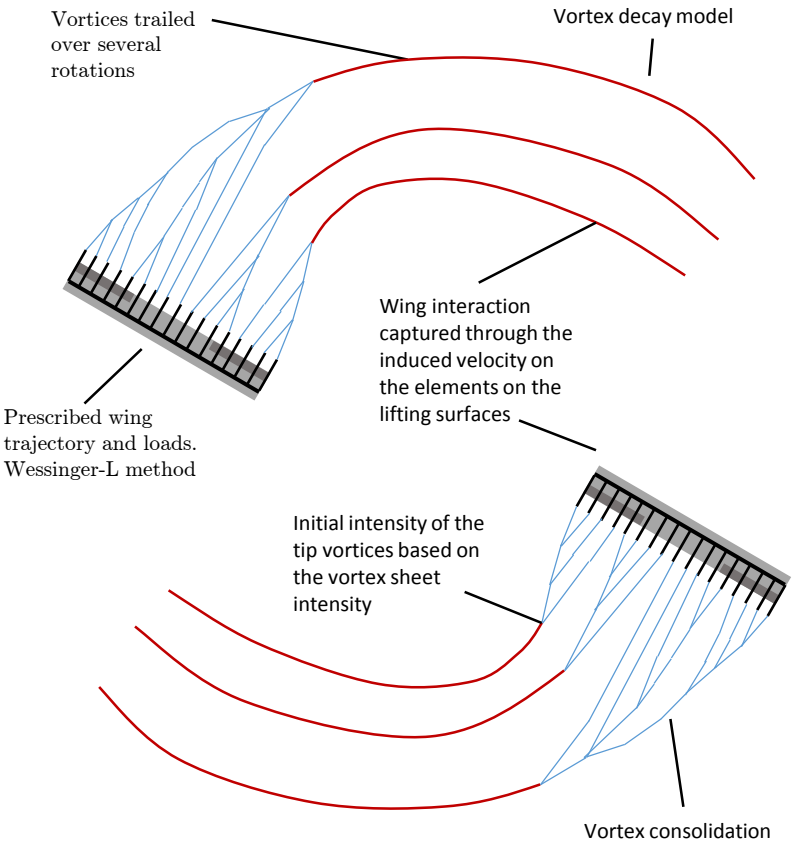

Figure 46: Overview of the higher fidelity aerodynamic model. The lifting line is depicted by the thick solid black line on the wings. The consolidation phase is depicted by blue vortex segments and the far wake propagation is characterized by a vortex decay model. The shed vortices are not shown for clarity.

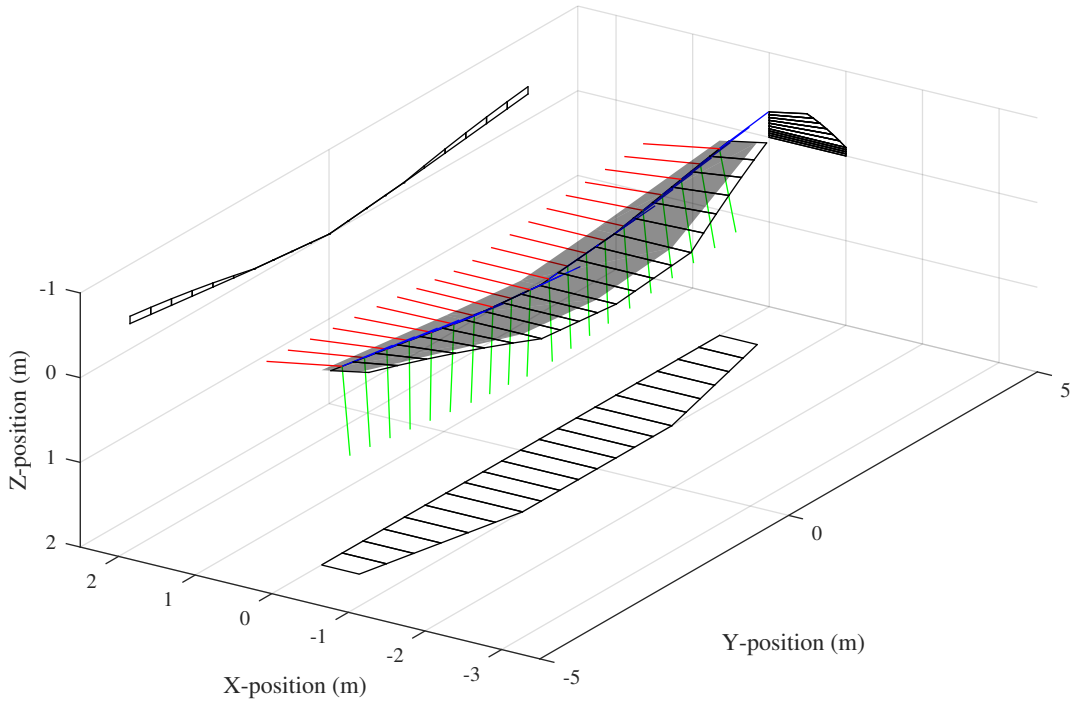

Figure 47: Wing discretization with the element coordinate system. The three wing projections are depicted to illustrate the presence of wing dihedral and wing twist. The local element coordinate system is shown with colored lines (red: +X, blue: +Y, green: +Z)

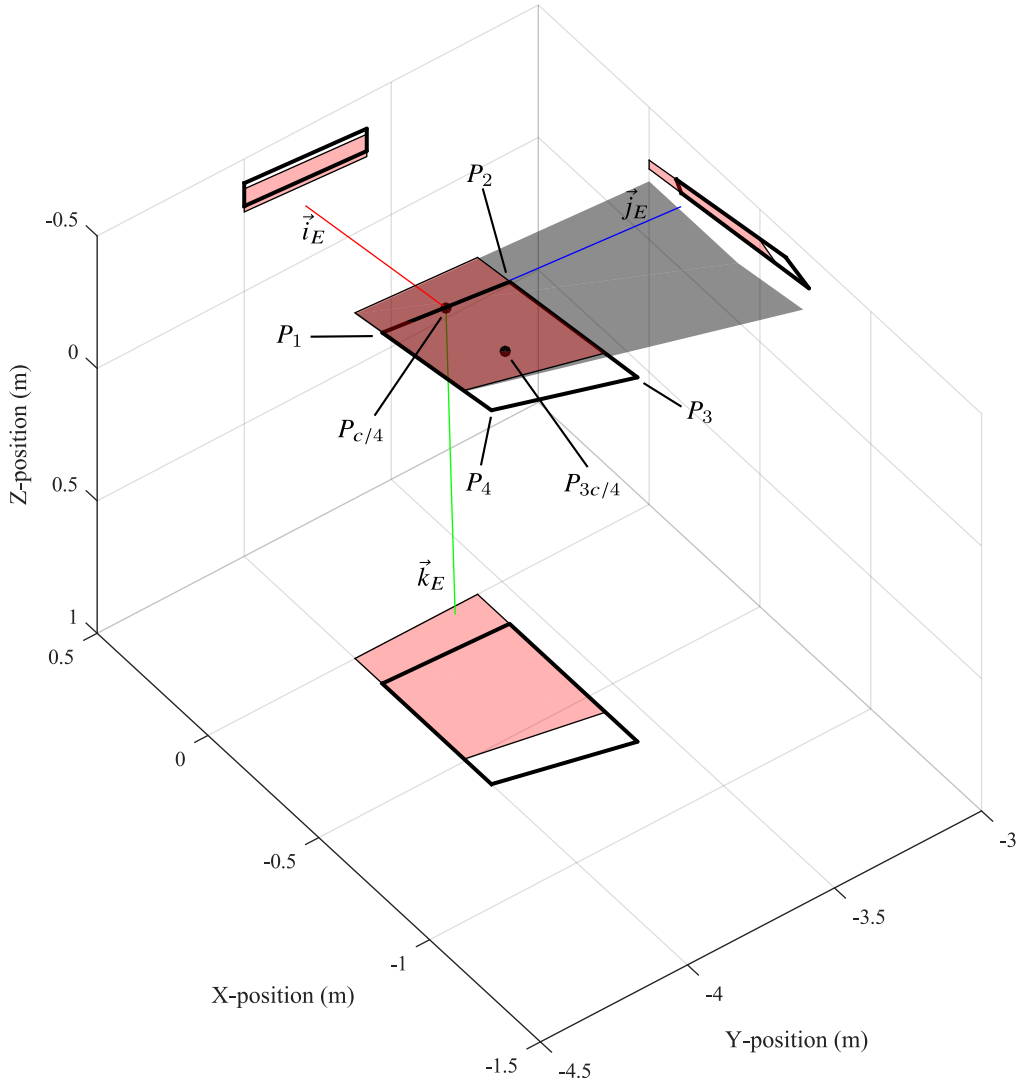

Figure 48: Close view of one element on the wing. The local element coordinate system is depicted with colored lines (red: +X, blue: +Y, green: +Z)

of the element is located at the 1/4 chord, from P_1 to P_2, in a clockwise direction. The trailing vortex, defined positive from P_3 to P_4 is located at $5c/4$, or $c/4$ behind the trailing edge of the wing, as described by Johnson [90] and Katz [93] to reproduce the Theodorsen and Sears functions. The two trailed vortices are defined positive from P_1 to P_3 and from P_4 to P_1 to complete the vortex ring.

The origin of the element reference frame E, O_E is located at the 1/4 chord, mid-distance between P_1 and P_2, which is also a control point denoted $P_{c/4}$. Let θ_t be locally defined as the wing twist at the center of the element. The unit vector that defines the positive x-axis of the element coordinate systems, $\vec{i}_E$, is obtained with Equation 98

$$ {}_B\mathbb{C}\left(\vec{i}_E\right) = \begin{bmatrix} \cos\theta_t & 0 & -\sin\theta_t \end{bmatrix} \tag{98} $$

where ${}_B\mathbb{C}$ is the measure number operator in the body frame B. Let $\boldsymbol{v}_1$ be a vector from P_3 to $P_{c/4}$ and $\boldsymbol{v}_2$ be a vector from P_3 to P_2, as detailed in Equation 99.

$$ \boldsymbol{v}_1 = \boldsymbol{r}_{O_B \to P_{c/4}} - \boldsymbol{r}_{O_B \to P_3} \tag{99} $$

$$ \boldsymbol{v}_2 = \boldsymbol{r}_{O_B \to P_2} - \boldsymbol{r}_{O_B \to P_3} \tag{100} $$

The vector aligned with the positive Y axis of the element is found using Equation 101.

$$ \vec{j}_E = \frac{\left(\boldsymbol{v}_1 \cdot \frac{\boldsymbol{v}_2}{|\boldsymbol{v}_2|}\right) \cdot \frac{\boldsymbol{v}_2}{|\boldsymbol{v}_2|} - \boldsymbol{v}_1}{\left|\left(\boldsymbol{v}_1 \cdot \frac{\boldsymbol{v}_2}{|\boldsymbol{v}_2|}\right) \cdot \frac{\boldsymbol{v}_2}{|\boldsymbol{v}_2|} - \boldsymbol{v}_1\right|} \tag{101} $$

The vector aligned with the Z-direction of the element reference frame is perpendicular to both $\vec{i}_E$ and $\vec{j}_E$, and is therefore easily obtained through a cross product.

$$ \vec{k}_E = \vec{i}_E \times \vec{j}_E \tag{102} $$

In summary, each element has four vertices, two at the 1/4 chord and two at the 5c/4 pass the trailing edge, with a vortex ring defined positively in the clockwise direction. Control points are defined at $P_{c/4}$ and $P_{3c/4}$. The next section details how the second order lifting line method is implemented for the near-wake modeling.

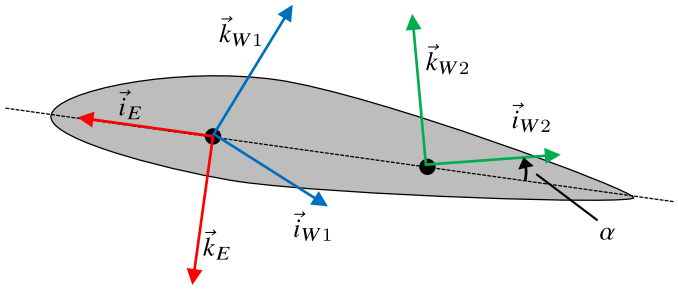

Figure 49: Definition of the coordinate systems on the element. Two coordinate systems are defined with respect to the local relative velocity, W_1 and W_2. The unit vectors $\vec{i}_{W1}$ and $\vec{i}_{W2}$ are aligned with the in-plane relative velocity while $\vec{k}_{W1}$ and $\vec{k}_{W2}$ are normal to the in-plane local relative velocity.

4.8.3 Near-Wake Modeling

The method used to evaluate the near wake aerodynamics is a second order implementation of the lifting line theory [90]. This method shows similarities with the Weissinger's L-theory [156], which can be seen as a panel method with a single chordwise element. For completeness, a short description of the method is described.

Let W_1 and W_2 be 2D reference frames aligned with the relative velocity in the plane defined by $\vec{i}_E$ and $\vec{k}_E$ at $P_{c/4}$ (for W_1) and at $P_{3c/4}$ (for W_2). The unit vectors $\vec{i}_{W1}$ and $\vec{i}_{W2}$ are aligned with the in-plane relative velocity, and vectors $\vec{k}_{W1}$ and $\vec{k}_{W2}$ are normal to the in-plane local relative velocity. Figure 49 illustrates the location of the two new coordinate systems.

The relative wind velocity with respect to the element at $P_{c/4}$ and $P_{3c/4}$ is denoted $\boldsymbol{v}_{1/O_E}$ and $\boldsymbol{v}_{2/O_E}$ respectively. With those variables defined, the norm of the relative velocity is $U_1 = \left|\boldsymbol{v}_{1/O_E}\right|$ and $U_2 = \left|\boldsymbol{v}_{2/O_E}\right|$.

The circulation of the bound vortex of the k^{th} element, Γ_k is evaluated using Equation 103

$$\Gamma_k = \frac{C_{l,k} \cdot U_{1,k} \cdot c_k}{2} \tag{103}$$

where c_k is the mean chord of the element and $U_{1,k}$ is the magnitude of the local velocity. The sectional lift coefficient $C_{l,k}$ is function of the local angle of attack at

the three-quarter chord and the aileron deflection δ_a if this section is flapped. Let θ_0 be the geometric angle of attack, θ be a variation in incidence angle (a variable described later), $v_{3c/4}^{\text{near}}(\Gamma)$ be the induced velocity along $\vec{k}_E$ by the near wake, and $v_{3c/4}^{\text{far}}$ be the induced velocity along $\vec{k}_E$ by the far wake. Then, the local angle of attack α is obtained with Equation 104.

$$\alpha = \theta_0 + \theta + \frac{\left(v_{3c/4}^{\text{far}} + v_{3c/4}^{\text{near}}(\Gamma)\right)}{U_2} \tag{104}$$

Using Equations 103 and 104, the second-order implementation of the lifting-line theory as presented by Johnson [90] can be obtained, as shown in Equations 105.

$$\frac{2\Gamma}{c} = U_1 \cdot C_l\left[\alpha(\Gamma, \theta), \delta_a, \right] \tag{105}$$

The lift and drag vectors from each vortex ring use the velocity at $P_{c/4}$, but use the induced velocity at $P_{3c/4}$ to evaluate the angle of the vectors, as shown in Equations 106 and 107.

$$\boldsymbol{L} = \frac{1}{2}\rho C_l U_1^2 S\vec{k}_{W2} \tag{106}$$

$$\boldsymbol{D} = \frac{1}{2}\rho C_d U_1^2 S\vec{i}_{W2} \tag{107}$$

where S is the element area. The forces evaluated for each element can be summed up to compute the total forces and moments applied to the aircraft. Let $\boldsymbol{L}_k$ and $\boldsymbol{D}_k$ be the lift and drag vectors of the k^{th} element, $1 \leq k \leq n_k$, and $\boldsymbol{r}_{O_B \to O_{E,k}}$ be the position vector of $P_{c/4}$ with respect to the origin of the body reference frame. The sum of forces and moment on a single body are evaluated using Equations 108 and 109.

$$\boldsymbol{F}_{\text{tot}} = \sum_{k=1}^{n_k} \boldsymbol{L}_k + \boldsymbol{D}_k \tag{108}$$

$$\boldsymbol{M}_{\text{tot}} = \sum_{k=1}^{n_k} \left(\boldsymbol{r}_{O_B \to O_{E,k}}\right) \times \left(\boldsymbol{L}_k + \boldsymbol{D}_k\right) \tag{109}$$

Two equality equations must be satisfied for the sum of forces and moments,

$$\boldsymbol{F}_{\text{tot}} \cdot \vec{k}_B = L \tag{110}$$

$$\boldsymbol{M}_{\text{tot}} \cdot \vec{i}_E = M_{l,\text{target}} \tag{111}$$

where L is the calculated target lift, and $M_{l,\text{target}}$ is the target rolling moment, usually set to zero in the present work.

The main difference in the implementation of the second-order lifting line and the traditional approach is to maintain the trailing vortices and the shed vortices just behind the wing (at c/4) in the near wake. Therefore, there is no iteration between the near wake and far wake calculation.

At each timestep, a set of $n_k + 2$ coupled and non-linear equations must be solved. The unknowns are the angle of attack α for each section, the variation in incidence angle θ of the whole wing, and the aileron deflection δ_a. The $n_k + 2$ equations are: the lifting line equation (Equation 105) for each element, the vertical force (target lift, Equation 110) and the target rolling moment (Equation 111). The variation in the incidence angle is defined as the angle between the aircraft attitude (input to the model) and the required attitude to obtain the target lift.

In summary, the lift and rolling moment generated are enforced automatically *at each timestep* since the aileron deflection and incidence angle are solved when the lifting line is also solved. However, since the airfoil sections can have non-linear aerodynamic properties, a non-linear solver must be used.

The velocity induced by a vortex segment on a control point is a linear function, as shown in the Biot-Savart equation [93], where $\boldsymbol{r}_1$ and $\boldsymbol{r}_2$ are locally defined as the vector from any reference point to the starting and ending points of the vortex, $\boldsymbol{r}_0$ is the control point location, and $\boldsymbol{q}_{1,2}$ denotes the induced velocity vector.

$$\boldsymbol{q}_{1,2} = \frac{\Gamma}{4\pi} \frac{\boldsymbol{r}_1 \times \boldsymbol{r}_2}{|\boldsymbol{r}_1 \times \boldsymbol{r}_2|^2} \boldsymbol{r}_0 \cdot \left(\frac{\boldsymbol{r}_1}{|\boldsymbol{r}_1 - \boldsymbol{r}_0|} - \frac{\boldsymbol{r}_2}{|\boldsymbol{r}_2 - \boldsymbol{r}_0|} \right) \tag{112}$$

The evaluation of the induced velocity on all the control points on the wing from all the vortex rings is performed through the multiplication of the aerodynamic influence coefficient (AIC) with the circulation Γ. Since the effects of the ailerons are considered in the airfoil properties and do not affect the geometry of the panels, the AIC does not change over time and can be pre-calculated.

In order for that property to be valid, it must be assumed for a multiple-aircraft configuration that the induced velocity from the near wake only affects the aerodynamics of its own aircraft. In this case, the solving process of the near wake is then local to each aircraft. The effects of the far-wake on its own aircraft and all other aircraft bodies are considered for all aircraft.

4.8.4 Far-Wake Modeling

This section details the approach to model the far-wake, defined as all the vortex segments other than the vortex rings in the near-wake. Figure 50 presents the general nomenclature of the far-wake modeling, which will be detailed in this section.

The approach presented here is very similar to the vortex-ring method by Katz and Plotkin [93], with a few adaptations, especially for the vortex consolidation. The model shows the following characteristics:

- **Free or prescribed formulation** – The model can handle (with minor modifications) a free or a prescribed far-wake geometry. For hover cases or when wake interaction is assumed to be important, a free-wake implementation is required.

- **Wake consolidation** – Conventional helicopter rotor models require at least five complete rotor revolutions of wake aging to appropriately capture the induced velocity at the rotor. In order to reduce the computational cost, the current model has a consolidation model implemented, that combines vortices in an automated approach, with a variable number of vortices based on the lift distribution shape. It also allows for a better vortex definition and control on

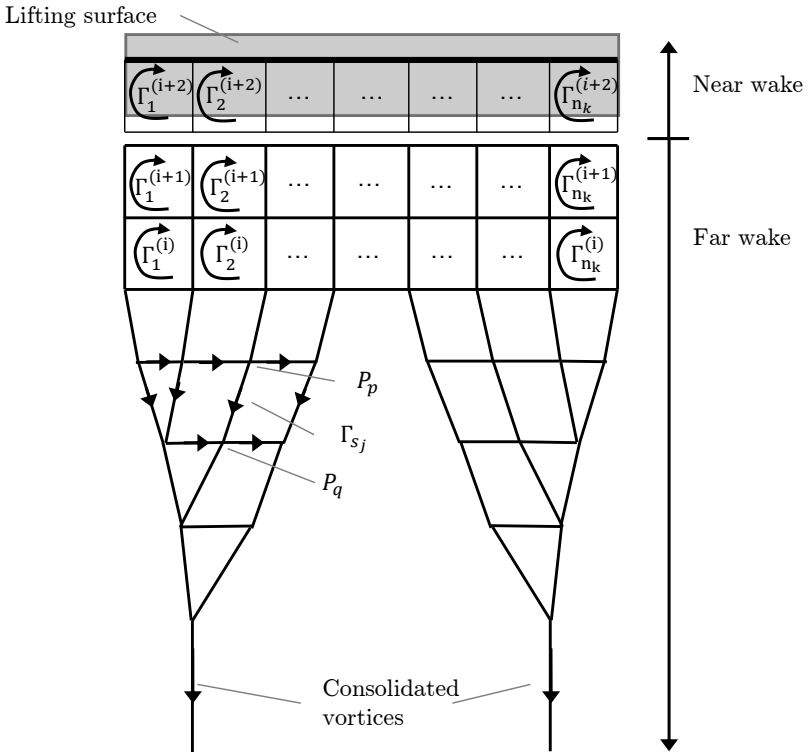

Figure 50: Global structure of the far wake modeling. The far wake is structured with straight vortex segments, both the trailing vortices and the shed vortices. A consolidation process can be added to merge the vortices based on the circulation to reduce the computational cost.

the aging process. The induced velocity of the consolidated vortices considers the roll-up process and the initial lift distribution.

- **Wake aging** – For a small helicopter like the Robinson R-44, five rotor revolution lasts only 0.75 s, compared to approximately 15 s for the EPR[2] based on the initial work by Demers Bouchard and Rancourt [44]. Therefore, the developed far-wake model contains a vortex decay model.

The near wake model solves for the circulation for each vortex ring on the wing, denoted $\Gamma_j^{(i+2)}$ on Figure 50 at timestamp $i+2$ and element j. The vortex segments (rings) are attached to the wing and their location is fixed in the body-carried frame.

The far wake model consists of all the shed and trailed vortices that are not attached to the lifting surface. In order to reduce the computational cost and allow for wake consolidation, the vortex segments in the far wake are defined by the position vector of two points, as shown in Figure 50. In this example, the vortex segment s_j is defined by P_p and P_q. The position vector of those two control points are $\boldsymbol{r}_{O_B \to P_p}$ and $\boldsymbol{r}_{O_B \to P_q}$ respectively.

The initial circulation of s_j, Γ_{s_j}, is calculated from the circulation of the two vortex rings on each side when they were created. By convention, the circulation on the vortex segments are defined positive from left to right for the shed vortices, and from front to back for the trailing vortices.

The number of control points in the far wake is:

$$n_P = (n_k + 1) \cdot n_t \tag{113}$$

where n_k is the number of elements on the wing and n_t the number of timesteps. Since individual vortex segments are considered instead of the complete vortex rings, the number of vortex segments is $\approx 2 \cdot n_k \cdot n_t$.

The induced velocity from the vortex segments on the control points are evaluated with the Biot-Savart law, detailed previously in Equation 112 for vortex segments that

are not consolidated (details about the consolidation is provided later in this section).

At each timestep, the control points in the wake are convected. In the prescribed wake implementation, the position of the control point P_q in the system-carried frame is,

$$\boldsymbol{r}_{O_S \to P_q}^{(t+1)} = \boldsymbol{r}_{O_S \to P_q}^{(t)} + \left(\boldsymbol{v}_{\infty/E} - \boldsymbol{v}_{S/E}\right) \cdot \Delta t \tag{114}$$

where $\boldsymbol{v}_{S/E}$ is the velocity of the system-carried frame in the earth-fixed reference frame E, and $\boldsymbol{v}_{\infty/E}$ is the direction of the freestream velocity in the earth-fixed reference frame. In the free vortex wake implementation, the position vector of P_q also considers the induced velocity of all the vortex segments (both from the near wake and far wake) from all the lifting bodies in the system.

$$\boldsymbol{r}_{O_S \to P_q}^{(t+1)} = \boldsymbol{r}_{O_S \to P_q}^{(t)} + \left(\boldsymbol{v}_{\infty/E} - \boldsymbol{v}_{S/E} + \sum_{\text{all elements}} \boldsymbol{v}_{\text{ind @ } P_q}\right) \cdot \Delta t \tag{115}$$

For the free vortex wake implementation, when there is a possibility of having two vortex segments in close proximity, or with the presence of wake aging, a vortex core model should be used. Details about those models are provided in Section 4.8.6.

Appendix C.3 presents a set of test cases to validate the model. The first set of validation cases described below aims at the validation of the aerodynamic model except for the consolidation model, and the wake aging.

- Test Case 1: Steady-state lift distribution in steady level flight
- Test Case 2: Aileron effectiveness
- Test Case 3: Impulse start – Wagner function
- Test Case 4: Sinusoidal variation in angle of attack – Theodorsen function

It is shown that the model can reproduce the analytical solution of the lift distribution for an elliptical wing planform in steady level flight, and capture the rolling moment associated with an aileron deflection with the current wing configuration. Morever,

the circulatory unsteady aerodynamic effects are validated by reproducing the Wagner function and the Theodorsen function with a wing with an aspect ratio of 100 (to simulate an infinite wing).

4.8.5 Wake Consolidation

Section 4.8.4 detailed how the far-wake model is constructed to capture both the effect of the trailing and shed vortices on the lifting line and on the other elements of the wake. If a free vortex implementation is used, the computational time grows approximately $\mathcal{O}(n^2)$, where n is locally defined as the number of elements. For a large number of elements, a complete far-wake "mesh" can also become memory intensive. In the present project, this effect is even truer than for a conventional helicopter. Since the characteristic dimensions of the lifting surfaces are *much* smaller than the length of the flight path, the number of elements that have to be considered in the wake is large. A reduction of the number of elements for the lifting line could reduce this computational time, but would also reduce the ability to accurately represent the local vortices that result from control surface deflection.

The second reason for the need of a consolidation model is to represent with greater accuracy the roll-up process. As explained by numerous authors (Donaldson [45, 47], Bilanin [19], Spalart [149], and Johnson [90]), a free-vortex wake representation can only represent partially the roll-up process even if a high number of elements are used. The lack of consideration for viscosity also reduces the accuracy of the results. Consolidation models are then used to "mimic" the roll-up process and convert the vortex sheet (or set of discrete trailing vortices) into a small finite set of trailing vortices. The number of elements in the wake therefore do not grow as $\mathcal{O}(n_t)$ with n_t being the number of timesteps. Such approaches allow modeling the wake for long durations behind an aircraft without prohibitive computational cost.

The third reason to consider wake consolidation for the current application is to

facilitate the wake aging modeling. As previously explained, the wake modeling must consider the wake and its reduction in intensity for several seconds due to the long time for the wake to be convected away from the aircraft. Most wake aging models (such as the one used in this work) evaluate the effect of time on single, large vortices. Those are obtained from the consolidation of the trailing vortices after some time.

The consolidation model is very similar to the model developed by Johnson [90, 89], except that the condition to assign trailing vortices to specific consolidated vortices differs to better capture the effect of control deflection. Numerical validations of the location of the vortices as a function of time are performed and compared to experimental results. The velocity induced from a consolidated vortex also differs from the current approach in the literature, which is the traditional Biot-Savart function with a core model.

Let $\Gamma(y)$ be the spanwise circulation at time t on one lifting surface. The intensity of the trailing vortex sheet is,

$$\gamma(y) = -\frac{d\Gamma(y)}{dy} \tag{116}$$

where $\gamma > 0$ near the right wingtip to generate a counter-clockwise vortex seen from the back. The distribution of the vortex sheet associated with each consolidated vortex is obtained from the lift distribution. Let y_i be the boundary on the vortex sheet to separate the "future" consolidated models, or the wingtip locations. The values of y_i at time t are determined using Equation 116.

$$y_i = \arg\min |\gamma(y)| \tag{117}$$

$$= \arg\min \left| -\frac{d\Gamma(y)}{dy} \right| \tag{118}$$

with the addition of the two wingtips. This method was developed and validated with experimental data by Donaldson [45] from an extension of a previous work by Bilanin [19] and Yates [171]. Figure 51, reproduced from Donaldson [45], illustrates a lift distribution that produces three vortices.

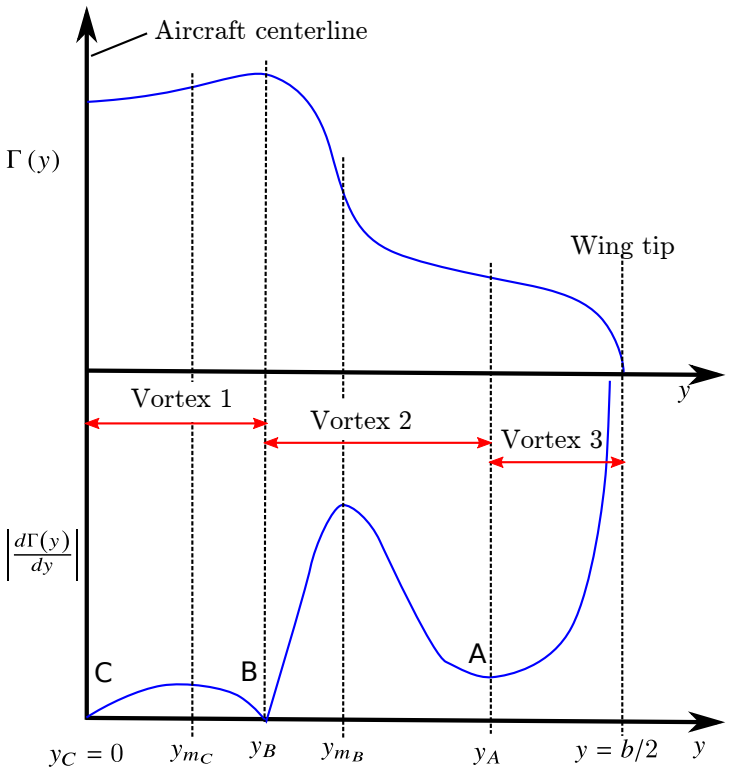

Figure 51: Load distribution which will produce three vortices [45]. The spanwise locations that define the boundary between two vortices are the minimum of the absolute value of the trailing vortices intensity.

Johnson [90, 89] proposes to consolidate the trailing vortex sheet (or trailing vortices) based on the sign of $\gamma(y)$. In his formulation, the boundary of the vortex sheet to separate into "future" consolidated models is found from the solution of Equation 119.

$$\frac{d\Gamma(y)}{dy} = 0 \tag{119}$$

This modification does not affect the size and number of consolidated vortices for helicopter blades under normal operation, as this method is intended to be used. However, for conventional fixed-wing aircraft with control surface deflection, Johnson's approach would only have identified two vortices in Figure 51, while experimental data shows the presence of a strong flap vortex (Vortex 2) separated from the tip vortex (Vortex 3). Figure 52 shows the streamwise vorticity in the wake of an airliner with flap deflection. Although $\gamma(y)$ is lower than zero for the left wing and greater than zero for the right wing, more than two vortices are produced due to the sharp change in the lift distribution between the control surfaces.

The trailing vortices are attributed to each future consolidated model as soon as they are generated on the wing. The rate of consolidation is based on the method developed by Johnson [89]. Let $y_j^{(-1)}$ and $y_j^{(+1)}$ be the left and right bounds on the wing for the j^{th} future consolidated vortex. The total circulation of this vortex $G_{j,0}$ calculated using Equation 120.

$$G_{j,0} = -\int_{y_j^{(-1)}}^{y_j^{(+1)}} \gamma(y)\, dy \tag{120}$$

The strength of the j^{th} consolidated wake as a function of time is

$$G_j(t) = G_{j,0} \cdot f_{\text{cons}} \tag{121}$$

$$= G_{j,0} \cdot \frac{t - t_0}{k_t} \tag{122}$$

where t is the current time, k_t is a time constant, and t_0 is the time at which the circulation was created. This equation is valid for $k_t \geq t \geq t_0$. Finally, the time

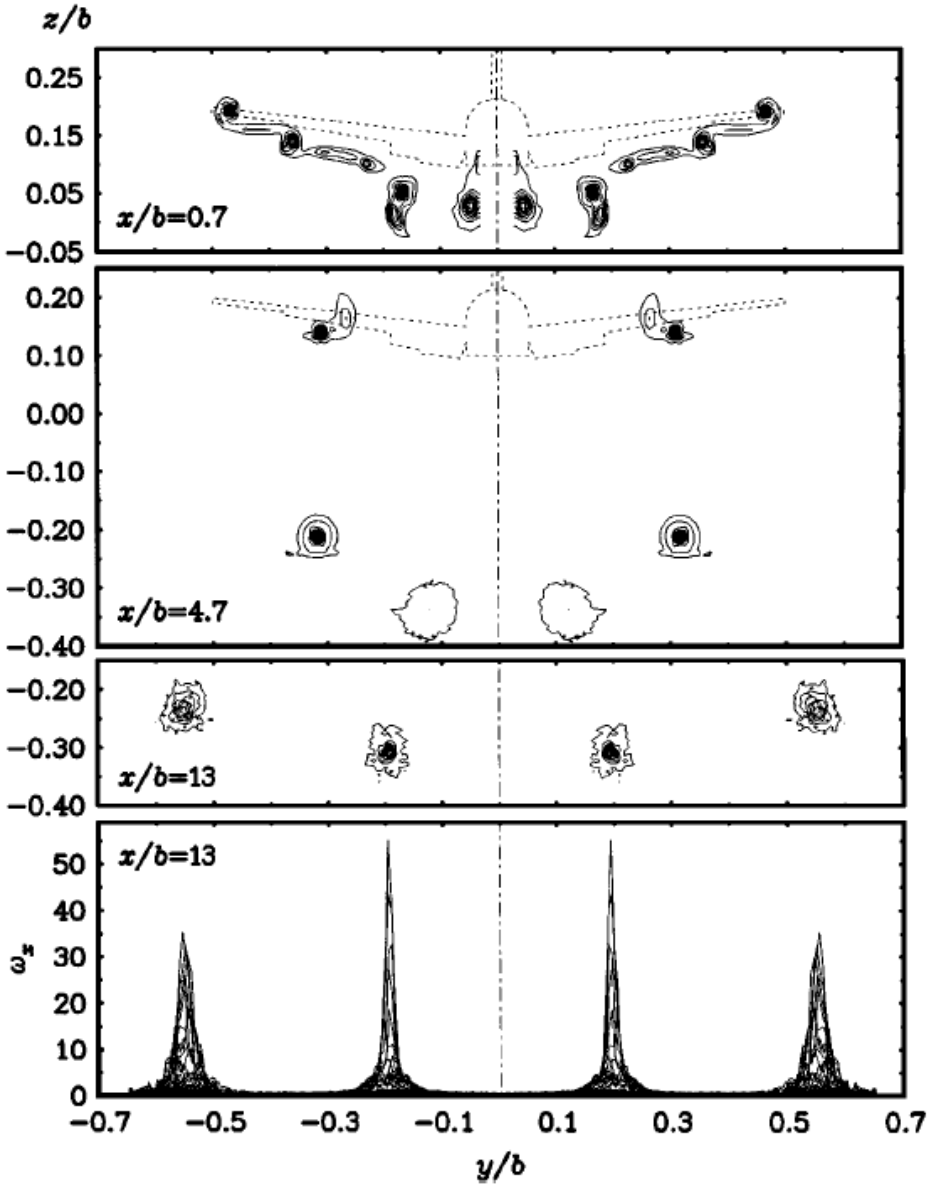

Figure 52: Streamwise vorticity in the wake of an airliner. Figure reproduced from Sparlart [149]. Flap deflection 35° inboard, 5° outboard, angle of attack 7°. The results were initially presented by de Bruin [42].

constant k_t is a function of the radius of gyration and the vortex strength. The radius of gyration, r_G and the centroid, r_C are calculated as follow,

$$G = \int_{y_j^{(-1)}}^{y_j^{(+1)}} \gamma(y)\, dy \tag{123}$$

$$G\boldsymbol{r_C} = \int_{y_j^{(-1)}}^{y_j^{(+1)}} \gamma(y)\, \boldsymbol{r}(y)\, dy \tag{124}$$

$$Gr_G^2 = \int_{y_j^{(-1)}}^{y_j^{(+1)}} \gamma(y)\, (r(y) - r_C)^2\, dy \tag{125}$$

where G is the consolidated vortex strength.

For helicopter rotors, the rate at which the consolidation occurs is critical since the process is usually not completed before the passage of the next blade. For fixed-wing aircraft flying along a periodic flight path, the distance between the aircraft is sufficient for the roll-up process to be completed, and thus, reduces the sensitivity of the responses to k_t.

At each timestep, the target circulation of the consolidated vortex $G_j(t)$ is evaluated. In order to meet this target, vortices closest to the consolidated vortex based on Euclidean distance are consolidated to the main vortex. The position of the consolidated vortex is now at the centroid of both the initial vortex and the added vortices. The process is completed when all trailing vortex filaments within the set defined from the wing circulation are consolidated in a single vortex. Since this process is very similar to the entrainment form of the vortex consolidation developed by Johnson [89], the reader should refer to his work for more details.

Appendix C.3 presents a set of test cases to validate the model. The second set of validation cases described below aims at the validation of the consolidation model. The numerical simulations with the consolidation model are compared to the free-vortex wake model without consolidation.

- Test Case 5: Flap deflection in steady level flight
- Test Case 6: Rapid roll rate

It is shown that the model with the consolidation reproduces the results of the model without consolidation within 1% error.

4.8.6 Wake Aging and Vortex Core Model

This section presents the approach to desingularize the vortex cores and to consider the vortex decay over a long period of time (order of one minute) after the passage of the aircraft. Core models are used to reduce the velocity near the vortex segment due to the air viscosity. The reduction in velocity due to the vortex roll-up process is described later in this section.

The wake roll-up process is typically rapid enough that viscous effects can be neglected during this phase [158]. However, the extended tip vortex filaments should undergo a reduction in intensity over time to account for the viscous effects, which have greater effects in the analysis of the reconfigurable rotor concept than a conventional helicopter.

A recent paper by Ning [121] proposed a model to evaluate the benefits of extended formation flight, which shows similarities to the current problem. In both cases, there is a need to evaluate the intensity and motion of the tip vortices over a long period of time, in Ning's case for a distance up to 100 wing spans. An older report by Donaldson and Bilanin [47] summarizes numerous models that capture the wake roll-up process, the aging of vortices and their stability. Before going into the details of the models and their implementation, the following assumptions are made.

- *Vortex stability* – Ning [121] highlights in his work on long distance formation flying that vortex stability is affected by the separation distance and the presence of other vortices (in Ning's case from another aircraft). The distance between the aircraft was greater than 40 spans. Aircraft flying along circular flight paths in hover are expected to be influenced by vortices generated many seconds after the aircraft passage. The current work neglects the vortex stability

as do most (if not all) helicopter and fixed-wing aircraft aerodynamic models.

- *Atmospheric stability* – Atmospheric stability can affect the rate of dissipation of a vortex [121]. The current work is based on standard atmospheric properties.

Due to the very low disk area of the "rotor," any system motion (forward flight) removes the influence of the trailing vortices within seconds. In these cases, the effects of the assumptions (especially vortex stability) are minor. It is acknowledged that vortex stability should be considered in future work in hover since the vortices are expected to remain in the vicinity of the aircraft flight path for long periods. The remainder of this section presents the vortex core model followed by the vortex decay model.

The roll-up process of the trailing vortices can neglect the effect of viscosity due to the short duration. However, the assumption that the total circulation is concentrated into a single vortex is too simplistic. The roll-up process of the continuous vortex sheet at the trailing edge can be evaluated using the Betz method, made visible by Donaldson in 1971 [46]. Donaldson [45] developed an extension of this model to consider the effect of a nonsymmetrical lift distribution and the presence of control surfaces on the roll-up process for fixed-wing applications.

Vortex core models have been used for numerous years for rotorcraft to desingularize the vortex tip, and at the same time, consider the roll-up process. It should be mentioned that the tip vortex of a helicopter blade is highly concentrated due to the very sharp change in the circulation, compared to a fixed-wing aircraft tip vortex. In the present work, there is a need to consider the reduction of velocity in the small viscous core, and to consider that the vortex is *not* as highly concentrated as on a helicopter rotor, while maintaining a low computational cost.

Based on physical experiments by Leishman [100], it was shown that the Vatistas core model with a coefficient $n = 2$ fits well the experiments for helicopter rotors.

The tangential velocity based on the Vatista model is evaluated using Equation 126,

$$V_\theta(\bar{r}) = \left(\frac{\Gamma}{2\pi r}\right) \frac{r^2}{(r^{2n} + r_c^{2n})^{1/n}} \tag{126}$$

where r_c is the vortex core and $\bar{r}$ is the distance from the vortex core. Numerous experiments were performed to evaluate how the vortex core grows over time for helicopter and fixed-wing aircraft. For helicopter rotors, it was shown that the vortex core grows asymptotically from 5% to about 15% of the blade chord within the first 900 degrees of wake age, which is a very short period of time for a conventional helicopter [99]. For fixed-wing aircraft, the vortex core radius was shown to be approximately constant at 1% of the wingspan for a normalized time t^*[1] from 0 to 5 seconds. As a reference, for a wing with an aspect ratio of 8 and a lift coefficient of 0.5, a normalized time of 5 is equivalent to 500 spans.

The method developed in this work combines the roll-up model by Betz and extended by Donaldson with the Vatistas core model. This method is only used once the consolidation of the trailing vortices is completed. For simplicity, the process is demonstrated for a simply loaded wing (Betz model) with the Vatistas core model. The Betz roll-up model calculates the distribution of circulation about the centroid of the trailing vortex as a function of the distance. The description of the model was greatly simplified by Rossow [136] and Jordan [91]. The center of the consolidated vortex is located at the centroid, evaluated with Equation 127.

$$\bar{y} = \frac{-\int_0^{b/2} \frac{d\Gamma(y)}{dy} y dy}{\Gamma_0} \tag{127}$$

By using the conservation of circulation and radius of gyration, Betz derived an approach to predict the distribution of circulation in the rolled-up vortex. The distance from the center of the vortex centroid at which one finds the circulation equal

[1]The normalized time is defined as the ratio of the initial descent rate of the vortex pair divided by the wing span, multiplied by the actual time $t* = \frac{\Gamma_0}{2\pi b_0^2} t$

to the circulation at the spanwise location y on the wing is equal to the distance from y to the centroid of the shed vorticity *outboard* of y, as shown in Equation 128,

$$\Gamma(y) = \Gamma'(\bar{y}(y) - y) \tag{128}$$

where $\bar{y}(y)$ is the location of the centroid outboard of y and Γ' is the circulation of the rolled-up vortex. The reader can refer to Donaldson [45] for a more detailed description of the model.

The addition of the Vatistas model to reduce the velocity in the vortex core is done by varying the circulation Γ as a function of r. The induced velocity from a consolidated vortex (for an infinite vortex) is then

$$V_\theta(r) = \left(\frac{\Gamma'(r)}{2\pi r}\right) \frac{r^2}{\left(r^{2n} + r_c^{2n}\right)^{1/n}} \tag{129}$$

where $\Gamma'(r)$ is the consolidated vortex circulation predicted by Donaldson's method. Before additional details are provided for the extension of this approach to wings with control surface deflection, a simple example is provided. Let the circulation on an elliptical wing without aerodynamic and geometric twist be

$$\Gamma(y) = \left(1 - \frac{y^2}{16}\right) \quad \text{for } 0 \leq y \leq 4 \tag{130}$$

for a maximum circulation (at the symmetry plane) of 1 m^{2}s and a half-span of 4 m. First, the centroid of the consolidated vortex is located at

$$\bar{y} = \frac{-\int_0^{b/2} \frac{d\Gamma(y)}{dy} y dy}{\Gamma_0} \tag{131}$$

$$= -\int_0^4 \frac{d\Gamma(y)}{dy} y dy \tag{132}$$

$$= 3.1436 \text{ m} \tag{133}$$

as predicted by the consolidation model presented in Section 4.8.5. The induced velocity as a function of the distance from the vortex is compared in Figure 53 with three different methods: Betz model only, vortex filament with Vatistas core model, and the Betz model with Vatistas core model.

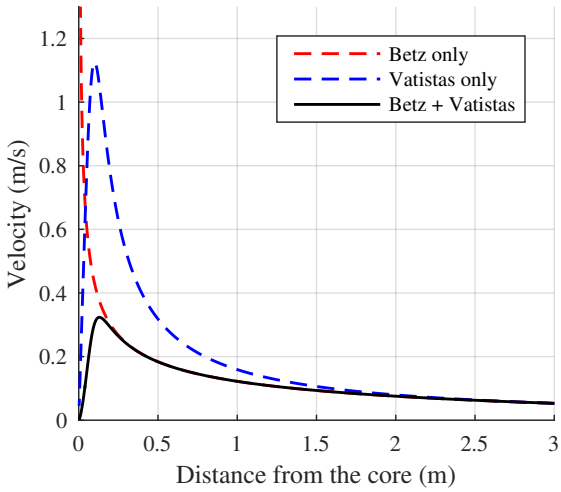

Figure 53: Comparision of methods to model the induced velocity

The induced velocity by the wake roll-up process evaluated by Betz is presented with the dashed red line. Although it shows similarity with a simple vortex filament, the velocity near the core does not extend to infinity, but to 3.58 m/s since the vorticity is still distributed over a finite area greater than zero.

The prediction made with the Vatistas core model with $n = 2$ and $r_c = 0.1$ shows primary features from this model. The velocity reduces to zero at the center of the core but grows rapidly since the circulation Γ is still concentrated near the center. The core radius r_c is the main driver in how the circulation is distributed, without consideration from the lift distribution it was generated from.

The novel method combines both the advantages of the Betz method and the Vatistas core model. The velocity near the center of the core reduces to zero due to the strong effects of the fluid vorticity. However, the spread of the vorticity is also driven by the Betz' model, which depends on how the circulation is distributed on the lifting body. In other words, two vortices with the same intensity can have a different induced velocity distribution.

The method presented previously can only be applied with a monotonically decreasing circulation from the aircraft symmetry plane to the wingtip, or simply loaded

wings due to the limitations of the Betz method. The method implemented in this work is the extension of the Betz method by Donaldson [45] that considers the roll-up process of an arbitrary lift distribution. His model was validated with experimental data for commercial transport aircraft. It should be noted that the original model did not include the core model, and therefore, presents a discontinuity at the core. For completeness, his method is described hereafter.

Let the vorticity between points A and B identified in Figure 51 from the consolidation model be rolled-up into a single vortex at the centroid of the shed vorticity, denoted $\bar{y}_B$. This location is identified using Equation 134,

$$\bar{y}_B \int_{y_B}^{y_A} \frac{d\Gamma}{dy} dy = \int_{y_B}^{y_A} y \frac{d\Gamma}{dy} dy \tag{134}$$

where the integrant on the left side is the total circulation of the consolidated vortex. The method developed by Donaldson is based on the Betz invariants between y_1 and y_2, two arbitrary points between y_A and y_B detailed hereafter. It is assumed that the most intense region of vorticity shedding $|d\Gamma/dy|$, located at y_{m_B}, is centered in the consolidated vortex and that the vorticity on both sides is then rolled-up around it.

Let y_1 and y_2 be two arbitrary points on each side of y_{m_B}, and $\bar{y}_{12}$ the centroid of the shed vorticity between y_1 and y_2. Donaldson showed that y_1 and y_2 should always be equidistant from $\bar{y}_{12}$. Let r_b be the distance between the centroid $\bar{y}_{12}$ and the two points y_1 and y_2.

$$r_B = y_2 - \bar{y}_{12} = \bar{y}_{12} - y_1 \tag{135}$$

The circulation as a function of distance from the center of the consolidated vortex is evaluated with Equation 136.

$$\Gamma'(r_B) = \Gamma(y_1) - \Gamma(y_2) \tag{136}$$

In other words, given the distance from the vortex core r_B, one finds y_1 and y_2 such that the centroid is located at mid-distance from y_1 and y_2. The circulation $\Gamma'(r_B)$ is the difference between the circulation at y_1 and y_2.

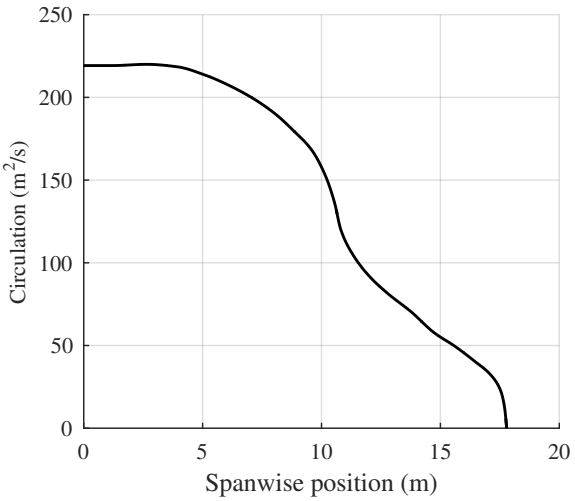

Figure 54: Circulation distribution of a DC-7 in takeoff configuration. The takeoff configuration is characterized with 20° inboard flap deflection. The sharp lift changes at 11 m is located at the flap tip [45]

This approach holds as long as $y_1 \geq y_B$ and $y_2 \leq y_A$. If one of those two conditions is violated, the variable y_1 or y_2 is held at its maximum until the other variable reaches its maximum too.

As for the demonstration with the simply loaded wing, the Vatistas model is added as shown in Equation 137, except that the circulation is now a function of r_B instead of r.

$$V_\theta(r_B) = \left(\frac{\Gamma'(r_B)}{2\pi r_B}\right) \frac{r_B^2}{\left(r_B^{2n} + r_c^{2n}\right)^{1/n}} \tag{137}$$

This method is compared to the same experimental data presented by Donaldson of a DC-7 in takeoff configuration with 20° flap deflection. The data was selected from the results of full-scale tower flyby tests at the National Aviation Facilities Experimental Center (FAFEC) by the Federal Aviation Administration (FAA).

Figure 54 presents the circulation distribution for the DC-7 provided by the manufacturer during the flyby. As expected, a sharp change in the lift distribution is shown, which results from the deflection of the inboard flap, thus creating a strong flap vortex. Using the method developed by Donaldson, the flap vortex intensity is predicted to be 171.3 m^2/s and the tip vortex intensity is predicted to be only

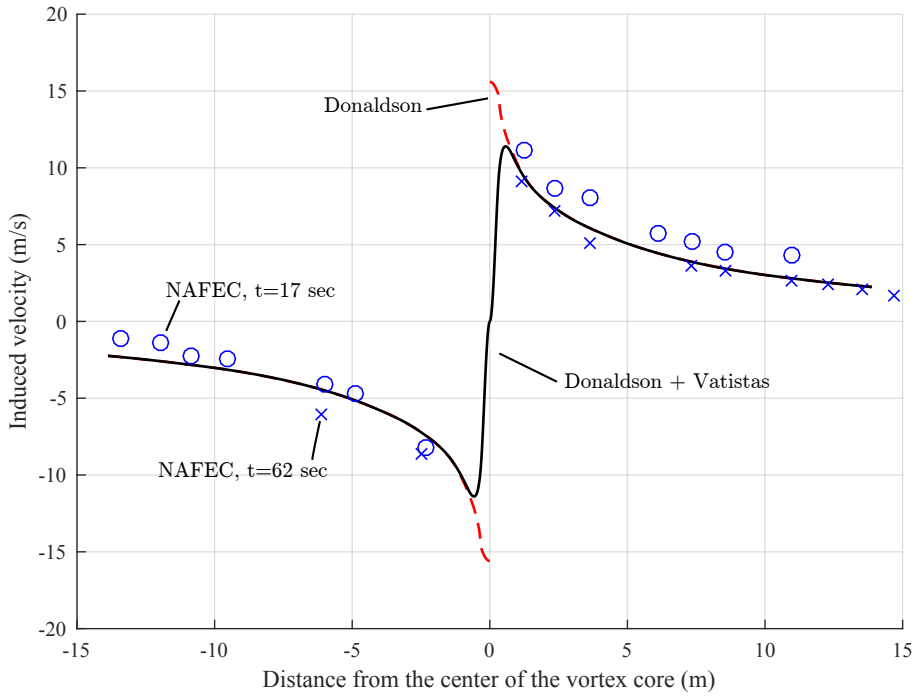

Figure 55: Flap vortex induced velocity by a DC-7 in takeoff configuration. Two numerical methods are compared: Donaldson (red dashed curve) and Donaldson + Vatistas' core model (solid black curve). Experimental induced velocities are provided with blue markers.

46.5 m^2/s. However, the distribution of the circulation about the core varies greatly between the two vortices.

Figure 55 compares the tangential induced velocity by the consolidated flap vortex using Donaldson's method, and the improved method with the Vatistas' core model with $n = 2$ and $r_c = 0.35$ m (1% span). Experimental data is also provided from the flight test at two wake ages. The agreement between the novel model and the experimental results is satisfactory. The salient advantage of the novel method, which combines the roll-up model by Donaldson and Vatistas' core model, is the absence of a velocity discontinuity at the core. Outside the vortex core, both methods are equivalent. Donaldson validated his method with more than 25 different flight tests, and the induced velocity predictions were shown to be satisfactory for multiple aircraft

types and flight configurations.

Vortex aging is usually not considered in rotorcraft aerodynamic models since five rotor revolutions happen within approximately 1 sec or so. Wake aging is partially considered for helicopter wakes through small variations in the vortex core radius, but the reduction of circulation over a few seconds can be neglected.

In the current application, it is expected that a vortex decay model is required in hover since the aircraft wake can remain close to the aircraft (no significant convection) for numerous seconds.

In his study about long distance formation flying, Ning [121] used a probabilistic, two-phase wake vortex decay and transport model developed by Holzäpfel [78, 77]. A simplification of this model is used in this work. The reader should refer to Ning [121] for a few of the major vortex decay models developed over the years and Spalart [149] for a literature review about aircraft vortices.

The Holzäpfel model assumes that the vortex decay occurs in two phases as suggested by Large Eddy Simulation (LES) and experimental data. The form of the circulation decay is based on the analytical solution of the Navier-Stokes equation a for vortex in a viscous flow,

$$\frac{\Gamma(r,t)}{\Gamma_0} = 1 - \exp\left(\frac{-r^2}{4\nu t}\right) \tag{138}$$

where ν is the fluid kinematic viscosity, and Γ_0 is the initial vortex strength at $t = 0$. Based on this functional form and on the observations that vortex decay is comprised of a diffusion phase and a rapid decay phase [31, 78], the vortex decay is evaluated using Equations 139-140. During the diffusion phase, the normalized circulation decay is given by

$$\frac{\Gamma(r,t)}{\Gamma_0} = \Gamma^* = A - \exp\left(\frac{-R^{*2}}{\nu_1^*(t^* - T_1^*)}\right) \tag{139}$$

while the rapid-decay phase shows a much more rapid reduction in circulation as

shown in Equation 140.

$$\Gamma^* = A - \exp\left(\frac{-R^{*2}}{\nu_1^*\left(t^* - T_1^*\right)}\right) - \exp\left(\frac{-R^{*2}}{\nu_2^*\left(t^* - T_2^*\right)}\right) \tag{140}$$

The coefficients A, R^*, T_1^*, T_2^*, ν_1^*, and ν_2^* can be obtained from numerical simulations. The normalized time $t*$ is defined in Equation 141.

$$t^* = \frac{\Gamma_0}{2\pi b^2} t \tag{141}$$

where b denotes the wingspan.

It is acknowledged that this model first requires significant tuning based on atmospheric conditions. Moreover, the reduction of circulation by this model is the mean of the reduction in circulation between 5 and 15 meters from the vortex center, denoted Γ_{5-15}. For smaller-scale vehicles, such as the 8-meter span aircraft presented in Section 5.1, very few studies exist on vortex decay. Finally, this model does not consider vortex interaction in the vortex decay, which can trigger instabilities and therefore, the rapid vortex decay. Spalart [149] mentions that even a slight deviation by the airplane from a straight flight path can trigger the rapid decay.

Figure 56 shows the reduction in circulation Γ_{5-15}/Γ_0 for a moderate turbulence level in a neutrally stratified atmosphere, where the diffusion phase and rapid decay phase can clearly be identified.

4.9 Propulsion

The output from the aerodynamic model is the drag, both parasitic and induced. The actual thrust is calculated by adding the inertial reaction of the aircraft, the external forces (tether) and gravity. The thrust as a function of time for the i^{th} aircraft is denoted $F_{Th}^{(i)}$.

The objective of the propulsion model is to evaluate the power requirements by the power source (batteries and generator) to be sent to each aircraft as a function of

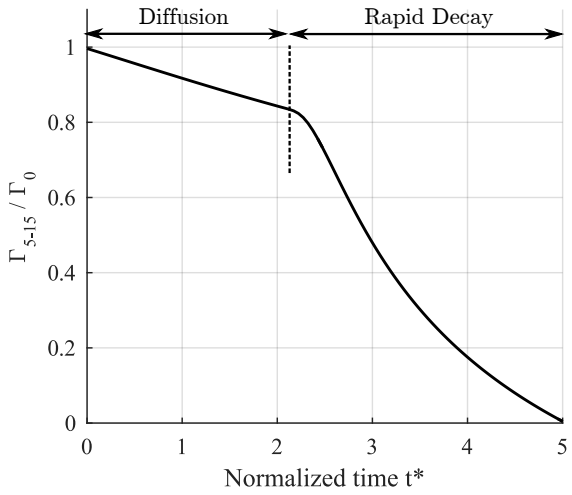

Figure 56: Vortex decay in a neutrally stratified atmosphere. The parameters used in this example are: $A = 1.1$, $R^{*2} = 0.0121$, $\nu_1 = 1.78 \cdot 10^{-3}$, $T_1^* = -3$, $\nu_2 = 0.01$, $T_2^* = 2$.

time during the periodic flight path. The propulsion model is comprised of the three submodels, based on a physical decomposition:

- Propeller
- Motor, drive, and conductors
- Power source

The propellers must maneuver the aircraft along complex flight paths, with a rapid variation in velocity, thrust, and aircraft attitude. The following assumptions are made to allow design space exploration without the need for very expensive CFD.

- *Independence* – It is assumed that there is no interaction between the propellers (each propeller is independent) and between the propellers and the lifting surfaces.
- *Quasi-steady-state* – Although the thrust requirement changes over time, it is assumed that a quasi-steady-state approximation can be used to remove the time dependency.

- *Normal flow* – The propellers are assumed to operate with the relative velocity aligned with the axis of rotation at all time. This approximation is valid as the sideslip angle is small, at small angles of attack.

- *Optimal propeller* – Since the propellers are operated most of the time at off-design conditions, there is the possibility that the optimal propeller geometry for the application is *not* a propeller optimized for a specific flight condition. The optimization process of such propeller is much more complex. In the present work, it is assumed that the family of fixed-pitch propellers considered are resulting from an optimization process about a single flight condition.

Based on these assumptions, Sections 4.9.1 and 4.9.2 present the methods and tools used to predict the power requirement given the target thrust.

4.9.1 Propeller Design and Operation

Most empirical approaches to calculate the propeller efficiency of aircraft assume a constant propeller efficiency, or simple relationships that take into account the advance ratio J and the design advance ratio J_D. However, those relationships use empirical data of propellers developed for fuel-powered aircraft, with their limitations in operating conditions. Since the tethered aircraft require strong variation of thrust and velocity, and the propellers are driven by electric motors, the optimal propeller design is expected to differ from traditional designs. Therefore, a physics-based method is required to optimize the propeller design and to operate the propeller through the whole flight envelope.

The selected programs that meet the criteria are QMILL and QPROP, developed by Dr. Mark Drela at MIT [48]. The first code provides an optimal propeller geometry given the design conditions and general propeller characteristics (design tool). The second code analyzes the propeller with different angular velocities and wind velocities given the details of the blade geometry are provided (analysis tool). Both codes

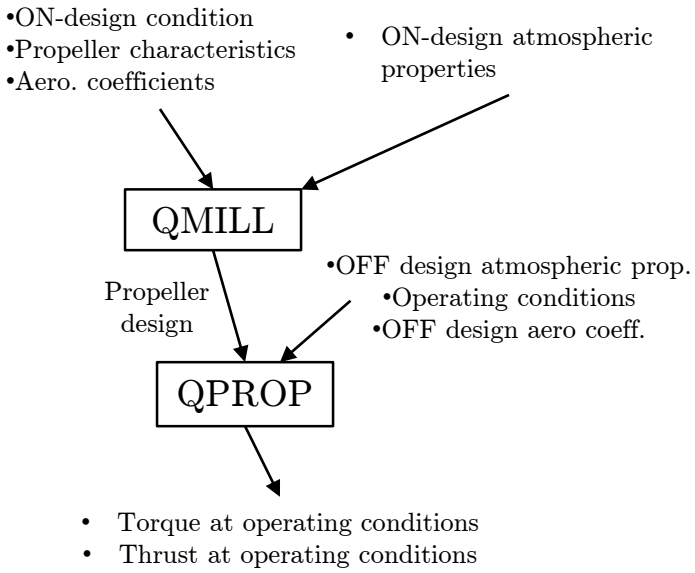

Figure 57: Propeller software architecture, adapted from Rancourt [129].

are based on an extension of the classical blade element/vortex formulation with radially varying self-induction velocity and circulation. This method is well adapted for heavily-loaded actuator disks [48] such as wind turbines and propellers.

The two programs, QPROP and QMILL, are integrated into a single modeling and simulation environment developed by Rancourt for micro wind turbines [129] and adapted in the present work for propeller design and operation. Figure 57 shows the main inputs and outputs of the two models and how they are used in a design mode or to predict propeller performance.

Let $\boldsymbol{X}_I$ be the set of variables that are required to design a propeller,

$$\boldsymbol{X}_I = \left\{ \begin{array}{c} \text{Radius} \\ \text{Design velocity} \\ \text{Thrust} \\ \text{RPM} \\ \text{Design lift coefficient} \\ \text{Number of blades} \\ \vdots \\ \text{Air density} \\ \text{Airfoil properties} \end{array} \right\} \tag{142}$$

The geometry of the optimal propeller is provided by QMILL, such that,

$$\boldsymbol{G} = \boldsymbol{G}\left(\boldsymbol{X}_I\right) \tag{143}$$

where $\boldsymbol{G}$ is the blade chord and twist distribution. The propeller performance can then be analyzed in various flight conditions, defined by $\boldsymbol{X}_O$,

$$\boldsymbol{X}_O = \left\{ \begin{array}{c} \text{Relative velocity} \\ \text{RPM} \\ \text{Air density} \\ \text{Airfoil properties} \end{array} \right\} \tag{144}$$

where variation in air density and airfoil properties can be modified. The most efficient way to use QPROP is to solve for the thrust and power requirement (or torque) given the propeller geometry and the operating condition.

$$P = P\left(\boldsymbol{X}_O, \boldsymbol{G}\right) \tag{145}$$

$$= P\left(\boldsymbol{X}_O, \boldsymbol{G}\left(\boldsymbol{X}_I\right)\right) \tag{146}$$

$$T = T\left(\boldsymbol{X}_O, \boldsymbol{G}\right) \tag{147}$$

$$= P\left(\boldsymbol{X}_O, \boldsymbol{G}\left(\boldsymbol{X}_I\right)\right) \tag{148}$$

$$\tag{149}$$

In order to reduce the computational time to explore the design space, a surrogate modeling approach is used. The conventional approach would be to create a surrogate of the power ($\hat{P}$) and a surrogate of the thrust ($\hat{T}$) as a function of the design and operating variables ($\boldsymbol{X}_I, \boldsymbol{X}_O$). However, the objective is to solve for the power and the operating RPM *given* the thrust requirement.

The simplest approach is to create a surrogate model by using the response T as an input, since the function $P\left(T|\boldsymbol{X}_O \setminus \Omega_O, \boldsymbol{X}_I\right)$ is monotonic for $T > 0$, where Ω_O denotes the angular velocity of the propeller in operation[2]. However, two limiting factors must be considered:

1. *Infeasible/unrealistic propeller designs* – It is seldom possible to properly identify a range of the propeller design variables $\boldsymbol{X}_I$ to obtain propellers that have a reasonable geometry (maximum chord-to-span ratio for example). This problem is even more true with hypercubic design spaces.

2. *Wide range of the design variables* – A wide range of the operating variables $\boldsymbol{X}_O$ can lead to very high power requirements or negative thrust, which should not be considered in this study. For a given vehicle of interest, there is a good knowledge about the power available from the motors, and the surrogate model should only focus on that region to increase the surrogate model accuracy.

The method developed in this work combines machine learning algorithms and surrogate modeling techniques to create high accuracy surrogate models of the propeller mechanical power required and angular velocity. Although simple, this structured method has shown its potential in previous work by Rancourt [130] in the field of wind energy. The method can be summarized in four steps:

1. *Generate data* – Generate a design of experiments and perform the numerical simulation. In the present case, the design variables are $\boldsymbol{X}_I, \boldsymbol{X}_O$ and the desired

[2]The operator $\setminus$ is used to exclude a variable from the set

outputs are $P, T, \boldsymbol{G}$, where $\boldsymbol{G}$ is the propeller geometry.

2. *Filtration* – Filter out cases that are not of interest, such as:

   - The thrust predicted is below zero, $T < 0$
   - Power is extracted by the propeller, $P < 0$
   - The power requirement is above the maximum power available (including some margin), $P > P_{\max}$
   - Invalid propeller geometry (chord-to-radius too wide or too narrow)

3. *Create the surrogate models* – Create surrogate models (of any form) of the metric of interest using all the samples that were not filtered out. In the present case, the two surrogate models are of the form:

$$\hat{P} = \hat{P}\left(T, \boldsymbol{X}_O \setminus \Omega_O, \boldsymbol{X}_I\right) \tag{150}$$

$$\hat{\Omega}_O = \hat{\Omega}_O\left(T, \boldsymbol{X}_O \setminus \Omega_O, \boldsymbol{X}_I\right) \tag{151}$$

4. *Create the neural network, non-linear classifiers* – The key element is to create one neural-network classifier per condition used to filter out the data in Step 2. In the present case, up to five non-linear classifiers are generated (two for the propeller geometry).

Given a numerical value of the input variables $\{T, \boldsymbol{X}_O \setminus \Omega_O, \boldsymbol{X}_I\}$ within the side constraints used to generate the initial data, the non-linear classifiers are used to evaluate if the sample is within the region of interest, in numerous dimensions. If all the classifiers predict that the sample is within the feasible range, then the power and angular velocity are evaluated using the surrogates.

In specific flight conditions, it is possible that the required thrust be below zero, for example, if the tether is "towing" the aircraft or a rapid deceleration is required. For optimized propellers, it could be possible to harvest this power and reuse it for

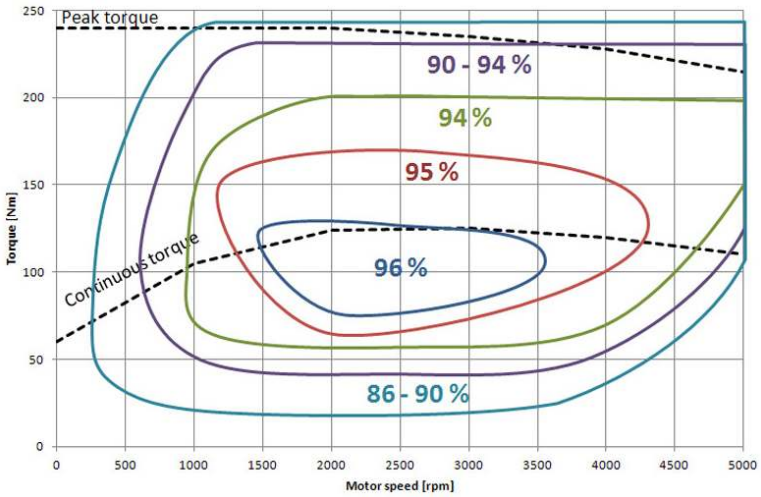

Figure 58: Emrax-228 efficiency map

the other aircraft or to recharge the batteries. In this work, it is assumed that this excess power is spoiled.

4.9.2 Electric Motors, Drives and Conductors

As introduced in Section 1.3, electric motors have a high efficiency over their entire operating envelope. Permanent magnet generators and superconducting machines can have efficiencies well above 90% depending on the application [145, 16]. For completeness, Figure 58 shows the efficiency as a function of RPM and torque for the Emrax-228 electric motor [52], a commercially available electric motor for aircraft electric propulsion. Although more advanced electric motor and drive models could be implemented in the future, this work assumes a constant efficiency of 90% for the combined motor and drive.

The electrical resistance in the long tethers is modeled using Ohm's law,

$$V = RI \tag{152}$$

where the electrical conductor resistance R is based on the material properties and the conductor cross-sectional area. This approach is similar to the technique used by Rancourt in the design space exploration of gyrocopter-type wind turbine [130].

Direct current is used as for Makani's airborne wind turbine concept, where the motor drives are located onboard the UAVs.

CHAPTER V

RESULTS

This section presents numerous studies based on a single aircraft, the Makani's *Wing 7*. The objective is to explore and optimize the flight paths (which include changes in the velocity) to reduce the power requirement. This section first introduces the baseline aircraft for the study. Then, a first design space exploration and optimization is performed by using exclusively the lower fidelity environment. The higher fidelity dynamic tether model is then compared to the lower fidelity tether model model with appropriate calibration to reduce payload motion.

5.1 Description of the Baseline Aircraft: Makani's Wing 7

The baseline aircraft used throughout this chapter is the Makani's *Wing 7* tethered aircraft, developed for wind power harvesting. As mentioned early in this document, the main goal of this work is to develop the required methods and models to optimize the flight path of the aircraft through a design space exploration, excluding the design of the aircraft itself. Figure 59 and 60 show the *Wing 7* aircraft during flight and a top-view [105].

This aircraft is designed to fly with relative wind velocities of up to 100 mph while tethered to the ground and technical specifications are available. In other words, there is no need to "develop" an aircraft and estimate its performance or guess its weight; those specifications were made available throughout the years by the company. Table 4 presents the main characteristics of the *Wing 7* aircraft compiled from a set of references [106, 6] and reverse engineering.

The motor power rating was obtained from the motors used on the Wing 7 prototype developed by Joby Motors. It is assumed that due to the very efficient cooling

Figure 59: Makani's *Wing 7* in flight

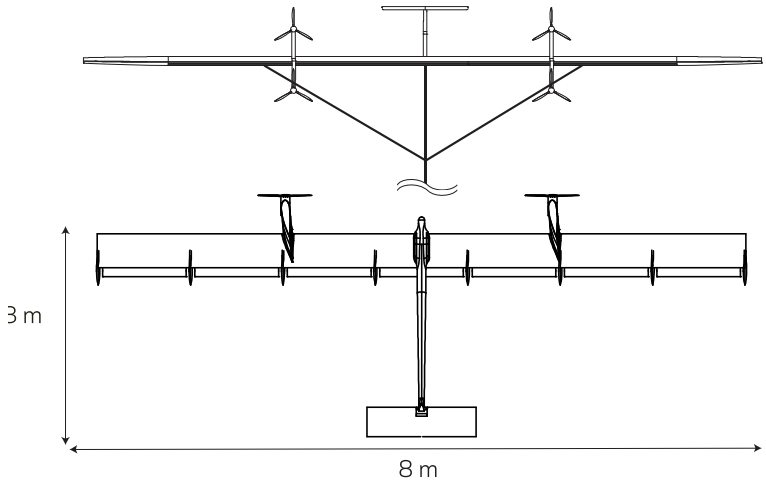

Figure 60: Makani's *Wing 7* front and top-view drawings [105]

Table 4: *Wing 7* salient characteristics [106, 6]

Characteristic	Metric properties
Wing area S	4.96 m^2
Aspect ratio $\mathcal{R}$	12.9
Oswald efficiency (approx) e	0.85
Power rating per motor	8.2 kW
Number of motors	4
Parasitic drag coeff C_{D_0}	0.015
Mass	60 kg

at the flight speed, peak powers in the order of 15 kW can be achieved per motor. The parasitic drag coefficient is evaluated using a wetted area approach described by Raymer [133]. Given its slim fuselage and its high aspect ratio, the maximum lift-to-drag ratio of this aircraft is above 20.

The tether properties are provided in Table 5 for completeness. They are based on previous studies by the authors [44], Ahrens [6] and the document provided by Makani to the FAA for flight test approval in 2011 [105].

Table 5: Tether properties [106, 44]

Characteristic	Metric properties
Mass per unit length	0.1 kg/m
Outside diameter	7 mm
Operating voltage (DC)	1,100 V
Conductor diameter	2.2 mm
Conductor material	Copper

A high voltage is used for the electric-powered tethered aircraft to minimize the conductive losses. The *Wing 7* aircraft was designed with a 144 m tether. In the current design space exploration, it is assumed that the tether length is a parameter in the optimization process, and therefore, can be changed prior to the optimization.

The propellers are the only components that have to be designed since the baseline aircraft was optimized for power generation. The propellers are constrained to a diameter of 52 cm, which is derived from the *Wing 7* drawings as illustrated in

Table 6: Propeller parameters for design

Characteristic	Variable	Properties
Propeller radius	r_{tip}	26 cm
Hub radius	r_{hub}	7 cm
Number of blades	n_b	3
Minimum lift coefficient	$C_{l,\min}$	-0.7
Maximum lift coefficient	$C_{l,\max}$	1.5
Lift coefficient at $\alpha = 0$	$C_{l,0}$	0.6
Parasitic drag coefficient at $\alpha = 0$	$C_{d,0}$	0.01
2nd order drag coefficient, upper	$C_{d,2u}$	0.01
2nd order drag coefficient, lower	$C_{d,2l}$	0.02
Lift coefficient at minimum drag	C_{l,cd_0}	0.5
Reference Reynolds numbers	Re_{ref}	200,000
Reynolds numbers exponent (see QPROP manual)	Re_{exp}	-0.5
Design lift coefficient	$C_{l,d}$	0.5
Lift curve slope	$C_{l,\alpha}$	1.8π

Figure 60. Table 6 lists the assumed parameters for the propeller design.

The baseline propeller airfoil is a NACA 2412. The properties for this airfoil are obtained from Abbott [1]. However, the propeller performance is not significantly affected by minor modifications in the airfoil properties. The reader should refer to the QPROP theory manual [48] for more details on the effect of each of those airfoil properties on the lift and drag of the blade section.

5.2 Lower Fidelity Design Space Exploration

5.2.1 Propeller Model

The propeller model for the lower fidelity design space exploration has to be low cost but still provide an insight as to what efficiency could be expected given the required thrust at a given velocity. In the lower fidelity environment, a baseline propeller is designed and then operated at various conditions (thrust and velocity) to extract the efficiency. In other words, the propeller design is not affected by the exploration of

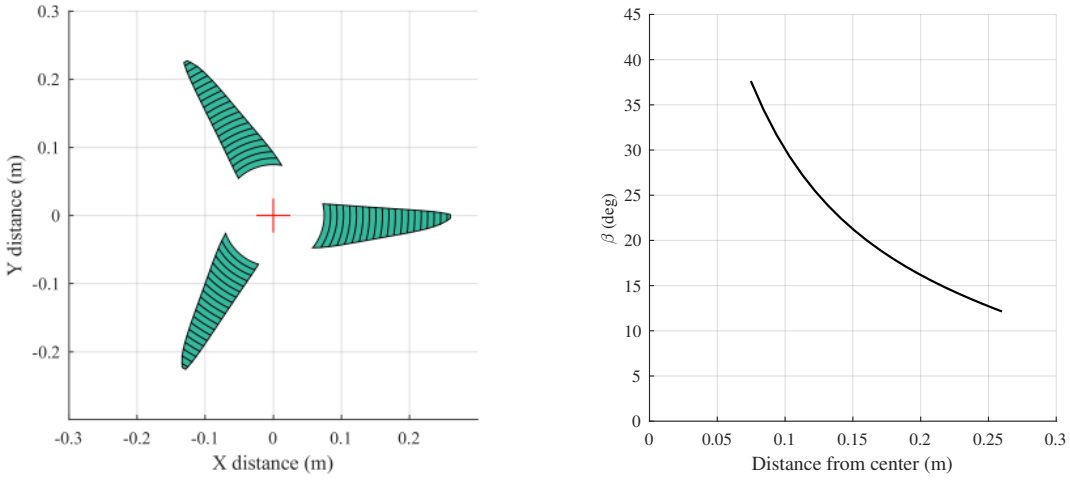

(a) Propeller geometry

(b) Blade twist

Figure 61: Propeller design optimized for a single operating point, for the low-fidelity environment. This three-bladed propeller is optimized for 35 m/s, 8 kW, and 200 m/s tip speed.

the various analyzed flight paths. The propeller model is then reduced to:

$$\hat{P} = \hat{P}\left(T, V\right) \tag{153}$$

$$\hat{\Omega}_O = \hat{\Omega}_O\left(T, V\right) \tag{154}$$

where T is the thrust, and V the relative velocity. In order to obtain this relation, a baseline propeller is first designed with $V = 35$ m/s and power of 8 kW. The design propeller tip-speed is fixed at 200 m/s for noise and shock considerations. Under those conditions, an optimized propeller is designed and used for the simulations using the lower fidelity environment. Figure 61 shows the optimized propeller geometry and twist.

The thrust and torque for various angular velocities and velocities were evaluated using QPROP. A 300 cases, latin hypercube space-filling design of experiments is used on the two design variables, for which $0 \leq V \leq 80$ m/s and $200 \leq \Omega \leq 1200$ rad/s. Then, a surrogate model of the power required $\hat{P}$ is obtained as a function of T and V. As explained in Section 4.9, a non-linear classifier is used to bound the

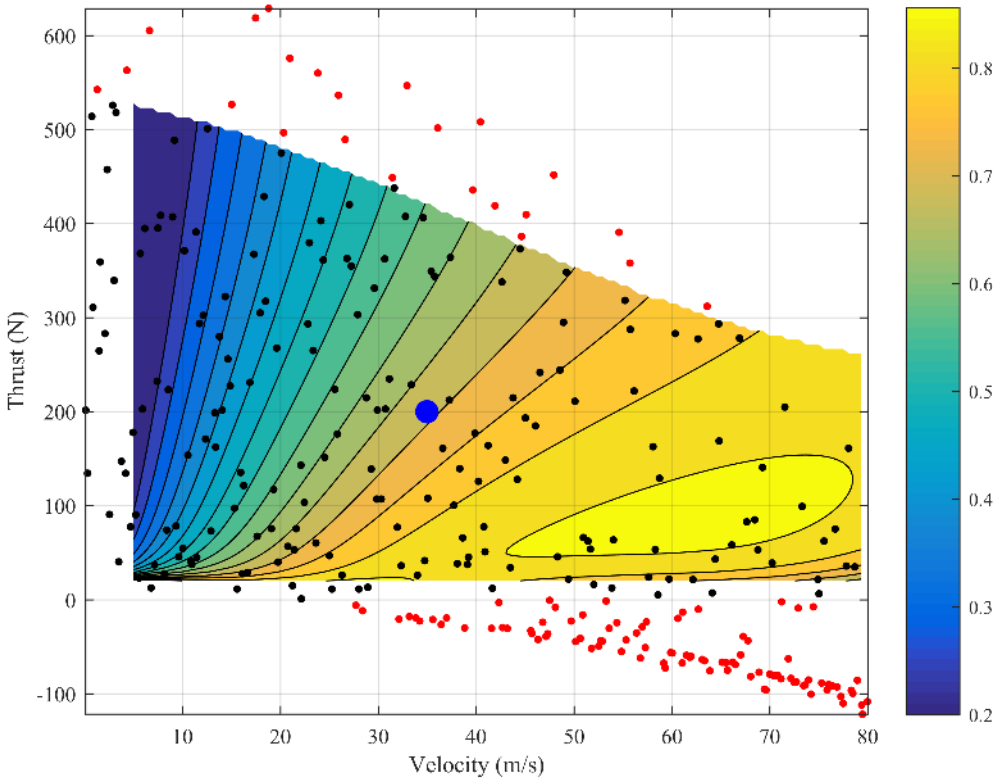

Figure 62: Propeller efficiency as a function of thrust and velocity, designed for the lower fidelity environment. This propeller is designed for 35 m/s and 8 kW shaft power, depicted by a large blue dot. The black dots are the cases considered to create the surrogate, while the red dots are the cases outside the range of interest, and therefore, discarded for the surrogate. Those cases are only used to bound the surrogate.

model. Since the thrust is *not* a design variable of QPROP, but rather a response, the surrogate model on power $\hat{P}$ is not trained with equally-spaced experiments, nor the design space has simple side constraints. Figure 62 shows the propeller efficiency as a function of the thrust and velocity bounded by the non-linear classifier.

The red and black dots represent the results from the design of experiment (since the thrust is a response from QPROP). The lower and upper limits on velocity are imposed by side constraints. The lower limit on thrust is bounded by a side constraint, an input to the model. The upper limit on thrust is obtained from a neural-network, non-linear classifier. The classification of the feasible and unfeasible samples for

training and test are determined from a maximum shaft power of 15 kW.

Although this example is simple, it is used to demonstrate the use of classifiers to bounds surrogate models by "inverting" the equation, where the design space becomes highly non-hypercubic. As expected, the thrust available reduces as a function of velocity for a given maximum shaft power.

The propeller efficiency at the design point is 71% due to the high disk loading of the propeller. A larger propeller at 8 kW and 35 m/s would be more efficient, but the current Joby motor would require modifications to ensure proper torque and rpm matching. Since the objective of this paper is to explore how the *Wing 7* aircraft could be used to lift payloads, the propeller diameter is kept fixed.

At low velocity and high thrust, the efficiency drops sharply due to the large induced velocity. The efficiency at a thrust level less than 30 N reduces drastically due to the parasitic drag of the blade and non-uniform flow associated with a mismatch in the blade twist.

One important conclusion from this model is that the propeller efficiency cannot be considered constant for tethered aircraft since they must operate through a variety of flight speeds and thrust levels. For completeness, Figure 63 presents the predicted propeller angular velocity (in RPM) as a function of the thrust required and velocity. The same classifier is used to bound the limits of the model.

Although the propeller can be operated over a large operating space, it should be mentioned that a fixed-pitch propeller has limitations due to tip-speed and motor maximum speed. As an example, the tip-speed reaches 300 m/s for a thrust requirement of 270 N at a flight speed of 80 m/s. In those conditions, the validity of the model is reduced since shocks are expected to appear, and thus, reduce the propeller efficiency.

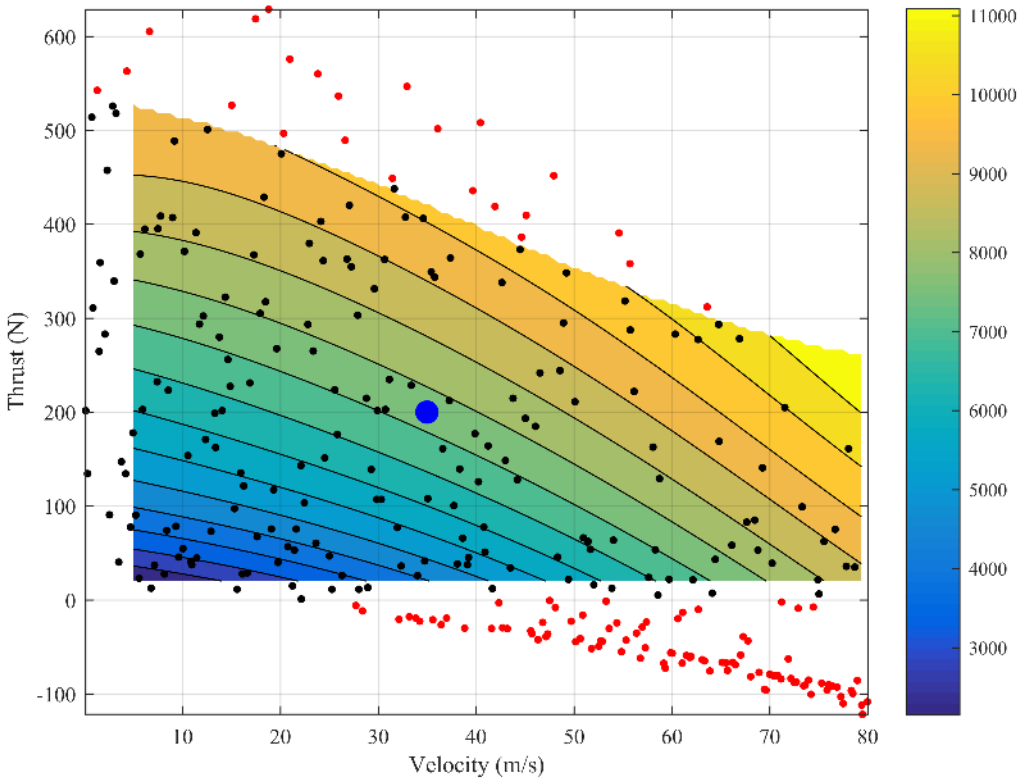

Figure 63: Propeller angular velocity (rpm) as a function of thrust and velocity, designed for the lower fidelity environment. This propeller is designed for 35 m/s and 8 kW shaft power, depicted by a large blue dot. The black dots are the cases considered to create the surrogate, while the red dots are the cases outside the range of interest, and therefore, discarded for the surrogate. Those cases are only used to bound the surrogate.

5.2.2 Study 1 – Effect of Flight Speed

In order to first explore the benefits of using non-circular flight paths to minimize the power requirement, the first set of flight path optimizations are performed using the lower fidelity environment. For a fixed fuselage mass of 800 kg, the flight path parameters $\boldsymbol{P}$ are optimized to minimize the mean power requirement, constrained by the maximum lift coefficient.

The optimization problem can be formulated as follow,

$$\begin{aligned}
&\underset{\boldsymbol{P}}{\text{minimize}} && f(\boldsymbol{P}, t) = \frac{1}{t_f - t_i} \int_{t_i}^{t_f} P_E(\boldsymbol{P}, t)\, dt \\
&\text{subject to} && \text{– Constraints in the flight path parameters (side constraints)} \\
& && \text{– } \max\left[C_L(t)\right]_{t_i}^{t_f} \leq C_{L,\max} \\
&\text{given} && \text{– Aircraft geometry and properties} \\
& && \text{– Fuselage mass} \\
& && \text{– Tether length} \\
& && \text{– Flight speed and atmospheric conditions}
\end{aligned}$$

where P_E is the electrical power requirement from the power source in the fuselage, and t_i and t_f are the timestamps of the start and end of a complete rotor revolution. In this simulation, it is assumed that the three aircraft are performing the same periodic flight path. The maximum aircraft lift coefficient is fixed at two.

The optimization process is repeated for tether lengths of 50 m, 75 m, and 100 m. The rationale for keeping the tether length outside the optimization process is the wake interaction. It is expected that a longer tether will minimize wake interaction, but such interaction cannot be captured with the lower fidelity aerodynamic model. By keeping the variable L as a parameter, the sensitivity of the power requirement to the tether length can be captured. Flight speeds were varied between 0 m/s

Table 7: Range of the design variables for the test cases

Parameters	**Lower bounds**	**Upper bounds**
a	0.3	0.7
b	0.3	0.7
V_m (m/s)	20	40
V_{a1}	-0.2	0.2
V_{b1}	-0.6	0.1
θ_S (rad)	-0.35	0.35
ϕ_S (rad)	-0.35	0.35

and 30 m/s by increments of 2.5 m/s. The optimization was performed using the *fmincon()* Matlab built-in gradient-based optimizer. Each simulation is performed at least three times to avoid local minima, where only the global minimum is retained. The tolerance on the maximum lift coefficient constraint was set to 0.001. The bounds on the seven design (flight path) variables are detailed in Table 7. The bounds were selected based on the results of test cases, in order to minimize the computational cost associated with wide bounds.

The first set of results presented in this section considers the case in forward flight, where the flight paths of the three aircraft are the same, with only a phase lag between the three aircraft as described in Section 4.4. Figure 65 presents the variation in the mean total power requirement (from the power supply) as a function of the system airspeed for four different configurations: Three cases with completely flexible flight paths, and one case with a circular flight path and constant relative speed with respect to the fuselage (constant angular velocity).

The first observation in Figure 65 is the significant reduction in power required if the flight path is completely free to vary. The black curve represents the power requirement as a function of velocity for a set of UAVs constrained to a circular flight path with a constant velocity with respect to the payload. In other words, this case is very similar to a conventional helicopter rotor, except that the circular flight path is allowed to vary in radius, as well as the flight speed as a function of the wind velocity.

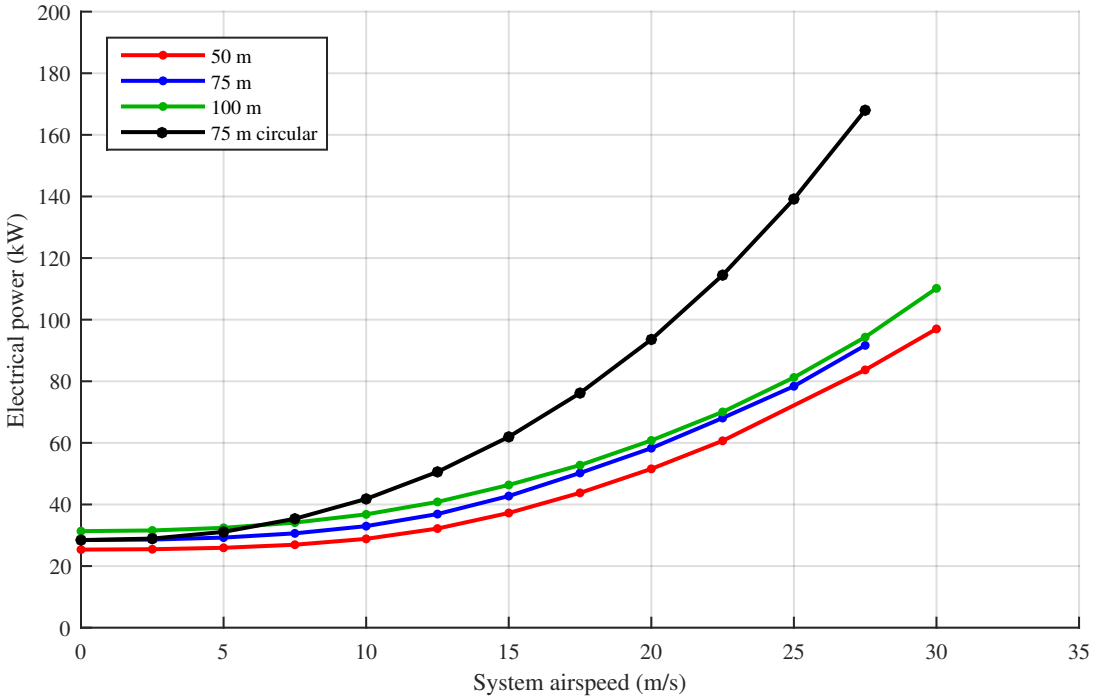

Figure 64: Electrical power requirement as a function of velocity for three different tether lengths and one case constrained by a circular flight path at a constant speed with respect to the payload. Each sample in this figure represents the optimized flight path configuration.

Only V_m and $a = b$ were allowed to vary.

The three other curves represent the power requirement for an optimized flight path with the seven design variables presented in Table 7. The resulting power requirement is exactly the same at zero velocity since there is no advantage of having a non-circular flight path nor a variation in the flight velocity as a function of the UAV position along its circular flight path. Then, significant gains are made around 10 m/s, where the effect of the advancing and retreating "blades" are observed. At a velocity of 25 m/s, the power reduction reaches 43%.

The effect of the tether length is depicted by the three curves. An increase in power requirement is seen for the longer tether due to the increase in the tether drag without a significant gain in aerodynamic efficiency or reduction in loads. However, it should be noted that the lower fidelity aerodynamic model cannot capture the wake interaction, and therefore, cannot consider the reduction in aerodynamic efficiency by reducing the distance between the aircraft. In order to better understand the evolution of the optimized flight path as a function of velocity, Figure 65 presents a plot with the variation of the seven design variables as a function of time for the optimized cases with a 75 m long tether.

At a system flight speed of 0 m/s (hover), the optimized flight path is circular with $a \approx b \approx 0.43$, or a radius of 32 m, illustrated by the normalized variables X1 and X2 (red and orange curve). The mean flight speed of the UAVs with respect to the payload (light green curve) is near the low bound at 25.6 m/s. The variable X4 represents the first order variation in velocity term in the Fourier series, with the lower bound set to -0.2, and the upper bound set to 0.2. As expected, in hover, the UAV flight speed with respect to the fuselage is constant, so the actual value of the variation in the speed terms are both approximately zero (note that zero for the sin term of is obtained at X5 = 0.85 due to the bounds). The last two variables (X6 and X7) represent the tilt of the hub plane. In hover, both angles are approximately zero

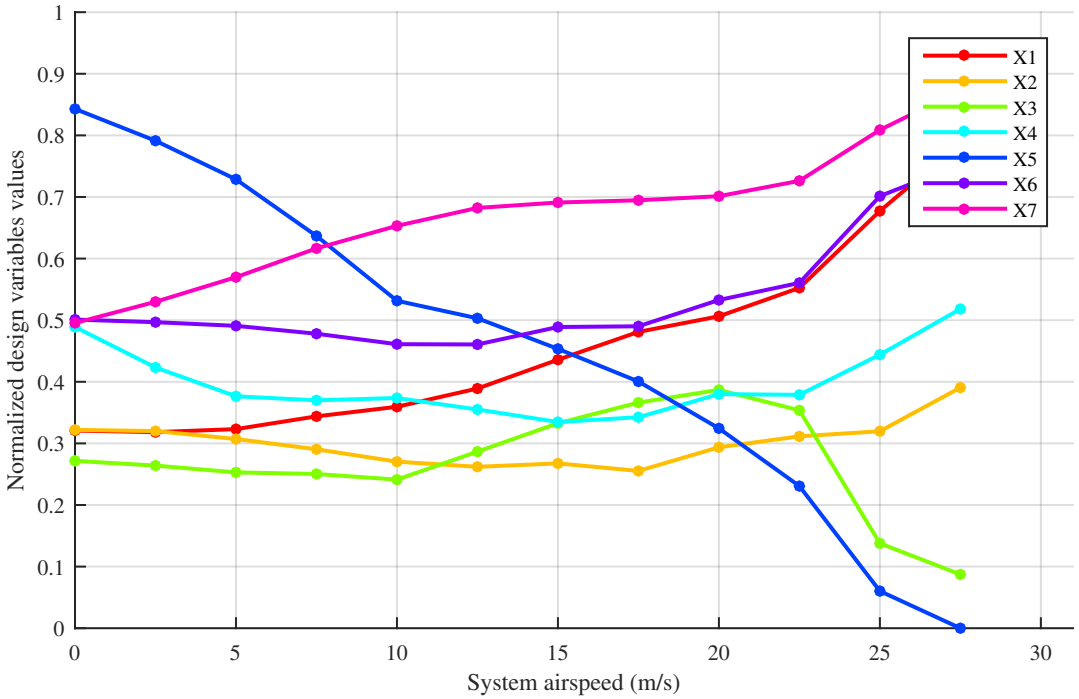

Figure 65: Evolution of the flight path variables as a function of the system flight speed. The variables are presented in the same order as in Table 7.

(X6 $\approx$ X7 $\approx$ 0.5). In summary, the optimized flight path in hover is a constant speed, no tilt, circular flight path.

Non-conventional flight paths are obtained as the velocity increases, and the large number of operational degrees-of-freedom are used to minimize the power requirement by "reconfiguring" the rotor. The following observations are made as the system flight speed increases:

- **Flight path geometry** – An increase in the flight speed leads to a transformation of the optimal flight path from a circle to an ellipse, with the longest dimension being along $\vec{i}_S$.

- **Mean UAV speed** – The mean UAV speed with respect to the payload remains approximately constant at about 26 m/s, even at a system flight speed reaching 25 m/s where the optimal speed even drops below 25 m/s. Such a flight condition can only be reached if a non-circular flight path is performed, otherwise, the relative velocity on the retreating side would be near zero. A slight reduction of velocity is seen at higher velocities to minimize the drag from the tether.

- **Variation in the UAV speed** – As the free stream velocity increases, a strong reduction in the velocity on the advancing side is observed. A value of X5 below 0.85 indicates a reduction in the velocity on the advancing side. A rapid acceleration and deceleration can be obtained since the aircraft are lightweight, and a high thrust is available from the electric motors.

- **Tilt of the hub plane** – In order to shift the fuselage weight mainly on the advancing side, a left bank angle of the hub plane is obtained with an increase in the system flight speed (X7). There is no significant change in the pitch angle until 17.5 m/s, where a gradual nose-up attitude is obtained as the system flight speed increases.

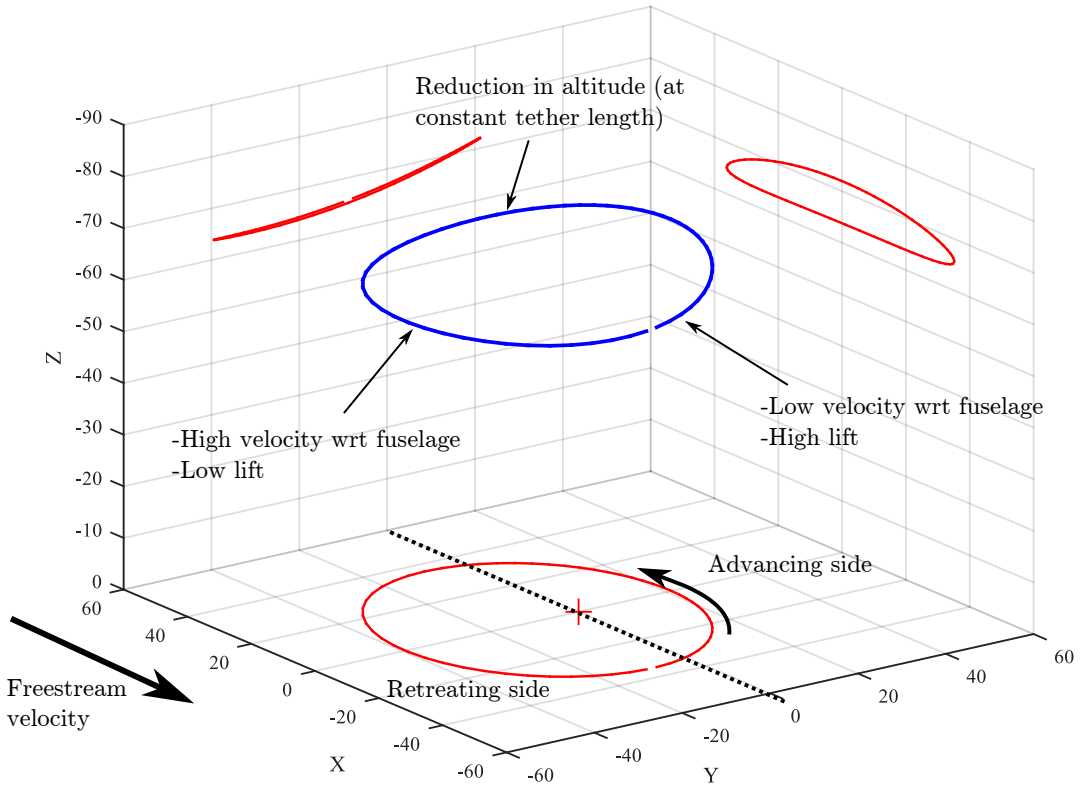

Figure 66: Optimized flight path at 15 m/s with a 75 m long tether. The fuselage mass is fixed at 800 kg. The freestream originates from the positive x-axis at 15 m/s. The optimized flight path shows an elliptical shape with a visible bank angle of the hub plane on the left side for load transfer.

In order to better understand how the system reacts to an increase in system flight speed, one specific case is analyzed in detail. The optimized flight path at 15 m/s for a 75 m long tether is presented in Figure 66.

The optimized flight path for this flight condition clearly shows the left bank of the hub plane to allow the aircraft on the advancing side to take more load than on the retreating side. Due to the fixed tether length constraint, the flight path is curved and a variation in altitude of more than 10 m is observed. However, one should note that the increase in altitude occurs at the same time that the UAV reduces its flight speed with respect to the payload (transitions from the retreating side to the advancing side), and therefore converts its kinetic energy into potential energy. The

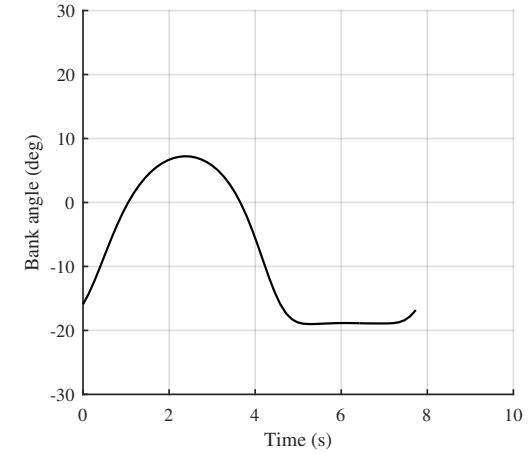

(a) Bank angle

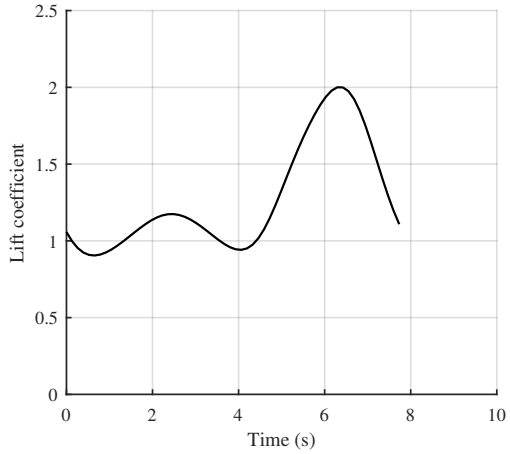

(b) Lift coefficient

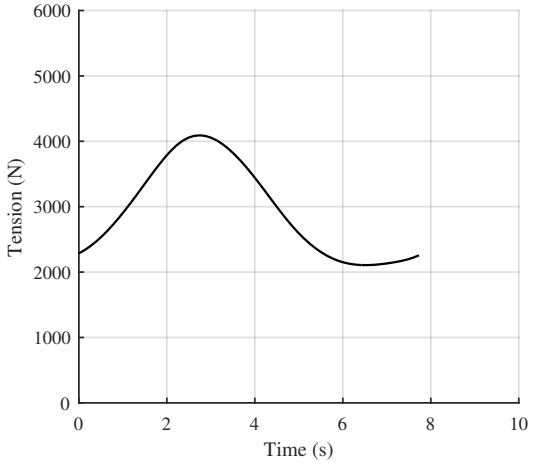

(c) Tether tension (at aircraft)

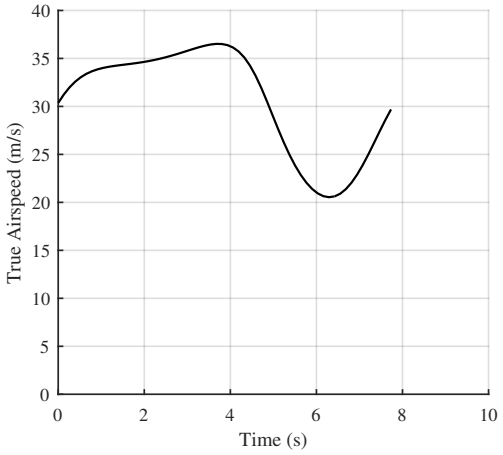

(d) UAVs true airspeed

Figure 67: Main flight parameters for one period of a tethered aircraft at 15 m/s. One period lasts just under 8 seconds.

reverse condition is seen in the forward section of the rotor.

The complex flight path leads to load transfer from the aircraft on the retreating side to the aircraft on the advancing side, depicted by the peak in tether tension at $t = 2.5$ sec. Although the lift required is high during this period, the lift coefficient remains under $C_{L,\max}$ since the true airspeed is higher than average. The relative velocity with respect to the payload is reduced on the advancing side. At this position, the aircraft must bank to the right by approximately 10 degrees to orient the lift vector to perform the prescribed kinematic motion. On the retreating side, the relative wind

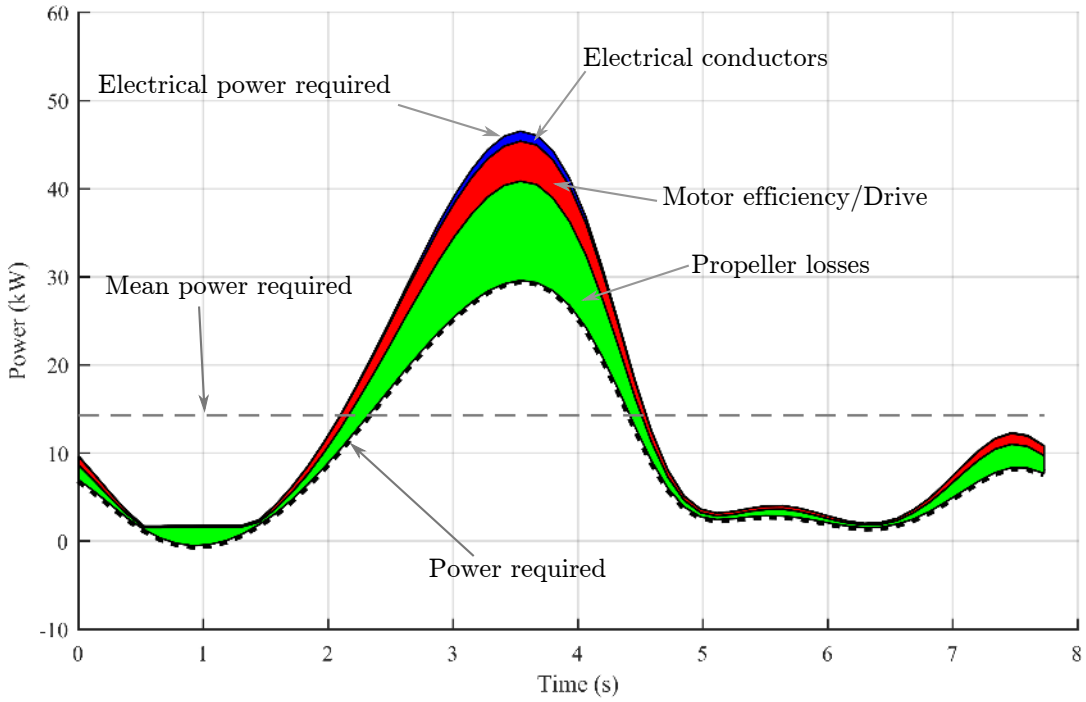

Figure 68: Power breakdown during an optimal flight path at 15 m/s. The power required ($T \cdot V$) is represented by a black dashed curve. The propeller losses are shown with a shaded green area. The motor and drive losses (constant efficiency of 90%) are shown with the red area. Finally, the tether electrical losses are shown with the dark blue area.

velocity reduces drastically, even with the increase in velocity with respect to the payload. However, since the aircraft position is further out than on the advancing side, the lift requirement drops by approximately 50%. The maximum lift coefficient is 2.0 (per the constraint) on the retreating side.

Since the flight velocity varies by 50% and the thrust requirement goes from -5 N to 205 N per propeller, the electrical power requirement varies from zero to 46 kW peak *per aircraft*. Figure 68 presents the loss mechanisms as a function of time during one period.

The power required, defined as the thrust multiplied by the relative velocity, varies from -1 kW to 29 kW, with both velocity and thrust variations. The minimum power requirement is at $t = 0.9$ sec early on the advancing side. The low power requirement

is due to the strong reduction in the velocity. Then the power requirement increases until it reaches a maximum at $t = 3.5$, near the end of the advancing phase. It should be noted that since the flight speed is not constant, there is not a linear conversion between time and position along the flight path. The motor and drive efficiencies are assumed to be constant at 90%, as depicted by the red shaded area on Figure 68.

There is a general thought that long electric conductors, which are typical for airborne wind energy applications, generate high losses. If the conductor diameter is assumed to be 2.2 mm, the electrical losses account for less than 5% of the total power requirement if operated at 1,100 V as the *Wing 7*.

Since the propellers must operate through a wide variety of flight conditions, they seldom operate at their design point. To capture the limitation of the propulsion system to harvest power from the wind, the propeller efficiency is forced to zero if the thrust required is negative. In order to detail the consequence on the propulsion system to vary the thrust requirement, Figure 69 overlays the thrust required as a function of velocity for a single period over the propeller efficiency (which was fully considered in the previous analysis).

On the advancing side, the thrust requirement reaches 205 N per propeller at 36 m/s. At this flight condition, the propeller efficiency is reduced to 72% while the efficiency increases to 85% at lower power setting. A first observation is that the propellers should most likely have a larger capture area to maximize the efficiency at those flight conditions. Second, in order to produce this variation in velocity, the propeller rpm must vary between 4,000 and 7,900 rpm (well within the propeller and motor limits), which shows the need for electric propulsion to support such rapid variations. In order to complete the analysis of the optimized flight configuration, Figure 70 presents the power requirement for the three aircraft and the total power requirement by the power source located in the fuselage.

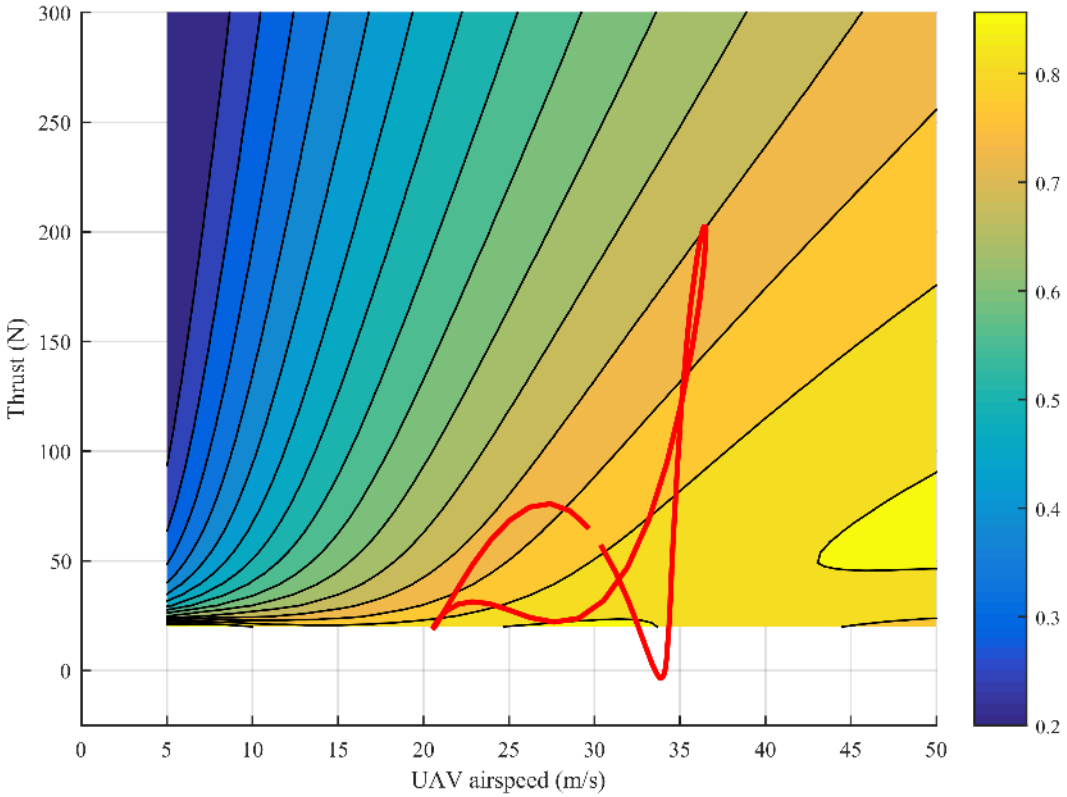

Figure 69: Propeller efficiency during an optimal flight path at 15 m/s. The propeller operating condition is depicted by a solid red curve on top of the efficiency map initially shown in Figure 62.

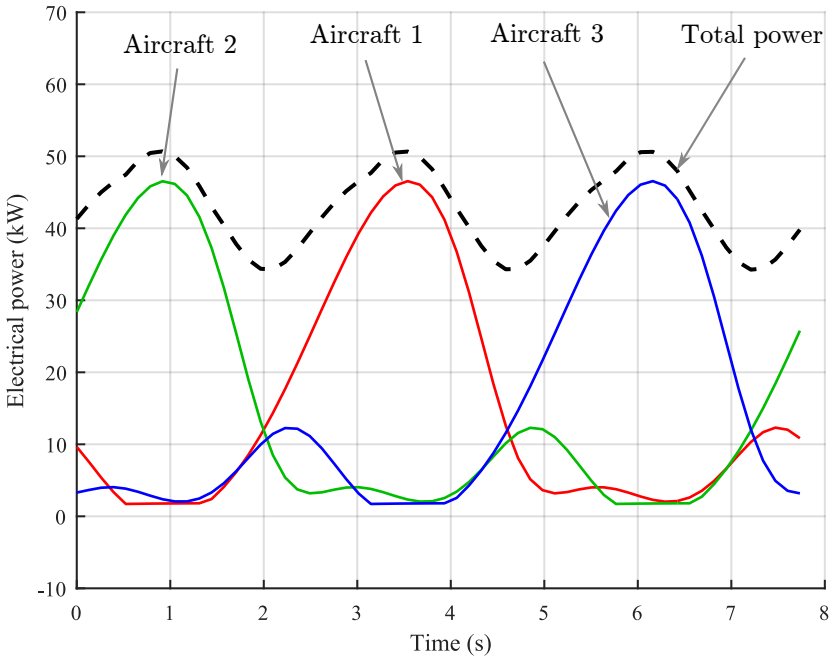

Figure 70: Total power requirement as a function of time during a complete period. The power requirement of each aircraft is shown with a red curve (AC 1), green curve (AC 2), and a blue curve (AC 3). The total power requirement for the power supply is shown with a dashed black curve.

The power requirement for each aircraft is summed up to retrieve the power required by the power source located in the fuselage. Although the presence of three aircraft reduces the variation of required power, it does not entirely eliminate it. To handle such variations, there is the need to use either capacitors or high-discharge rate batteries to augment the performance of the main power supply, most likely a small-scale gas turbine coupled with a generator.

In summary, this first design space exploration using the lower fidelity environment demonstrated the advantages of using the numerous degrees of freedom in the flight path of the tethered aircraft to minimize the power required to fly in the presence of wind. It was shown that the power requirement can be reduced by 43% at a system flight speed of 25 m/s under the conditions presented early in this chapter. This reduction is attributed to a strong variation of the flight speed of the tethered aircraft with respect to the fuselage throughout the flight path, and a transfer of

the loads on the advancing side using a left tilt of the hub plane. The design space exploration presented in the next section focus on the hover phase.

5.2.3 Study 2 – Hover

Section 5.2.2 presented the optimization of the flight path and flight speed of the three tethered aircraft in forward flight. In hover, it was shown that a circular flight path with a constant velocity was optimal to minimize the mean power requirement. In this specific flight configuration, the power requirement from the power source is constant.

However, the lower fidelity aerodynamic model cannot capture wake interaction between the aircraft. It should be noted that the greatest power losses for a helicopter in hover is due to the induced velocity, which in the present case is equivalent to the wake interaction. Therefore, the optimal flight path was simply a circle at a constant speed, with a radius that allowed the inertial forces of the aircraft and the tether tension to be balanced such that the lift vector of each UAV was oriented in the opposite direction from the gravity vector. Moreover, the increase in induced drag due to the required aileron deflection to perform this flight path was not considered, only an approximation of the aircraft stall was enforced through an inequality constraint.

The objective of this second flight path optimization using the lower fidelity environment is to *explore the impact of non-circular flight path on the predicted power requirement*. For a prescribed elliptical flight path defined by the major and minor axes, the aircraft velocity is optimized to minimize the mean power requirement. This process is repeated for multiple combinations of a and b. The mathematical formulation for every simulation is presented hereafter. Let's recall that V_{a2} is the percentage variation in velocity in the Fourier series, second order, associated with the cosine function.

$$\underset{\Delta V_{a2}, V_m}{\text{minimize}} \quad f\left(V_{a2}, V_m, t\right) = \frac{1}{t_f - t_i} \int_{t_i}^{t_f} P_E\left(V_{a2}, V_m, t\right) dt$$

subject to
- Constraints in the flight path parameters (side constraints)
- $\max\left[C_L\left(t\right)\right]_{t_i}^{t_f} \leq C_{L,\max}$

given
- Ellipse shape (a and b)
- Constant phase shift term between the aircraft
- Phase angle between the elliptical flight paths
- Aircraft geometry and properties
- Payload mass
- Tether length
- Atmospheric conditions

Only two design variables are optimized for each simulation, the second order cosine variation in velocity V_{a2} from the Fourier series and the mean velocity along the flight path, V_m. The rationale behind this reduction in dimensionality in hover is the need for symmetry. For example, if the velocity needs to be higher at the end of the major axis of the ellipse to avoid a stall, it also needs to be higher at the other end of the major axis. Therefore, first-order terms in the Fourier series in the velocity are defaulted to zero.

Two main concepts are studied, with and without phase shift along the flight path. Figure 71 illustrates the two concepts. The initial position of the aircraft at $t = 0$ is shown with a circular marker, and the position of the aircraft after 1.5 seconds is shown with an "x" marker.

Figure 71a illustrates the configuration with no phase lag between the aircraft along their respective flight paths. A constant azimuthal phase shift of 120° between the three elliptical flight paths is enforced for both cases. In other words, the flight

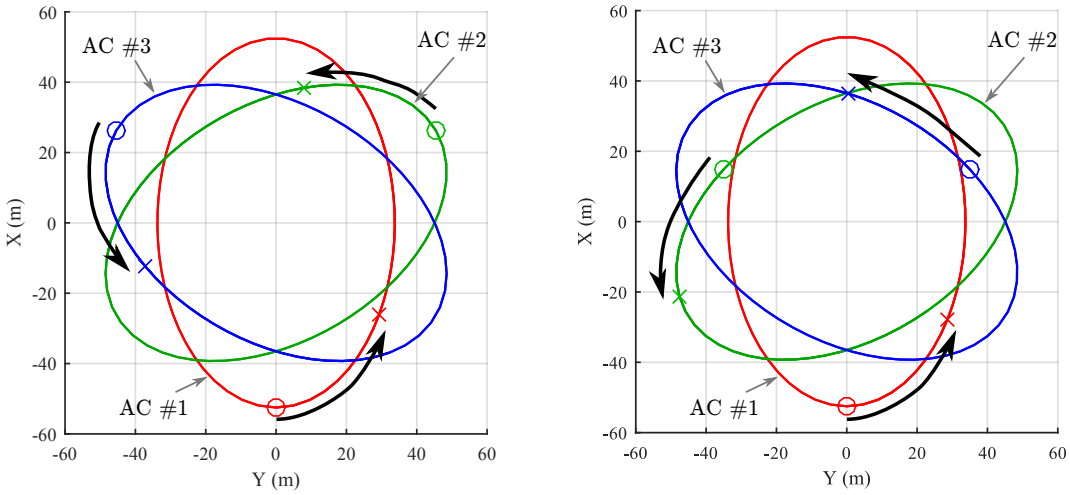

(a) No Phase difference

(b) With 120° lag between aircraft

Figure 71: Comparison of two concepts of flight path in hover. The initial position of the aircraft at $t = 0$ is shown with a circle and the position at $t = 1.5$ sec is shown with a "x".

paths are identical with a 120° rotation of the hub plane between each one. The second configuration enforces a 120° lag *along* each flight path, meaning that the three aircraft do not reach the apex of the ellipse at the same time. In this configuration, the tether tension is not identical for each aircraft. Moreover, this configuration maximizes the distance between the aircraft at all time not letting all the aircraft to "meet" near the center at the same time.

Based on the concept of set-based design, the objective of this lower fidelity design space exploration is to identify the consequence of a non-circular flight path in hover in terms of mean and maximum power requirements for the two different configurations. Based on these results, one of the two concepts will be tested in the higher fidelity environment.

A full-factorial design of experiments with 18 levels (324 cases) is performed on a and b for a fuselage mass of 800 kg and a fixed tether length of 75 m. The lower bound on a and b is 0.2, and the upper bound is 0.8 for both variables. No optimization was performed for the cases where the ratio of the major axis to the minor axis exceeded 2.

Figure 72 presents the salient results of the design space exploration. The left column is for configuration 1 where there is no phase difference between the aircraft along their respective flight path. The right column presents the same results but for configuration 2 characterized by a 120° phase offset between the aircraft.

Figure 72a first illustrates the mean power requirement of the power source for both configurations. The first observation is that both configurations require the same power when $a = b$, which results in a circular flight path. By varying the radius, the electrical power varies between 27 and 39 kW. In this specific case, the flight path represented in the system-carried frame is exactly the same. The minimum power requirement matches the result from the previous optimization for a 75 m long tether presented in Figure 64.

For non-circular flight paths (off-diagonal), configuration 1 shows a slightly reduced power requirement by only a few percent compared to configuration 2. As expected, the power requirement is symmetrical about the diagonal. Although an elliptical flight path with $a = 0.7$ and $b = 0.45$ increases the mean power requirement by 4 kW, it is expected that the benefits from the reduction in the wake interaction should overcome this increase in power. One of the main benefits from enforcing a phase difference between the aircraft is shown in Figure 72b where the maximum power required by the power supply is illustrated as a function of the ellipse shape parameters.

For configuration 1 (no phase difference), the tether tension in the three tethers must increase when the aircraft are at the end of the major axis of the ellipse since the angle between the vertical and the three tethers increases. The additional lift (and required increase in velocity to avoid stall) increases the power requirement by up to 100% for a short duration. For configuration 2, there are no significant power peaks since the tether tension is naturally higher for the aircraft near vertical with respect to the payload, thus taking most of the lift while the aircraft away from the

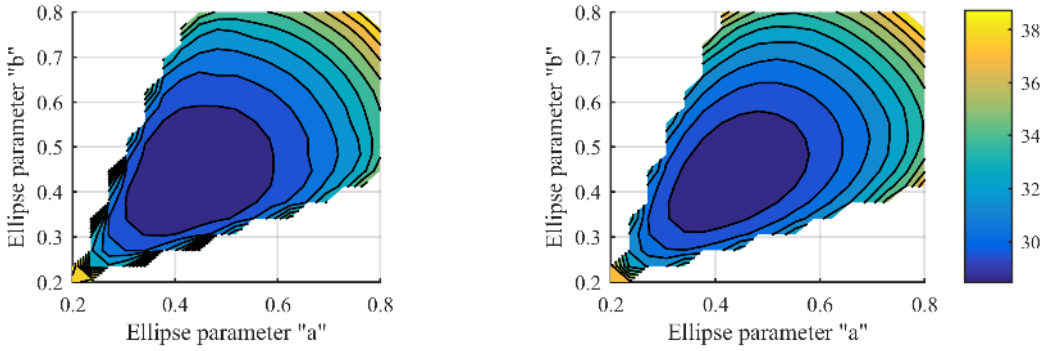

(a) Mean electrical power (kW)

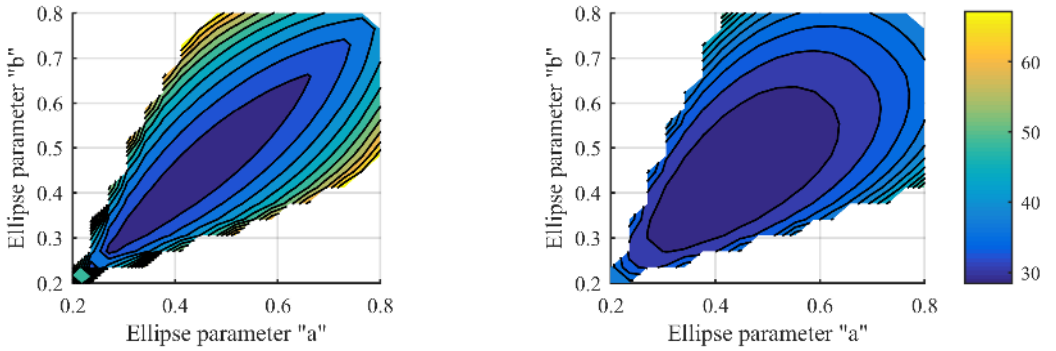

(b) Maximum electrical power (kW)

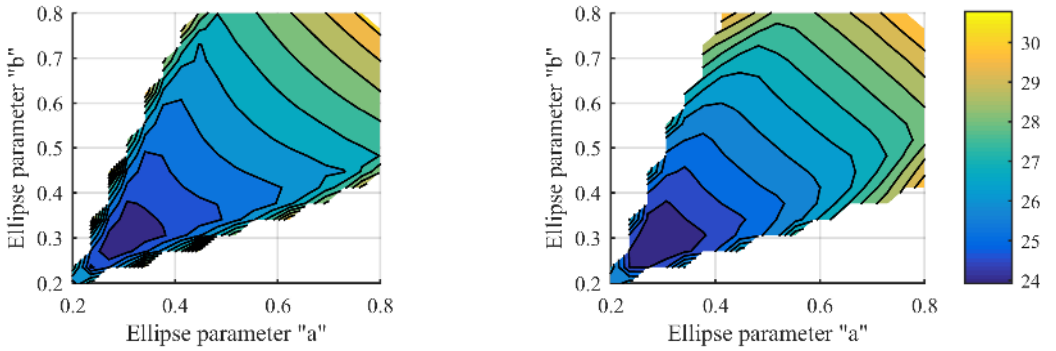

(c) Optimized mean velocity (m/s)

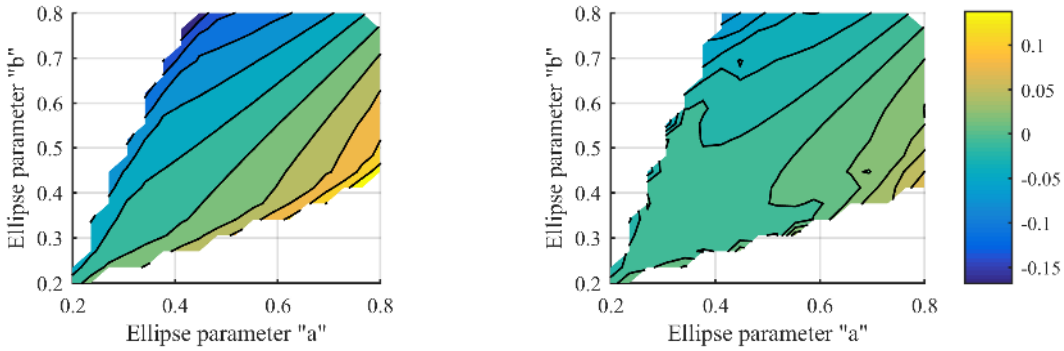

(d) Optimized second order cosine velocity variable V_{a2}

Figure 72: Optimized system performance and design variables given a flight trajectory in hover, defined by the ellipse shape. Left: no phase shift between the aircraft, right: 120° phase between the aircraft

payload have reduced lift requirements. Figure 73a illustrates the power requirement for each aircraft and the total electrical power requirement for a complete period with $a = 0.7$ and $b = 0.45$.

The power requirement at $t = 0$ is about 50 kW while the mean power requirement is 32 kW. The maximum power requirement occurs at both ends of the major axis due to the increase in tether tension and the need to accelerate to avoid a stall. Since the three aircraft have the same power requirement as a function of time, the increased power requirement at this location is not distributed over the whole period.

At the opposite, configuration 2 shows a much flatter power requirement in Figure 73a with a peak power requirement of 35 kW. Although the tether tension of aircraft 3 at $t = 0$ is 2.14 kN while the two other tethers see a tension of 3.72 kW, aircraft 3 requires the most power. One reason for this phenomenon is the vertical velocity of aircraft 3 at that time, which reaches 5.5 m/s upward which increases the power requirement. In summary, the presence of the phase offset between the aircraft does not increase the power requirement for the power supply but reduce the strong variations. Figures 72c and 72d illustrate the optimal mean velocity V_m and the required variation in velocity (cosine, second order) V_{a2} as a function of the ellipse shape.

For configuration 1, the need to increase the velocity when $a \neq b$ is not significant. However, the velocity along the flight path varies as shown in Figure 72d. When $a > b$, the second order sine term in the UAV speed Fourier series is greater than zero ($V_{a2} > 0$), so the velocity increases near the ends of the major axis. The opposite is also shown to be true for $b > a$. As expected, there is no need for a lead-lag motion for a circular flight path (along with the diagonal).

For configuration 2, the mean velocity V_m increases more rapidly for an elliptical flight path (off-diagonal). However, the optimal solution does not require a variation of the velocity along the flight path as shown in Figure 72d.

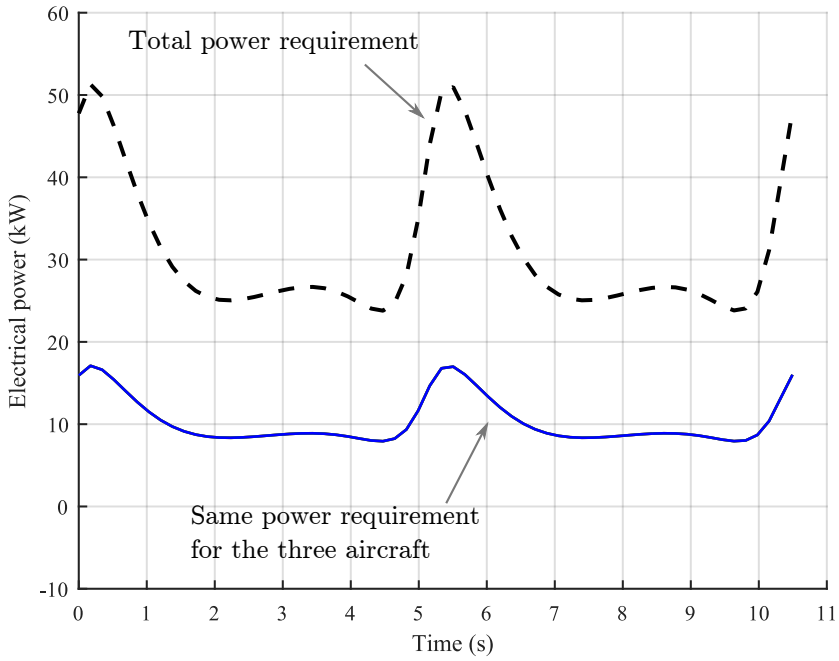

(a) Without phase shift, configuration #1

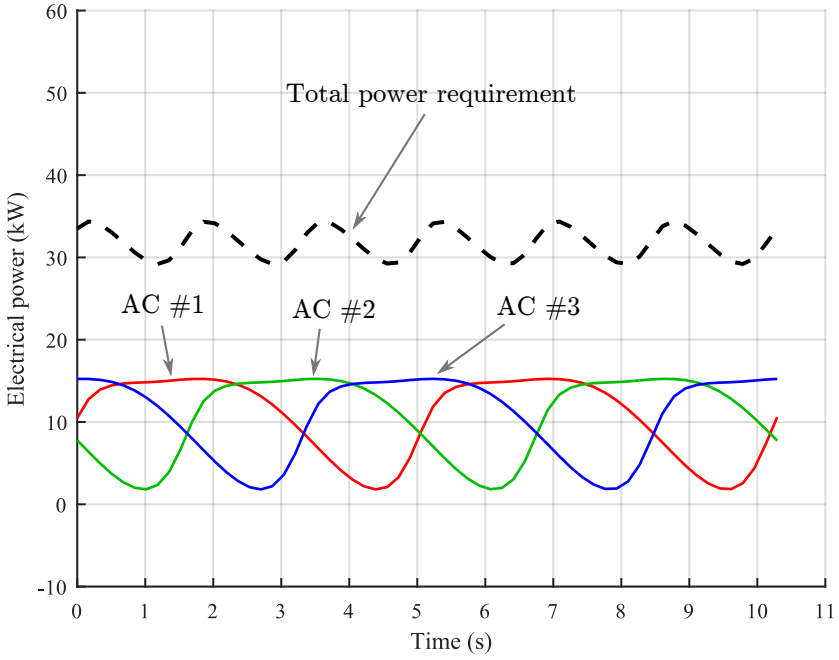

(b) With 120° phase shift, configuration #2

Figure 73: Power requirement as a function of time through a complete period in hover with $a = 0.7$ and $b = 0.45$ for an optimized velocity to minimize the mean power requirement.

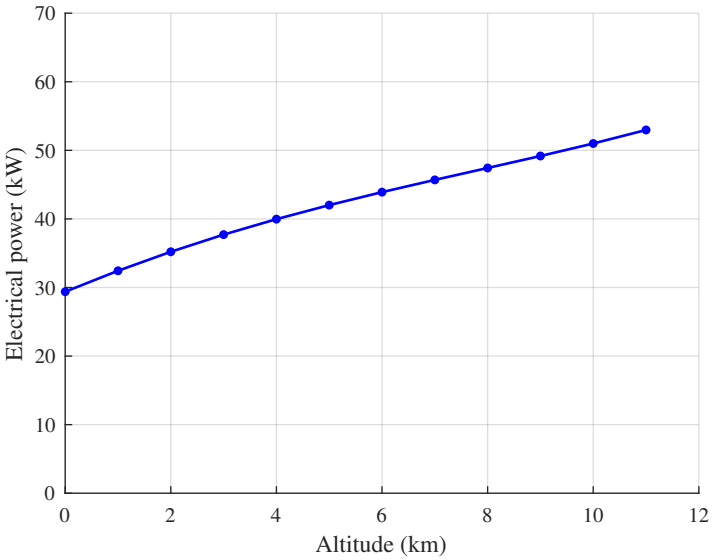

Figure 74: Electrical power requirement as a function of altitude. Each marker represents the mean power requirement for an optimized flight path. This study assumes a fuselage mass of 800 kg, with 75 m long tethers at 10 m/s.

5.2.4 Study 3 – Effect of Density Altitude

This third study using the lower fidelity environment focuses on the effect of air density on the optimal flight path of the tethered aircraft. The density is varied between 1.22 kg/m^3 and 0.36 kg/m^3 to simulate a variation in altitude from ground level to 11 km (36,000 ft), assuming a standard atmosphere.

The system flight speed is fixed to 10 m/s with an 800 kg fuselage mass and a 75 m long tether. The rationale for the selection of a positive system flight speed instead of hover is driven by the assumptions involved in the lower fidelity aerodynamic model. The objective of the optimization is to minimize the mean power requirement, constrained by a maximum power available and propeller tip-speed, as detailed in Study 1. The design variables considered are the same as in Study 1: the ellipse shape, the velocity along the flight path, and the tilt of the hub plane, for a total of 7 variables. Figure 74 shows the optimized electrical power requirement as a function of altitude.

The electrical power requirement increases with altitude as for a conventional

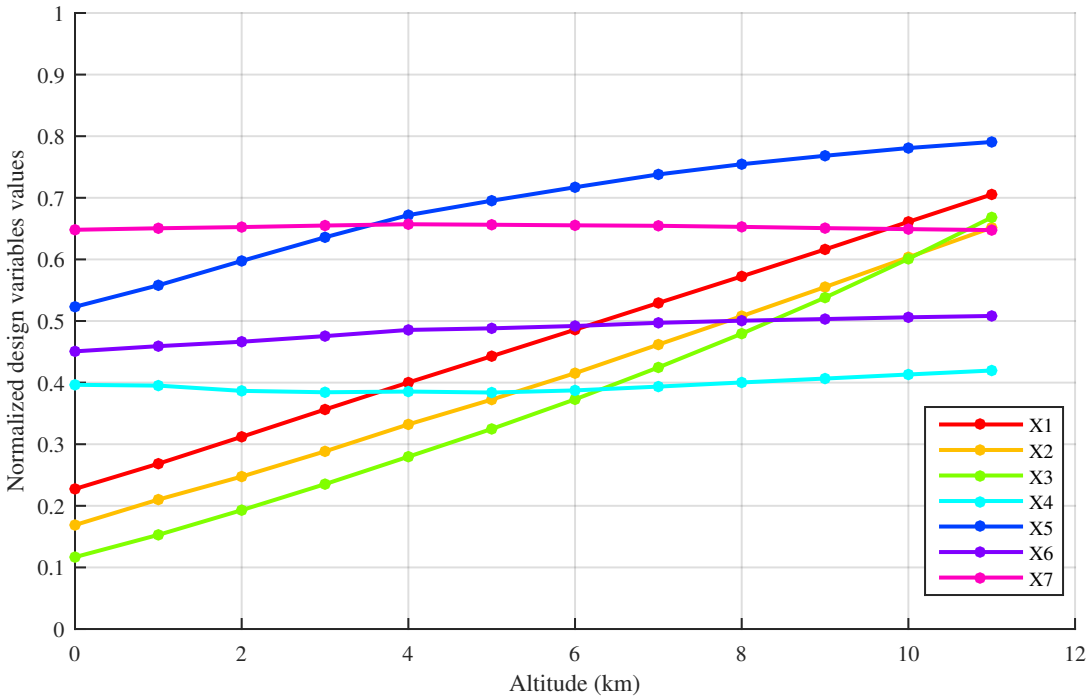

Figure 75: Evolution of the optimized design variables with altitude. The increase in altitude requires an increase in the flight path radius (X1, X2) and an increase in the flight speed to avoid stall (X3). There is also an increase in the velocity variation using the sine term of the Fourier series (X5). The other variables remain relatively constant.

helicopter, from approximately 30 kW at ground level to 53 kW at 11 km altitude. The increase in power is mainly associated with the increase in UAV flight speed in order to avoid a stall. As a reference, the power requirement to fly the EPR^2 VTOL Concept at the summit of Mount Everest is slightly below 50 kW or 66% higher than at ground level. This last power requirement would allow the system to fly at 18 m/s at ground level. It should be reminded that the increase in power with altitude is not related to the increase in wake interaction (and induced velocity) since the low-fidelity aerodynamic model cannot capture this phenomenon. In order to better understand how the optimized flight path evolves, Figure 75 illustrates the normalized design variables as a function of altitude, and Table 8 lists the actual range of the design variables in the same order.

Table 8: Range of the design variables for study 3

Parameters	**Lower bounds**	**Upper bounds**
a	0.3	0.9
b	0.3	0.9
V_m (m/s)	20	60
V_{a1}	-0.2	0.2
V_{b1}	-0.6	0.1
θ_S (rad)	-0.35	0.35
ϕ_S (rad)	-0.35	0.35

The transition from ground level to 11 km requires an increase in the flight path ellipse dimensions by approximately 65% and an increase in the flight velocity from 24.5 m/s to 47 m/s. The increase in radius is mainly a consequence of the increase in velocity to avoid the need to bank the aircraft to sustain the inertial loads. At 11 km altitude, the centripetal acceleration of the UAVs is on the order of 40 m/s^2. This radical change in the flight path geometry can be seen in Figure 76.

Most of the other flight path parameters remain constant, except the sine term in the Fourier series of the velocity. In other words, the variation in velocity as a function of time is greater with an increase in altitude.

The optimization process was carried out up to 12 km, but no feasible solution was found that met all the requirements. Upon a detailed review of the thrust requirement as a function of time for the solution at 11 km, it was found that the propulsion system is limited by the propeller tip-speed in those low-density environments, although more power is available.

Electric motors do not show a reduction in the power available with a reduction in air density as do airbreathing engines, except supercharged (or turbocharged) internal combustion engines at low to medium altitudes (through turbo-normalization). The latter engines must use a variable pitch propeller to fully exploit the power at high altitude, otherwise there would be a mismatch between the engine torque at a given rpm and the propeller torque. The same situation is seen here, where the electric

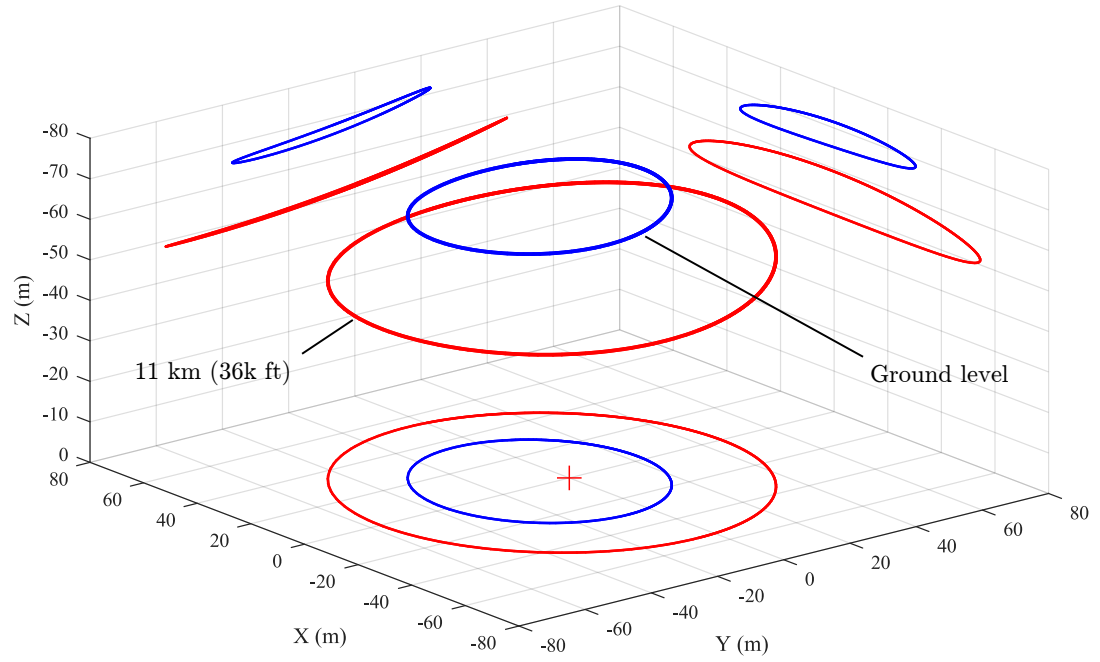

Figure 76: Comparison of the optimized flight path at ground level and 11 km. An increase in the flight path radius is the result of the increase in velocity.

motor would still be able to produce more torque, but the propeller would need to have a higher activity factor or a higher pitch angle to convert the torque to thrust in a low-density environment. In this case, since the propeller was optimized for operation near the ground, it cannot meet the requirement at high altitude. To keep the concept simple, it would be recommended to optimize the propeller for a high altitude operation if the aircraft is intended to operate in those conditions instead of adding a heavy variable-pitch propeller.

In summary, this example showed the evolution of the optimal flight path as a function of density altitude. The results showed that the rotor reconfigures itself to maximize the efficiency and allow for low-density operation. However, since the propellers were optimized for low-altitude operation, the system is limited in altitude by maximum tip-speed at 11 km. An optimized propeller for higher altitude operation would allow for a larger flight envelope.

5.3 Higher Fidelity Tether Dynamic Simulation

Section 5.2 demonstrated how tethered aircraft can reconfigure as a function of flight condition. Three conditions were of particular interest: hover, forward flight (positive system flight speed), and variation with density altitude. Those studies were conducted using the lower fidelity environment to allow direct optimization. However, this environment cannot capture the tether and payload dynamics due to tether elasticity.

This section studies the benefits and drawback of using the higher fidelity dynamic tether model (in the lower fidelity environment), with a specific focus on performance prediction and payload stability. Since the higher fidelity tether model considers the full dynamics of the system given the flight path of the aircraft, it is expected to give more realistic results than the simplified tether kinematic model. The dynamic model considers both the influence of the elastic tether and the payload motion on the aircraft loads.

This section presents the need to "tune" the flight path to minimize the fuselage motion due to the tether elasticity. Section 4.4 presented the flight path parameterization which assumes a constant distance between the UAVs and the fuselage reference position $\boldsymbol{r}_{O_S \to P_i}(t)$. This distance is only affected by the additional term, the "height variation", which changes this distance by using a Fourier series, detailed in Section 4.4.2. Since the tethers are assumed to be rigid in the lower fidelity tether model, the "height variation" terms are all defaulted to zero. This section also shows that the lower fidelity tether model performs as well as the higher fidelity tether model for a design space exploration phase.

5.3.1 The Need to Compensate for Tether Elasticity

In the lower fidelity M&SE, the tethered aircraft flight path is optimized by keeping the distance with respect to the origin of the system-carried frame O_S constant.

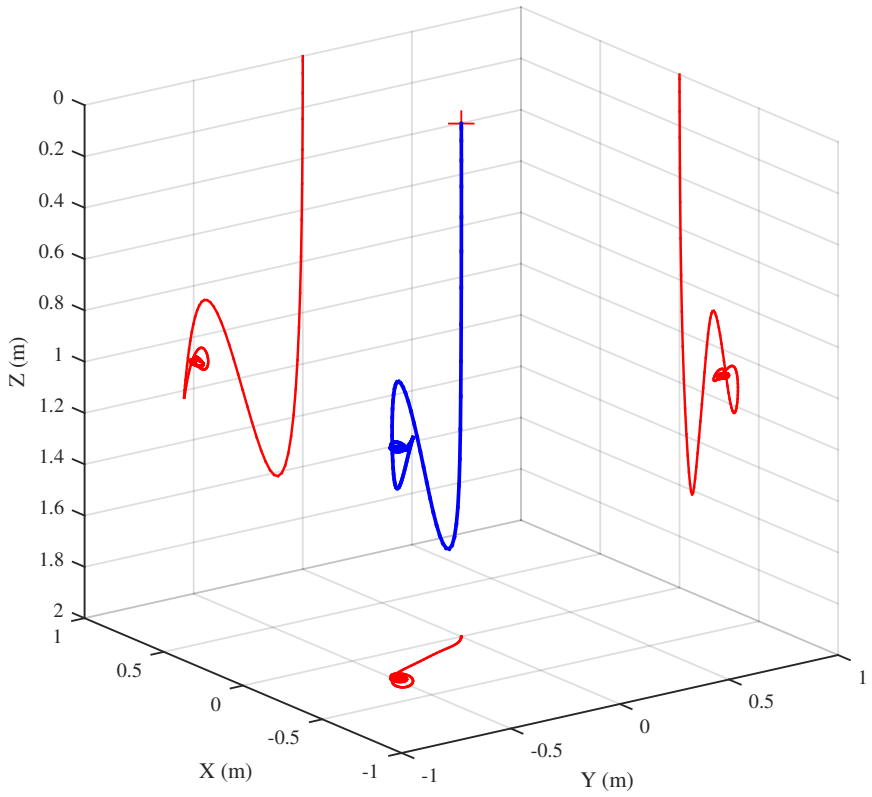

Figure 77: Fuselage motion without compensation for elasticity. The periodic fuselage motion (after the transient phase) is off-center by 0.5 m in both X and Y directions. The fuselage also stabilizes at about 1.1 m below its reference position at O_S. The periodic motion shows a displacement of about 0.15 m in the three orientations.

However, since the tether are in reality elastic, the actual fuselage location is not the reference location. The optimized flight path at 15 m/s presented in details in Section 5.2.2 is used to demonstrate this concept. Figure 77 presents the fuselage motion as a function of time using the dynamic tether model with 10 elements. The tether elastic properties were presented in Table 5. To reduce the transient phase time, a damper is added to the fuselage in the first few seconds of the simulation.

The first observation is that the center of the periodic fuselage location is off-center by 0.3 m in X, by 0.5 m in Y, and over 1 m in Z. The periodic fuselage location motion creates slight accelerations in the three axes, as shown in Figure 78.

During the first few seconds, a strong acceleration magnitude near 8 m/s^2 is

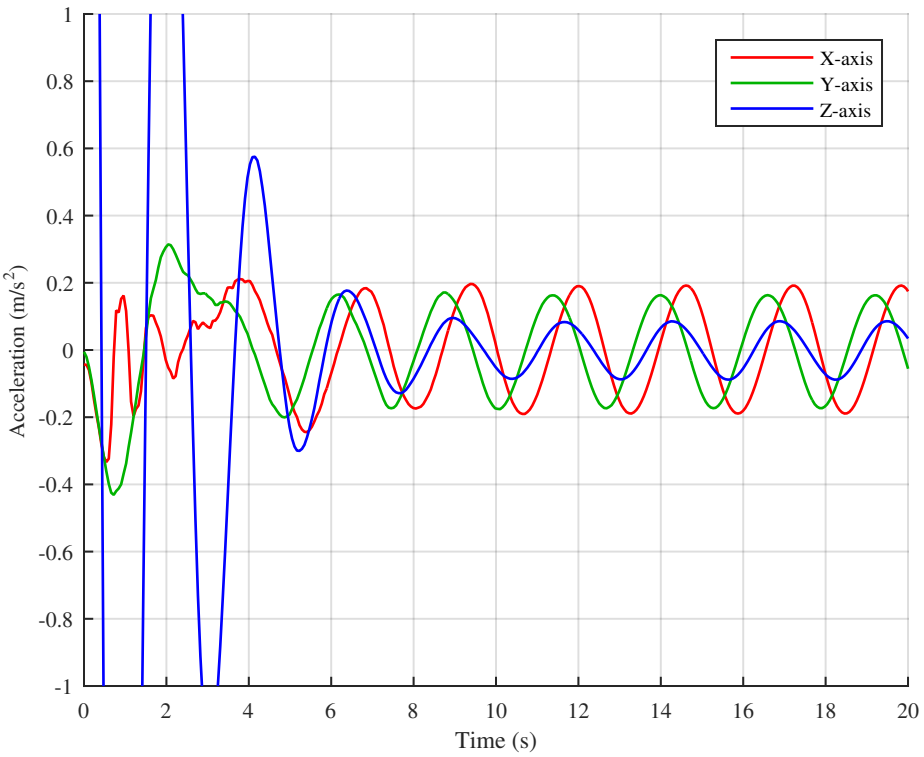

Figure 78: Acceleration of the payload without compensation for elasticity.

observed. Then, the acceleration in the periodic steady state reaches 0.2 m/s^2 in X and Y, while the acceleration in Z is limited to 0.1 m/s^2. Although this acceleration seems minimal, the resulting forces in the three directions, given a fuselage mass of 800 kg, are over 150 N. Then, those variations are transmitted to the tethers, which show tension variation of up to 500 N *due to the fuselage motion*. The consequence of the tether tension is also observed on the predicted lift coefficient as shown in Figure 79. The predicted lift coefficient for the higher fidelity dynamic model without compensation is compared to the lift coefficient evaluated with the lower fidelity tether model.

At first, it could be possible to accept the solution as is: the peak lift coefficient predicted by the higher fidelity tether model differs by approximately 5% and the discrepancy reaches up to 20% at $t = 10$ and $t = 18$. Those could be accounted as an error due to the fidelity of the model. However, the control system on the EPR^2 is

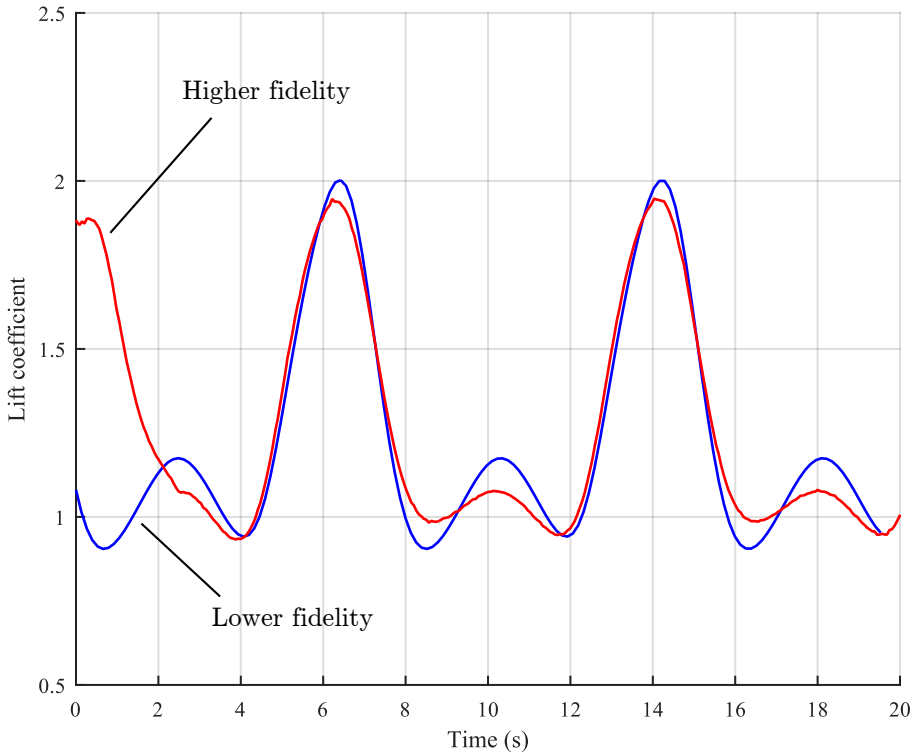

Figure 79: Aircraft 1 lift coefficient as a function of time (LF and HF without compensation). The discrepancy on the lift coefficient varies between 5% and 20% in the periodic steady-state.

likely going to be based on tether tension, not aircraft position. In other words, for the prescribed flight path presented in this case, the control system will adjust the lift on each aircraft to maintain the target lift, and thus, the fuselage should remain steady. It is very unlikely that a control system can be based on the aircraft position in the Z direction, only in the X and Y position. For the prescribed flight path, a control system based on the tether tension would slightly change the UAV altitude ($\Delta h\,(s)$) to minimize the fuselage motion.

Under this assumption, the true objective is to find the aircraft position in order to get the target tether tension, and thus avoid fuselage motion. However, the first assumption of this work was that the power requirement could be extracted by prescribing the position. The proposed iterative method attempts to compensate for the tether elasticity by using a third-order Fourier series on the variation in height, as described initially in Section 4.4.2 in order to minimize fuselage motion. In other words, a variation in height of a few centimeters might seem impossible to prescribed for a controller. However, if this variation in height results in variation in 10% of the tether tension, then a control system can track the tether tension and not the position. The main objective of this relatively expensive compensation process is to evaluate how the power prediction of the compensated model compares to the lower fidelity tether model for power prediction and load prediction on the UAVs.

5.3.2 Iterative Method for Compensation

The iterative process used to calibrate the flight path parameters (variation in height) to minimize the payload motion is shown in Figure 80. The process is initiated by providing an initial set of flight path parameters. In the example presented in this section, the flight path parameters were initially optimized using the low fidelity environment for minimal mean power requirement with 15 m/s wind speed. Then, the 5-step procedure is initiated.

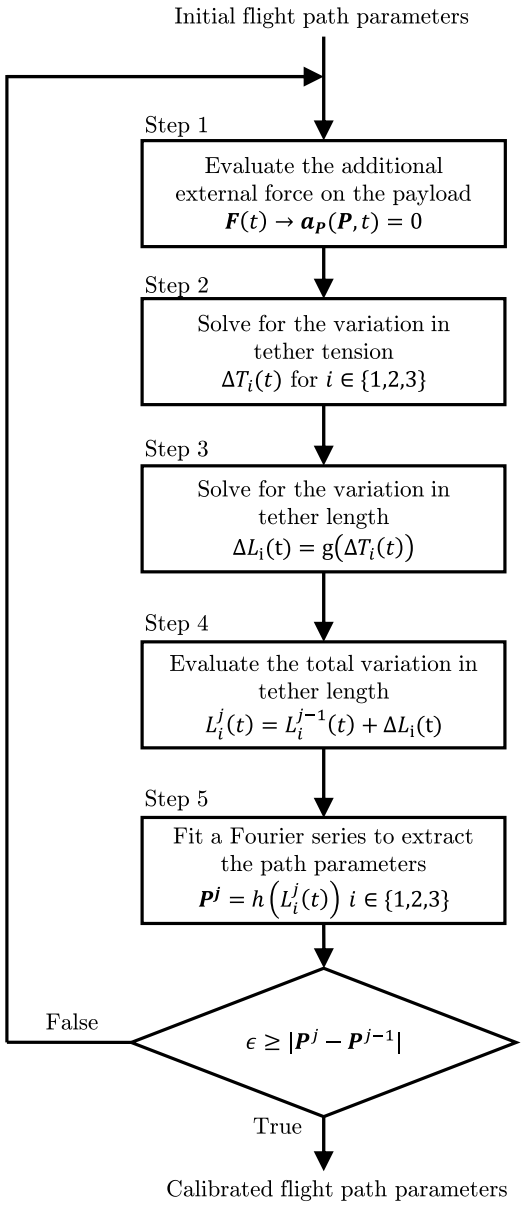

Figure 80: Iterative process to calibrate the flight path parameters for minimal fuselage motion

STEP 1 – Given a set of flight path parameters $\boldsymbol{P}$, the higher fidelity tether dynamic model is executed. The fuselage is forced to remain at the origin of the system-carried frame for the whole simulation, and the external forces required to minimize the fuselage motion, $\boldsymbol{F}(t)$, are saved.

STEP 2 – The variation in the tether tension to provide the external forces is obtained by solving a set of three linear equations and three unknowns (since three aircraft are used). During this process, it is assumed that the force provided by the tether on the payload is a vector oriented from the fuselage location to the actual position of the aircraft.

STEP 3 – As a first order approximation, the required variation in the tether length, $\Delta L_i(t)$, is estimated using Hooke's law, given the variation in the target tension and the tether properties. This step is repeated for each tether.

STEP 4 – The total variation in the tether length (from the baseline) is obtained by adding the current variation in the tether length to the total variation obtained from the previous iteration. This step is repeated for each tether.

STEP 5 – The total variation in the tether length is likely to have high-frequency components due to the longitudinal waves and numerical errors. Moreover, since very rapid changes in the aircraft flight path are not physical, a Fourier series to approximate the variation of tether length can filter out the higher frequencies depending on the number of terms used. The parameters are fit using the least squares method to minimize the discrepancy between the required tether length and the model tether length.

If the error is within some threshold, the process is completed and a calibrated set of flight path parameters is obtained to minimize the fuselage motion. Otherwise, the process is repeated again until convergence is reached.

The variation in height is provided using a Fourier series as shown in Equation 155,

$$\Delta h\left(s\right) = h_0 + h_{a1}\cos\left(s\right) + h_{b1}\sin\left(s\right) + h_{a2}\cos\left(2s\right) + h_{b2}\sin\left(2s\right) + h_{a3}\cos\left(3s\right) + h_{b3}\sin\left(3s\right) \tag{155}$$

where h_0, h_{a1}, h_{b1}, h_{a2}, h_{b2}, h_{a3}, and h_{b3} are the seven constants to calibrate. More terms can be added to the Fourier series if required.

5.3.3 Application of the Compensation Method

The process described in Section 5.3.2 is applied to the optimized flight path at 15 m/s, described in detail in Section 5.2.2. Figure 81 first presents the required variation in tether length, $\Delta L_i\left(t\right)$ at iterations 1, 2, 4, and 9.

The required variation in tether length reaches over 1 m during the first iteration. The fit using a Fourier series with seven terms is sufficient since the resulting fuselage motion become on the order of a few centimeters after calibration. At each iteration, the required variation in tether length $\Delta L_i\left(t\right)$ is reduced, but higher frequency variations become dominant. Those variations cannot be modeled using the first few terms of the Fourier series, as shown for iteration 9 in Figure 81d. However, given the amplitude of the variation (in the order of 1 cm), it is appropriate to filter them out.

The variation in tether length is maximal at $t = 2.8$ which matches with the highest tether tension as shown initially in Figure 67c using the lower fidelity tether model. The increase in the flight path height can be qualitatively observed in Figure 86 which compares the flight paths with and without calibration. The final validation to confirm that the calibrated flight path parameters minimize the fuselage motion is to rerun the dynamic model with the new parameters without constraining the payload motion. Figure 83 illustrates the payload motion for both the high fidelity tether model with and without compensation. In order to better observe the motion of the payload after calibration, Figure 84 shows the fuselage motion only for the case with

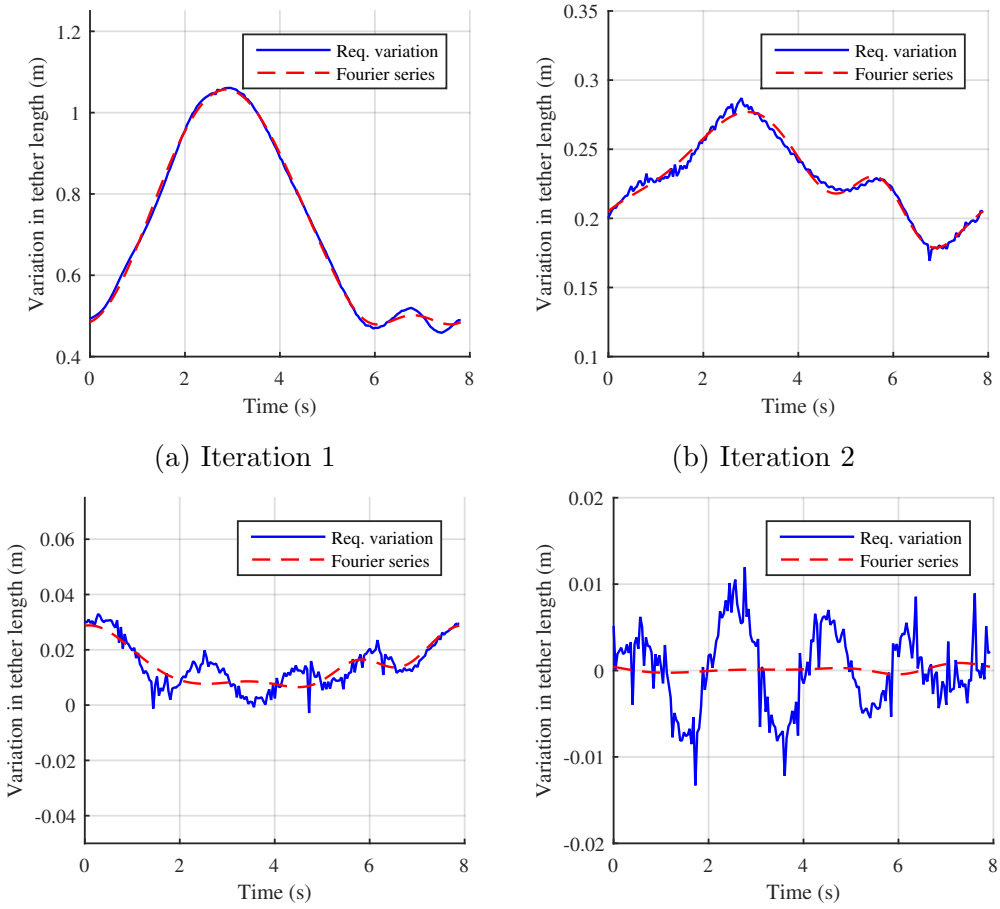

(a) Iteration 1

(b) Iteration 2

(c) Iteration 3

(d) Iteration 9

Figure 81: Convergence of the calibration method for minimal payload motion applied to the optimized flight path at 15 m/s. The variation in the tether length at iterations 1, 2, 3, and 9 is provided. The variation in the tether length are reduced at each iteration (the reader should note to the relative change in the vertical axis range between each figure).

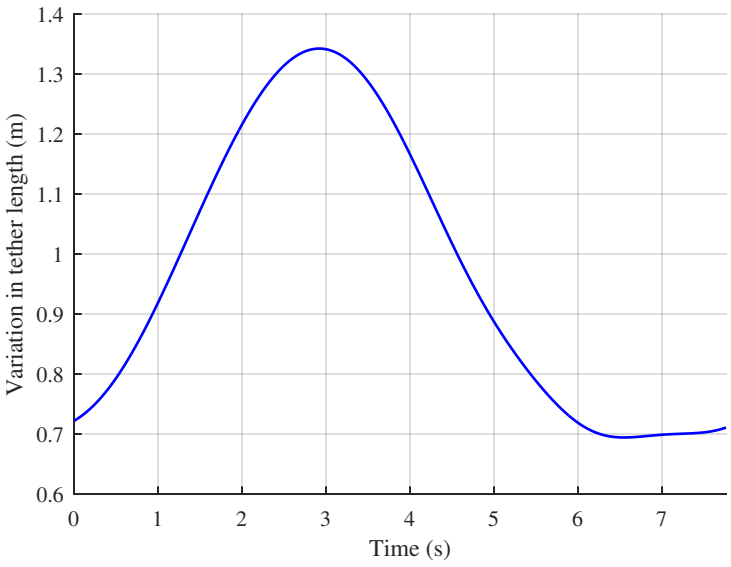

Figure 82: Calibrated variation in the tether length for minimal fuselage motion.

calibration.

The payload motion after calibration remains centered at (0,0,0) with very slight oscillations, characterized by a displacement in the order of only 1 cm. The calibration process detailed in Figure 80 is therefore validated. Only the motion associated with higher tether tension frequencies could not be removed by the Fourier series.

Now that the flight path is adjusted to minimize payload motion as the control system would do in flight, the objective is to compare the loads seen by the aircraft from the different methods. Figure 85 compares the tether tension of UAV 1 as a function of time through a complete period. Three results are presented: the lower fidelity tether model prediction, the higher fidelity without calibration, and the higher fidelity with calibration for tether elasticity.

The tether tension as a function of time for the lower fidelity tether model and the higher fidelity without calibration differ significantly even if the exact same flight path is followed by the aircraft. Without calibration for the tether elasticity, the payload undergoes significant oscillatory motion. Since the ratio of the fuselage-to-tether mass is in excess of 35, the fuselage motion has an impact of the tether forces.

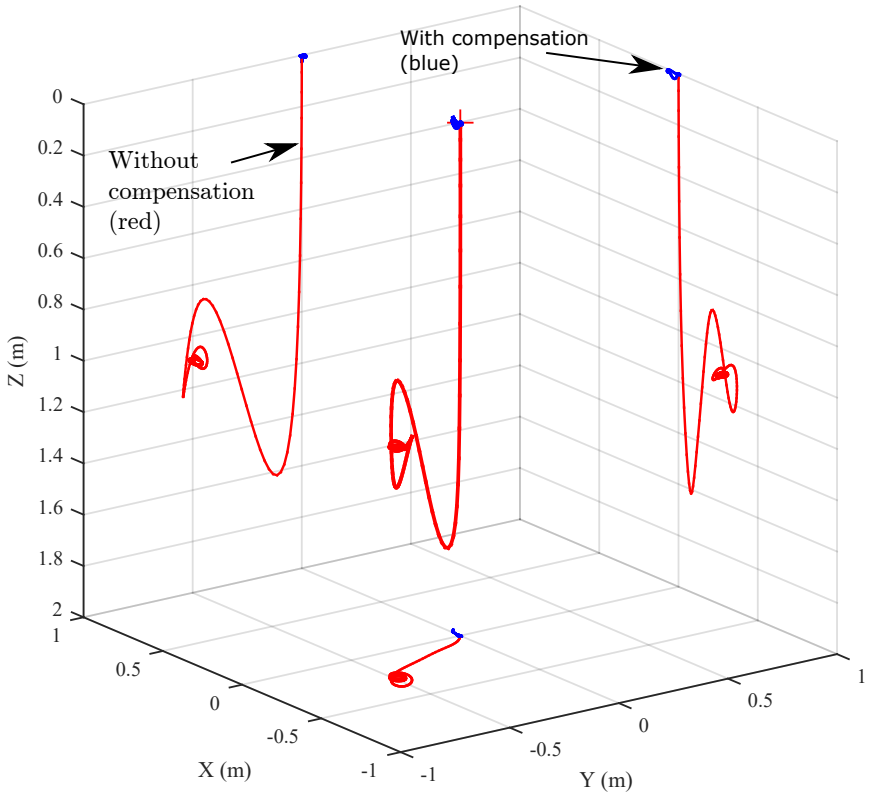

Figure 83: Comparison of the payload motion with and without calibration. The initial payload location is (0,0,0) for both cases.

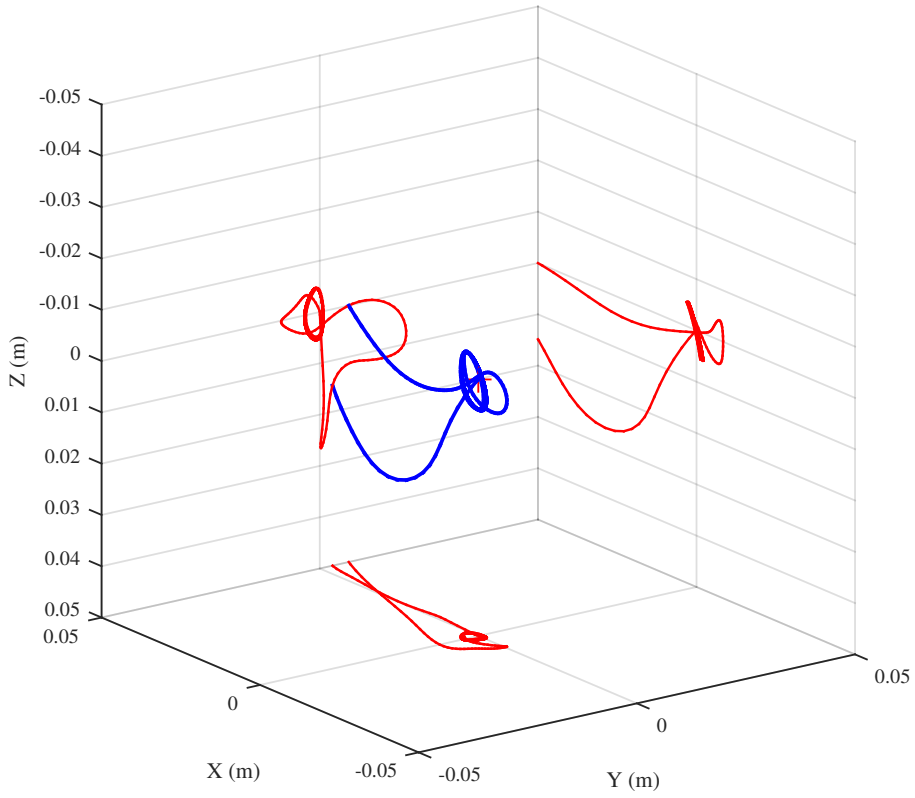

Figure 84: Fuselage motion with tether elasticity calibration for minimum motion.

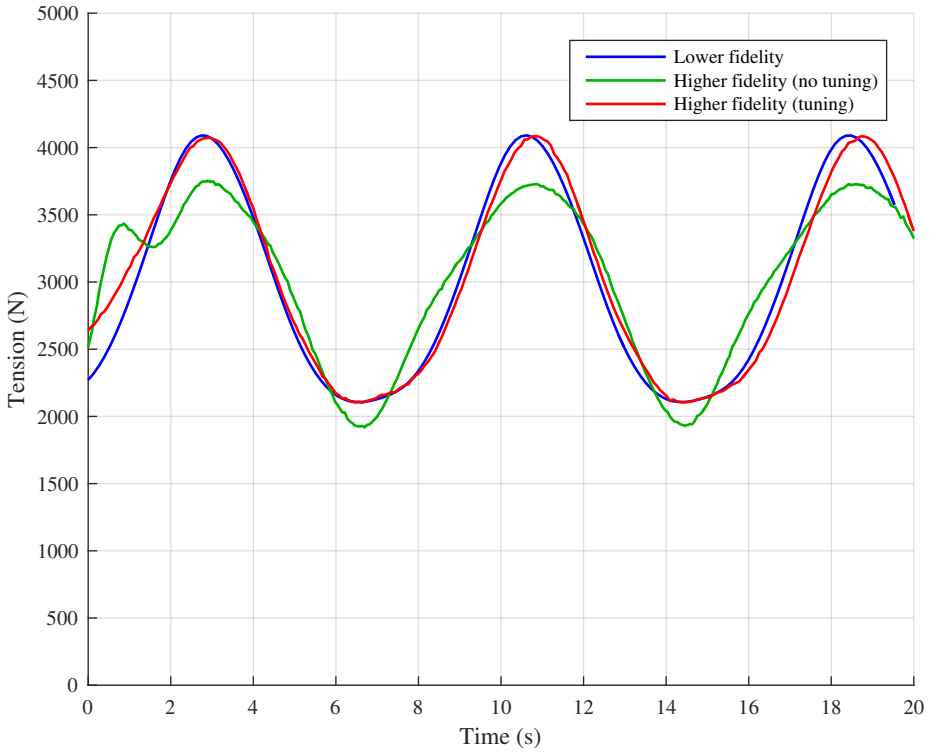

Figure 85: Tether tension as a function of time for three cases.

Once the flight path is calibrated to minimize the motion of the fuselage, the tether tension is almost identical to the lower fidelity approximation. The cause of the slight phase lag that exist between the two cases is explained by the difference in the length of the flight paths. The calibration process shifted the flight path upward and outward with respect to the fuselage, a shown in Figure 86. Since the velocity parameters are kept the same for both cases, the time to complete one revolution increases approximately 1.5%.

Based on those results, an important conclusion is made. In actual operation, the tethered aircraft will be operated to minimize the fuselage motion through a control system most likely based on tether tension and UAV position. *For the performance prediction of the system in a design space exploration exercise, the lower fidelity tether model is as efficient as the higher fidelity tether model* ***with*** *compensation for the tether elasticity.* The latter model provides the *actual* flight path that would have to

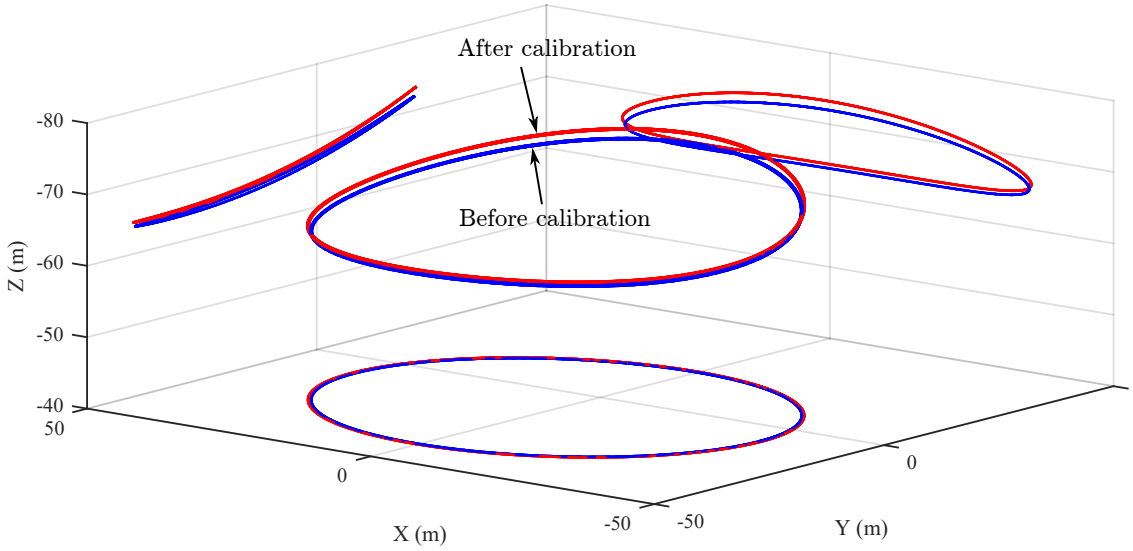

Figure 86: Qualitative comparison of the flight paths with calibration (red curves) and without calibration (blue curves). In order to compensate for the tether elasticity, the calibrated flight path is slightly above its initial position.

be performed, but since the difference between the flight path is small, the effect of neglecting the difference for the power prediction of the aircraft is minimal compared to the two orders of magnitude difference in the computational time. The higher fidelity tether model should then be used to evaluate the stability of the system and to analyze the tether deflection in operation. Moreover, this model will be critical in the future development of this technology, especially in the development of the control system.

5.4 Higher Fidelity Aerodynamic Simulation

Section 5.2 presented the design space exploration and optimization of the flight paths using the lower fidelity environment, which includes the approximation of the lifting line for the drag prediction and a rigid tether model. Section 5.3 demonstrated that the rigid tether segment approach is sufficient for power prediction. This section

presents the results of simulations using the higher fidelity aerodynamic model.

The high fidelity aerodynamic model uses the aircraft attitude (Euler angles), position, lift, and rolling moment as a function of time obtained from the tether and aircraft models, for each aircraft. Then, the aerodynamic model solves for the required angle of attack and aileron deflection as a function of time, with numerous options for the wake modeling as initially detailed in Section 4.8. In other words, this section presents the results from the higher fidelity M&SE where the higher fidelity tether model is replaced with the lower fidelity tether model. The objective of this section is to validate the following hypotheses.

1. Due to the high roll rate of the aircraft and the varying relative airspeed across wingspan, a large aileron deflection should be required. Under those conditions, the predicted drag based on the approximation of the lifting line (with a constant value of the Oswald efficiency factor) should fall below the actual value predicted by the high fidelity aerodynamic model

2. Under the same conditions stated in 1, a significant yawing moment should result, which could have the potential to increase drag through a large rudder deflection.

3. Due to the strong variation in the relative freestream velocity across the span, the lift distribution should be far from symmetrical, especially since the aileron deflection is constant across the span. As a consequence, local lift coefficient is expected to be higher than the maximum *aircraft* level lift coefficient prescribed in the optimization.

All of these hypotheses are based on the overarching hypothesis that a higher fidelity aerodynamic model is important for the power prediction of tethered aircraft to lift payloads, which has been shown to be a shortcoming of the previous studies on the topic. The remainder of this section is presented as follows. First, the optimized

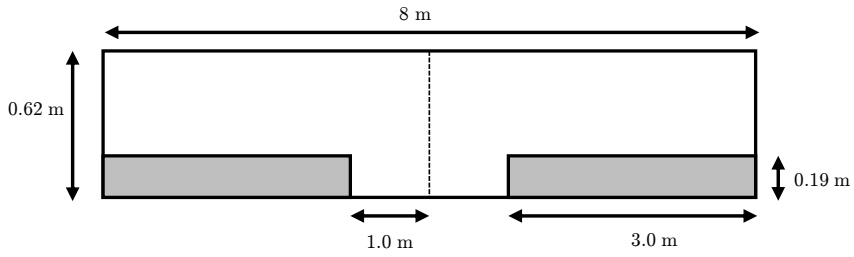

Figure 87: *Wing 7* geometry with aileron size and position. The reader should note the difference between this wing geometry and the wing used for Test Case 2 presented in Figure 137. The wing chord in the present case is smaller as presented in Table 4, and the aileron span is increased to cover 75% of the span.

flight path used to derive the power curve presented in Section 5.2 is first reanalyzed to quantify the difference in power requirement between the aerodynamic models. Second, an analysis in hover is conducted to quantify the effect of wake interaction for this particular flight path.

5.4.1 Comparison of the Power Curves in Forward Flight

The wing geometry used in this section is presented in Figure 87. The aileron covers 75% of the wing span to ensure proper control during a rolling maneuver. Details about the aileron geometry are just provided now since it is not considered in any lower fidelity simulation. The aileron effectiveness (through a change in the local lift coefficient on the wing) is the same as presented in Figure 137. The total aircraft parasitic drag coefficient is 0.015 as presented in Section 5.1.

The objective of the first study is to evaluate the system-level impact (in terms of power prediction) to use the higher fidelity environment[1] on the optimized flight paths obtained in Section 5.2.2. For this study, the consolidation model was used, and the wake geometry is considered prescribed to reduce computational cost. Details are provided in the second study to justify this choice for advance velocities below 5 m/s.

[1]From this point on, when referring to the higher fidelity M&SE, it considers that the lower fidelity tether model is used.

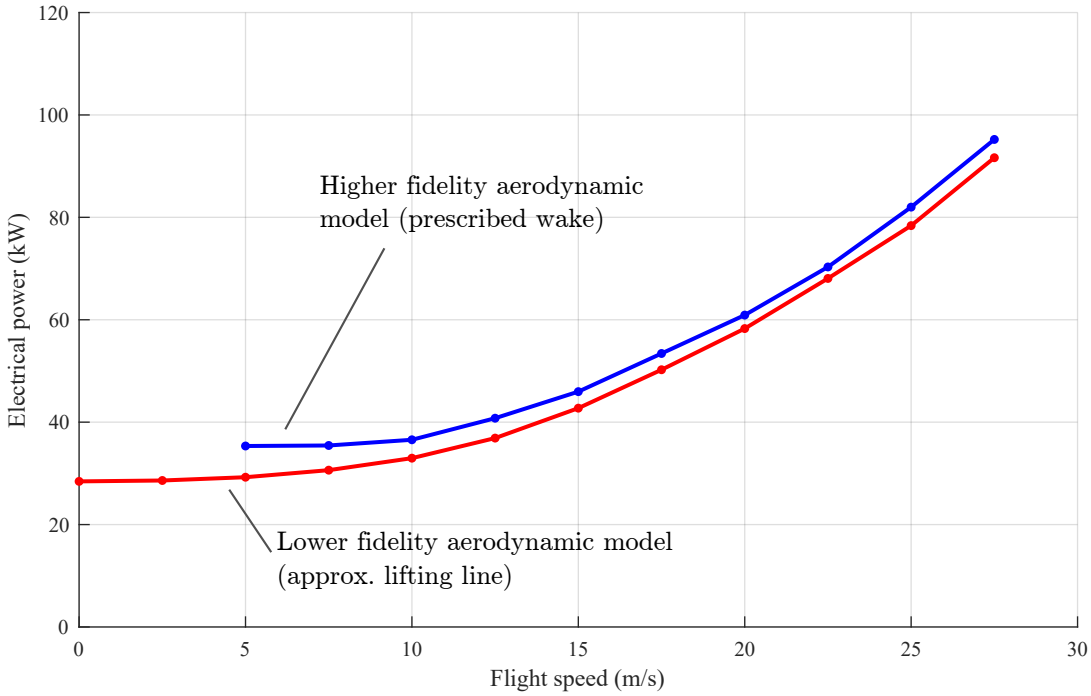

Figure 88: Comparison of the power curves for the two aerodynamics codes.

Figure 88 shows the difference between the power curve as a function of flight speed, where the lower fidelity aerodynamic model prediction is depicted by a red curve, and the higher fidelity aerodynamic model prediction is shown with the blue curve. Both approaches use the exact same flight paths.

The difference between the power prediction from the two models can be explained by two phenomena. First, the increase in relative discrepancy at low flight speed is explained by the wake interaction between the aircraft. Aircraft fly through the wake of the previous aircraft on the advancing side and at $\psi = 0^o$ at a slow flight speed. At higher flight speed, the difference between the curves remains approximately constant but does not go near zero as expected if the difference only came from the induced velocity and wake interaction. At high flight airspeed, most of the additional losses are the consequence of non-symmetrical lift distribution due to the varying velocity across the span and the need for strong aileron deflection to maintain the target

rolling moment. In order to support these claims, the optimized flight path at 15 m/s is presented in detail in the next section.

5.4.2 Details of the 15 m/s Optimized Case

The flight path optimization presented in Section 5.2.2 showed that the mean power requirement at 15 m/s is approximately 42 kW for the system. The optimized flight presented in Figure 66 shows a left tilt of the hub plane and variation in the velocity as a function of the location on the ellipse. At this time, the wake interaction was not considered.

A sensitivity analysis was then performed to evaluate the sensitivity of the power requirement if the flight path is constrained in the pitch angle of the hub plane. The optimization returned a penalty of approximately 200 W for a prescribed pitch attitude of 5.7°. The objective of this change in the flight path is to attempt to minimize the wake interaction. Figure 89 show the comparison of flight paths in the system-carried frame.

The actual flight path in the Earth-fixed reference frame is actually quite different. Figures 90a and 90b illustrate the prescribed wake shape obtained from the higher fidelity aerodynamic model for both cases. The wake consolidation can clearly be observed.

The optimized flight path with the presence of a nose-down attitude of 5.7° of the hub plane will be considered for the remainder of this section due to the reduced wake interaction and the larger separation between the aircraft and wake. Figure 91 presents the drag prediction of aircraft 1 as a function of time for a full revolution. The predictions from three models are compared: lower fidelity, higher fidelity with a prescribed wake, and higher fidelity with a free vortex wake.

The reader can refer to Figure 92a to relate time to a position along the flight in the system-carried frame. There are two regions of interest which show a discrepancy

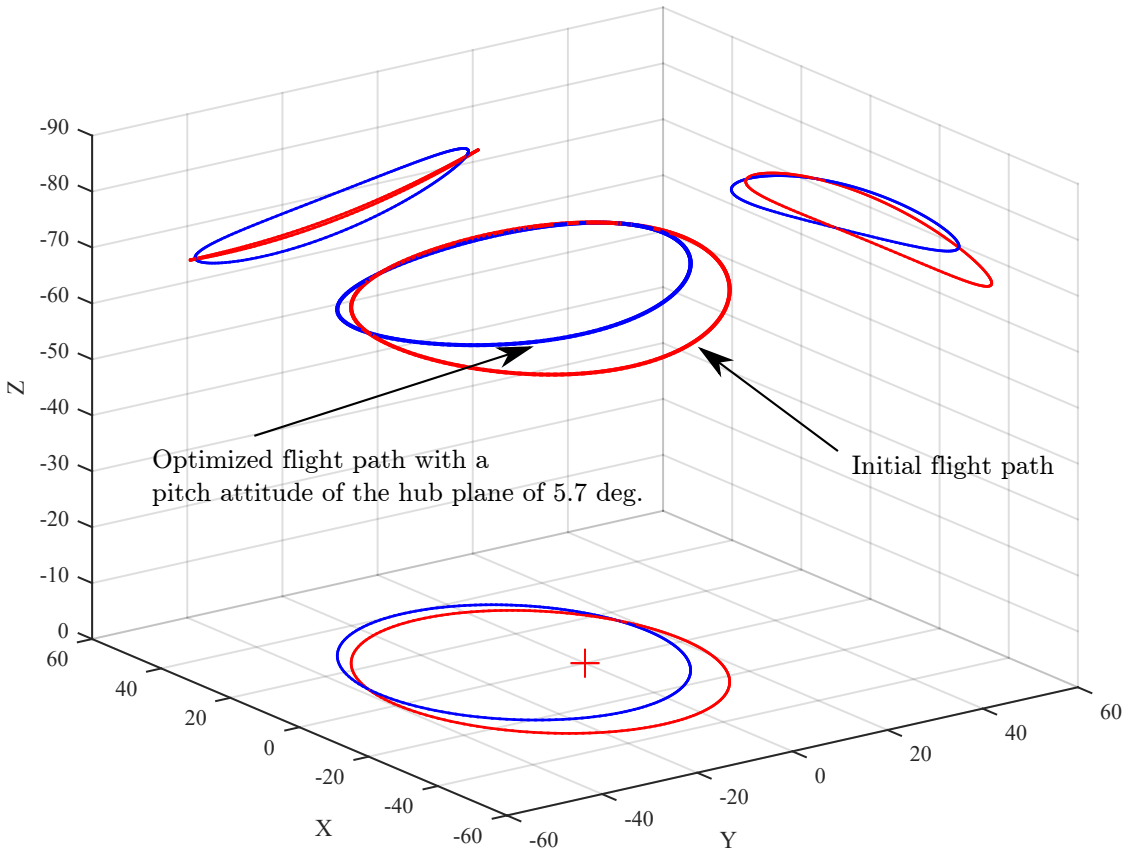

Figure 89: Comparison of two optimized flight paths at 15 m/s.

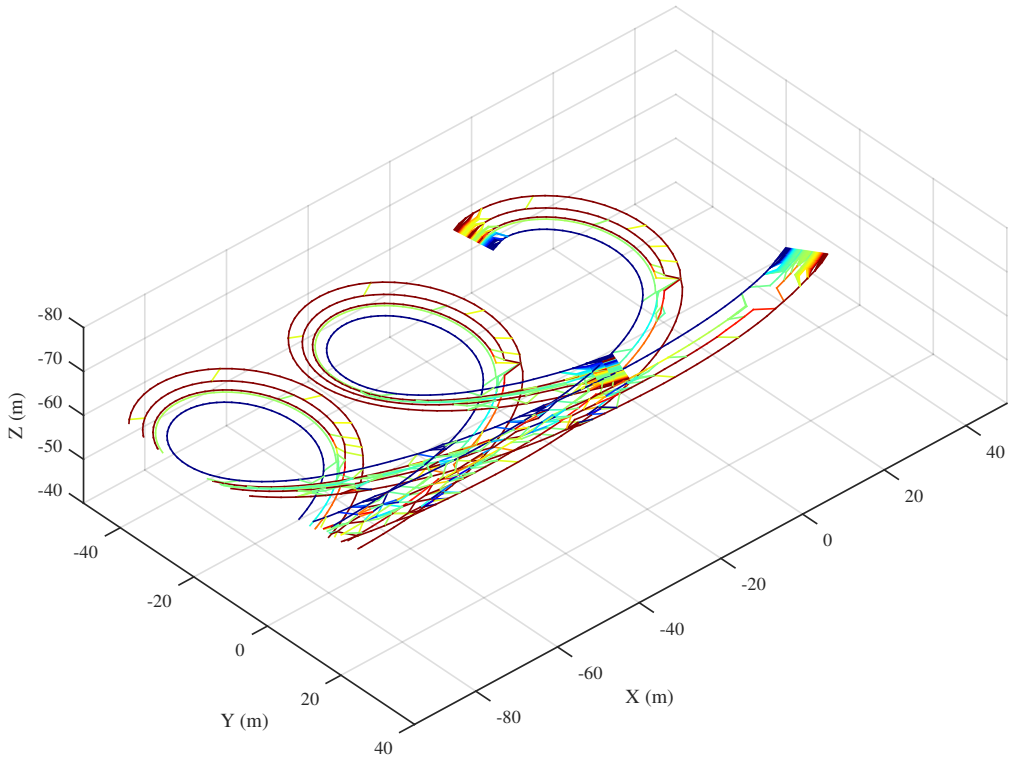

(a) Optimal flight path (without pitch of the hub plane)

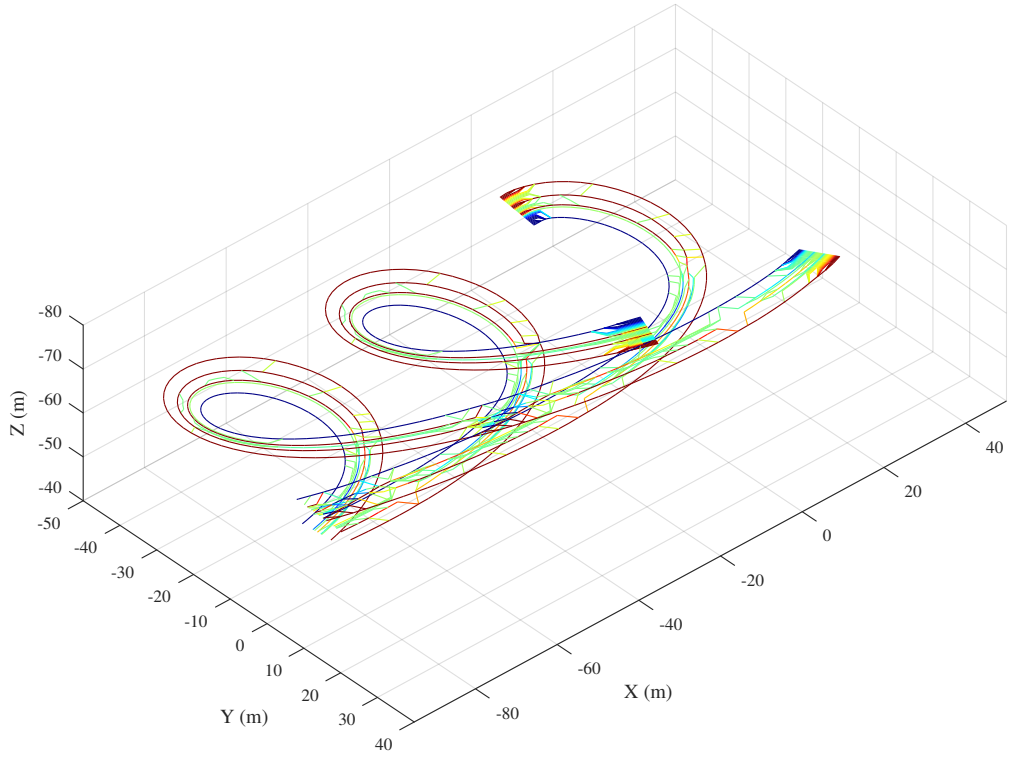

(b) Optimal flight path (with 5.7° nose-down pitch of the hub plane)

Figure 90: Rigid wake shape for two optimized flight path at 15 m/s. The consolidation model can clearly be observed in the two cases.

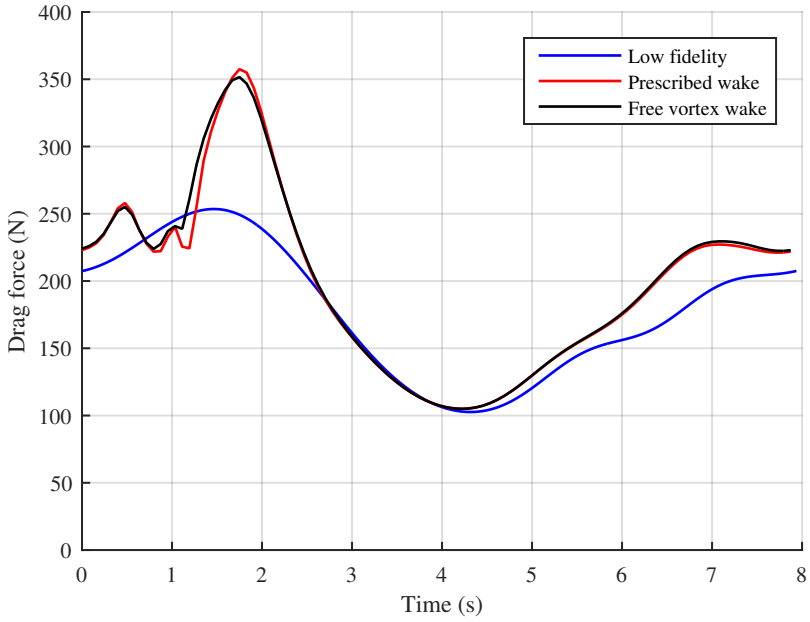

Figure 91: Comparison of drag prediction for aircraft 1 as a function of time for three aerodynamic models.

between the lower fidelity and both higher fidelity models. The first region is between $t = 0$ and $t = 2.5$ seconds, when the aircraft transitions from the most rearward position to about half way of the advancing side. During that period, the aircraft sees a lot of wake interaction, which affects the drag prediction and requires sharp changes in the control surface deflection. The peak drag occurs when the aircraft must go through a region with a local downward induced velocity from the previous aircraft. Since the lift is prescribed, the pitch attitude of the aircraft must increase to maintain the lift. With the lift vector oriented a few degrees more backward, the induced drag increases by almost 100 N or 50%.

The second discrepancy occurs on the retreating side, starting at approximately $t = 6$ seconds. During that low-speed operation in the tight turn, the airspeed along the wing varies significantly. In order to maintain the target rolling moment at zero, a large aileron deflection is required, as will be detailed later. The lift distribution is therefore far from optimal, which increases the induced drag and creates a yawing

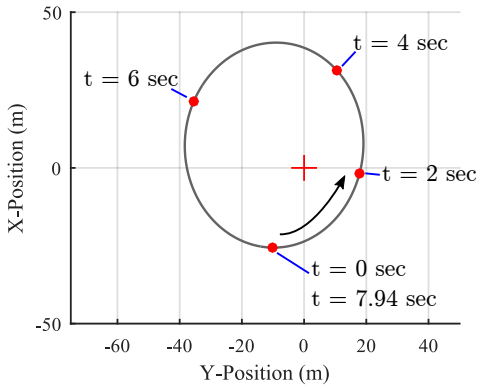

(a) Position as a function of time

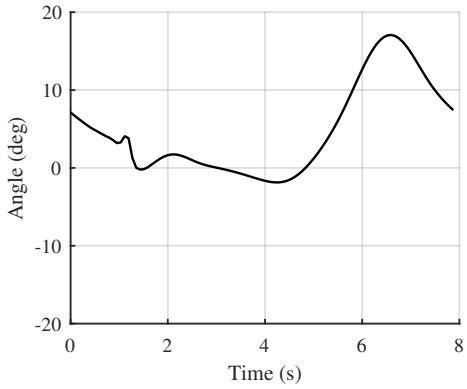

(b) Aileron deflection

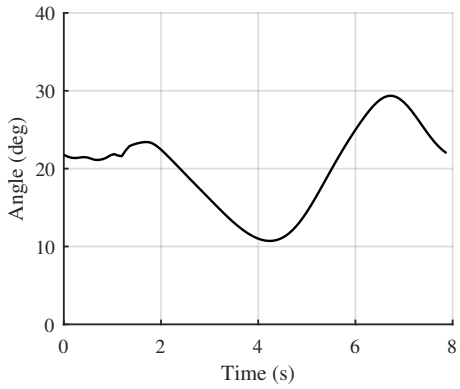

(c) "Pitch" angle of the aircraft

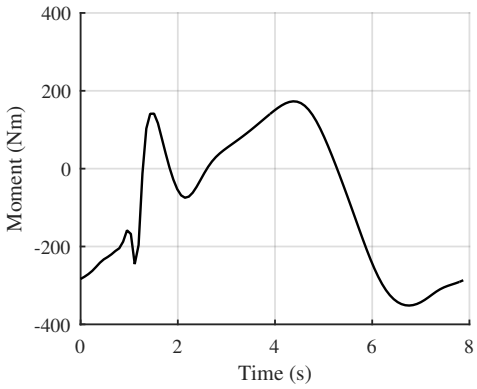

(d) Yawing moment

Figure 92: Aileron deflection, aircraft pitch and yawing moment for the optimal flight path at 15 m/s obtained using the higher fidelity aerodynamic model

moment (moment about the body z-axis).

The small difference between the two wake modeling approaches suggests that the wake displacement over time does not affect significantly the drag prediction of the aircraft. This assumption is valid for flight speed in excess of 5 m/s in the present configuration. A free vortex wake model is still needed for the simulation in hover. In order to better understand the phenomena that occur along the flight path, Figure 92 presents the aileron deflection, the yawing moment, and the angle of attack as a function of time.

The wake interaction can clearly be observed on the response of the aircraft between $t = 0$ and $t = 2.2$ seconds. First, a sharp change in the aileron deflection is required to maintain a rolling moment of zero, and a yawing moment reaching 175 Nm is observed. Since the aircraft flies in sinking air due to the induced velocity, the "pitch" angle of the aircraft is higher than seen without wake interaction. The geometric angle of attack is defined here as the angle between the relative wind velocity seen by the aircraft (without induced velocity) and the mean chord of the wing. It differs from the angle of attack since it does not consider the induced velocity by other aircraft, nor its self-induced velocity.

On the retreating side, a large aileron deflection[2] (to roll to the right) is required to maintain a zero rolling moment since the left wing sees a much slower relative airspeed than the right wing. As a consequence, a strong left yawing moment is created, the "adverse yaw effect" as commonly referred to by airplane pilots. During that part of the flight, the aircraft lift coefficient averages two, as limited by the optimizer, which explains the high pitch angle. The airfoil assumed in this study is a symmetrical airfoil, with a lift curve slope of 1.8π, which also explains the need for a high pitch angle. Details about the lift coefficient distribution and circulation distribution along the lifting line are presented in Figures 93a and 93b.

The most important observation from Figure 93a is the non-symmetrical lift coefficient distribution about the centerline. The presence of an almost continuous, non-zero roll rate combined with a varying relative airspeed across the wingspan creates a relatively complex distribution. The complex circulation distribution also shows a non-symmetry about the centerline.

The rapid change in lift coefficient around $y = -1$ and $t = 6.5$ is associated with the end of the flapped surface. The end of the right aileron can also be seen in the circulation distribution at $t = 6.5$ and $y = 1$. The wake interaction described above

[2]A positive aileron deflection is defined as one that creates a positive rolling moment.

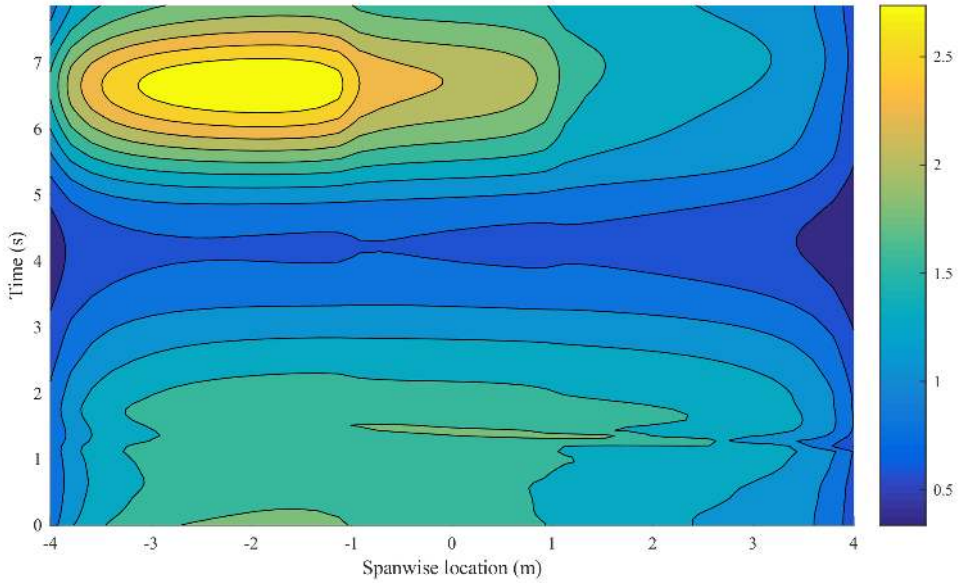

(a) Local lift coefficient as a function of time and spanwise location.

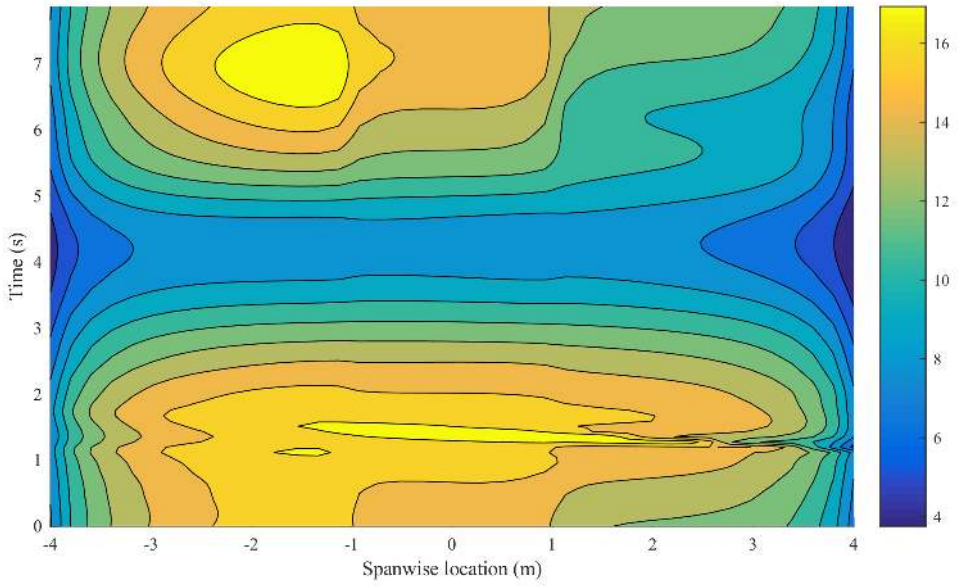

(b) Bound circulation (m^2/s) as a function of time and spanwise location.

Figure 93: Local lift coefficient and circulation along the wing as a function of time. The reader should refer to Figure 92a to relate time to position along the flight in the system-carried frame.

at $t \approx 1.75$ is also clearly seen in the circulation distribution through a sharp change as a function of time.

The direct optimization process using the lower fidelity aerodynamic model had a side constraint on the maximum aircraft lift coefficient equal to 2.0. However, the detailed analysis here shows that the local lift coefficient reaches over 2.5 on the left wing (inboard of the turn) due to the low airspeed and the requirement to maintain a zero rolling moment. Given these observations, it would be advisable to reduce the allowable lift coefficient during the low fidelity optimization process. On an final note, it might be advisable to use aircraft with a non-symmetrical wing geometry if the system is to be operated in this flight mode for long durations. Drag reduction and the risk of an inner wing tip stall could be reduced.

5.4.3 Hover

The aerodynamics of tethered aircraft is more complex in hover due to the need to consider the induced velocity of the wake itself and to calculate its motion over time. Numerical stability of the analysis codes is also a major concern to obtain the mean power requirement.

The approach taken in this work to obtain the power requirement in hover for both circular and elliptical flight paths is to initiate the wake with a climbing velocity of 1 m/s for two complete rotor revolutions, or approximately 15 seconds. Then, the climbing velocity is reduced to 0.5 m/s for two other rotor revolutions. Finally, the climb rate is reduced to zero for four rotor revolutions. The power requirement and the associated aircraft drag are calculated for the last two revolutions. A total of 280 timesteps equally spaced are used for the simulation.

This section is divided into two parts. First, the analysis of a conventional circular flight path is performed for various radii and the results are compared to the lower fidelity approximations. Then, the more complex non-circular flight path is presented

Table 9: Test cases in hover at various flight path radii

Case #	Radius	Velocity (m/s)	A/C Lift (N)	Bank angle (deg)
1	0.341	24.5	3,315	-8.7
2	0.412	25.3	3,278	-1.6
3	0.553	26.7	3,348	11.9
4	0.694	28.5	3,640	25.8
5	0.800	30.8	4,151	37.9

to confirm or infirm that the power requirement can be reduced with unconventional flight paths in hover.

A total of five test cases are analyzed in hover with a circular flight path. These cases are obtained from the lower fidelity optimization in hover for various flight path radii, presented in Section 5.2.3. A fixed tether length of 75 m is imposed, with an 800 kg fuselage, and an air density of 1.21 kg/m^3. Table 9 presents the details of test cases, where the normalized radius is equal to the flight path radius divided by the tether length.

For large radii, the required lift for each aircraft increases due to the bank angle required to maintain the position. For small radii flight paths, the required lift is reduced, but a negative bank angle (bank towards the center of the turn) is required since the inertial response of the aircraft are more important than the horizontal force provided by the tether. The optimal velocity is also directly a function of the lift required since all these optimal cases are constrained by the maximum lift coefficient of 2.0.

Figure 94 presents the wake shape for a few rotor revolutions for Test Case 1, characterized by a short turn radius and a negative bank angle. The wake is only convected vertically as the three aircraft show a bank angle of less than 10 degrees. However, there is no visible wake contraction as for a conventional helicopter since the major part of the disk is not covered by the aircraft, only a small annulus is covered. A complex interaction between the aileron vortices and the strong wing tip vortices can be observed. The aileron vortices are convected downward at a faster rate than

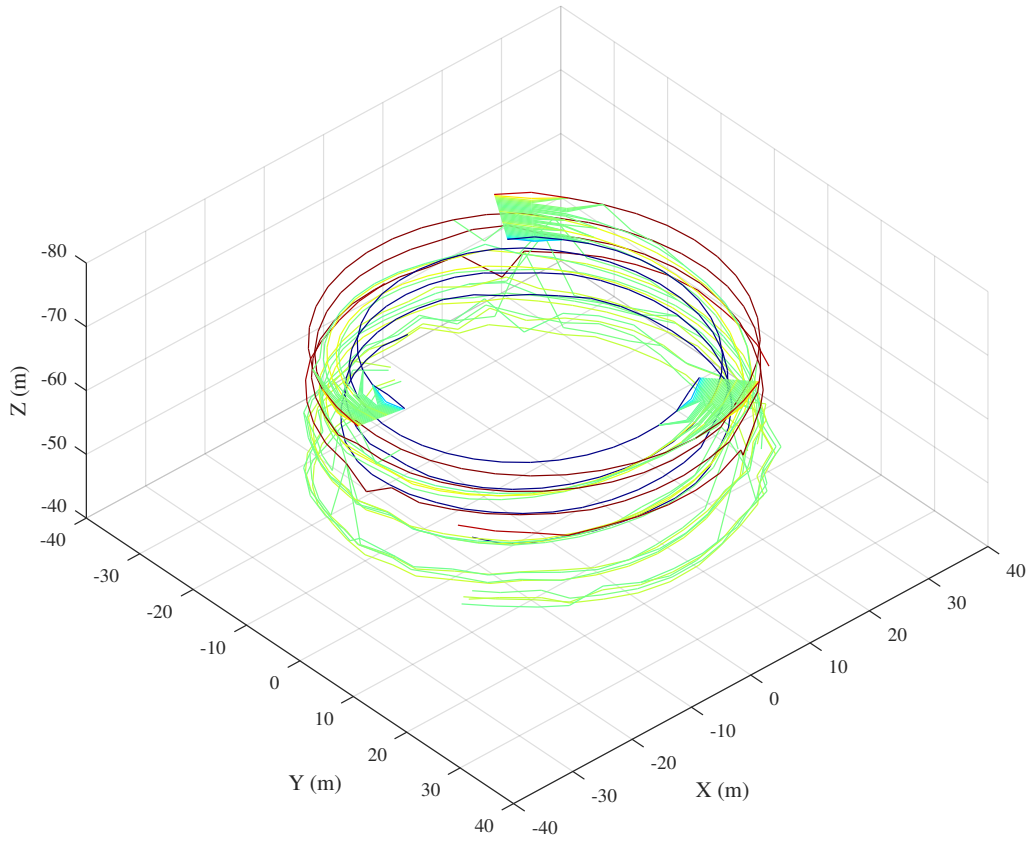

Figure 94: Wake shape for Test Case 1, with a small radius. The aircraft are slightly banked towards the center of rotation since their inertia forces overcome the horizontal component of the tether tension. The color scheme represents the circulation intensity of each vortex from < -8 (blue) to $> +8$ (red). The shed vortices are hidden for clarity.

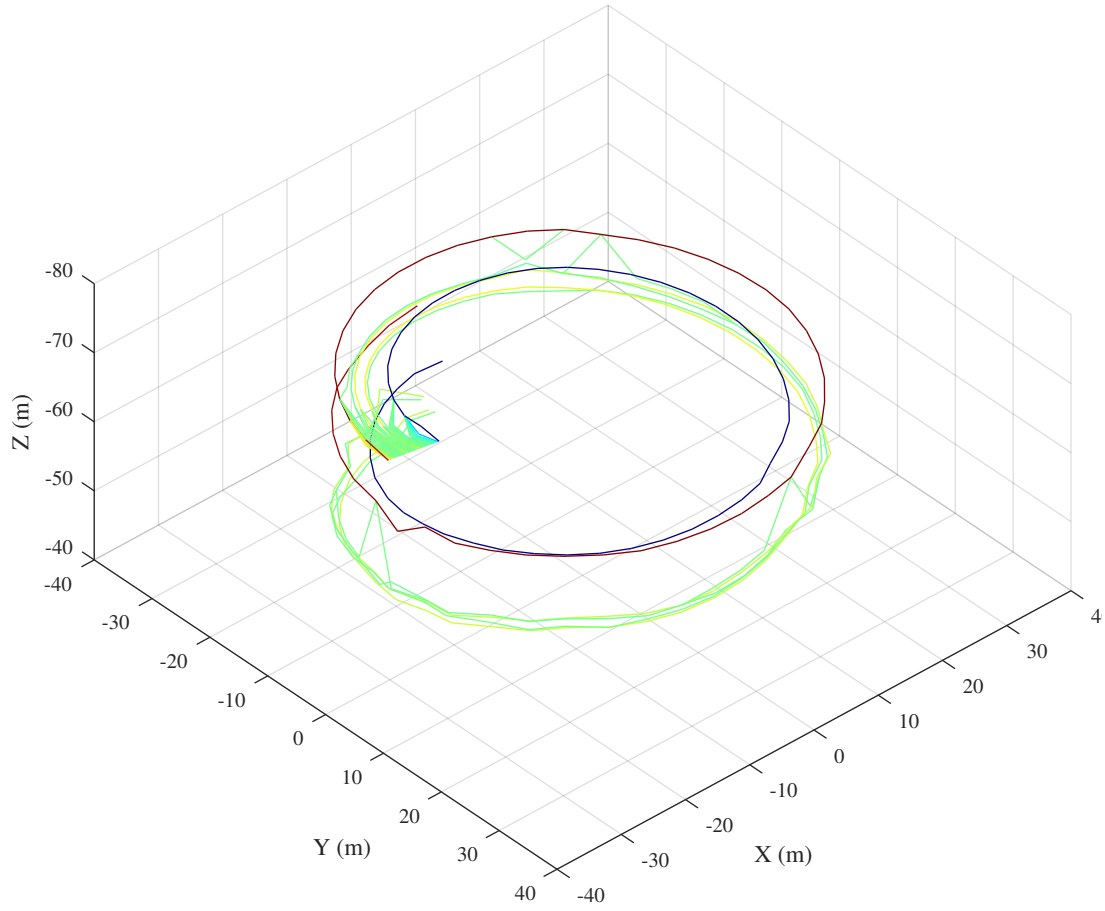

Figure 95: Wake shape from aircraft 1, for Test Case 1, with a small radius. The color scheme represents the circulation intensity of each vortex from < -8 (blue) to $> +8$ (red). The aileron vortices are convected downward at a fast rate, and get "caught" in the wake of the next aircraft.

the main vortices and get entrained by the main vortices created by the next aircraft. Moreover, since they are of opposite sign, they show a high self-induced convection rate. In order to better observe this phenomenon, Figure 95 shows the wake from only one aircraft.

The simulation shows some numerical instability in the solution after a few revolutions. Since the wake is far down from the aircraft and that the wake intensity is already greatly reduced, this instability does not significantly affect the solution.

The wake shape from Test Case 5 is presented in Figure 96. This test case is

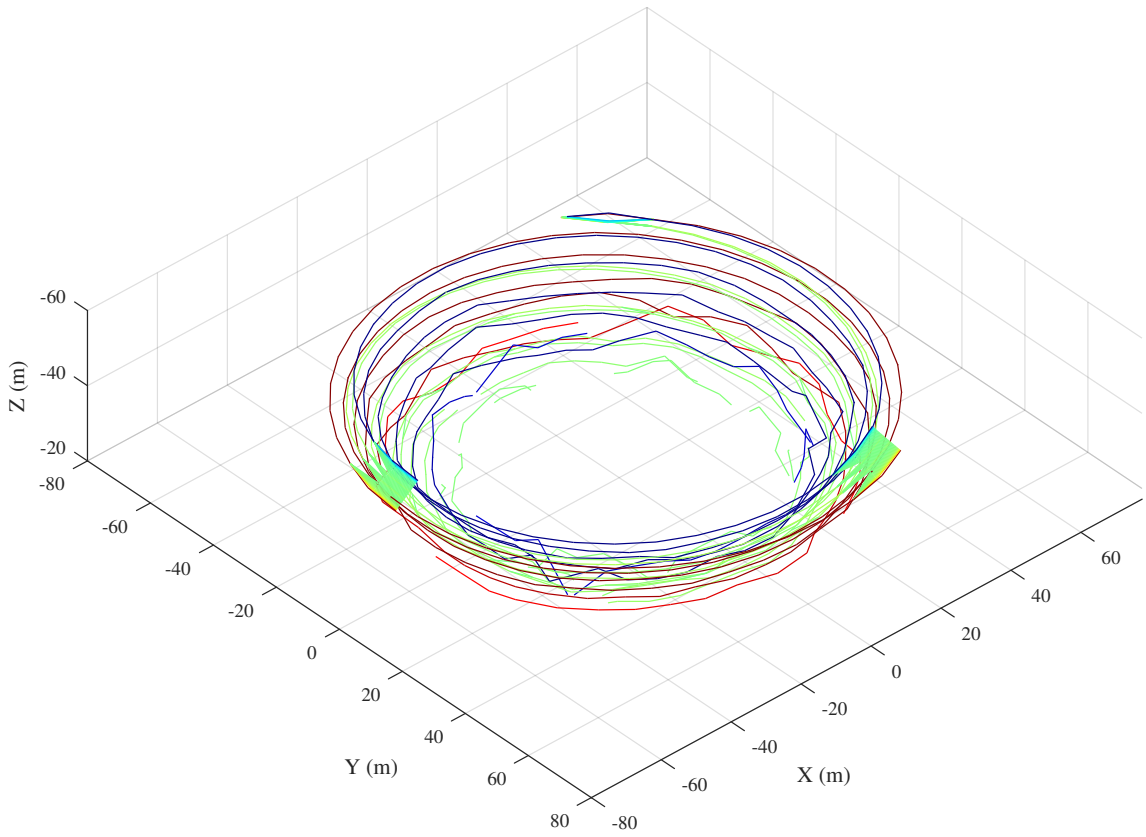

Figure 96: Wake shape for Test Case 5, with a large radius. The aircraft are banked towards the opposite direction of the center of rotation since their inertia forces are smaller than the horizontal component of the tether tension. The color scheme represents the circulation intensity of each vortex from < -8 (blue) to $> +8$ (red). The shed vortices are hidden for clarity.

characterized by a large flight path radius, which requires the aircraft to be banked outward by over 35 degrees in order to compensate for the tether tension. Moreover, the lift required by the aircraft must be augmented to compensate for the aircraft bank.

The first observation from Figure 96 for Test Case 5 is the cone shape of the wake. Since the three aircraft are banked outward, the wake is convected near a normal direction below the aircraft, or towards the center of the axis of rotation. The numerical simulation is more stable since the timesteps are larger, and the vortex segments are longer. The downward convection rate is lower than for Test Case 1

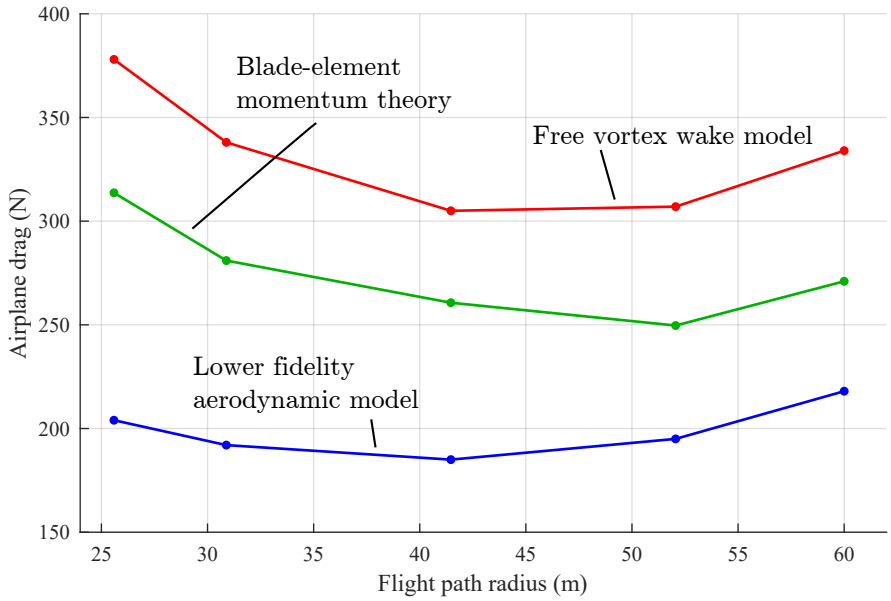

Figure 97: Drag per aircraft as a function of the flight path radius (Test cases 1-5). Three aerodynamic methods are presented: the approximation of the lifting line (low fidelity), the complete free vortex wake model (high-fidelity) and the blade-element momentum theory from the helicopter sector.

since the disk area covered by the aircraft (annulus) is larger.

The drag prediction from the five test cases are presented in Figure 97. Three aerodynamic methods are presented and compared: the approximation of the lifting line (lower fidelity), the complete free vortex wake model (higher fidelity) and the blade-element momentum theory from the helicopter sector. (The blade-element momentum theory (BEMT) was initially presented in Section 2.2.2.)

Figure 97 shows very important trends which will be described in detail. In a nutshell, it describes how well a lower fidelity aerodynamics model for airplanes compares to a lower fidelity aerodynamic model for helicopters, which has been shown as one of the important gaps in the literature for fixed-wing aircraft flying along circular flight paths.

First, the drag prediction for each airplane using the approximation of the lifting line is shown with a blue curve. The increase in drag for the lowest flight path radius

can be explained by two phenomena:

1. *Increase in lift requirement* – An increase in lift requirement is seen for smaller flight path radii since the lift vector of the aircraft must be pointed inside the turn to overcome the inertial effects. As a consequence, more lift is required.

2. *Optimal flight condition occurs at a higher lift coefficient* – For Test case 1, the flight regime that minimizes the power requirement occurs in slow flight, on the maximum lift coefficient constraint, which shows a higher drag than at the best lift-over-drag ratio.

At larger flight path radii, an increase in drag occurs due to the increase in lift requirement resulting from the need to bank the aircraft outside the turn to compensate for the horizontal force from the tether. It should be recalled that the drag coefficient evaluated using this aerodynamic model is only comprised of only two terms: the parasitic drag coefficient (constant for all aerodynamic models) and the lift-dependent term (which also depends on the wing geometry). Therefore, the variation in drag does not consider the wake interaction.

Second, the drag prediction using the well-known BEMT method is shown with a green curve. This method neglects the aircraft bank angle and does not change the wing geometry through aileron deflection to ensure a zero rolling moment. However, it captures the induced velocity from the three "blades" by assuming that the disk area is the annulus area covered by the aircraft. Tip and root loss models are also included.

The results from the BEMT show a strong increase in the aircraft drag for small radii, which is simply explained by the increase in induced velocity from the reduction in disk area. As the flight path radius increases, the induced power requirement decreases, and finally increases for Test Case 5 due to the increase in lift requirement. An important observation is the difference between the BEMT and approximation of

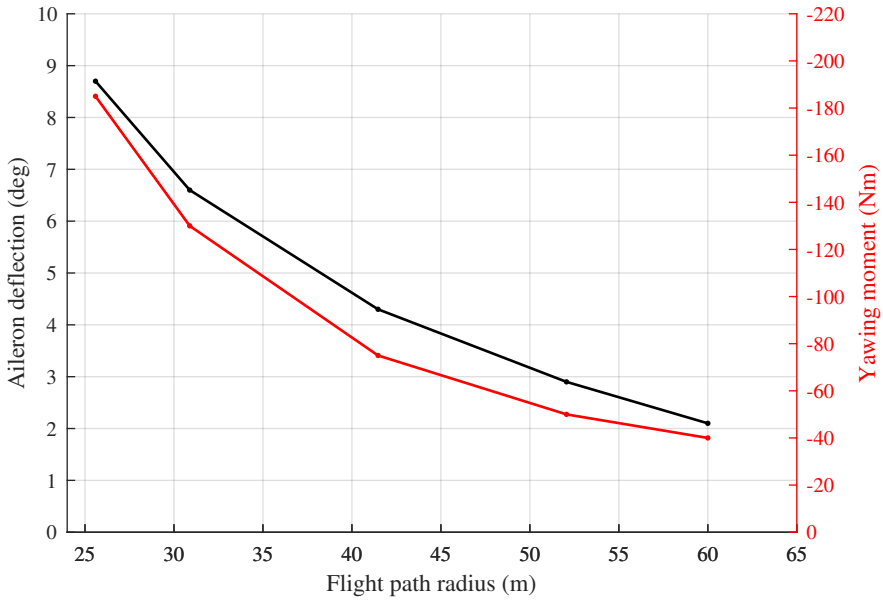

Figure 98: Aileron deflection and adverse yaw as a function of the flight path radius. At smaller flight path radii, a larger aileron deflection is required to compensate for the reduced lift on the slower wing (left). As a consequence, an adverse yaw is created.

the lifting line, which decreases monotonically as a function of the flight path radius. The difference is approximately the wake interaction between the aircraft.

Third, the free-vortex wake model shows the same general trend as the BEMT, as it also captures the wake interaction. However, the drag prediction is higher since the aileron deflection required to maintain the condition of a zero rolling moment reduces the wing efficiency.

Figure 98 presents the required aileron deflection and the adverse yaw seen by the aircraft as a function of the flight path radius. For smaller flight path radii, a large aileron deflection is required (left aileron down) to compensate for the variation in airspeed seen by both wings. As a consequence, adverse yaw is created. It should be reminded that the adverse yaw would need to be compensated by a rudder deflection, but the increase in drag required to overcome this moment is not considered.

Finally, the electrical power requirement for the three aircraft estimated by the

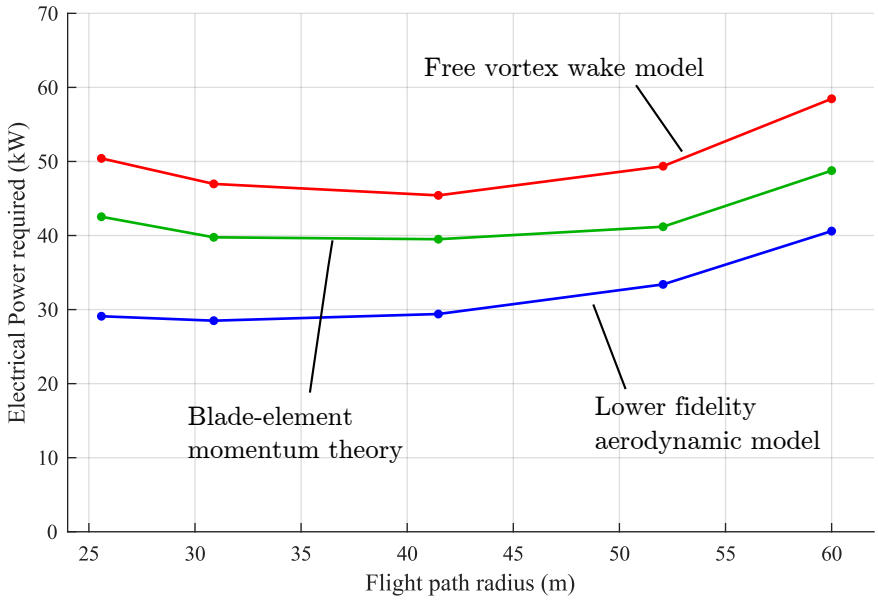

Figure 99: Electrical power requirement in hover using three aerodynamic models.

three aerodynamic models is presented in Figure 99. As expected, the free-vortex wake model has the highest power prediction with 46 kW in hover. The blade-element momentum theory predicts that the minimum power requirement is with a flight path radius of 42 m like the higher fidelity aerodynamic model.

In summary, the power prediction using the higher fidelity aerodynamics model is approximately 50% higher than using the approximation of the lifting-line method. However, one important finding is how well the blade-element momentum theory captures the salient aerodynamic phenomena, such as the wake interaction. Given these results, it can be concluded that the flight path optimization of tethered aircraft in hover along a circular flight path *should* use the BEMT method with an additional calibration factor instead of the approximation of the lifting-line to consider the wake interaction.

This section now presents the analysis of the performance of tethered aircraft flying along *elliptical* flight paths in hover using the higher fidelity aerodynamic model. As for the circular flight path cases, the free vortex wake model is used with the

Table 10: Test cases in hover with non-circular flight path at optimal flight speed

Case #	a	b	Elec. pwr. LF (kW)	Elec. pwr HF (kW)	Diff.
#1	0.412	0.341	29.0	48.0	40.0%
#2	0.553	0.341	30.8	42.0	26.5%
#3	0.553	0.412	29.5	42.2	30.2%
#4	0.694	0.412	33.1	43.5	23.9%
#5	0.694	0.553	31.5	43.2	27.1%
#6	0.800	0.412	40.0	50.9	21.5%
#7	0.800	0.553	34.7	44.6	22.1%
#8	0.800	0.694	36.6	50.5	27.6%

consolidation model and vortex decay. It was shown in Section 5.2.3 that an elliptical flight path with 120 degrees phase lag between the aircraft (and 120 degrees between the ellipse) represents an architecture that reduces the peak power requirement by the power source. Therefore, the concept presented in Figure 71b is considered. As for the previous study, the higher fidelity M&SE is used except that the lower fidelity tether and fuselage dynamic model is used.

Table 10 present the eight non-circular test cases. The values a and b represent the normalized ellipse parameters. It should be noted that the power requirement is symmetrical. In other words, a and b could be interchanged.

The electrical power prediction using the lower fidelity aerodynamic model is lower than the power prediction using the higher fidelity aerodynamic model as previously shown in hover. The difference varies between 20% and 40%. In the upper range, the main cause is a large wake interaction, such as in Test Case 1, with a very short radius.

Figure 100 compares the power requirement of circular and elliptical flight paths, both aerodynamic models. The red dots are for the test cases presented in Table 10 (note the symmetry) and the black dots are from the five circular flight paths presented in Table 9. In Figure 100b, 225 cases were analyzed, but the the markers are used to denote where the cases that are analyzed using the higher fidelity model in Figure 100b.

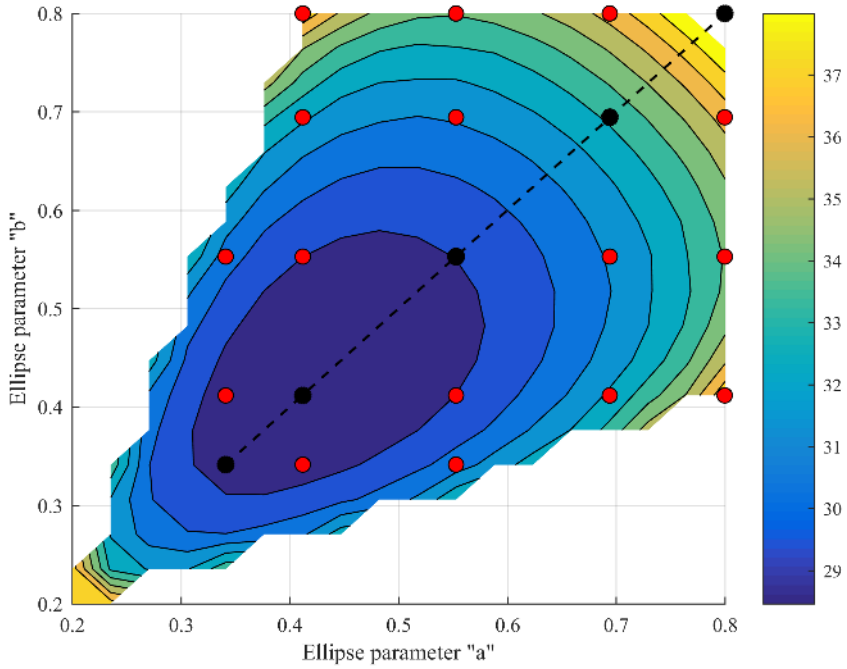

(a) Lower fidelity aerodynamic model

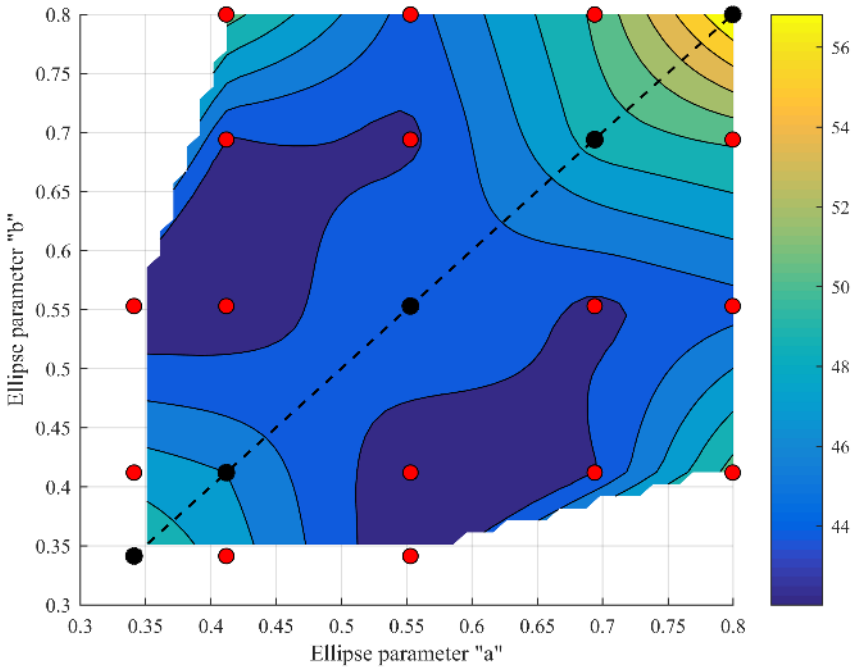

(b) Higher fidelity aerodynamic model

Figure 100: Electrical power prediction in hover for non-circular flight paths. The red dots are for the test cases presented in Table 10 (note the symmetry) and the black dots are from the five circular flight paths presented in Table 9.

The minimal power requirement evaluated using the higher fidelity aerodynamic model *does not occur on the diagonal*, or in other words, is not a circular flight path. Therefore, it can be concluded that non-circular flight paths can actually reduce the power requirement by approximately 10% when compared to circular flight path in hover. However, such complex flight path must require a much more complex control system.

5.5 Power Curve and Return on the Research Questions

The results from Sections 5.4.1 and 5.4.3 are combined to produce the complete power curve of this novel helicopter concept. Figure 101 presents the optimized power curve from hover to a relatively high-speed periodic flight path. The power requirement in the high-speed flight mode, with the three aircraft facing in the same direction, is not included.

In hover, it was shown that a non-circular flight path is optimal and can reduce the power requirement by approximately 10% for the specific case extensively analyzed in this work: three *Wing 7* aircraft with an 800 kg fuselage mass at ground level. The mean electrical power requirement in hover is approximately 20% higher than with a small 5 m/s system flight speed due to the presence of wake interaction. However, the effect in hover is minimized by the ability of the rotor to "reconfigure" to minimize the power requirement. At higher system flight speeds, the power requirement increases rapidly even with the flight path optimization procedure presented in this work. Nevertheless, the optimized flight path reduces the power requirement by 40% compared to a more traditional circular flight path with constant system flight speed.

Although this VTOL concept shows an increase in power at higher velocities, a relative comparison to conventional helicopters demonstrates the benefits of this concept. More details on this statement are presented in Section 5.6 with the conceptual sizing of a vehicle based on the EPR^2 VTOL Concept.

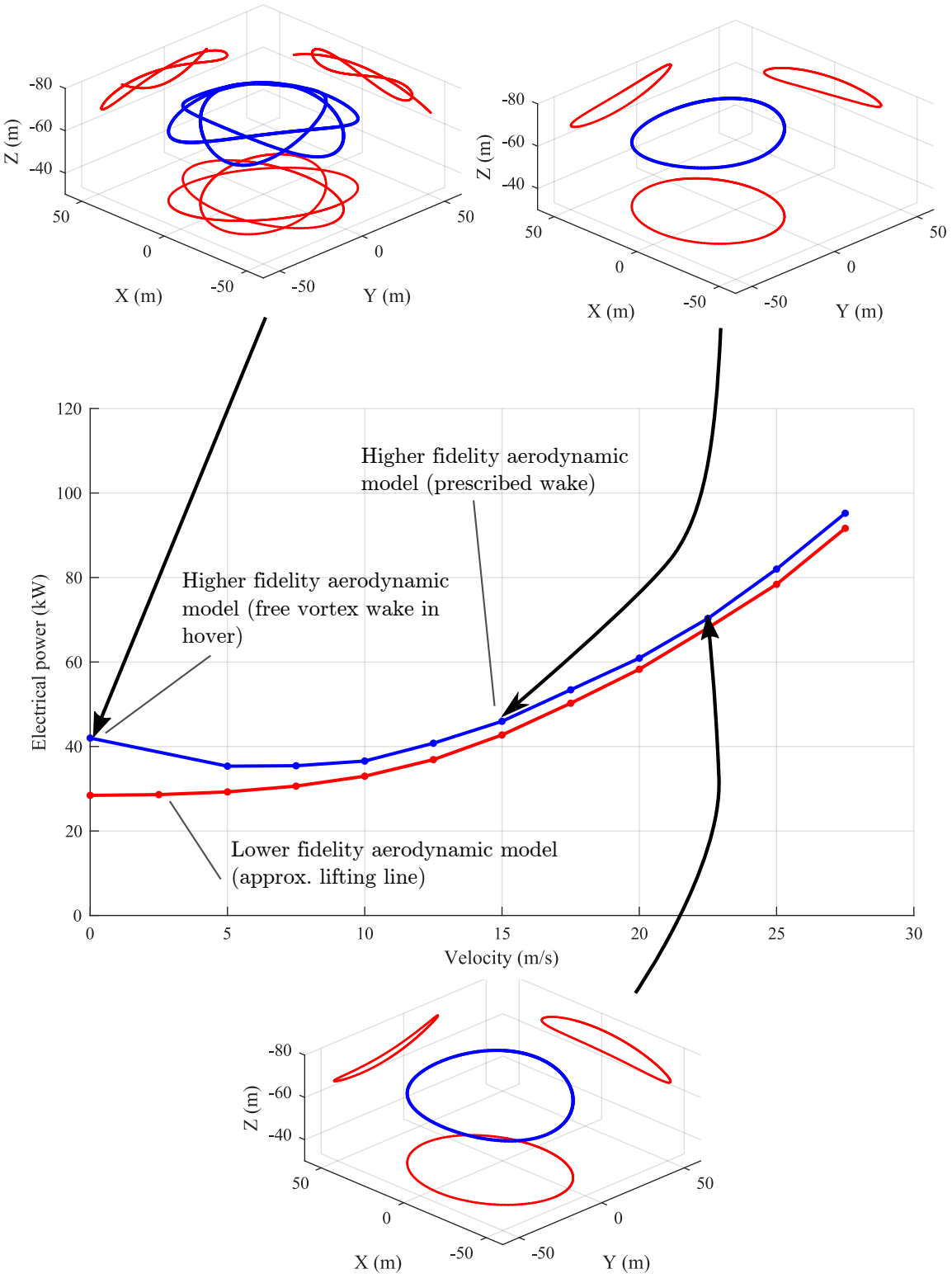

Figure 101: Complete power curve for the EPR^2 VTOL concept during periodic flight path. The optimal flight paths for three velocities are presented.

The results presented in Section 5.5 can be used to review the research questions initially presented in Section 3.2. The first (overarching research question) was:

Research Question 1

How can the flexibility in the tethered aircraft flight path of the EPR^2 VTOL Concept be used to minimize the power required to fly throughout the flight envelope?

The optimization results show that the "rotor" system of the EPR^2 VTOL Concept reconfigures itself as a function of the flight condition to minimize the power requirement. The optimal flight path varies as a function of the system flight speed, fuselage mass, and air density (altitude) for a fixed tethered aircraft design. This research question was then separated into two research questions about the optimal flight path for the hover phase and with positive system flight speed.

Research Question 2

What is the most efficient flight path for each aircraft of the *Electric-Powered Reconfigurable Rotor* VTOL Concept to minimize the power required to fly in hover?

The hypothesis for Research Question 2 is presented hereafter.

Hypothesis to RQ 2

A non-circular and periodic flight path with a continuous phase offset can reduce

the induced power and therefore the power required to hover assuming the dynamic behavior of the tether and the aircraft do not increase significantly the losses.

The test case used for most of this work was based on the flight path optimization of three Makani's *Wing 7* with 75 m long tether at ground level. In Section 5.4.3, it was demonstrated that for this system, a non-circular flight path can reduce the power requirement by approximately 10% compared to an optimal circular flight path. In details, each aircraft should follow its own elliptical flight path offset by 120° each. It was also demonstrated using the lower fidelity environment that if each aircraft is separated by 120° *along* their respective flight path, the peak power requirement can be reduced by more than 25%.

The main reason to explain this reduction in power requirement with a non-conventional flight path is the reduction in wake interaction between the aircraft. When the vertical induced velocity is lower, the lift vector is "closer to perpendicular" to the flight path, and therefore reduces the induced power. The benefits for the reduction in induced power overcome the increase in tether drag due to the higher flight speed, the increase in drag from the aileron, and the increase lift requirement during the sharp turn. Therefore, this hypothesis is validated.

However, it should be noted that for non-circular flight paths in hover, the tether tension varies with time, such as the bank angle. The complexity of the control system will definitely increase, and the penalty of an error in position has not been considered. Also, this study has shown the presence of adverse yaw, both for circular and non-circular flight path. Adverse yaw is usually compensated with rudder deflection, which in return, increases drag. This contributor to drag has not been considered in this work.

The forward flight phase (or hover with the presence of wind) is different since

the wake is convected away from the tethered aircraft. Research Question 3 focuses on this flight phase.

Research Question 3

In forward flight, what flight path should be used to minimize the impact of the forward velocity on the tethered aircraft (advancing and retreating side), and thus, improve the efficiency?

The hypothesis for Research Question 3 is presented hereafter.

Hypothesis to RQ 3

A non-circular flight path with a non-center payload with load transfer between the tethered aircraft will mitigate the consequences of the reduction of the relative airspeed on the retreating side, and therefore reduce the power requirement compared to a conventional circular flight path.

The highly flexible flight path of the EPR^2 "rotor" system has demonstrated a power reduction of 40% in forward flight, compared to a conventional circular flight path. The baseline flight path is assumed to be a circular flight path with constant UAV flight speed with respect to the fuselage, optimized to meet the non-stall requirement. The resulting baseline configuration shows a very high relative airspeed on the advancing side which increases tether losses and the aircraft parasitic drag. A fast mean airspeed is required to avoid stall on the retreating side since the tension in the three tethers is approximately the same.

The optimized flight path to minimize the power requirement in forward flight is an almost circular flight path with a strong left tilt of the hub plane. This tilt transfers

most of the lift requirement on the aircraft located on the advancing side, while it unloads the aircraft on the retreating side. The aircraft stall is also mitigated with a variation of ±40% of the mean velocity at each revolution. Such a rapid maneuver can only be performed if the aircraft mass is small, and electric propulsion is used.

The presence of wake interaction has been shown to be less important in forward flight, which simplifies the wake calculation. However, as for the hover cases, the presence of adverse yaw due to aileron deflection should not be neglected since it increases drag.

In summary, Hypothesis 3 is also validated. In order to truly show the benefits of the EPR^2 VTOL Concept compared to the conventional helicopter, Section 5.6 presents the conceptual sizing of an efficient, long endurance VTOL system based on Makani's *Wing 7* aircraft.

5.6 Conceptual Sizing of an Efficient, Long-Endurance VTOL System Using Makani's Wing 7 *aircraft*

The need for an efficient VTOL concept has been highlighted early in this dissertation. In some applications, such as construction or for observation, a low power consumption is required in hover or near hover. Small helicopters such as the Robinson R22, have a maximum takeoff weight around 1,370 lbs (635 kg), with an empty weight of about 800 lbs (390 kg). With a full fuel tank of 75 liters, the actual payload capacity is reduced to approximately 450 lbs. For this vehicle, the maximum endurance is in the order three hours. The objective of this section is to evaluate the payload capacity of the EPR^2 VTOL Concept using three Makani's *Wing 7* aircraft and its endurance with a focus for the hover phase and compare it to conventional helicopters.

The maximization of the endurance of a VTOL concept is also the objective of the newly announced *Sikorsky Hover Challenge*, for which a VTOL concept must be designed with the following characteristics:

- Hover for 24 hours
- Carry 80 kg payload
- Unoccupied

One objective of this section is to demonstrate that a tethered aircraft concept could fulfill the requirements. However, no tethered aircraft design is performed; the optimal performance using the Makani's *Wing 7* are demonstrated. The remainder of this section goes as follow. First, a study on the impact of fuselage weight on power requirement is presented. Then, a conceptual sizing of an electric power pack and the main structure is performed. Finally, the performance prediction in hover (or near hover) is detailed, with an estimate of the maximum hover time.

5.6.1 Influence of Payload Mass on Power Requirement

The flight path of the tethered aircraft has been optimized to minimize the power requirement in near hover (5 m/s) for a fuselage mass varying between 200 kg and 1200 kg. To reduce the computational time, the lower fidelity environment was used for the optimization. Since it was shown in Figure 88 that the power discrepancy between the lower fidelity and higher fidelity environments is approximately 30%, the power predictions were augmented by the same percentage. Figure 102 presents the electrical power requirement using the lower fidelity environment, augmented by 30%, and Figure 103 shows the evolution of the normalized flight path variables as a function of the fuselage weight. The ranges of the design variables for the optimization are presented in Table 11.

The maximum power, loads and electric current that each *Wing 7* aircraft and tether are designed are achieved with a mean electrical power of approximately 30 kW each, for 90 kW total. According to the optimization, the maximum fuselage that can be lifted with three aircraft along the optimal flight path is 1650 kg. For a fuselage

Table 11: Ranges of the design variables for the study on the influence of fuselage weight

Parameters	**Lower bounds**	**Upper bounds**
a	0.15	0.7
b	0.15	0.7
V_m (m/s)	10	40
V_{a1} (rad)	-0.2	0.2
V_{b1} (rad)	-0.6	0.1
θ_S (rad)	-0.20	0.20
ϕ_S (rad)	-0.20	0.20

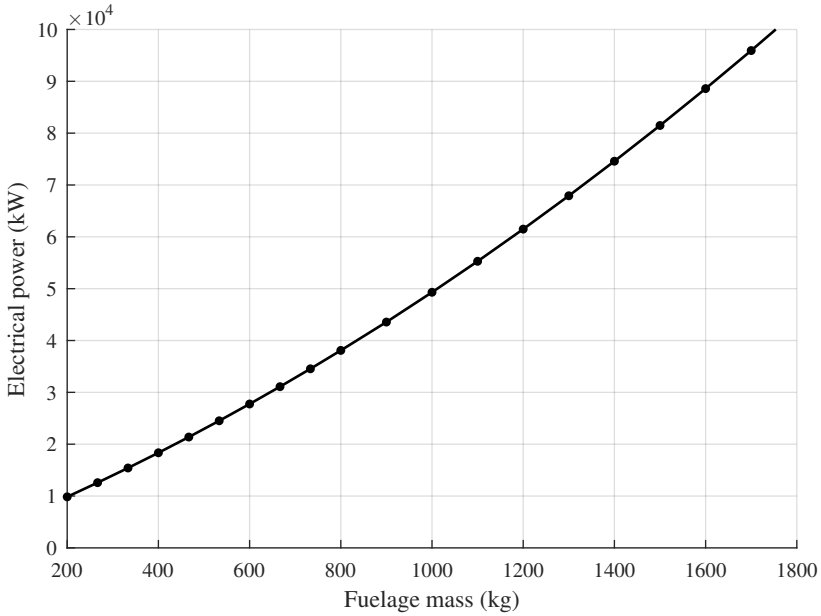

Figure 102: Mean electrical power requirement as a function of fuselage mass for $V = 5$ m/s at ground level.

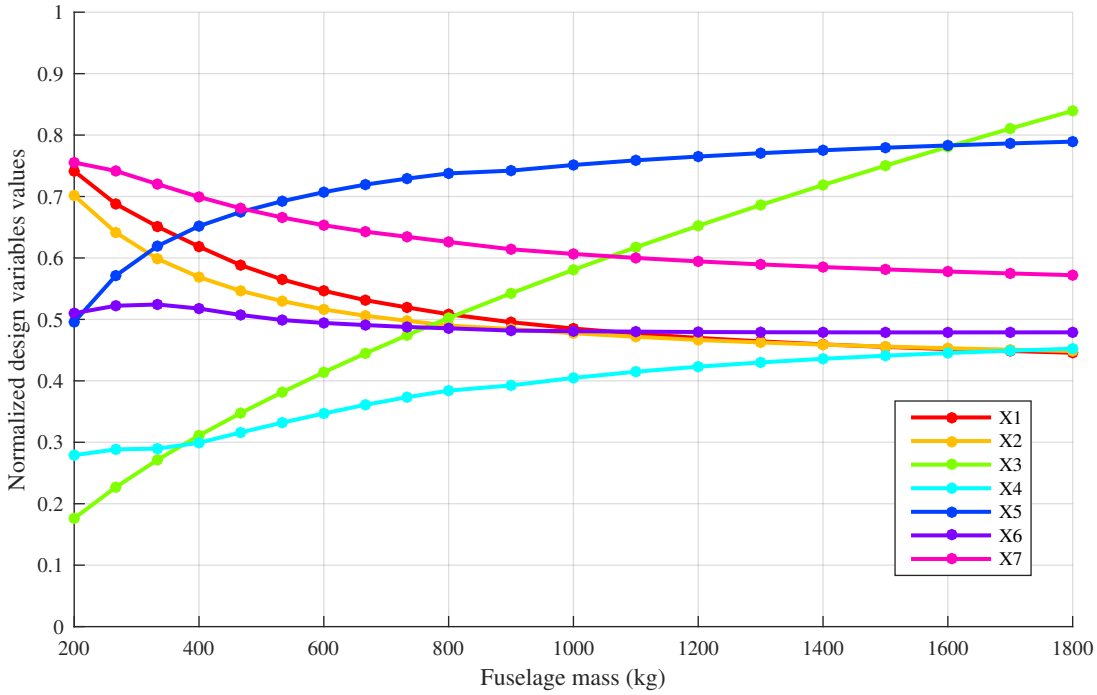

Figure 103: Optimal flight path parameters (normalized) as a function of fuselage mass. The reader should refer to Table 11 for the lower and upper bounds. A reduction in fuselage mass increases the flight path radius and reduces the flight speed of the UAVs. A variation in the sine terms of the Fourier series of the UAV speed is also observed. Most other design variables stays at their nominal values.

mass of 200 kg, the total power requirement is reduced to as low as 10 kW. Recall that the combined mass of the three aircraft and tethers is only 185 kg.

The rotor system adapts to the flight condition to reduce the power requirement. As shown in Figure 103, the aircraft flight path increases in mean radius with a reduction in fuselage mass. The flight speed of the tethered UAV also reduces drastically to maintain the aircraft in their optimal flight conditions. Such a wide range of flight conditions can only be efficiently achieved with electric propulsion. The next section presents a conceptual sizing of the fuselage and electric power production unit.

5.6.2 Conceptual Sizing of the Fuselage with an Electric Power Pack

High-efficiency electric range extenders for general aviation aircraft is a rich field of research, both in academia and in the industry. Recent discussions with a Canadian-based propulsion company, Ceragy Engines Inc, and a propulsion research laboratory, CAMUS, at the Université de Sherbrooke confirmed that high-efficiency turboelectric generators can have efficiencies between 35-40% for a conservative power density of 1 kWe/kg. Based on those numbers, the electric power generation unit could weigh on the order of 90 kg. To be on the conservative side, the efficiency will be assumed to be only 30%. The power generator efficiency is however expected to reduce at part load, which has not been taken into account in the present work.

To reduce the strong variation in power requirement, and increase the reliability, a battery pack that allows hovering capability for a few minutes at maximum gross weight, without the turboelectric generator, is added. Based on current estimates of the power density of lithium batteries (150 Wh/kg), the battery mass would be on the order of 50 kg. Finally, the main structure to hold the power pack, the sensors and electronics, the empty fuel tank, and the "hook" to attach the payload is estimated to have a mass of 75 kg. (Recall that the main structure does not have to sustain any strong torsional or bending loads as a conventional helicopter.

With those numbers, the empty weight of the whole system is only 400 kg (including 185 kg for the three aircraft and tethers, 215 kg for empty fuselage weight), or just slightly higher than a Robinson R-22 helicopter. The total useful load is then 1435 kg. The empty-to-gross weight ratio could then be as low as 400/1835 = 22%! Moreover, the fuel burn in hover at 90 kW could be as low as 35 liters per hour using Jet-A. (As a comparison, the fuel burn of the R22 is in the order of 32 liters per hour, and it can only carry two people).

It is acknowledged that these performance predictions are based solely on the conceptual sizing of the fuselage, and that a more detailed design is required. However, since the UAVs and tethers were actually flown, their total mass (185 kg for the three aircraft) is considered exact. By using those numbers, the estimated endurance is presented in the next section.

5.6.3 Endurance Calculation

For the calculation of the endurance, the variation in aircraft weight is assumed to only come from fuel burn. The variation in the total aircraft weight is evaluated using Equation 156,

$$W(t) = \underbrace{[W_E + W_P + W_{F,TO}]}_{\text{Total weight w/o the UAVs}} - W_F(t) \tag{156}$$

$$= [W_E + W_P + W_{F,TO}] - W_F(P_E(W(t))) \tag{157}$$

where W_E is the empty weight of the fuselage only, W_P is the payload weight, $W_{F,TO}$ is the fuel weight on takeoff, and $W(t)$ is the weight of everything attached underneath the tethers (the total fuselage weight). Since there is a dependency of the fuel flow on the system weight, a time-marching method is used to solve the equation. Figure 104 presents the evolution of the fuel weight over time.

The first very surprising observation is the possibility to almost hover (5 m/s) in excess of 150 hours, which is many times higher than the most efficient helicopter

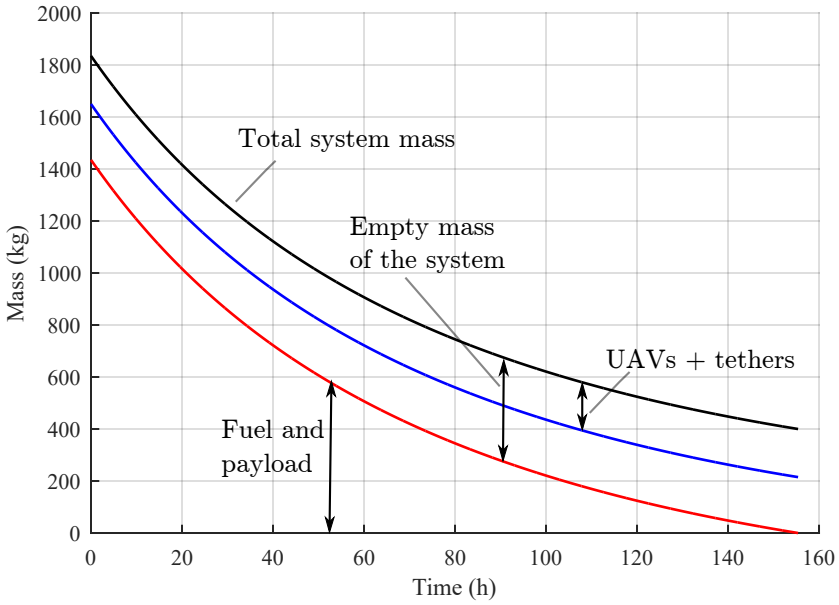

Figure 104: Variation of system weight as a function of time. At $t = 0$, the takeoff gross weight is 1835 kg, including 1435 kg of fuel and payload. The 400 kg left is the aircraft mass, tether mass, empty fuselage mass.

available today. The main reason is the extremely low empty weight fraction, slightly under 25%. This low number is the result of the novel architecture, that avoids heavy helicopter hub (high torque), complex transmission systems, tail rotor, and other heavy mechanical components. Also, the reconfigurable rotor minimizes the power requirement given a total aircraft weight. Not to mention that the mechanical design of those UAVs and tethers are adapted for months of airtime without maintenance.

The fuel flow is the highest at $t = 0$ with 35 liters per hours. As the fuel depletes, the fuel burn reduces to only 4 liters per hour for an electrical power requirement of 10.4 kW. Recall that the optimal flight path for a fuselage mass of 215 kg (400 kg with the UAVs) has a mean aircraft velocity of 15.4 m/s. Since the optimization does not consider the effect of gusts, very low flight speeds are possible when the system becomes lightweight.

The proposed concept could therefore easily meet the AHS requirements for 24

hour hover time with 80 kg payload. The author of this work is confident that much smaller UAVs, in the order of 3 m span could also meet the requirements. Future development is required to validate this hypothesis. In any case, it can be concluded that the EPR^2 VTOL Concept has the potential to be a very efficient helicopter in hover or at low flight speed. Faster flight speed can be met with another flight configuration, such as with the three UAVs flying in formation.

CHAPTER VI

CONCLUSION

Helicopters have shown great benefits to our society by allowing short flights between unprepared terrain or short runways. Although helicopters have seen a continuous improvement in performance over the last decades, they still fall short of fixed-wing aircraft in terms of fuel burn. Their limited range is the consequence of the low equivalent lift-to-drag ratio (L/D) in cruise and high empty weight fraction. Also, given the large number of moving parts and the higher level of vibration, helicopters incur a higher maintenance cost.

Advanced concepts have been proposed over the last few decades to improve the performance of VTOL concepts. Most of the novel architectures are based on fixed-wing aircraft augmented with VTOL capability (ie, V-22) or conventional rotorcraft with slight modifications, such as coaxial designs. In both cases, the objective is to maximize the cruise speed, while retaining the VTOL capability. None of those designs aim at reducing the power requirement in hover or at slow speed, while the need for such aircraft has been shown for construction work, heavy cargo transport (both military or civilian) or even as observation platforms.

A novel helicopter concept was proposed by Rancourt (the author of this dissertation) and Demers Bouchard based on electric-powered tethered aircraft. An electric power generation unit (batteries and turboelectric generator) are located in the fuselage and produces power for the three (or more) unmanned fixed-wing aircraft. Previous studies on tethered aircraft by other authors focused on the used of manned aircraft, with limited modeling fidelity. Moreover, since only manned aircraft were considered, simple flight paths were studied without consideration for complex wake

interaction. The literature review showed that there was a clear lack of an efficient method and models to answer the overarching research question: *How can the flexibility in the tethered aircraft flight path of the EPR^2 VTOL Concept be used to minimize the power required to fly throughout the flight envelope?*. This research question led to the main research objective, which can be summarized as the development of the tools and methods to analyze and optimize the flight path of the tethered aircraft for a design space exploration. The power curve for a VTOL concept is the first step to assess the performance of the system, prior to getting into complex control system optimization or maneuverability calculation.

The analysis and optimization of electric-powered tethered UAV was shown to be highly multidisciplinary. The optimal flight path depends on numerous factors, such as the air density, the fuselage mass, maximum wing lift coefficient, wind velocity, and others. The need to capture the coupling between the disciplines in the developed method was shown to be crucial. The salient scientific contributions presented in this thesis are listed below:

1. Development of a multifidelity, multidisciplinary method for the flight path optimization of electric-powered tethered aircraft for the EPR^2 VTOL concept – The multifidelity method detailed in this work is based on a prescribed flight path obtained from a minimal set of parameters $\boldsymbol{P}$. This approach removes any feedback loop in the higher fidelity environment, and is therefore, ideal for a design space exploration. The lower fidelity environment was used to explore the design space and perform direct optimization of the flight path parameters under specific flight conditions. Due to the computational cost, the higher fidelity model was used to quantify the discrepancy between the two approaches, in particular in relation to the aerodynamics modeling.

Both the lower fidelity and higher fidelity models were used to optimize the periodic flight path of the tethered aircraft from hover to approximately 30 m/s. The test case used in this work uses the Makani's *Wing 7*, initially developed for wind energy harvesting. It was shown that for an 800 kg fuselage mass, the power requirement is as low as 42 kWe. At 20 m/s, the power requirement increases to 62 kWe and reaches 95 kWe at 27.5 m/s. The absolute maximum takeoff weight of the whole system was estimated at 1,815 kg, with an estimated total empty weight of only 400 kg. This leads to an impressive empty weight ratio of 22%. The maximum hovering time could be as high as 150 hours (no payload), or 24 hours with a 900 kg payload mass.

2. Development of a rigid tether model with reduced computational cost – Simulations of tethered aircraft to lift payloads have exclusively been studied using dynamic tether models. Since three aircraft are tethered to the fuselage, the number of states that must be tracked grows rapidly, such is the case for the computational time. As an alternative for the design space exploration phase, a kinematic model was developed to evaluate the approximate tether forces. This model uses the same aerodynamic modeling method than the higher fidelity dynamic model, except that it assumes that the tethers are rigid. By using three aircraft, the system of equations is consistent (21 equations, 21 unknowns) and large timesteps are possible. The computational time was shown to be on the order of seconds, compared to ≈ 20 minutes for the complete dynamic problem.

The lower fidelity model was shown to be as accurate as the higher fidelity model *if* the tethered aircraft flight paths are compensated for tether elasticity. Since the control system will likely be driven by tether tension, not a vertical position, it is assumed that the payload should remain approximately stationary. After calibration, the tether tension for both methods was equivalent within sufficient accuracy since the ratio of the tether mass to the payload mass is almost negligible.

3. Improvement of the calculation of the aerodynamic forces on tether segments – An improvement on the location to calculate the velocity on the tether segment allowed a significant reduction in the number of tether segments for the same accuracy. An analytical approach was used to demonstrate the benefits of this method versus the standard approach presented in the recent literature.

4. Development of a wake consolidation model for application to fixed-wing aircraft aerodynamics – The higher fidelity aerodynamic model developed in this work bridges the gap between conventional helicopter aerodynamic methods, and fixed-wing aircraft methods. It considers both the wake interaction with a free-vortex wake implementation and the effect of control deflection on the loads and wake.

The main contribution in this model relates to the consolidation model and the induced velocity calculation by the consolidated vortices. The analytical method developed by Donaldson (which was based on Betz's roll-up vortex formulation) is augmented with the Vatistas' core model and implemented in the numerical model. The benefits are significant: reduction of the computational time by more than one order of magnitude (reduction in the number of wake control points) and greater wake stability. The latter phenomenon is explained by a reduction in the peak induced velocity by a consolidated vortex since the vortex segment represents the location of the actual vortex, but its circulation is distributed instead of being concentrated. It is acknowledged that such a method is not required for conventional helicopter rotors since the tip vortex is actually more concentrated, and therefore a simple core model is sufficient to properly represent the induced velocity. The effect on fixed-wing aircraft modeling is important since the discrepancy could reach 50% in the peak induced velocity by the aileron trailing vortex.

The prescribed loads, aircraft position, and aircraft attitude are inputs to the

aerodynamic model. At each timestep, the angle of attack and aileron deflection are solved simultaneously with the circulation on the wing. To the author's knowledge, this complete aerodynamic model which captures all the relevant physics required to analyze tethered aircraft is novel and shows potential for future studies.

Recommendations

The development of the tools and methods to analyze the power curve in steady level flight represents a first step to assess the full potential of the EPR^2 VTOL Concept. The next research efforts should focus on the control methods to be used and what is the minimal set of sensors required to monitor the system. As a first hypothesis, the author recommends to investigate a control system based on the aircraft position in the x-y plane but use the tether tension instead of the position in z. The novel simulation environment, with an in-the-loop controller, will require to couple the disciplines with feedback, and the efficiency of multidisciplinary analysis architectures should be investigated. In any cases, the author strongly recommends the development of a small-scale prototypes to validate the aerodynamic modeling.

This work also focused on one flight phase, where the tethered aircraft fly a periodic flight path. At high-speed, it was shown by Demers-Bouchard and Rancourt [44] that it would be more efficient to operate the three aircraft in formation flight. The transition between the periodic flight path and the forward flight mode should be investigated.

APPENDIX A

DEVELOPMENT OF ADVANCED VTOL CONCEPTS

A.1 VTOL Wheel

In order to remove the constraining limitations of helicopters, especially the need to fly faster [81], numerous advanced VTOL concepts were developed since the 1950s. Two approaches are used: to adapt conventional fixed-wing aircraft for vertical takeoff, or enhance the performance of rotary-wing aircraft with additional technology.

The Vertical and/or Short Takeoff Landing (V/STOL) Wheel presented in Figure 105 is a visual representation of all 45 types of V/STOL aircraft that have been built and tested up to 1996 [12] based on the first approach. It was developed by McDonnell Douglas in the 1960s, then updated for the Joint Strike Fighter (JSF) program office.

In order to fully understand the rationale behind the advanced VTOL aircraft concept presented in this thesis proposal, it is valuable to review the different categories of V/STOL concepts developed in the past. It should be noted that the aircraft listed are mainly airplanes that were augmented with VTOL capabilities, and having significant differences compared to helicopters.

As shown in Figure 105, all the concepts can first be divided into four categories, based on the source of power. Most vehicles use the same propulsion system for the hover and forward flight regimes. In order to provide the lifting force in hover, several concepts were developed, such as tilting the propulsors (propellers, ducts, or wing and engine combination). Other configurations include tail sitters, vectored thrust and deflected slipstream. All the concepts using the same propulsion system for hover and forward flight require a significant power input during the hovering phase due to

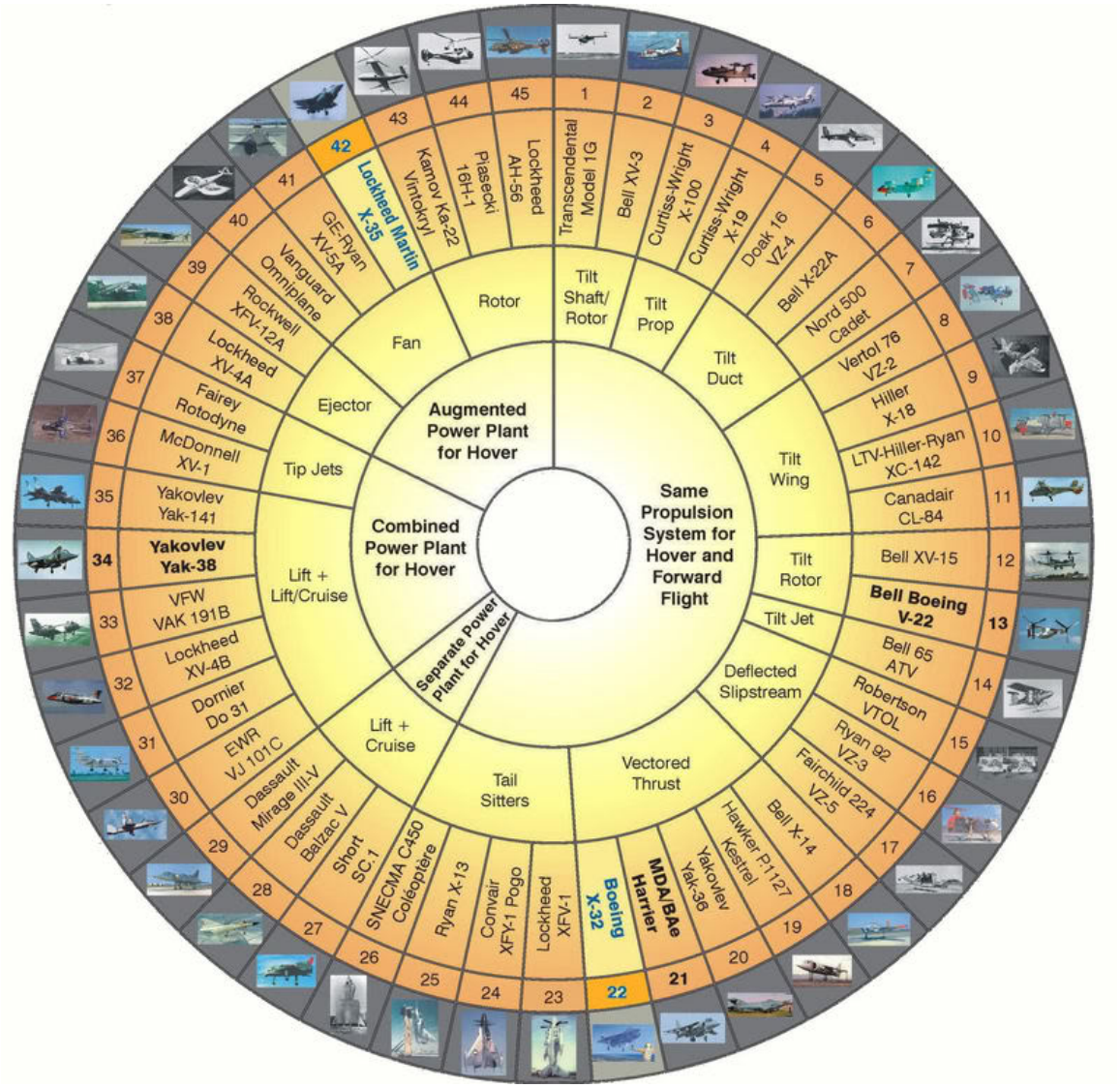

Figure 105: V/STOL Wheel updated for the Joint Strike Fighter (JSF) Program Office. Forty-five V/STOL concepts that flew prior to 1996 are presented and grouped by similarity of the propulsion system [12]

the low efficiency associated with high propeller disk loading. Also, the mechanical complexity associated with the rotation of the engines or the entire wing reduces the lifting capability of the vehicle due to the increase in empty weight. As an example, the empty-to-gross weight ratio of conventional transport helicopters ranges from 0.45 to 0.55; the empty weight fraction of tilt rotor helicopters is between 0.55 and 0.7 [133].

An alternative approach to generate thrust more effectively in hover is to augment the power plant for this specific flight phase, using either an ejector, a fan or an additional rotor. The well known Lockheed Martin F-35 (depicted X-35 in the V/STOL wheel) uses an additional fan to increase the thrust in hover for a given power available by increasing the mass flow. Despite the attempt of these concepts to reduce the power required in hover while maintaining the high forward speed of airplanes, a weight penalty must be considered for the additional components.

To augment the thrust requirement in the hover phase, a few VTOL concepts have more than one power sources, which are all used during hover. During cruise, only the main engine is operational. The Yak-38 is an example with a total of three engines.

Finally, only a few aircraft concepts were designed with dual propulsion systems, one only in use during the hover phase while a secondary system is in use for high speed flight. None of those aircraft concepts are flying today [12].

A.2 Novel Helicopter Concepts

Instead of converting fixed-wing aircraft for VTOL operation, advanced helicopter concepts were also proposed over the years. The Eurocopter X3, a high-speed compound helicopter, reached a flight speed above 250 kts in 2013 in straight and level

Figure 106: Sikorsky S-97 RAIDER. The coaxial configuration with load transfer on the advancing blade and a multibladed pusher propeller configuration allows for flight speeds on the order of 250 kts, but the fuel burn remains very high.

flight[1]. The Sikorsky X2 also broke the 250 kts barrier in 2010 with a coaxial rotor and pusher propeller concept[2]. Another derivative of the Sikorsky X2, the S-97 RAIDER[3] shown in Figure 106, is designed for a cruise speed approaching 250 kts and a climb rate of approximately 5,000 ft/min. In those cases, the cruise performance is significantly greater than conventional helicopters, but the power required for a payload weight is not reduced and therefore the payload capacity is not increased.

A.3 Novel VTOL Cargo Transport Concepts

In 2010, DARPA launched a program named *Transformer* to design an unmanned VTOL vehicle capable of lifting military payloads [3]. The desire to combine the capabilities of a ground vehicle and a VTOL aircraft motivated the design of the AT Black Knight Transformer, the world's first roadable VTOL aircraft. This vehicle uses

[1]http://www.lemonde.fr/sciences/article/2013/06/10/le-x3-un-helico-a-472-km-h_3427392_1650684.html, accessed 13 April 2015

[2]http://raider.sikorsky.com/x2-basics.asp, accessed 13 April 2015

[3]http://raider.sikorsky.com/, accessed 14 Septembre 2016

a set of eight motors attached to a light ground vehicle. Due to the high disk loading of the rotors, a high power is required to hover and the payload capability is also limited. The Aerial Reconfigurable Embedded System (ARES) is an unmanned tilt wing system, capable of lifting various payload types while maintaining the capability for high-speed flight using a tilting ducted fan and wing system [41]. As for the AT Black Knight Transformer, the hover performance is expected to be limited.

In summary, V/STOL aircraft concepts are either based on airplane designs adapted to allow vertical takeoff or on new helicopter concepts. For the first type, efficiency in the vertical flight phase is relatively poor, so the vehicles have limited capability to hover for extended periods of time.

The second type is much more efficient in hover than modified fixed-wing aircraft, but the power required in hover is still equivalent to a conventional helicopter or slightly worse due to the increase in empty weight. Both approaches increase significantly the mechanical complexity of the system, which translates to an increase in acquisition cost.

APPENDIX B

EARLY TETHER MODELING TECHNIQUES

Initial studies on the dynamics of tethers and cables date back to the time of Euler (1707-1783) and Bernoulli (1700-1782) for the specific case where there is no aerodynamic drag. Almost two centuries later, Kolodner [96] studied the nonlinear eigenvalue problem of a heavy string attached to one endpoint (where the rotation is forced) with the other end free. It was shown that above a critical velocity, multiple distinct modes of rotation can exist and that if a given mode is considered, the deflection is a continuous function of speed above the critical speed. As for most studies prior to the 1970s, they considered the tether as a continuum and the work focused on solving second order partial differential equations (PDE).

In 1958, Caughey [26] developed approximate solutions for the nonlinear problem of the forced whirling of a heavy chain, which also neglected the aerodynamic drag. Using the continuous representation of the chain, Caughey demonstrated that above the critical speed for a given mode, two solutions are stable while one is unstable. It is considered to be the first attempt to study the non-linear forced response (with non-zero tow radius). Figure 107 illustrates the problem solved by Caughey.

By the end of the 1960s and in the 1970s, the analysis of the dynamic behavior of tethers towed by aircraft in circular paths was largely funded by the U.S. military [168]. One of the applications was the TACAMO system, based on a modified C-130 aircraft and designated as the EC-130. A very long tether (15,000 ft to 25,000 ft) with a wire diameter on the order of 1/8 inch to 1/4 inch was used as a very low-frequency antenna for long distance communications [32].

Huang [80] was one of the first to develop the steady-state mathematical model to

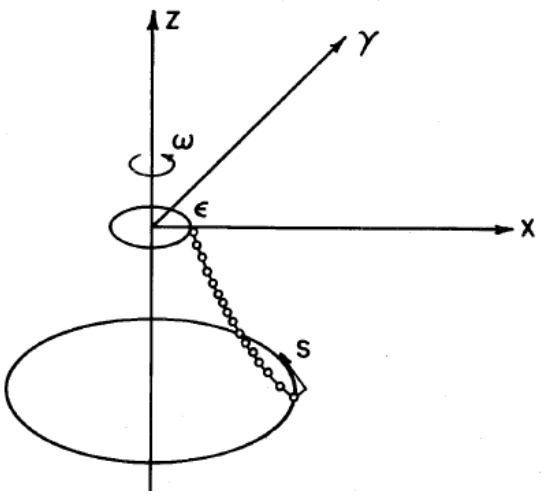

Figure 107: Representation of the model used by Caughey to obtain the stability of a whirling heavy chain [26]

evaluate the spatial configuration and tension distribution along an orbiting towline. The main interest was to maximize the verticality of the tether, as this response plays a significant role in the quality of the communication if the tether is used as an antenna. His model considered the effect of the aerodynamic drag and the tether was modeled as a continuum. It was shown that under specific operating conditions, multiple solutions can exist for the tether shape. Verticality can be improved by varying the towline diameter instead of using a constant cross section.

In the same period, Crist [40] predicted the static shape of a long wire towed from an orbiting aircraft with consideration for the aircraft maneuvers and wind shear such as the TACAMO system. Two cases are discussed. First, the effect of vertical sinusoidal oscillations from the aircraft on the tether during a constant radius turn. Second, the tether dynamics during a deorbit maneuver were analyzed. It was shown that 15 mass points are sufficient to model the tether and that the tension at the drogue can be considerably higher than the equilibrium tension due to dynamic effects.

Skop [146] at the U.S. Naval Research Laboratory examined the circular towing problem for a flexible and inextensible cable to enable pinpoint deliveries of payloads

from fixed-wing aircraft. The cable is modeled as a continuum and solved with a numerical integration scheme with consideration for aerodynamic drag. It was shown that the equilibrium shape can be determined by analyzing the forces at the end of the tether (where a mass can be attached) and then integrating the position up to the aircraft. Multi-valued regions were shown to exist for specific flight parameters.

The steady-state performance of a cable-body system towed in a circular path was studied by Choo [29] for a marine application, funded by the Office of Naval Research. The model assumed a continuous and inextensible tether with hydrodynamic drag. The set of differential equations were solved using a Runge-Kutta numerical integration method. The results showed that single solutions for the tether shape are obtained in water due to the large drag compared to aerial applications.

The whirling of a string has stirred a great interest from mathematicians for the multivalued nature of the boundary value problem. Wu [170] solved the non-linear eigenvalue problem of a heavy string rotating with a constant angular velocity about an axis parallel to the gravitational direction. The cable was also modeled as a continuous medium by differential equations as done in most of the previous studies.

By the end of the 1960s, most of the studies on tether dynamics modeled the string as a continuum using a set of nonlinear partial differential equations (PDE) of second order with one constitutive equation to relate the tension with longitudinal strain. However, due to the limited flexibility of this approach, other methods were developed. A review by Choo in 1973 [30] summarized the approaches to solve for tether-body systems in four categories:

1. *Method of characteristics*: Converts the six quasi-linear PDEs into six ordinary differential equations (ODEs) using a constitutive equation. This method can be used for any kind of unsteady motion of cable-body system. However, the method cannot be used on inextensible and viscoelastic cables, and requires a significant computational effort.

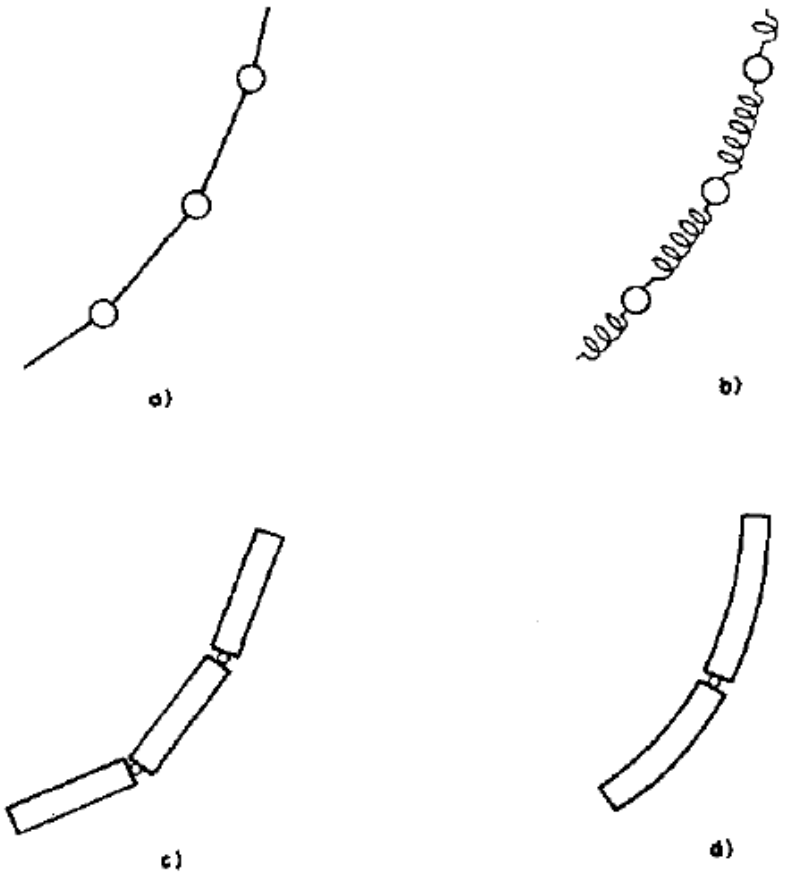

Figure 108: Methods to discretize a tether segment as survey by Choo [30]

2. *Finite element method*: The cable is represented as a series of segments joined at points called nodes. The equations governing the motions of the elements can be derived using Newton's law, Lagrange's equations or Hamilton's principle. This method can be used to study any kind of unsteady motion of a tether, and can have elements of varying properties. Figure 108 shows the four methods to discretize a tether to apply a finite element method.

3. *Linearized method*: The linearization of the governing equations is often used to study the stability and frequency response. The motion is assumed to be small about an equilibrium state.

4. *Equivalent lumped mass method*: The ODEs are solved for the rigid motion of the body only if the body motion is of interest. Effects of the tether are shown

as restoring, damping, and inertial forces on the body.

Due to the improvement in the computational power and flexibility of the method, the Equivalent lumped mass method is used in this work.

APPENDIX C

VALIDATION AND VERIFICATION CASES OF THE INDIVIDUAL MODELS

C.1 Flight Path Parameterization

In order to verify the parametrization method and its numerical implementation, a set of test cases is analyzed. Table 12 summarizes the setting of the parameters for each test case.

The second and third parameters (a and b) define the normalized ellipse shape. The parameters that specify the variation in speed of the UAVs with respect to the payload reference position are V_{a1} and V_{b1} for the first order Fourier series term normalized by the mean speed V_m. The parameters for varying the altitude as a ratio of the baseline tether length are Δh_{a2} and Δh_{a2}, the second order term in the Fourier series. Finally, the angular velocity of the hub reference frame about $\vec{k}_S$ is denoted $\dot{\psi}_S$.

C.1.1 Case 1: Baseline Circular Flight Path

The first case consists of the analysis of a circular flight path at a constant altitude, and constant speed, with a tether length of 40 m and a circle radius of 50% of the tether length, 20 m. First, Figure 109 shows the flight path in the system-carried frame (black curve) with its projections (red curves). The local velocity vectors are depicted with the red vectors and the local acceleration vectors are depicted with blue vectors.

From a qualitative perspective, the flight path remains in the X-Y plane at a height of 34.64 m above the payload reference point (in the negative direction since

Table 12: Parameter values for the test cases

Parameters	**1**	**2**	**3**	**4**	**5**	**6**
l_t (m)	40	40	40	40	40	40
a	0.5	0.3	0.5	0.5	0.5	0.3
b	0.5	0.55	0.5	0.5	0.5	0.55
V_m (m/s)	20	20	20	15	20	20
V_{a1}	0	0	0	0	0	0
V_{b1}	0	0	0	0.2	0	0
θ_S (rad)	0	0	0	0	0	0
ϕ_S (rad)	0	0	0	0	20	0
$\dot{\psi}_S$ (rad/s)	0	0	0	0	0	0.18
Δh_{a2}	0	0	0.1	0	0	0
Δh_{b2}	0	0	0	0	0	0

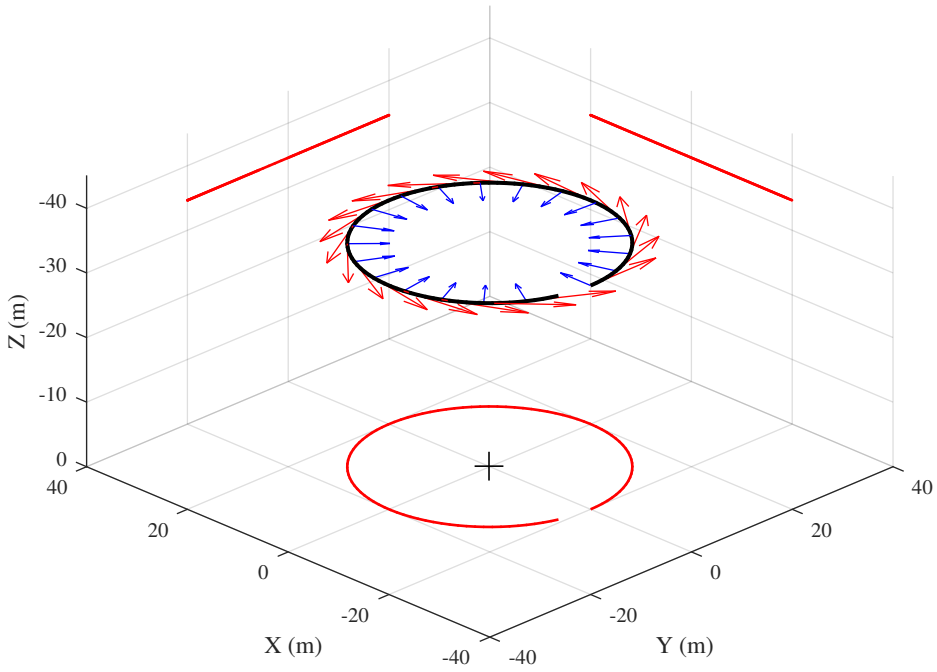

Figure 109: Verification of the parameterization: Test Case 1. The periodic flight path is shown with a black curve and its projections are shown with the red curves. The local velocity vectors are depicted with red vectors and the local acceleration vectors are depicted with blue vectors.

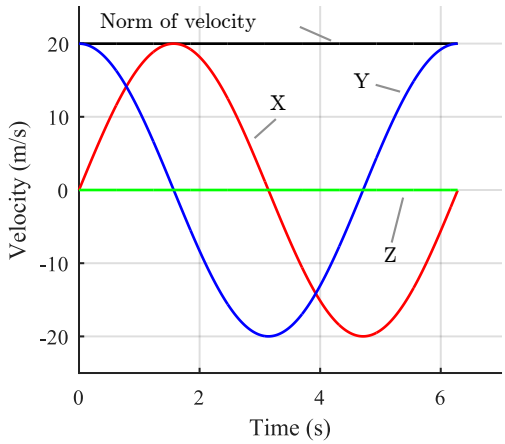

Figure 110: Velocity components as a function of time: Test Case 1.

$\vec{k}_S$ points downward), so that tether length remains 40 m.

Figure 110 shows the three components of velocity in red ($\dot{x}_4$), in blue ($\dot{y}_4$), and in green ($\dot{z}_4$). The total velocity along the flight path is depicted by the solid black line, at 20 m/s as prescribed by V_m.

Finally, Figure 111 illustrates the acceleration components. First, Figure 111a shows the acceleration components and the total acceleration while Figure 111b shows the tangential and normal acceleration components.

As expected, only the normal acceleration component is non-zero, at a constant value of 20 m/s^2 as calculated with Eq. 158 for the special case of no change in the magnitude of the velocity,

$$\left|\boldsymbol{a}_{P/S}\right| = \frac{V_m^2}{\rho} \tag{158}$$

where ρ is the local curvature of the flight path.

C.1.2 Case 2: Elliptical Flight Path

Case 2 is used to demonstrate the effect of changing the flight path from a circle to an ellipse, and then "adjusting" the height so that the flight path would lie on a sphere defined by the tether length. The only differences with Test Case 1 are the values of ellipse parameters, where $a = 0.3$ and $b = 0.55$. Figure 112 illustrates the flight path

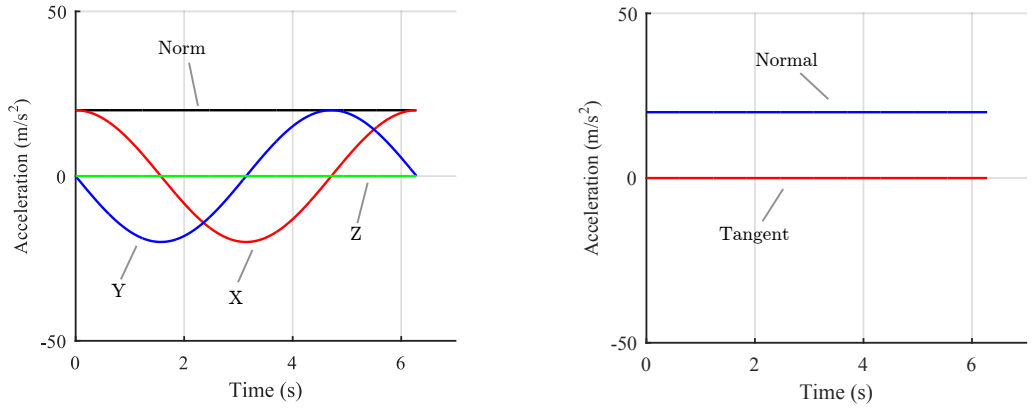

(a) Acceleration components along $\vec{i}_S$ (red), $\vec{j}_S$ (blue), and $\vec{k}_S$ (green)

(b) Acceleration components along $\vec{e}_N$ (blue), and $\vec{e}_T$ (red)

Figure 111: Acceleration components as a function of time: Test Case 1. Components are shown in the Cartesian coordinate system and in the path coordinate system.

and its projections, with the local acceleration (blue) and velocity (red) vectors.

First, the curvature of the flight path can be observed on the two of the three projections. Such a shape results from the desire of maintaining a constant distance with respect to O_H. Figure 113 shows the variation in the velocity components. Although the speed is constant along the flight path (black curve), strong variations are observed in the three components, including along $\vec{k}_S$, which is again the result of the projection of a non-circular flight path on a sphere. As expected, the velocity components in two directions out of three go to zero four times per period, when $x = 0$ or when $y = 0$.

Figure 114 illustrates the effect on the acceleration components of having a non-circular flight path at a constant flight speed. First, since there is no tangential acceleration, the normal acceleration is equal to the norm of the acceleration depicted by the black line in Figure 114a. The acceleration is maximum during tight turn radii, at $x = 0$.

For an ellipse defined by normalized ellipse parameters a and b, the curvature in

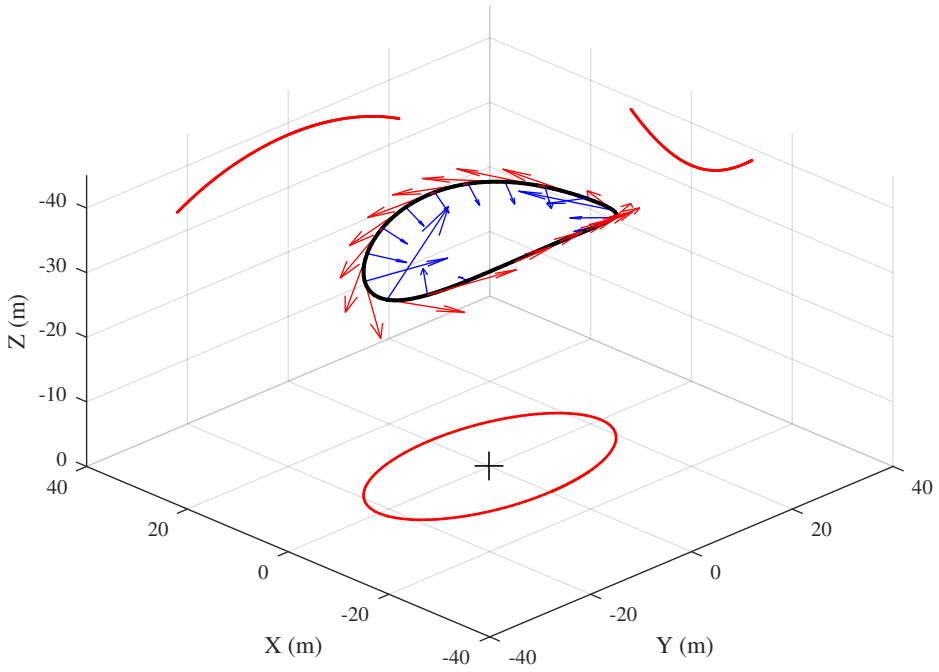

Figure 112: Verification of the parameterization: Test Case 2. The periodic flight path is shown with a black curve and its projections are shown with the red curves. The local velocity vectors are depicted with red vectors and the local acceleration vectors are depicted with blue vectors.

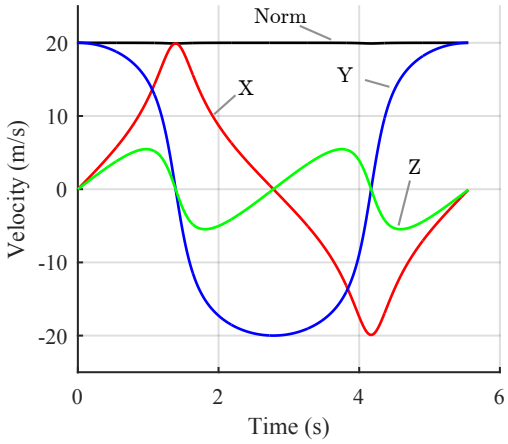

Figure 113: Velocity components as a function of time: Test Case 2

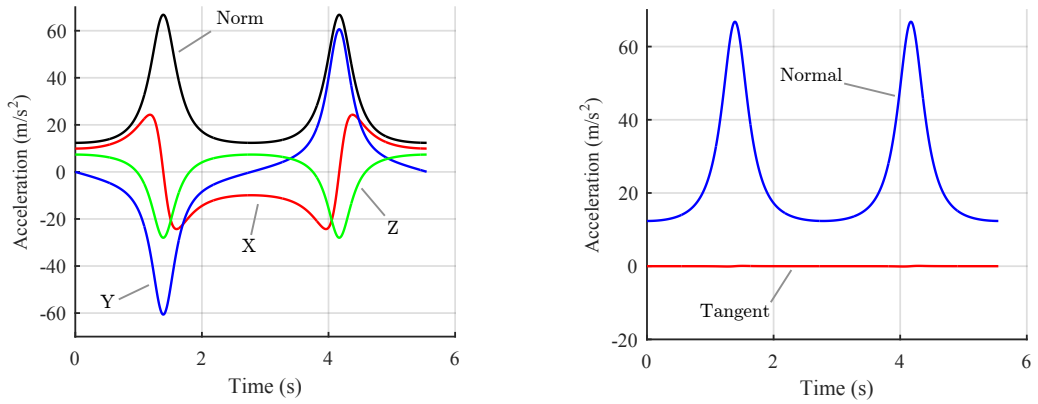

(a) Acceleration components along $\vec{i}_S$ (red), $\vec{j}_S$ (blue), and $\vec{k}_S$ (green)

(b) Acceleration components along $\vec{e}_N$ (blue), and $\vec{e}_T$ (red)

Figure 114: Acceleration components as a function of time: Test Case 2. Components are shown in the Cartesian coordinate system and in the path coordinate system

the X-Y plane is equal to:

$$\rho = t_l \cdot a^2/b \quad \text{at } x = 0 \tag{159}$$

$$\rho = t_l \cdot b^2/a \quad \text{at } y = 0 \tag{160}$$

On Figure 114a, the norm of the maximum acceleration along $\vec{j}_S$ is equal to 61 m/s^2 at $x = 0$, which fits the theory for a velocity of 20 m/s. The norm of the acceleration along $\vec{i}_S$ at $t = 0$ is 10 m/s^2, which also matches the theory. It must be noted that at those points, the acceleration along $\vec{k}_S$ is not zero due to the variation in height, and analytical solutions that include this parameter can quickly become complex. Also, as expected, the acceleration along the flight path remains zero and the normal acceleration varies between 12 m/s^2 and 68 m/s^2.

C.1.3 Case 3: Variation in Height

Case 3 is used to validate that the effect of a variation in height (variation in the distance between the tethered aircraft and O_S) performs as expected using a circular flight path. A maximum variation of the tether length of 10% is used, with only second order terms in the Fourier series ($\Delta h_{a2} = 0.1, \Delta h_{b2} = 0$).

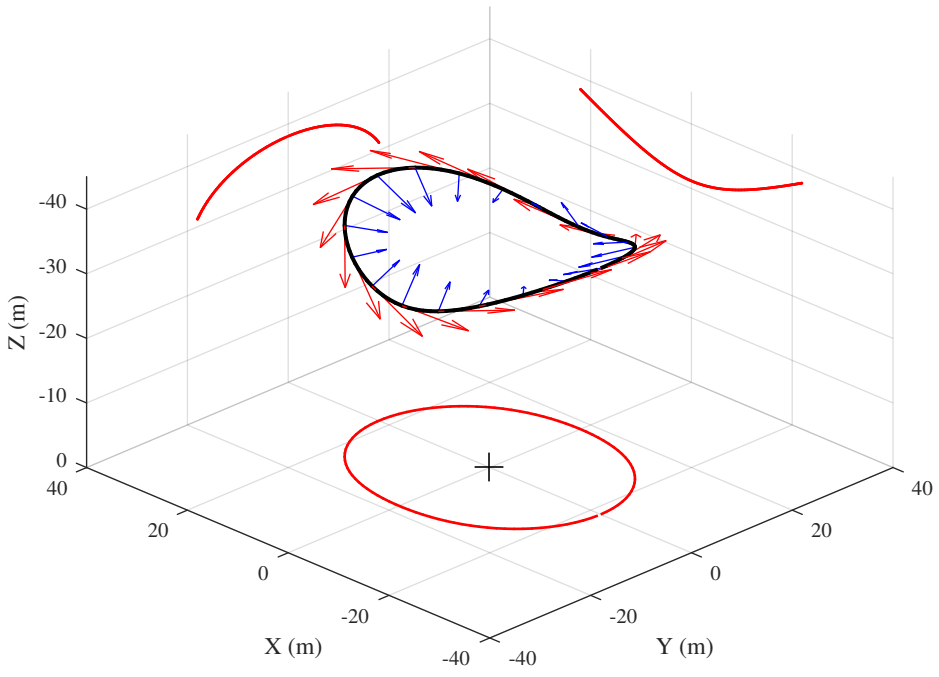

Figure 115: Verification of the parameterization: Test Case 3. The periodic flight path is shown with a black curve and its projections are shown with the red curves. The local velocity vectors are depicted with red vectors and the local acceleration vectors are depicted with blue vectors.

Figure 115 shows the flight path with a variation of the distance between the origin of the reference frame and the tether tip by $\pm 10\%$.The first observation is that the projection of the flight path on the X-Y plane is no longer circular. The increase in tether length transforms the circle into an oval, as detailed in the transformation in Eq. 30. Compared to Test Case 2, the curvature is the direct result of the increase distance between the origin of the reference frame and the tether tip, not from the projection of a non-circular flight path on a sphere. Figure 116 highlights the very unusual flight velocity components as a function of time.

For a circular flight path at a constant velocity, it is expected that the velocity along $\vec{j}_S$ be exactly of the shape of a cosine, and the velocity along $\vec{i}_S$ be of the shape of a sine. In the present case, a variation in the distance between the origin and the

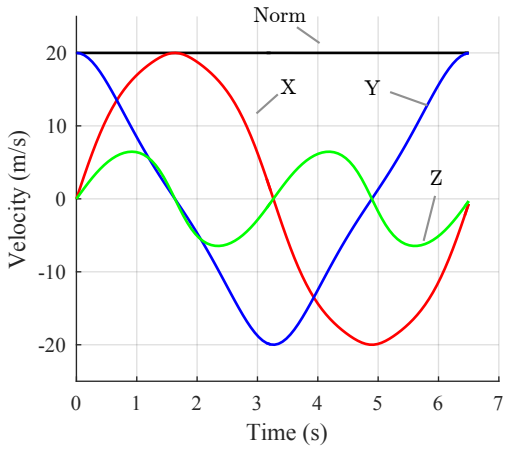

Figure 116: Velocity components as a function of time: Test Case 3.

tether tip affects those values, since the transformation shown in Equation 32 ensures that the norm of the velocity remains constant (if $V_{a1} = V_{b1} = 0$). The variation in height does affect the total path length in a non-uniform pattern and slightly changes the shape of the projected flight path. Therefore, the velocity along $\vec{i}_S$ and $\vec{j}_S$ deviate from the baseline value (simple sine and cosine functions).

The consequence of a variation of 4 m in height (along the tether direction) on the acceleration terms is shown in Figure 117. As expected, the tangential acceleration remains zero, but the normal acceleration exhibits the first mode at the same frequency than Δh. The second mode is the consequence of the change in velocity along $\vec{i}_S$ and $\vec{j}_S$ with the slight change in flight path curvature ρ.

C.1.4 Case 4: Mean Speed and Speed Perturbation

Test Case 4 is used to demonstrate the effect of the mean speed parameter and its perturbation. Moreover, the numerical simulations are compared to analytic solutions. In this case, a circular flight path is performed, but variation in the UAV flight speed with respect to the payload reference location is prescribed, as shown in Eq. 161,

$$V(t) = V_m - 0.2 \cdot V_m \cdot \sin(s_n(t)) \tag{161}$$

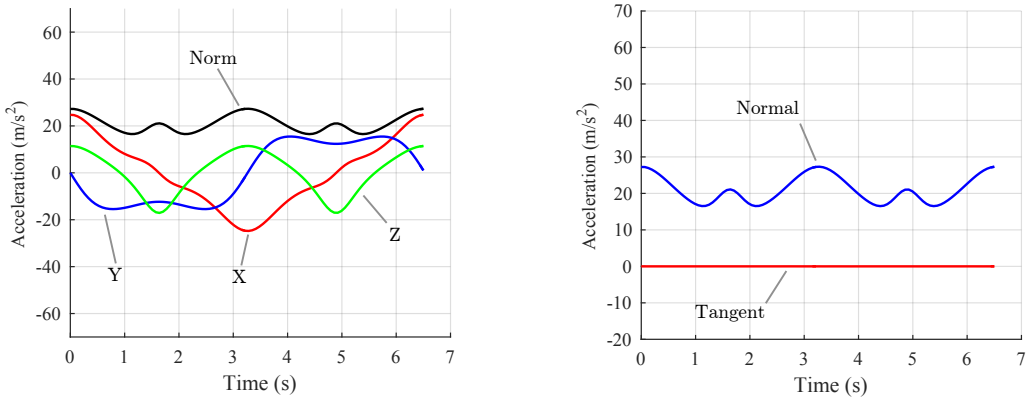

(a) Acceleration components along $\vec{i}_S$ (red), $\vec{j}_S$ (blue), and $\vec{k}_S$ (green)

(b) Acceleration components along $\vec{e}_N$ (blue), and $\vec{e}_T$ (red)

Figure 117: Acceleration components as a function of time: Test Case 3. Components are shown in the Cartesian coordinate system and in the path coordinate system

where s_n is the normalized location on the periodic flight path, with $0 \leq s_n < 2\pi$. Figure 118 presents the flight path with the velocity and acceleration vectors. The velocity is minimum after 1/4 of the flight path distance, and maximum after 3/4 of the flight path distance.

The flight path remains circular but the velocity reduces to 12 m/s on the advancing side of the rotor and accelerates to 18 m/s on the retreating side. Figure 119 shows the velocity, and Figures 120 depicts the acceleration, as for the previous test cases. The results from the numerical simulations represent within engineering accuracy the predictions using the analytical solutions for the prescribed velocity shown in Equation 161. Such variation in the flight speed along the flight path is reflected in the tangential acceleration.

This test case shows that the developed method to vary the UAV flight speed with respect to the fuselage reference location matches the analytical solutions for a simple case. It is expected that this parameter plays a significant role in reducing the impact of the system flight speed (in forward flight) by reducing the UAV flight speed on the advancing side, and accelerating the flight speed on the retreating side.

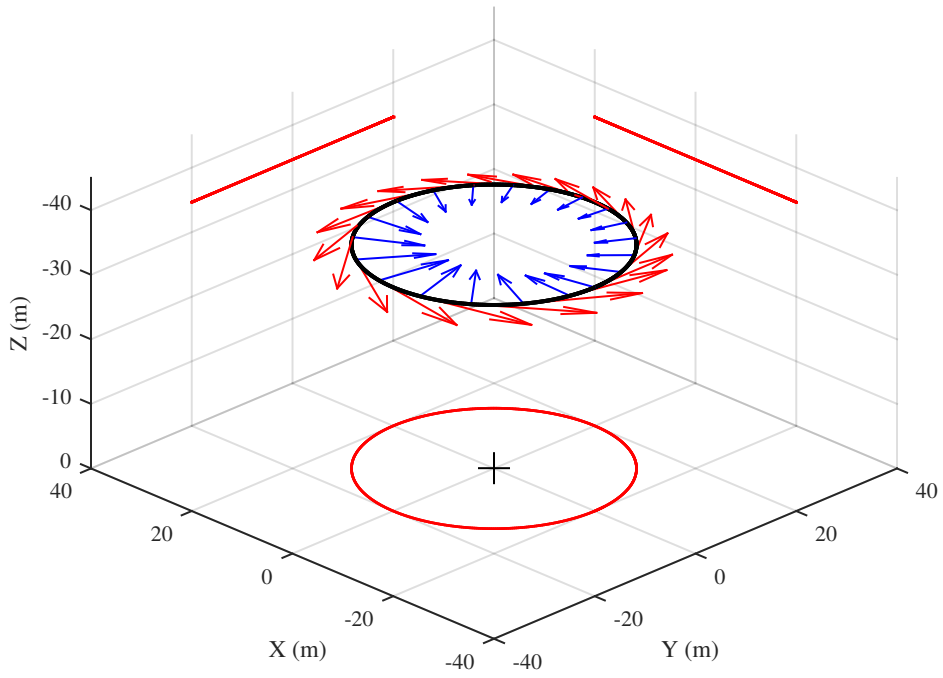

Figure 118: Verification of the parameterization: Test Case 4. The periodic flight path is shown with a black curve and its projections are shown with the red curves. The local velocity vectors are depicted with red vectors and the local acceleration vectors are depicted with blue vectors.

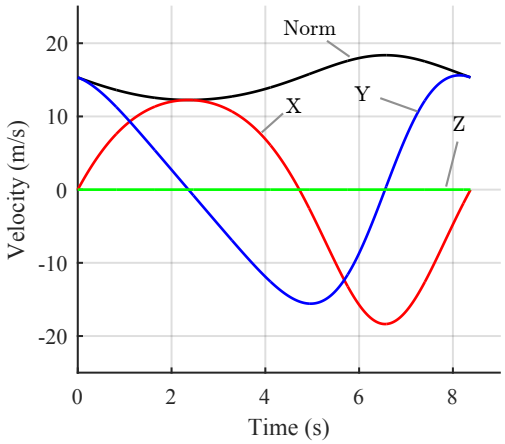

Figure 119: Velocity components as a function of time: Test Case 4.

.

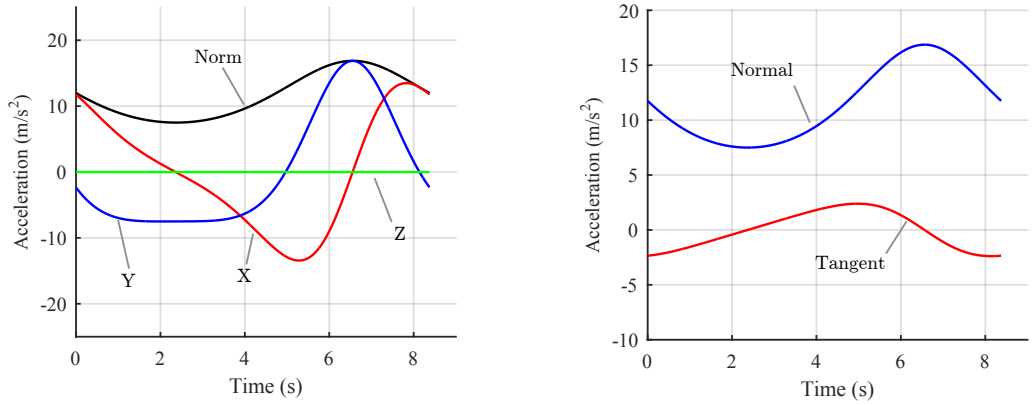

(a) Acceleration components along $\vec{i}_S$ (red), $\vec{j}_S$ (blue), and $\vec{k}_S$ (green)

(b) Acceleration components along $\vec{e}_N$ (blue), and $\vec{e}_T$ (red)

Figure 120: Acceleration components as a function of time: Test Case 4. Components are shown in the Cartesian coordinate system and in the path coordinate system

C.1.5 Case 5: Hub Plane Tilt

Two parameters can be used to "de-center" the location of the fuselage reference location with respect to the flight path when projected on the X-Y plane, θ_S and ϕ_S. For $\theta_S > 0$, the hub plane tilts backward and for $\phi_S > 0$, the hub plane tilts to the left. In both cases, that transformation does not affect the flight path trajectory defined in H, nor the distance of the UAV to the reference fuselage location.

Case 5 is used to demonstrate this feature of the model. Moreover, this test case is used to verify that the implementation of the method matches the predictions. A tilt to the left is prescribed to a circular, constant velocity flight path, as shown in Figure 121. It can be seen qualitatively from Figure 121 that the velocity and normal acceleration are both constant from the vector orientations. The projections also validate that the tilt is of 20° to the left, that and no tilt is observed in the other direction. The norm of the velocity and the acceleration components in the path coordinate system are identical to Test Case 1, since a rotation of the hub plane does not affect those quantities.

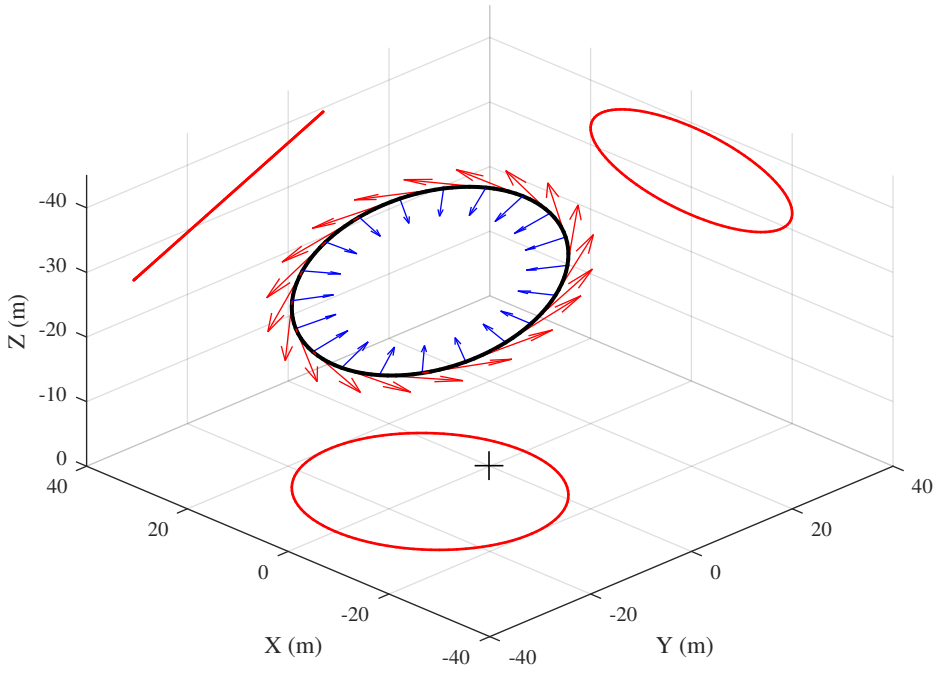

Figure 121: Validation of the parameterization: Test Case 5. The periodic flight path is shown with a black curve and its projections are shown with the red curves. The local velocity vectors are depicted with red vectors and the local acceleration vectors are depicted with blue vectors.

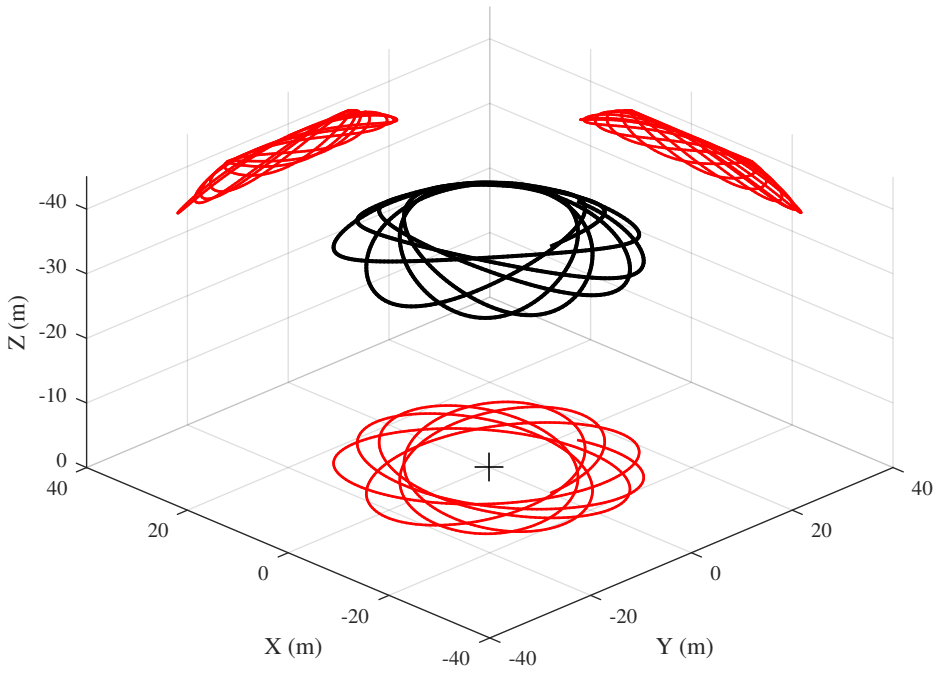

Figure 122: Verification of the parameterization: Test Case 6. The flight path is shown with a black curve and the projections on the three planes with red curves.

C.1.6 Case 6: Hub Reference Frame Rotation About $\vec{k}_H$

The last test case is used to demonstrate and verify the effect of a rotation of the hub reference frame about $\vec{k}_H$, the vertical axis. Since the tether tip motion is prescribed in the hub reference frame, it is expected that the flight speed in the system-carried frame will be affected by this rotation. Test Case 6 is similar to Test Case 2 with an elliptical flight path, but an angular velocity of $\dot{\psi}_S = 0.18$ rad/s of the hub frame about $\vec{k}_H$. Figure 122 shows the hypotrochoid flight path with continuous altitude variation to meet the tether length constraint (constant distance from the UAVs to the reference fuselage location). An elliptical flight path that rotates about the center axis results in a hypotrochoid flight path. The velocity and acceleration are both affected by the rotation, as shown in Figures 123 and 124.

A simple analytical solution exists for the norm of the velocity, especially when

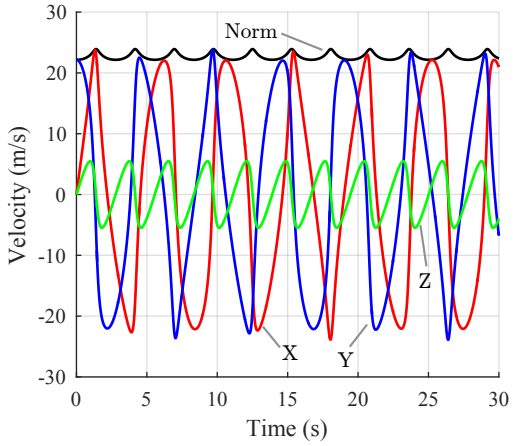

Figure 123: Velocity components as a function of time: Test Case 6.

.

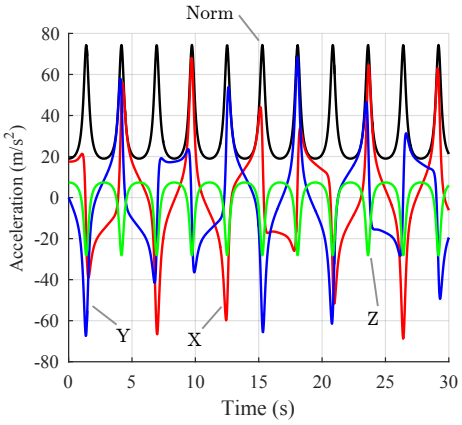

(a) Acceleration components along $\vec{i}_S$ (red), $\vec{j}_S$ (blue), and $\vec{k}_S$ (green)

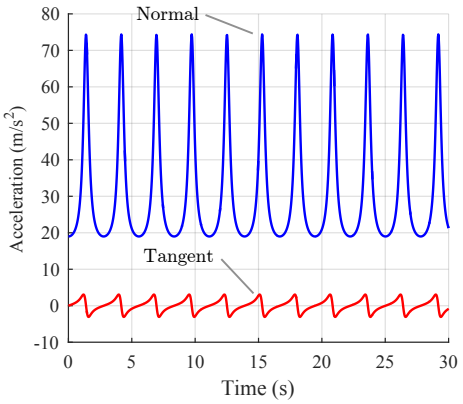

(b) Acceleration components along $\vec{e}_N$ (blue), and $\vec{e}_T$ (red)

Figure 124: Acceleration components as a function of time: Test Case 6. Components are shown in the Cartesian coordinate system and in the path coordinate system

$\dot{z}_3 = 0$, at the extremes of the ellipse. Using the vector derivative transport theorem,

$$\boldsymbol{v}_{P/S} = {}^{S}\frac{d\boldsymbol{r}_{O_S \to P}(t)}{dt} \tag{162}$$

$$= {}^{S}\frac{d\boldsymbol{r}_{O_H \to O_S}(t)}{dt} + \boldsymbol{\omega}_{H/S} \times \boldsymbol{r}_{O_S \to P} + {}^{H}\frac{d\boldsymbol{r}_{O_H \to P}(t)}{dt} \tag{163}$$

$$= \boldsymbol{\omega}_{H/S} \times \boldsymbol{r}_{O_S \to P} + {}^{H}\frac{d\boldsymbol{r}_{O_H \to P}(t)}{dt} \tag{164}$$

which does not contain the translation between the two reference frames. First, let t be such that $x = 0$ and $y = 22$ in the hub frame, which is also characterized by zero vertical velocity. For this specific case,

$$\left|\boldsymbol{v}_{P/S}\right| = \dot{\psi}_S \cdot y + V_m \tag{165}$$

$$= 0.18 \cdot 22 + 20 \tag{166}$$

$$= 23.96 \text{ (m/s)} \tag{167}$$

which matches the numerical results. Second, let t be such that $x = 12$ and $y = 0$ in the hub frame, which is also characterized by zero vertical velocity. For this case,

$$\left|\boldsymbol{v}_{P/S}\right| = \dot{\psi}_S \cdot x + V_m \tag{168}$$

$$= 0.18 \cdot 12 + 20 \tag{169}$$

$$= 22.16 \text{ m/s} \tag{170}$$

which also matches the numerical results. The accelerations are not analytically derived here since they were demonstrated valid in the few previous cases.

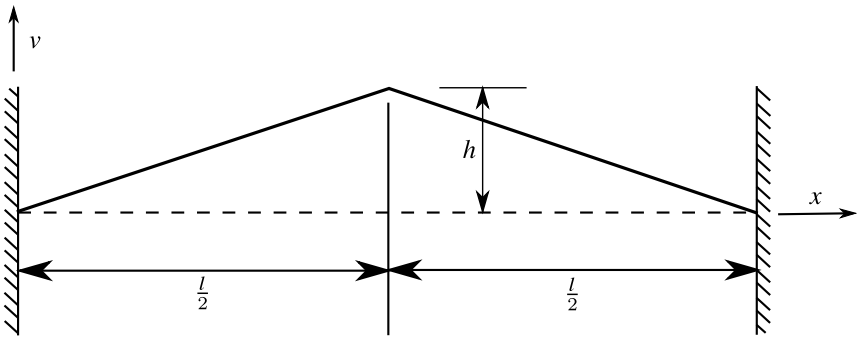

Figure 125: Initial condition of the Plucked String [75]: Test Case 1. The string is pre-stretched at a constant tension, with an initial shape as shown in the figure.

C.2 Higher Fidelity Tether Model

This section describes a series of test cases to verify and validate the tether and payload dynamics model. The objective is to ensure that both the theory and implementation of the code are valid.

C.2.1 Case 1: Plucked String Attached at Both Ends

The first test case consists of the analysis of the displacement of a simple plucked string attached at both ends with a high tension. Figure 125 from Hodges [75] depicts the initial conditions.

The analytical solution to the plucked string constrained at both tips is shown in Equation 171

$$v\left(x,t\right)=\frac{8h}{\pi^{2}}\sum_{i=1,3,\ldots}^{\infty}\frac{\left(-1\right)^{\frac{i-1}{2}}}{i^{2}}\sin\left(\frac{i\pi x}{l}\right)\cos\left(\omega_{i}t\right) \tag{171}$$

where

$$\omega_{i}=\frac{i\pi}{l}\sqrt{\frac{T}{m}} \tag{172}$$

T is the tension, and m the mass per unit length. Figure 125 compares the analytical results with 20 modes to the numerical results for the following tether properties: $m = 0.1$ kg/m, $T = 10$ N, $l = 1$ m. Only the tether elasticity is considered through $k_n = 1000$ N. Let's remind that k_n is the spring stiffness per unit strain. Both the aerodynamic damping and gravity are neglected and not considered.

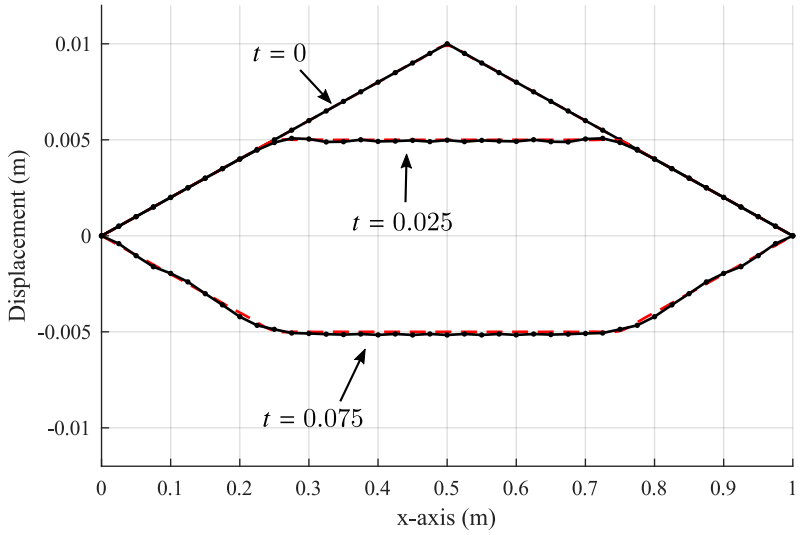

Figure 126: Test Case 1: Displacement at three timesteps, $t = 0$ s, $t = 0.025$ s, and $t = 0.075$ s. The analytic solution with 20 modes is shown in red dashed line, and the numerical results are shown with the solid black line with the masses depicted with black dots.

The predictions using the numerical model replicates the analytical solution of the plucked string with a root mean square error below 1% when divided by the maximum displacement of each node for the first two complete periods. Since a numerical integration scheme is used (*ode113*, Matlab), numerical errors contribute to the small discrepancy.

Figure 127 shows the vertical displacement of the mid-point of the string as a function of time for a few periods. The first observation is the slight difference in the measured frequency between the numerical model and the analytic solution. The slight difference, on the order of 1%, is due to the method that the tension was applied in the numerical model. A tether of length 0.99 m was stretched to 1 m with $k_n = 1000$, which resulted in a tension of 10 N. However, the total tether weight is reduced to $0.99 \cdot m$, or 1% less than the value used in the analytical model.

In summary, Test Case 1 verified the mass and stiffness models by replicating a string problem with an analytical solution.

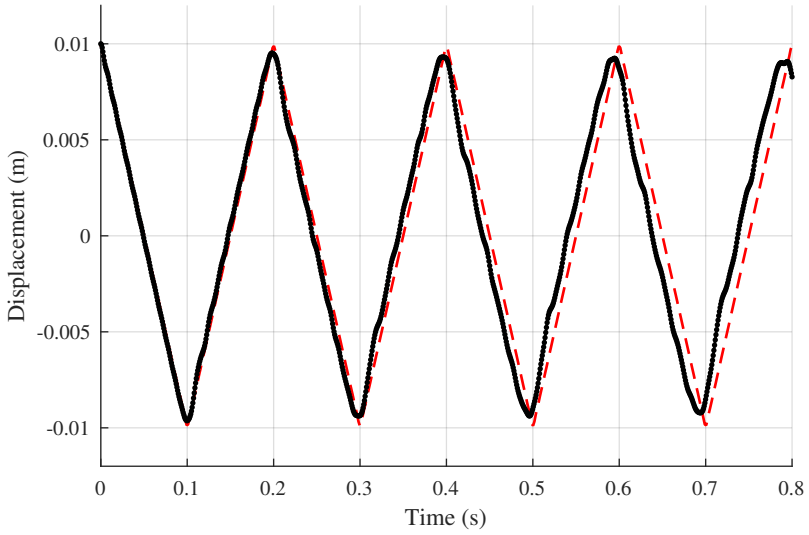

Figure 127: Test Case 1: Displacement at the center of the string as a function of time. The analytic solution with 20 modes is shown with a red dashed line, and the numerical results are shown with the solid black line.

C.2.2 Case 2: Free-Hanging Tether Attached at Both Ends

The second test case consists of a free-hanging tether attached at both ends. This case is used to verify that the gravity and elastic models are both valid, as well as the angle definition between each tether segment.

The analytical solution to an idealized hanging tether under its own weight when supported by its two ends is a catenary [141]. In Cartesian coordinates, the tether shape is described by Equation 173,

$$y\left(x\right) = a\cosh\left(\frac{x}{a}\right) \tag{173}$$

where x is the location with respect to the center of the tether, and a is a scaling parameter.

The numerical model considers a tether of length $l = 1.1$ m, attached between two points, at $x = 0$ and $x = 1$ m. The fully dynamic model is used with a large damping value, both from the aerodynamics and the internal damping, to quickly bring the tether shape to a steady state. Figure 128 shows the tether shape, superimposed with

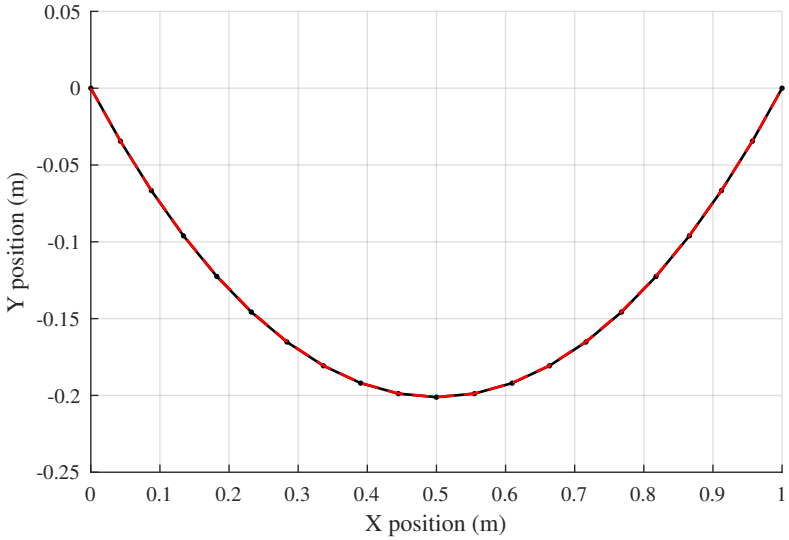

Figure 128: Test Case 2: Tether shape attached by its two ends. The analytical model (catenary) is depicted with the red curve, and the numerical model is shown with the solid black line with dot markers. The shape is within engineering accuracy of a catenary.

a catenary with parameter $a = 0.663$ and centered at $x = 0.5$.

As expected, the steady-state shape of a tether attached at both ends under its own weight is a catenary. The errors on the position compared to the analytical solutions are well below 1%. This verification using an analytical model validates the definition of the angles between each element, the gravity direction, and the uniformity (in this specific case) of the weight distribution along the tether.

C.2.3 Case 3: Towed Devices Behind Aircraft

The objective of this third test case is to demonstrate the validity of the aerodynamics model (tether and payload) since the mass model was already verified in Test Case 2. Two experimental data sets are used from the literature and compared to the prediction by the numerical model.

First, Gilbert [62] provides a data set of the sweptback angle of a probed towed behind a helicopter at a speed below 100 kts. A 6.5 kg probe with $C_dA = 0.051$ is towed using a 45.7 m tether. The aerodynamic properties of the probe were derived

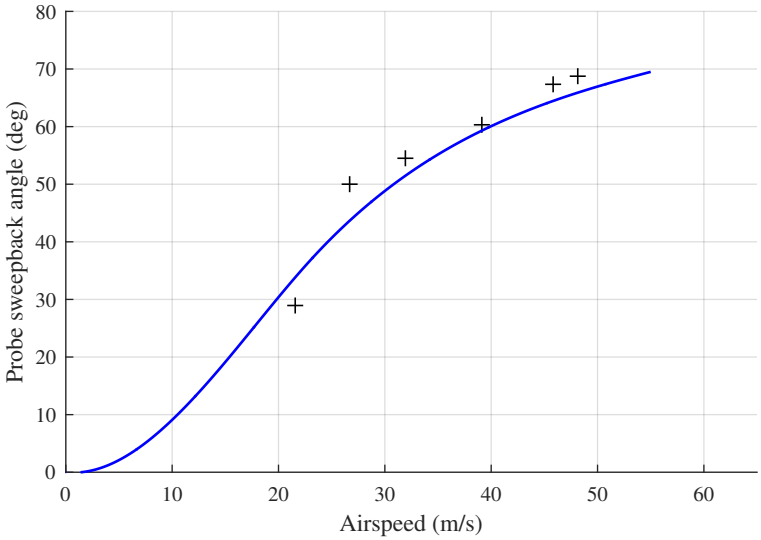

Figure 129: Comparison between experimental data versus predictions of the swept-back angle of a probe behind an aircraft. The experimental data is from Gilbert [62]. A 6.5 kg probe with $C_dA = 0.051$ is towed up to 60 kts behind a helicopter using a 45.7 m tether. The angle is defined between the vertical and the line formed by the probe and the tether attachment point on the helicopter.

from an independent experimental data set of drag measurements for the probe only, provided by the same author. The tow line has a diameter of $d = 0.0055$ m, with a mass per unit length of $\lambda = 0.0599$ kg/m. The sweptback angle between the vertical and a straight line between the probe and the tether attachment point on the helicopter was measured from a chase helicopter at velocities between 40 and 90 kts such that the helicopter wake does not interfere with the tether shape. The Reynolds number for the experiment was between 5,700 and 12,800, well below the critical Reynolds number for a cylindrical tether shape. Figure 129 compares the experimental results [62, 69] to the numerical predictions by the higher fidelity tether model.

The numerical results demonstrate that the drag and lift model are valid since most of the drag comes from the tether and not the probe itself. The tether shape due to the aerodynamic forces can be observed by the difference in the tether swept-back angle at the helicopter and at the probe. Figure 130 compares the numerical

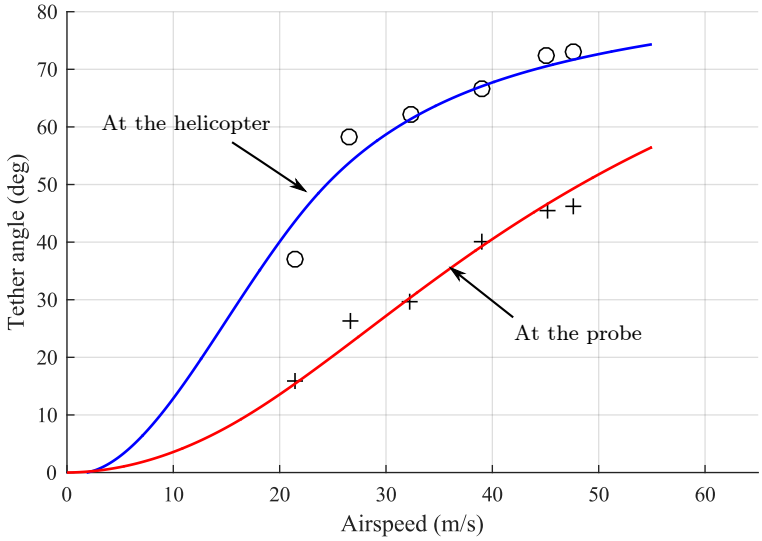

Figure 130: Experimental tether sweptback angles of a towed drogue versus numerical predictions. The black markers represent the experimental results presented by Gilbert [62].

predictions with the current tether model with the experimental data set.

The numerical prediction in Figure 130 are within a few percent from experimental data. It must be noted that the sweptback angle was measured using photographs, and therefore a significant (but not quantified) error can result in the measurements. The higher angle near the helicopter than at the probe is the result of the tether drag and lift. As a comparison, a simulation was performed at 30.8 m/s without any aerodynamic loads on the tether. The predicted tether angles are 18.0 degrees at the helicopter (59.7 degrees with tether drag) and 27 degrees at the probe (28.35 degrees with tether drag). The difference between the angles at the probe is due to gravitational forces applied on the tether segments. The total tether mass is not negligible at more than 33% the drogue mass.

The second test case designed to validate the tether drag model is based on the experiments performed by the Eclipse Project [117]. In February 1998, a series of flight tests at NASA's Dryden Flight Research Center involving a modified F-106 aircraft (named EXD-01) towed behind a C-141A aircraft was completed. The objective was

to evaluate the possibility of towing large aircraft and confirming their stability.

The flight tests were performed at an airspeed of 113.3 m/s, at an altitude of 3,050 m (10,000 ft) and in steady level flight. The elevator deflection of the EXD-01 aircraft was modified slowly between -7 deg to -2 deg. For each discrete angle, the towed aircraft changed altitude and stabilized to a new trim condition. Results provided in the work of Norris [122] include the variation in altitude behind the tow plane, the cable pitch angle at the glider (between the horizon and the cable), and the cable tension.

The tether used in this experiment had a diameter of 1.9 cm (0.75 in) and a length of 320 m (1,050 ft), for a total tether mass of 92 kg (205 lbs). Since both the airspeed and tether diameter had much higher values, the Reynolds number during the flight test was approximately 105,000, which is in the range of transition depending on the surface roughness.

Figure 131 shows the relationship between the vertical location of the towed aircraft with respect to the C-141A as a function of the elevator angle. The numerical predictions used the tether tension and the tether angle at the EXD-01 aircraft as boundary conditions to evaluate the final tether shape, and thus, the variation in height.

An offset of a few degrees between the predictions and the physical experiments exists, where the numerical simulations underestimate the glider height by a maximum of 25 m. The largest error occurs with a large negative elevator deflection, where the EXD-01 aircraft should be at approximately the same height as the tow plane. The article by Norris [122] highlights some discrepancies and the need for correction factors for the results. A part of this discrepancy is also associated with the high Reynolds number, which could affect the drag and lift coefficients of the tether if the flow is turbulent. Finally, the aircraft wake interaction on the tether is neglected.

In summary, Test Case 3 validated the aerodynamic forces in the tether model by

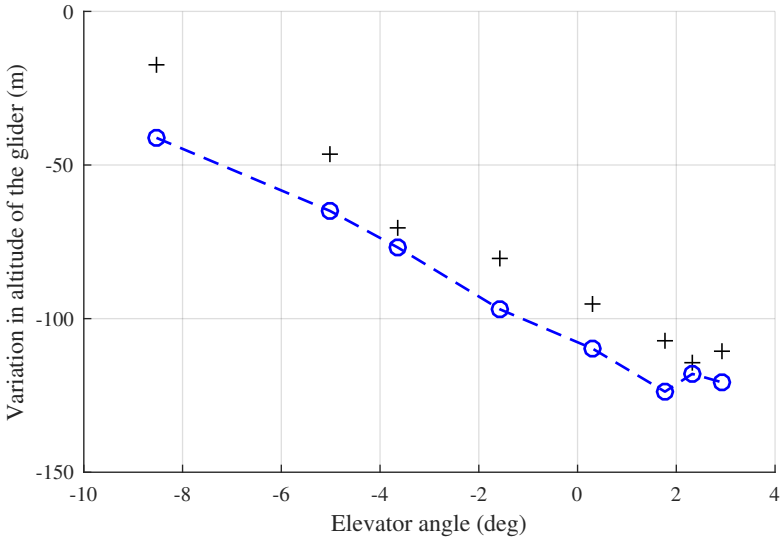

Figure 131: Comparison between experimental data versus predictions for the vertical offset between a tug aircraft and a glider, from the Eclipse project [117, 122].

reproducing experimental results of towed objects at two largely different Reynolds numbers and vehicle sizes. The results from both experiments were replicated with acceptable accuracy.

C.2.4 Case 4: Verticality Property of Long Tethers Towed Along a Circular Flight Path

Test Cases 1-3 verified and validated several features of the tether modeling code, including the aerodynamic forces, the inertial effects, and the spring system between the mass elements, both using analytic and physical experiments. The objective of this last test case is to replicate the tether shape prediction of a very long and lightweight tether along a circular flight path. In this case, a complete 3D motion of the tether tip is prescribed. The selected test case comes from the work of Williams [165]. Table 13 details the tether, flight path, and drogue characteristics for this test case.

Figure 132 illustrates the 3D predicted periodic flight path and its three projections. For completeness, the numerical results predicted by Williams are shown in Figure 133, where the "Light" aircraft results are replicated using the dynamic tether

Table 13: Tether, flight path, and drogue properties for Test Case 5 ([165])

Parameters	**Values**
Tether mass per unit length (g/m)	1.2
Tether Young's Modulus (GPa)	120
Tow radius (m)	214
Aircraft velocity (m/s)	52.6
Tether length (m)	3,000
Tether diameter (mm)	1.27
Drogue C_dA (m^2)	2
Drogue mass (kg)	10

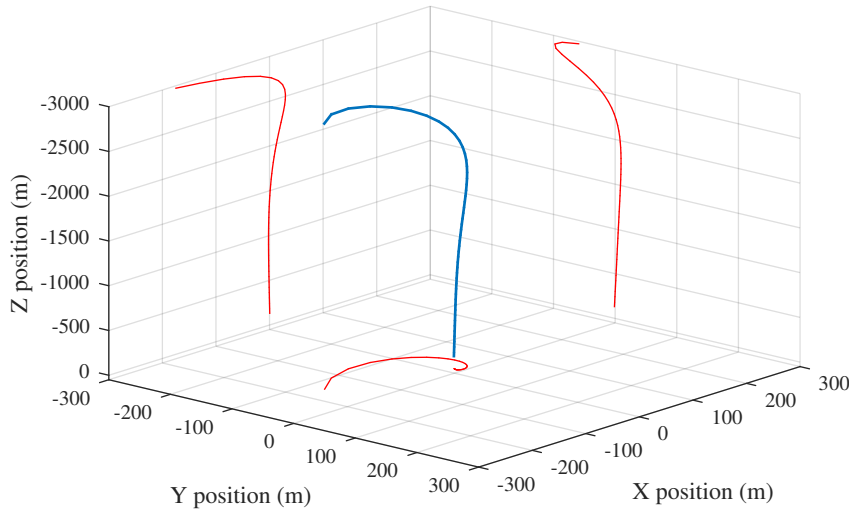

Figure 132: Periodic steady-state tether deflection for a 3 km long tether and drogue chute towed by a general aviation aircraft at along a circular flight path. The red curve shows the projection of the flight path on three planes

model presented in this work.

As expected, the long tether shows the "verticality" property, where a long tether with a drogue will tend to become vertical if towed along a circular flight path. This example demonstrates the technique used by a missionary pilot to deliver and recover payloads in the 1930's in regions without access to a runway in South America. The predicted drogue location in the periodic steady state is a circle of 1.3 m diameter at the center of the flight path. It should be noted that under normal operating conditions, such precise payload location could not be achieved due to the presence

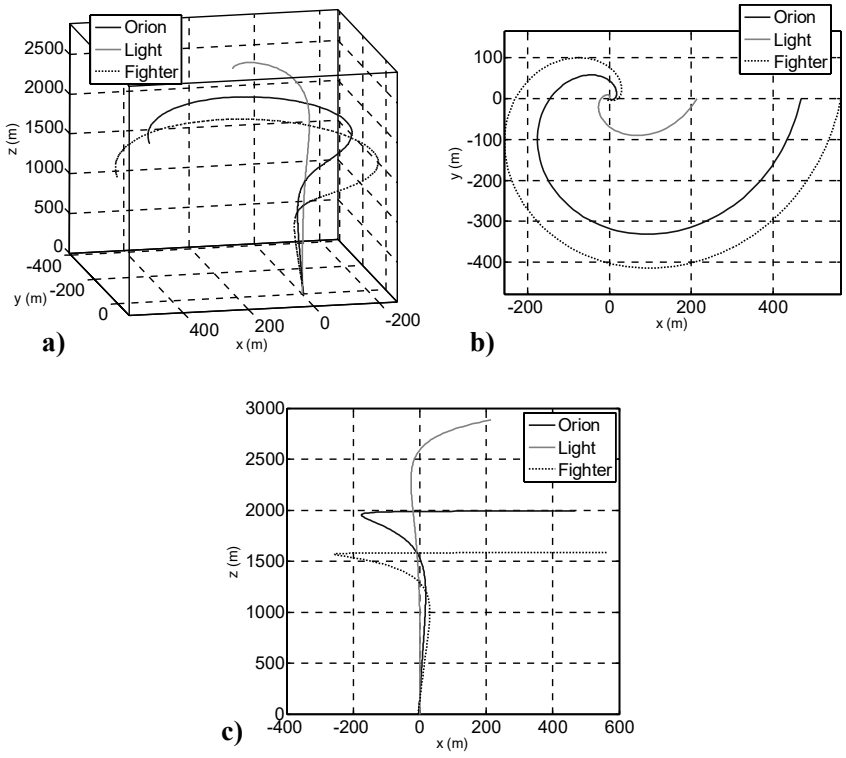

Figure 133: Numerical predictions of the periodic steady-state tether deflection for a 3 km long tether and drogue chute towed by three types of aircraft along a circular flight path. The replicated data set concerns the "Light" aircraft type, with the smallest radius [165].

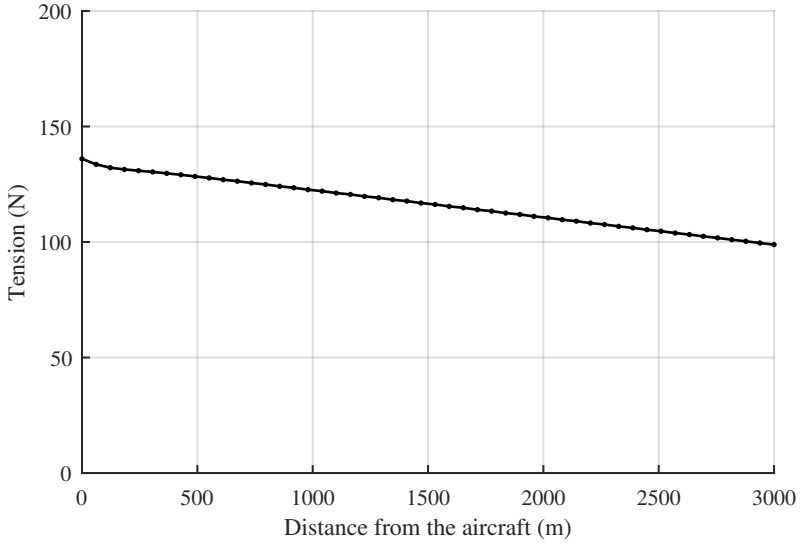

Figure 134: Tether tension as a function of distance from the tow plane.

of wind.

The predicted tether shape by both Williams (Figure 133) and the current tether model presented in Figure 132 are very similar, but the exact discrepancy could not be quantified since the data set by Williams was not made available. The drogue altitude is approximately 2,900 m below the tow aircraft for both simulations. The projected flight path on the three planes also reveals similar tether shapes, with over one revolution of lag in the payload location with respect to the tow plane. Both simulations returns a payload periodic steady state circular motion in the order of 1.3 m in diameter.

An interesting result is the vertical force applied to the towed aircraft. Due to the lift created by the tether segments moving in the fluid at an angle, lift is generated. In this case, the vertical force applied by the aircraft is only 38 N, while the total tether and drogue weight reaches 135.4 N. The tether tension as a function of the distance from the tug aircraft is shown in Figure 134.

The tension is higher near the aircraft mainly due to tether drag. The tether tension reduces to the drogue weight ($\approx$98 N) at the drogue attachment point since

the tether is vertical. As expected, the tension is a smooth function since the tether internal damping removed all the longitudinal waves during the transient phase.

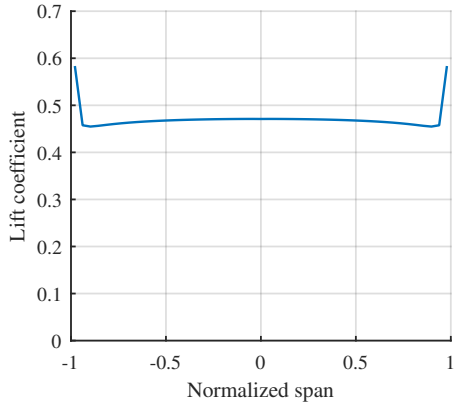

(a) Lift coefficient

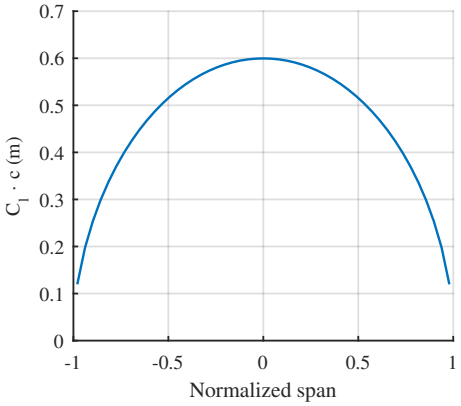

(b) Lift per unit span

Figure 135: Test Case 1: Lift coefficient and lift per unit span for an elliptical wing planform. The wing has an aspect ratio of 8, with an elliptical chord distribution, and the quarter-chord forming a straight line. The wing is tested at α =5.73° with 50 spanwise elements. The airfoil lift curve slope is assumed to be $C_{l\alpha} = 2\pi$ with $C_{l0} = 0$.

C.3 Higher Fidelity Aerodynamic Model

C.3.1 Case 1: Steady-State Lift distribution in Steady Level Flight

The first test case has the objective to validate the capacity of the model to predict the lift distribution of wings without control surface deflections in steady level flight. First, Figure 135 presents the spanwise lift coefficient and spanwise lift distribution for an elliptical wing.

The wing has an aspect ratio of 8, with an elliptical chord distribution, and the quarter-chord forming a straight line. The wing is tested at $\alpha = 5.73°$ with 50 spanwise elements. The airfoil lift curve slope is assumed to be $C_{l\alpha} = 2\pi$ with $C_{l0} = 0$. The predicted lift coefficient remains approximately constant as a function of span within a few percent, with an error of 30% or the last element near the tip. Such error on the last element is typical of panel methods, and a convergence analysis can show a reduction of this error with an increase in the number of elements. The consequence of the error in the lift coefficient on the spanwise lift distribution is minimal, as seen on Figure 135b. The actual lift distribution is elliptical, as predicted by the lifting

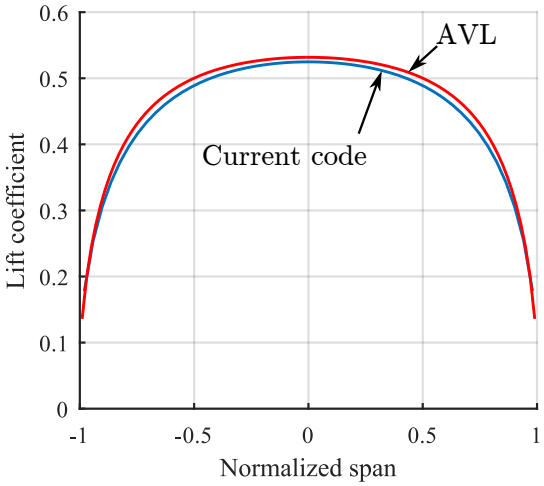

Figure 136: Test Case 1: Distribution of lift coefficient for a rectangular wing planform of aspect ratio of 8 at an angle of attack of 0.1 rad. The red blue curve represent the prediction from the current model and the red curve depicts the results from AVL, a well known vortex lattice method developed by Dr. Drela and colleagues.

line theory.

An estimation of the 3D lift curve slope can be obtained from Equation 174, obtained from the lifting line theory [9].

$$C_{L,\alpha} = \frac{C_{l,\alpha}}{1 + \frac{C_{l,\alpha}}{\pi \text{Æ} e}} \tag{174}$$

$$= 1.6\pi \tag{175}$$

The numerical simulation estimates the lift curve slope at 1.5π, slightly lower than the results for the lifting line with a high aspect ratio. The higher fidelity aerodynamic model developed in this work returns an induced drag coefficient of 0.0085, and the theory predicts a drag coefficient of 0.0087 for the same lift coefficient. This difference is also related to the number of elements and the low aspect ratio. This difference reduces for higher aspect ratios.

A rectangular wing with an aspect ratio of 8 was also tested under the same conditions. The lift distribution is presented in Figure 136. The numerical predictions from the present code are compared to the results predicted by a vortex lattice method.

Table 14: Wing characteristics and Test Case 2 conditions

Characteristics	**Value**
Airfoil lift curve slope, $C_{l\alpha}$	2 π /rad
Aileron lift increment slope, $C_{l\delta_a}$	4.34 /rad
Aileron deflection, δ_a	10^o
Angle of attack, α	0.1 rad (5.73^o)

The objective is to ensure that the prediction made using a single chordwise element is similar to a complete vortex lattice method for wings with an aspect ratio around 8. The Atena Vortex Lattice code (AVL)[48], developed by Dr. Mark Drela and Harold Youngren, is used since it has been validated by numerous experiments and it has been widely used over many years. The vortex lattice is comprised of 50 spanwise elements and 10 chordwise elements on a flat plate since the airfoil is assumed to be symmetrical.

The results in Figure 136 show a mean difference in the lift prediction between AVL and the current method of 3%. The discrepancy is the consequence of using an aspect ratio of 8, which is just high enough to obtain accurate results from a lifting line method. The difference between a full VLM versus the lifting line approach used in this work is considered acceptable.

C.3.2 Case 2: Aileron Effectiveness

The objective of Test Case 2 is to validate that the forces and moments generated by a lifting surface due to an aileron deflection are accurate. As for Test Case 1, the results from the aerodynamic model are compared to the numerical simulations by AVL. Table 14 details the conditions of the test and Figure 137 illustrates the wing geometry with details on the aileron size and location.

The airfoil lift increment per unit deflection of the aileron (only for the flapped section) is obtained from an inviscid simulation of a 2D panel method on a NACA0005 airfoil (5% thickness, symmetrical airfoil). The software used is XFOIL, a code also developed by Dr. Mark Drela at MIT. The numerical simulation with AVL to predict

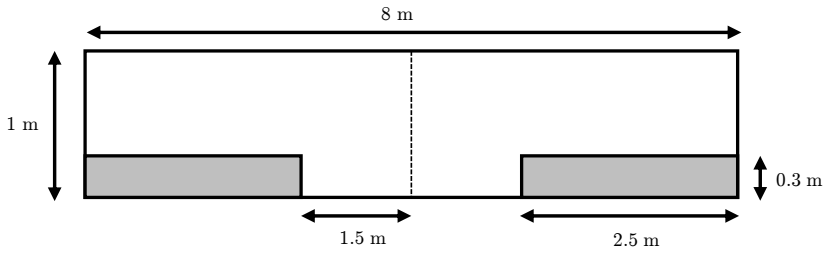

Figure 137: Test Case 2: Wing geometry. The ailerons extend on 62% of the wingspan and 30% of the chord.

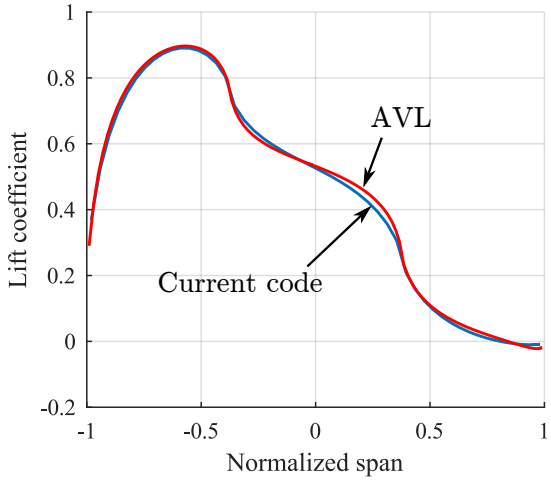

Figure 138: Test Case 2: Distribution of lift coefficient for a rectangular wing planform of aspect ratio of 8 at 0.1 rad angle of attack with 10 deg aileron deflection.The blue curve shows the model prediction and the red curve depicts the results from AVL

the loads (and coefficients) uses the same discretization as for Test Case 1 (50 spanwise elements, 10 chordwise elements). A much larger total number of elements is required for a pure vortex lattice method to capture the effect of the camber line on C_{l0}, while such a parameter is provided in the case of the lifting line. Figure 138 compares the lift coefficient distribution across the wing for both approaches.

The lifting line method with unsteady aerodynamics implemented in this work replicates the lift distribution predicted by AVL with an error below 1% on the predicted rolling moment. Table 15 compares quantitatively the forces and moments predicted by both methods.

Table 15: Test Case 2 forces and moments

Characteristics	**HF Aero Model**	**AVL**	**Discrepancy**
C_L	0.453	0.459	1.3%
C_{Di}	0.0167	0.0175	4.5%
$C_{\mathcal{L}}$	0.0813	0.0806	$< 1\%$
$C_{\mathcal{N}}$	-0.00494	-0.00495	≈ 0 %

This test case demonstrates that the second-order lifting line approach implemented for this work can capture with great accuracy the effect of aileron deflection on the lift, drag, and rolling moment in steady level flight. Although the aspect ratio of the wing is only 8, with about 60% of the wingspan covered with ailerons, the predictions are in good agreement with the vortex lattice method. A quick look at $C_{\mathcal{N}}$, the yawing moment, shows that an aileron deflection for a positive rolling moment creates a relatively strong adverse yaw effect, as observed in most conventional aircraft configuration. Such behavior is also expected for the tethered aircraft due to the strong aileron deflection.

The induced drag resulting from a 10 deg aileron deflection *doubles* compared to a symmetrical flight condition. This simple demonstration illustrates the need to better capture the aerodynamic behavior of tethered aircraft, in order to obtain a more accurate prediction of the power requirement.

C.3.3 Case 3: Impulse Start

Test Cases 1 and 2 validated the steady-state solution for lifting surfaces and the control surface effectiveness. The results of Test Case 3 are provided to validate that the code can capture the unsteady aerodynamics originating from the circulatory terms (no apparent mass) from an impulse start at a constant angle of attack.

The reduction in lift during an impulse start for a 2D airfoil can be approximated using the Wagner function [99],

$$\phi(t) = \frac{2}{\pi} \int_0^\infty \frac{\mathrm{Re}\,(C) \sin\left((\omega t)\right)}{\omega} d\omega \tag{176}$$

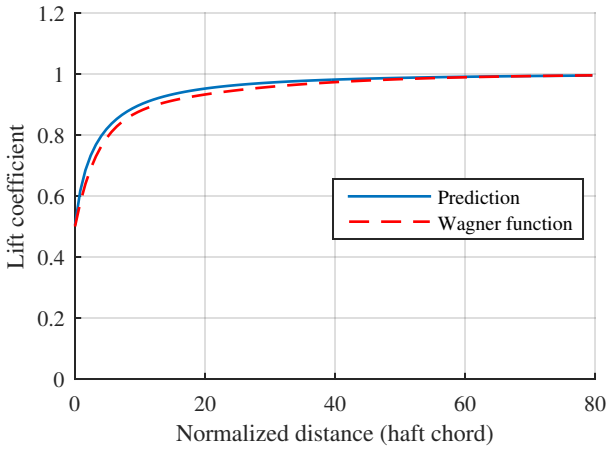

Figure 139: Test Case 3: Wagner function for an impulse start. The Wagner function is demonstrated from an impulse start on a high aspect ratio wing using the aerodynamic model. Those predictions are compared to an exponential approximation of the Wagner function (red dashed line).

where $C(\omega)$ is the complex conjugate of the Theodorsen function. The Wagner function can usually be approximated to an exponential decay,

$$\phi(t) = 1 - 0.165e^{-0.0455t} - 0.335e^{-0.3t} \tag{177}$$

where t is the normalized time, or the number of half chords traveled from the impulse start.

A rectangular wing with an aspect ratio of 100 is used to simulate an infinite wing (2D airfoil) with 50 spanwise elements and 200 timesteps over a distance of 80 half-chord lengths. The approximative 2D sectional lift is obtained by extracting the lift at the 25^{th} element, near the center of the wing. A constant angle of attack of 5.73^{o} is imposed throughout the impulse start. The Wagner function is then estimated by dividing the predicted lift at the section by the steady-state value. Figure 139 illustrates the difference between the prediction and the approximation of the Wagner function.

The differences between the curves are attributed to the temporal discretization. A reduction in the timestep size by 50% reduces the discrepancy by approximately

50%.

C.3.4 Case 4: Sinusoidal Variation in Angle of Attack

Test Case 4 is used to demonstrate that the aerodynamic model can predict the phase shift and amplitude reduction in the lift in the presence of a sinusoidal variation in the geometric angle of attack. The analytic solution to phase shift and amplitude reduction for 2D airfoils is known as the Theodorsen equation.

A rectangular wing with an aspect ratio of 100 as for Test Case 3 is used to mimic the behavior of an infinite wing (2D airfoil). The wing has a zero degree angle of attack prior to adding the heave motion. Let U be the norm of the relative velocity, b be the half chord length, and k be the reduced frequency. The variation in altitude along $\vec{z}_k$ to obtain a maximum variation in the angle of attack of 5° is

$$z_k = \frac{0.0875 \cdot U}{\omega} \sin\left(t \cdot \omega\right) \tag{178}$$

$$= \frac{0.0875 \cdot b}{k} \sin\left(\frac{U \cdot k}{b} t\right) \tag{179}$$

where t is the time, in seconds. Four experiments were performed at $1/k = 5, 10, 20, 40$. For each case, the simulation was run for more than three complete cycles to reach periodic steady-state. The amplitude reduction and phase lag were then compared to the predictions from the Theodorsen function [75], as shown in Figure 140.

The numerical simulations are in agreement with the analytic solution, which shows a reduction in the phase lag and an amplitude factor ϕ that converges towards 1 for very low frequency. The small discrepancies, in the order of a few percent on the phase shift, are associated with the timesteps size as for Test Case 3. For the cases with a very low oscillatory frequency (ie $1/k = 40$), a large number of steps were required, with the consequence to increase the computational time.

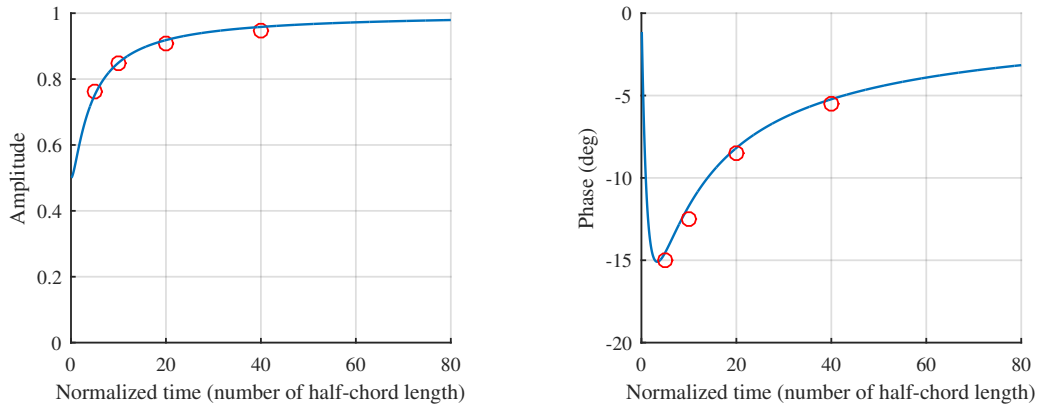

(a) Lift reduction (b) Phase shift

Figure 140: Test Case 4: Effect of a sinusoidal variation in geometric angle of attack. The effect of unsteady aerodynamics due to a sinusoidal variation in geometric angle of attack is seen as a reduction in the lift magnitude and a phase lag.

Table 16: Wing characteristics for Test Cases 5 and 6

Characteristics	**Value**
Wing span (m)	8
Wing chord (m)	1
Wing twist (deg)	0
Aileron position (m)	$-4 \leq y \leq -2,\ 2 \leq y \leq 4$
Flap position (m)	$-2 \leq y \leq 2$
Aileron chord (m)	0.3

C.3.5 Case 5: Flap Deflection

The consolidation model is validated using the following two test cases. The numerical simulations with the consolidation model are compared to the free-vortex wake model without consolidation. Table 16 summarizes the wing geometry and control surface characteristics for both test cases.

As for the Test Case 2, the effect on the aileron properties of an aileron deflection is obtained through XFOIL. The flap effectiveness is evaluated using the same approach. All simulations were performed using 100 equally-spaced elements along the lifting line.

The objective of this test case is to demonstrate that the loads and wake shape

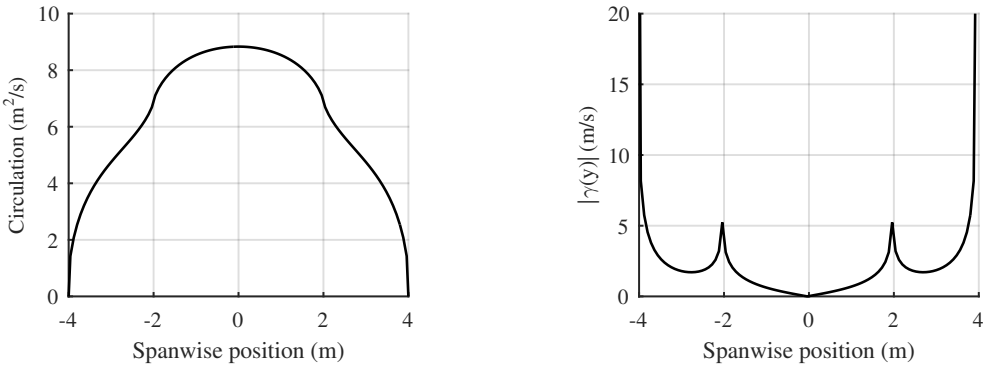

(a) Circulation (b) Trailing vortices intensity

Figure 141: Test Case 5: Effect of flap deflection on the lift distribution. The effect of the positive flap deflection can clearly be seen on Figure 141a with a strong increase in the circulation in the center section. As expected, the flap deflection created a strong vortex at $y = -2$ and $y = 2$, as shown in Figure 141b.

predicted by the free vortex wake model with and without consolidation are similar. Moreover, this test case is used to demonstrate the reduction in computational expense when using the consolidation model.

In this test case, the wing described in Table 16 is flown at 20 m/s at an angle of attack of 5.73° with a positive flap deflection of 6.9°, while keeping the aileron deflection at zero degrees. The wing was flown for over 5 seconds to remove the effect of the unsteady aerodynamics. Figure 141 presents the distribution of circulation and its derivative as a function of span in steady state.

The presence of the flap deflection increases the lift in the center section of the wing. The strong variation in the lift at the end of the flapped section of the wing creates a local vortex as illustrated by Sparlart in Figure 52. Although weaker than the tip vortex, the flap vortex does not mix (roll-up) with tip vortex as explained by the same author, and should be considered separately. The wake geometry for this test case can be seen in Figure 142.

The four trailing vortices can be identified by the roll-up of the wake sheet. The cut views of the vortex sheet at 0.333 s, 1 s, 1.667 s, and 2.333 s after the passage of the wing, depicted by the solid black lines, highlight the effect of the flaps.

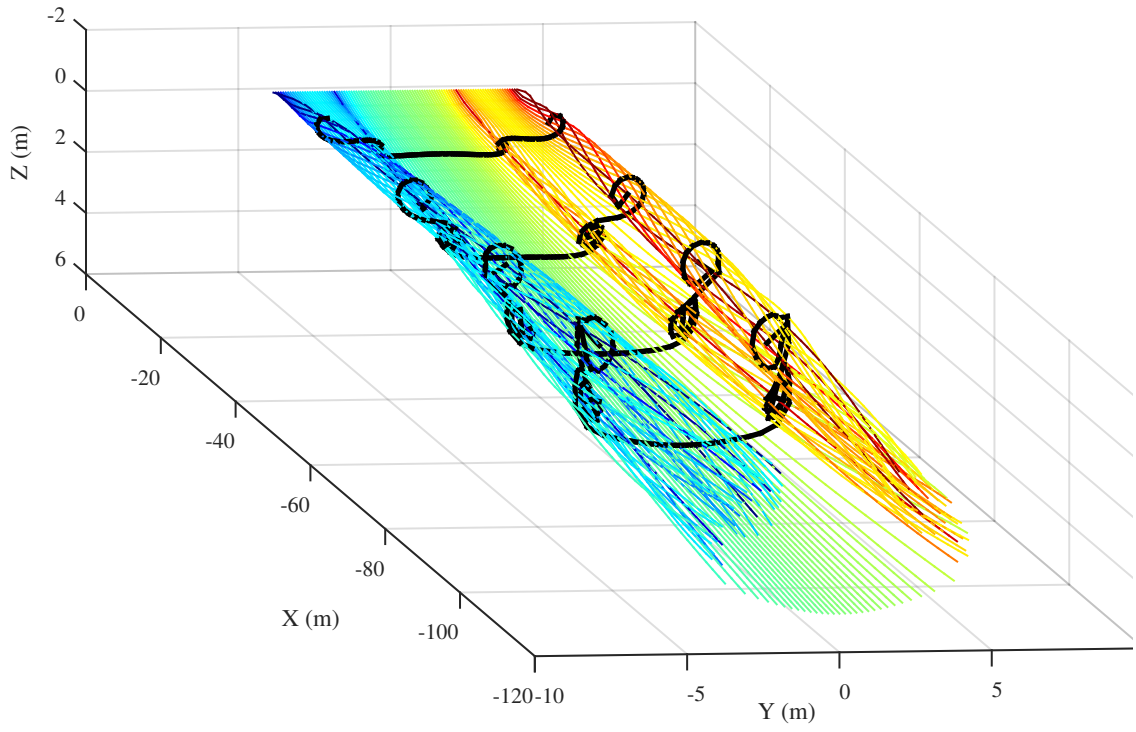

Figure 142: Test Case 5: Wake geometry and trailing vortex intensity. The trailing vortex intensity can be identified by the color of the segments, where a red segment represents a positive circulation of 0.5 m^2/s or more and a blue segment represents a circulation of -0.5 m^2/s or less. The wake shape can be seen through the cut-views of the wake, depicted by solid black lines. The cut views are shown at 0.333 s, 1 s, 1.667 s, and 2.333 s after the passage of the wing.

The roll-up process cannot be modeled appropriately using the free vortex wake model, even with a very large number of elements. One way to witness this phenomenon is to observe Figure 142 where the wake sheet rolls up on itself due to the insufficient number of elements for $t < 2.33$ s, even with 100 elements.

The results from this simulation are now compared with the addition of the consolidation model, which converts automatically the numerous trailing vortices into a small number of main vortices based on Equation 116. Figure 143 illustrates the wake shape and the four major trailing vortices after the consolidation process.

Figure 143 illustrates the strong effect of the flap on the wake shape. Five vortices are automatically identified with the consolidation model, two on the left side, two on the right side, and one in the plane of symmetry. This last vortex has an intensity of zero and is the result of the numerical process to identify the vortices, and therefore, should not be taken into account. The color of the consolidated trailing vortices should be only used to identify the sign of the circulation since the colors were adjusted for the near wake vortex intensity. Therefore, the colors are saturated.

As for Figure 142, cut views are provided in Figure 143 to better identify the shape of the wake at 0.333 s, 1 s, 1.667 s, and 2.333 s after the passage of the wing. After the wake consolidation, it should be noted that the black dashed lines do not represent the wake shape, but serve only to connect the consolidated vortices to better view them in space at a fixed timestep. For flaps that cover a large part of the wing, it is well known that the consolidated vortices on each wing should roll together. In other words, the tip vortex is initially pushed upward by the flap vortex. Figure 144 from Donaldson [45] illustrates the behavior seen both with and without the consolidation model.

The motion of the consolidated vortices compared to the vortex sheet (without consolidation) are better seen in Figures 145 - 147 at three different times after the passage of the wing.

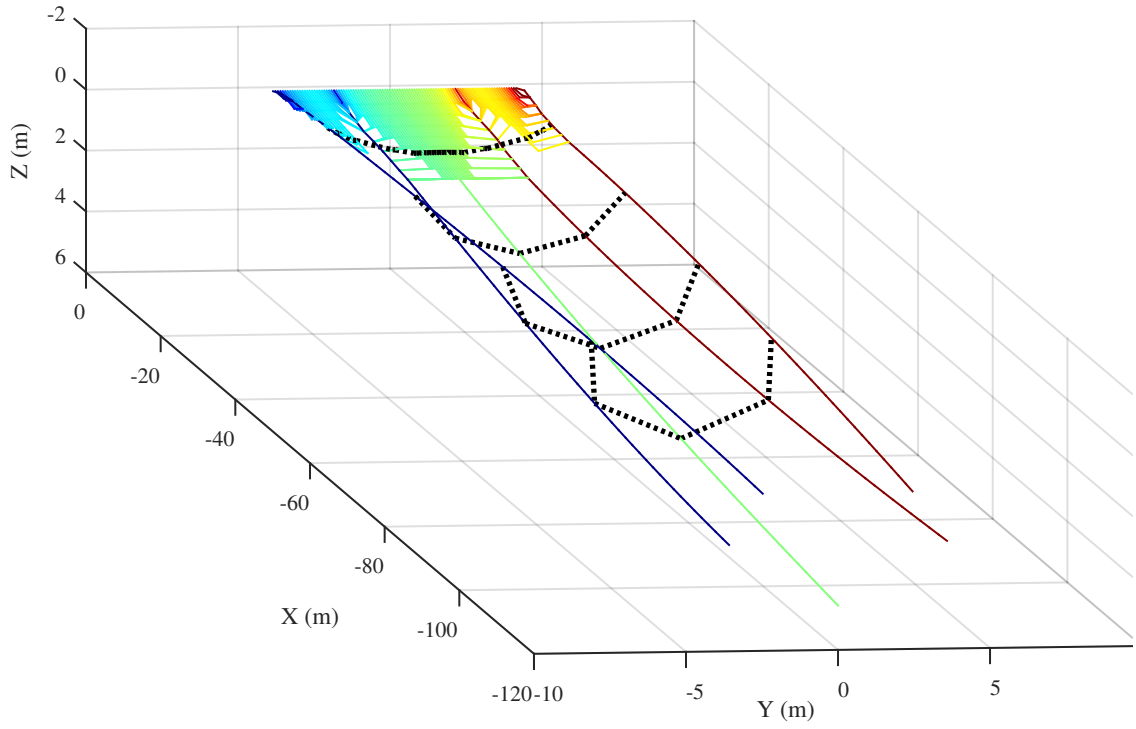

Figure 143: Test Case 5: Wake geometry and trailing vortex intensity with consolidation. The trailing vortex intensity can be identified by the color of the segments, where a red segment represents a positive circulation of 0.5 m^2/s or more and a blue segment represents a negative circulation of -0.5 m^2/s or less. The wake shape (before the consolidation) can be seen through the cut-views of the wake, depicted by black dashed lines. After the consolidation process, the dashed lines are used to facilitate indentifying the spatial localization of the vortices, since the vortex sheet itself does not exist anymore. The cut views are shown at 0.333 s, 1 s, 1.667 s, and 2.333 s after the passage of the wing.

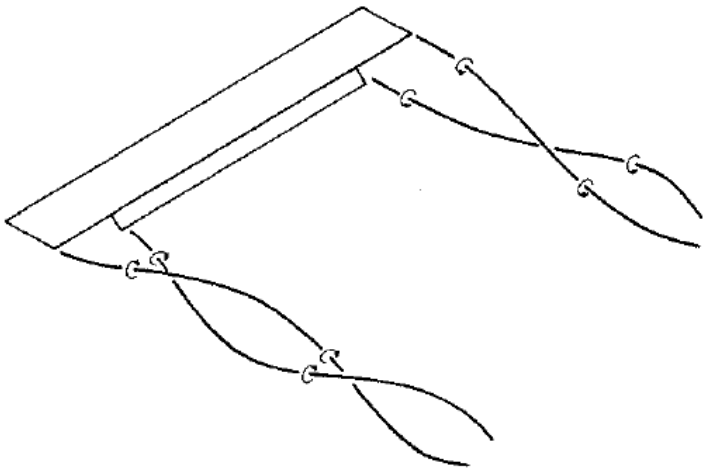

Figure 144: Notional representation of the trailing vortex trajectory with large flaps [45]. The tip vortices are initially pushed upward by the flap vortex, and then they roll about their centroid with a downward motion.

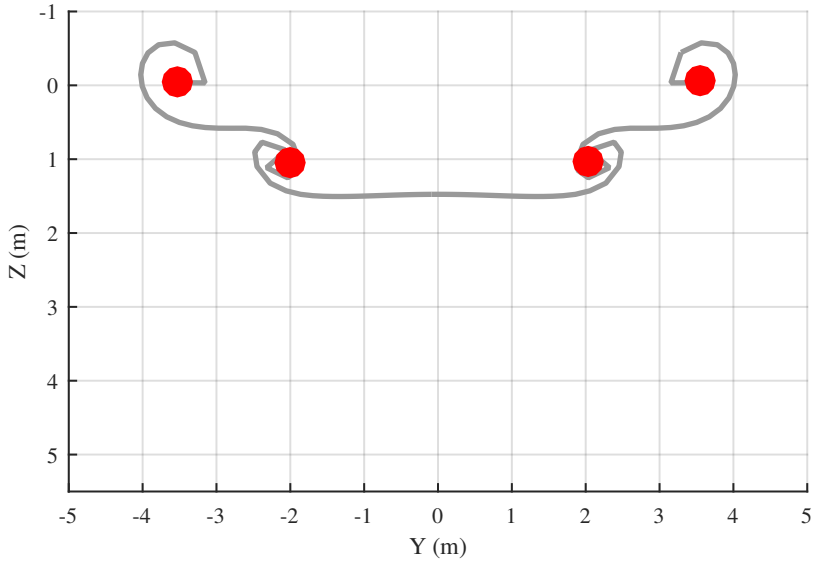

Figure 145: Wake shape and location of the consolidated vortices at $t = 0.667$ s with flap deflection. The wake shape is depicted with a solid grey curve and the consolidated vortices with a red dot.

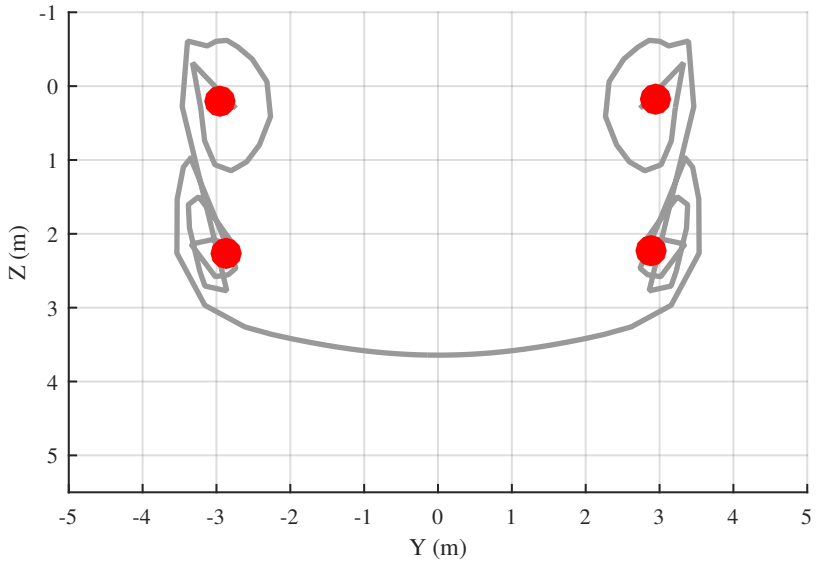

Figure 146: Wake shape and location of the consolidated vortices at $t = 2.333$ s with flap deflection. The wake shape is depicted with a solid grey curve and the consolidated vortices with a red dot.

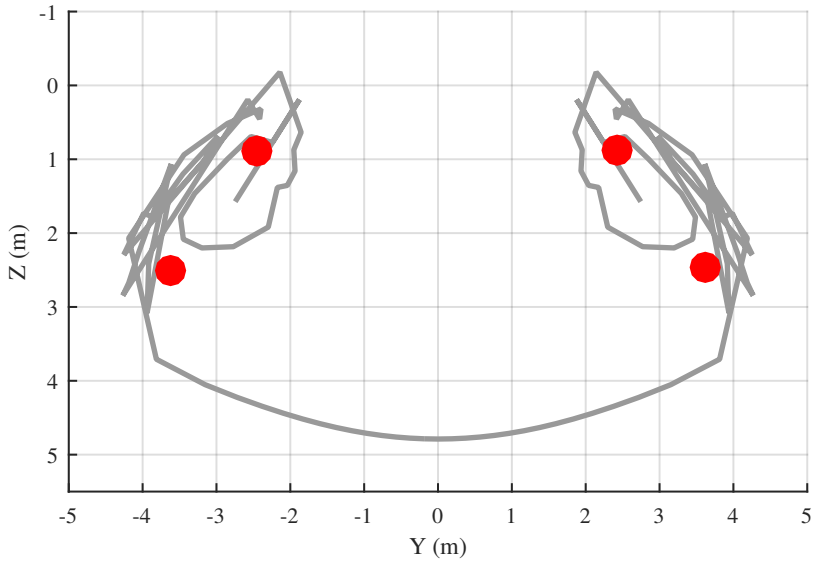

Figure 147: Wake shape and location of the consolidated vortices at $t = 3.667$ s with flap deflection. The wake shape is depicted with a solid grey curve and the consolidated vortices with a red dot.

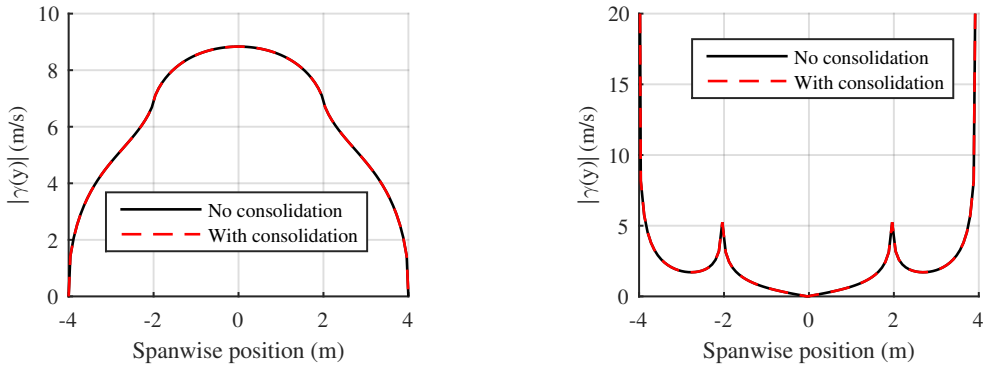

(a) Circulation

(b) Trailing vortices intensity

Figure 148: Test Case 5: Effect of flap deflection on the lift distribution with the consolidation model.

First, the location of the flap and tip vortices predicted by the consolidation model are in agreement with the vortex sheet shape at the three different timesteps. Due to the strength of the flap vortex, the tip vortices do not initially move downward; only the flap vortices are rapidly convected at more than 1.5 m/s. Then the flap and tip vortices initiate the descent as shown in Figures 146 - 147.

The complex behavior between smaller vortices due to control surface deflections and the main tip vortices is critical for formation flying. In this test case, it is shown that the strong tip vortex takes over one second to initiate its descent. The complex induced velocity behind the aircraft, even after a few seconds, cannot be reduced to only two vortices as is done for rotary wing applications.

Finally, the circulation on the lifting line and its derivative are presented in Figure 148 for both approaches. The objective is to compare if the predicted loads on the lifting surface differ with the addition of the consolidation model.

Both approaches predict the same circulation distribution within 0.1% accuracy. The consolidation model provides the same accuracy with a significant reduction in the number of function evaluations. Such a result can be explained by the fact that an accurate spatial distribution of the vortices far from the wing does not create a significant effect on the calculated induced velocity on the wing. However, those

vortices cannot be neglected and a consolidated vortex must replace the numerous vortices. In this example, the computational time was reduced by more than one order of magnitude with the use of the wake consolidation model. The improvement grows as the number of timesteps increases, such as for circling aircraft.

In summary, Test Case 5 demonstrated the need for a consolidation wake model. Conventional approaches, such as the one developed by Johnson, cannot capture the local flap vortex due to its method of assigning the trailing vortices to a few consolidated vortices. In the present implementation, the consolidation is based on the minima of the absolute value of the trailing vortex intensity, which automatically captures the control surface vortices. Extensive analyses showed that the developed consolidation model captures the flap (or any control surface) vortices and returns the same lift distribution as the same model without consolidation. The wake shape is also similar, as shown by comparing the predicted location of the consolidated vortices to the vortex sheet location without consolidation.

C.3.6 Case 6: Rapid Roll Rate

The objective of Test Case 6 is to demonstrate that the consolidation model is also effective in the presence of circulatory unsteady aerodynamics. Moreover, at this point, there is a need to demonstrate that an airplane under rapid roll rate with aileron deflection sees a strong increase in its induced drag and that yawing moments are present. Both those objectives are fulfilled with this example.

The same airspeed than for Test Case 5 is used here, but the flap deflection is kept at zero degree. A bank angle $\phi(t)$ is prescribed, as shown in Equation 180,

$$\phi(t) = 60 \sin t \qquad [\text{deg}] \tag{180}$$

which result in a roll rate $\dot{\phi}$ characteristic of aerobatic aircraft at slow flight speed,

$$\dot{\phi}(t) = 60 \cos t \qquad [\text{deg/s}] \tag{181}$$

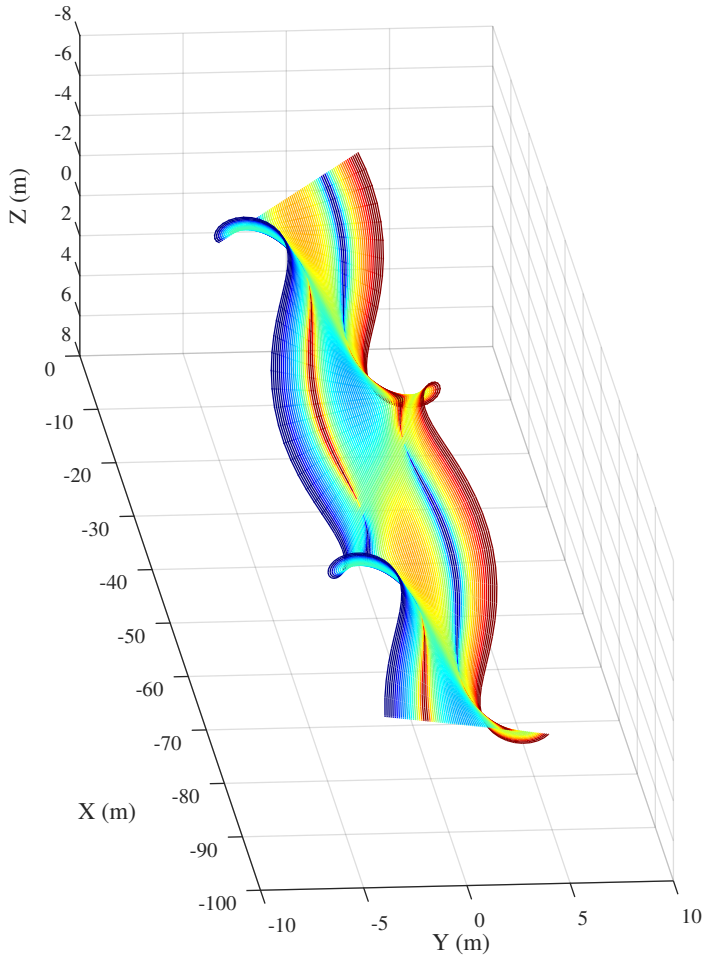

Figure 149: Test Case 6: Wake geometry and trailing vortex intensity. The trailing vortex intensity can be identified by the color of the segments, where a red segment represents a positive circulation of 0.5 m^2/s or more and a blue segment represents a circulation of -0.5 m^2/s or less. The last 4 seconds of the simulations are shown, during the periodic state. The shed vortices are hidden for clarity.

where the maximum bank angle is 60 deg, and the maximum roll rate reaches 60 deg/s. A prescribed lift of 1500 N is imposed, with zero rolling moment at all timesteps. The aileron deflection and the angle of attack are adjusted automatically at each timestep to meet those requirements, as described in Section 4.8.3. The same number of elements are used on the wing, but the far wake is prescribed for this case.

Figure 149 illustrates the trailing vortices circulation during the rapid roll motion. Local vortices form between the ailerons and the flaps due to the sharp change in the circulation at this location. Although the lift along the body z-axis is constant, the

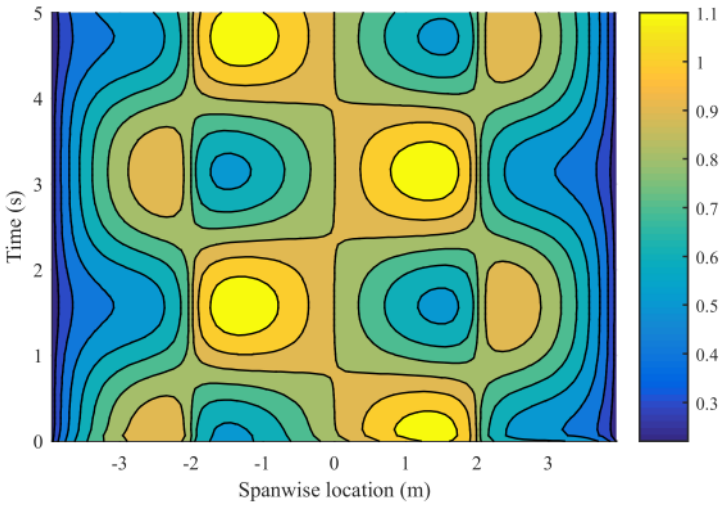

Figure 150: Test Case 6: Spanwise lift coefficient, $C_l\,(y,t)$ as a function of time. The lift distribution is far from symmetrical due to the aileron deflection, even for a rolling moment imposed to zero.

lift distribution is strongly affected by the aileron deflection, which is required to maintain zero rolling moment. The local lift coefficient as a function of span and time is illustrated in Figure 150.

Figure 150 shows that the lift distribution is far from symmetrical, although a prescribed rolling moment of zero is imposed. It could be possible to obtain this symmetrical lift distribution if non-linear wing warping was possible, but since the ailerons have a constant chord, and a constant deflection across the span, non-ideal lift distributions are obtained. Almost symmetrical distributions are seen when the roll rate goes to zero, at $t \approx 2.5$ sec, for example.

The consolidation model is then added to the simulation and compared to the results shown previously. Figure 151 shows the wake geometry with the consolidation model active.

The first observation is that the numerous trailing vortices attached to the lifting line are not always attached to the same consolidated vortex, since the number of consolidated vortices, their intensity, and their location vary over time. For example, at $x = -40$ m, the lift distribution is almost symmetrical with an aileron deflection

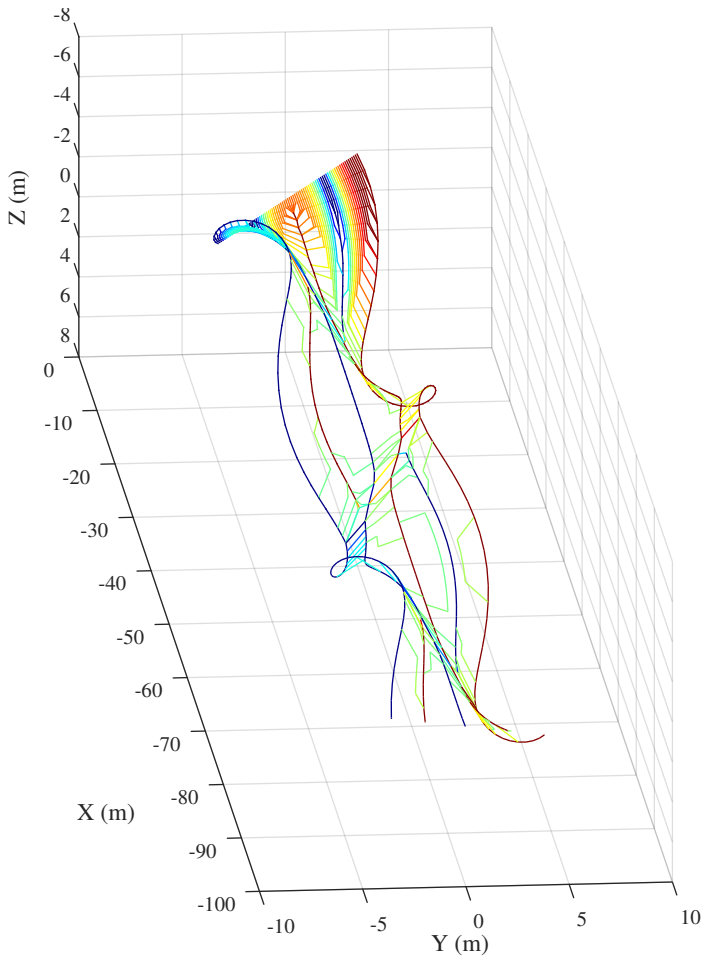

Figure 151: Test Case 6: Wake geometry and trailing vortex intensity with consolidation. The trailing vortex intensity can be identified by the color of the segments, where a red segment represents a positive circulation of 0.5 m^2/s or more and a blue segment represents a circulation of -0.5 m^2/s or less. The last 4 seconds of the simulations are shown, during the periodic state. The shed vortices are hidden for clarity.

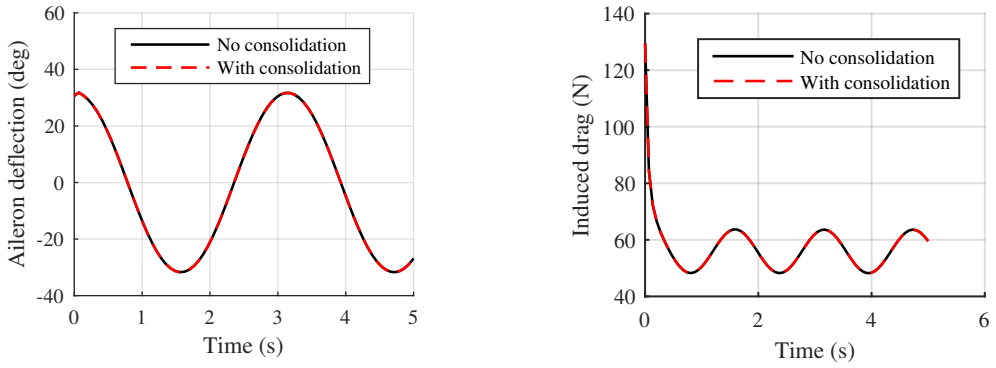

(a) Aileron deflection (b) Drag

Figure 152: Test Case 6: Aileron deflection and drag as a function of time for a sinusoidal roll attitude

of 0°. Before and after, there are major differences in the wake, especially the sign of the circulation of the aileron vortex at $y = -2$ and $y = 2$. The consolidation model behaves as expected in the presence of unsteady aerodynamics.

Figure 152 shows the aileron deflection and the induced drag as a function of time for this test case. The results without consolidation are compared with the results with consolidation. The difference in the drag prediction and the aileron deflection with and without consolidation is again within 0.1%. Figure 152 shows that the induced drag is initially very high due to the effect of the starting vortex. Then, the drag becomes periodic between 48 and 65 N, where the lowest value is obtained when the aileron deflection is small. Under those conditions, the Oswald efficiency factor, initially presented in Equation 97, varies between 0.71 and 0.95. In other words, the induced drag can reach up to 141% the value of an elliptical wing in cruise given the skewed lift distribution, under the constraint that the rolling moment must remain zero during a rapid roll rate.

A wing that undergoes the prescribed motion and loads detailed in Test Case 6 also creates strong adverse yaw. Figure 153a shows the calculated yawing moment about the $\vec{k}_B$ as a function of time and Figure 153b shows the roll rate as a function of time. It can be observed that for a positive roll rate, a negative yawing moment

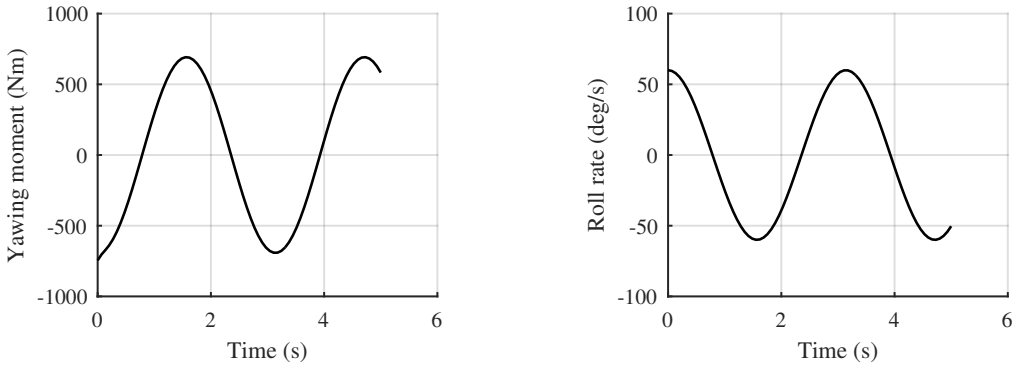

(a) Yawing moment (b) Roll rate

Figure 153: Test Case 6: Yawing moment resulting from a high roll rate

is produced. The adverse yaw can be compensated by a vertical tail (with rudder deflection) and methods to vary the drag generated by the ailerons. Such techniques increase drag, and should be considered in the power requirement of the tethered aircraft.

In summary, Test Case 6 verified that the consolidation model is effective even in the presence of unsteady aerodynamics. It also highlighted the need to consider the reduction in performance of the wing during rapid maneuvers due to the increase in induced drag.

REFERENCES

[1] Abbott, I. H. and VonDoenhoff, A. E., *Theory of wing sections: including a summery of airfoil data*. New York, NY: Dover Publications, 2010.

[2] Abkowitz, M., "Towed bodies," *Journal of Mechanical Engineering Science*, vol. 14, no. 7, pp. 20–28, 1972.

[3] Advanced Tactics, "Advanced tactics unveils the AT transformer: The future of roadable VTOL aircraft and modular cargo systems," 2014. https://www.advancedtacticsinc.com/advanced-tactics-unveils-the-at-transformer/. Accessed 20 February 2015.

[4] AgustaWestland, "Project zero all-electric tilt rotor technology demonstrator." http://www.agustawestland.com/node/6902, Accessed 15 February 2015.

[5] Ahmed, M., Hably, A., and Bacha, S., "High altitude wind power systems: A survey on flexible power kites," in *2012 International Conference on Electrical Machines (ICEM)*, (France), pp. 2085–2091, IEEE, Sept. 2012.

[6] Ahrens, U., Diehl, M., and Schmehl, R., *Airborne wind energy*. Green Energy and Technology, New York, NY: Springer, 2013.

[7] Alabrune, F., "Art of aerial transportation." US Patent # 2,298,912, 1942.

[8] Alabrune, F., "Transportation methods." US Patent # 2,373,086, 1945.

[9] Anderson, J. D., *Aircraft performance and design*. Boston, MA: McGraw-Hill, 1999.

[10] Anderson, J. D., *Fundamentals of aerodynamics*. Boston, MA: McGraw-Hill, 5th ed., 2011.

[11] Anderson, V., "Method and apparatus for pick-up and delivery by aircraft in flight." US Patent # 2,295,537, 1942.

[12] Andrews, H., "Rolling along – the VSTOL wheel," *Vertiflite*, vol. 43, pp. 32–33, Apr. 1997.

[13] Ardema, M. D., "Vehicle concepts and technology requirements for buoyant heavy-lift systems," Tech. Rep. NASA Technical Paper 1921, NASA, Moffett Field, CA, 1981.

[14] Asselin, M., *An introduction to aircraft performance*. AIAA education series, Reston, VA: American Institute of Aeronautics and Astronautics, 1997.

[15] Bangash, Z. A., Sanchez, R. P., Ahmed, A., and Khan, M., "Aerodynamics of formation flight," *Journal of aircraft*, vol. 43, no. 4, pp. 907–912, 2006.

[16] Barnes, P. N., Sumption, M. D., and Rhoads, G. L., "Review of high power density superconducting generators: Present state and prospects for incorporating YBCO windings," *Cryogenics*, vol. 45, no. 10, pp. 670–686, 2005.

[17] Bell Helicopter, "Bell 206l4 product specification." http://www.bellhelicopter.com/commercial/bell-206l4. Accessed 1 March 2015.

[18] Bertin, J. J. and Cummings, R. M., *Aerodynamics for engineers*. Upper Saddle River, NJ: Pearson, 6th ed., 2013.

[19] Bilanin, A. J. and Donaldson, C., "Estimation of velocities and roll-up in aircraft vortex wakes," *Journal of Aircraft*, vol. 12, no. 7, pp. 578–585, 1975.

[20] Board, D. S., "Future need for VTOL/STOL aircraft," Tech. Rep. ADA473069, Department of Defense, Washington, D.C, July 2007. http://www.dtic.mil/docs/citations/ADA473069. Accessed 10 March 2015.

[21] Borer, N. K. and Moore, M. D., "Integrated propeller-wing design exploration for distributed propulsion concepts," in *53rd AIAA Aerospace Sciences Meeting*, no. AIAA-2015-1672, (Kissimmee, FL), Jan. 2015.

[22] Borer, N. K., Moore, M. D., and Turnbull, A. R., "Tradespace exploration of distributed propulsors for advanced on-demand mobility concepts," in *14th AIAA Aviation Technology, Integration, and Operations Conference*, no. AIAA-2014-2850, (Atlanta, GA), June 2014.

[23] Bramesfeld, G., *A Higher Order Vortex-Lattice Method with a Force-Free Wake*. PhD thesis, The Pennsylvania State University, 2006.

[24] Bramesfeld, G. and Maughmer, M. D., "Relaxed-wake vortex-lattice method using distributed vorticity elements," *Journal of Aircraft*, vol. 45, no. 2, pp. 560–568, 2008.

[25] Brown, E., *The helicopter in civil operations*. London, UK: Granada, 1981.

[26] Caughey, T. K., "Whirling of a heavy chain," in *Third U.S. National Congress of Applied Mechanics*, (Providence, RI), pp. 101–108, June 1958.

[27] Chen, R. T., "A survey of nonuniform inflow models for rotorcraft flight dynamics and control applications," Tech. Rep. NASA Technical Memorandum 102219, NASA Ames Research Center, Moffett Field, CA, 1989.

[28] Chilowsky, C., "Method and device for establishing communication between aircraft in full flight and the ground." US Patent # 1,829,474, 1931.

[29] Choc, Y.-I. and Casarella, M. J., "Configuration of a towline attached to a vehicle moving in a circular path," *Journal of Hydronautics*, vol. 6, no. 1, pp. 51–57, 1972.

[30] Choo, Y.-i. and Casarella, M. J., "A survey of analytical methods for dynamic simulation of cable-body systems.," *Journal of Hydronautics*, vol. 7, no. 4, pp. 137–144, 1973.

[31] Ciffone, D. L. and Orloff, K., "Far-field wake-vortex characteristics of wings," *Journal of Aircraft*, vol. 12, no. 5, pp. 464–470, 1975.

[32] Clifton, J. M., *Modeling and control of a trailing wire antenna towed by an orbiting aircraft*. PhD thesis, Naval Postgraduate School, Montery, CA, Sept. 1992.

[33] Clifton, J. M., Schmidt, L. V., and Stuart, T. D., "Dynamic modeling of a trailing wire towed by an orbiting aircraft," *Journal of Guidance, Control, and Dynamics*, vol. 18, no. 4, pp. 875–881, 1995.

[34] Cochran, J., Innocenti, M., No, T., and Thukral, A., "Dynamics and control of maneuverable towed flight vehicles," *Journal of guidance, control, and dynamics*, vol. 15, no. 5, pp. 1245–1252, 1992.

[35] Conlisk, A., "Modern helicopter aerodynamics," *Annual Review of Fluid Mechanics*, vol. 29, no. 1, pp. 515–567, 1997.

[36] Conlisk, A., "Modern helicopter rotor aerodynamics," *Progress in aerospace sciences*, vol. 37, no. 5, pp. 419–476, 2001.

[37] Cormier, M., "Optimization concept forward flight operation for a reconfigurable rotor concept." School of Aerospace Engineering, Georgia Institute of Technology, Atlanta, GA, March 2015.

[38] Cormier, M., Rancourt, D., Demers Bouchard, E., and Mavris, D. N., "Optimization of the forward flight operation for a reconfigurable rotor concept," in *AHS Technical Meeting on Aeromechanics Design for Vertical Lift*, (San Francisco, CA), Jan. 2016.

[39] Cotton, R. B., "Aerial pick-up and delivery system." US Patent # 3,351,325,, 1967.

[40] Crist, S., "Analysis of the motion of a long wire towed from an orbiting aircraft," *The Shock and Vibration Bulletin*, vol. 41, no. 6, pp. 61–73, 1970.

[41] DARPA, "Aerial reconfigurable embedded system (ARES)." http://www.darpa.mil/program/aerial-reconfigurable-embedded-system. Accessed 20 February 2015.

[42] De Bruin, A. C., Hegen, S. H., Rohne, P. B., and Spalart, P. R., "Flow field survey in trailing vortex system behind a civil aircraft model at high lift," in *AGARD Conference Proceedings*, (Trondheim, Norway), pp. 25–25, May 1996.

[43] Delbert H., J., Eiichi, K., and Aldo, S., "Airborne tethered sensor system." US Patent # 5,722,618,, 1998.

[44] Demers Bouchard, E., Rancourt, D., and Mavris, D. N., "Design space exploration of reconfigurable rotor," in *AHS 71st Annual Forum and Technology Display*, (Virginia Beach, VA), May 2015.

[45] Donaldson, C. d., Snedeker, R. S., and Sullivan, R. D., "Calculation of aircraft wake velocity profiles and comparison with experimental measurements," *Journal of Aircraft*, vol. 11, no. 9, pp. 547–555, 1974.

[46] Donaldson, C., "A brief review of the aircraft trailing vortex problem," Tech. Rep. TR-71-1910, U.S. Air Force Office of Scientific Research, May 1971.

[47] Donaldson, C. and Bilanin, A., "Vortex wakes of conventional aircraft," Tech. Rep. AGARD-AG-204, North Atlantic Treaty Organisation, Neuilly sur Seine, France, 1975.

[48] Drela, M., "Qprop theory document." http://web.mit.edu/drela/Public/web/qprop/. Accessed 1 July 2015.

[49] Ducote, R. and Speelman, R., "US Air Force concepts for accurate delivery of equipment and supplies.," *Journal of Aircraft*, vol. 4, no. 4, pp. 383–392, 1967.

[50] Durkee, S. and Muetze, A., "Conceptual design of an electric helicopter powertrain," in *5th IET International Conference on Power Electronics, Machines and Drives*, (Brighton, United Kingdom), pp. 1–6, IET, Apr. 2010.

[51] Ehang, "EHANG 184, Autonomous Aerial Vehicle." http://www.ehang.com/ehang184. Accessed 14 September 2016.

[52] Emrax, "Emrax 228 technical data table." http://www.enstroj.si/Electric-products/emrax-228-motorsgen.html. Accessed 1 August 2016.

[53] EVolo, "Volocopter - the world's first green helicopter." http://www.e-volo.com/. Accessed 1 February 2015.

[54] Fagiano, L. and Milanese, M., "Airborne wind energy: an overview," in *American Control Conference (ACC)*, (Montréal, Canada), pp. 3132–3143, IEEE, June 2012.

[55] Fagiano, L., *Control of tethered airfoils for high–altitude wind energy generation*. PhD thesis, Politecnico di Torino, 2009.

[56] Frawley, G., *The international directory of civil aircraft, 2003/2004*. Shrewsbury, England: Airlife, 2003.

[57] Fredericks, W. J., Moore, M. D., and Busan, R. C., "Benefits of hybrid-electric propulsion to achieve 4x increase in cruise efficiency for a VTOL aircraft," in *2013 International Powered Lift Conference*, (Los Angeles, CA), Aug. 2013.

[58] Frost, G. and Costello, M., "Improved deployment characteristics of a tether-connected munition system," *Journal of Guidance, Control, and Dynamics*, vol. 24, no. 3, pp. 547–554, 2001.

[59] Gajetti, M. and Maggiore, P., *Route Profitability for Helicopters*. Bologna, Italy: Societa Editrice Esculapio, 2 ed., May 2013.

[60] Gamzon, E., "Method and system for supporting an airborne vehicle in space." US Patent # 5,074,489, 1991.

[61] Gardner, B., *The Complete Multi-Engine Pilot*. The Complete Pilot series, Newcastle, WA: Aviation Supplies and Academics, Inc, 3rd ed., May 2009.

[62] Gilbert, N., "The shape of a cable used for towing a pitot-static probe from a helicopter," Tech. Rep. ARL-AERO-NOTE-397, DTIC Document, Melbourne, Australia, 1980.

[63] GlobalSecurity, "Future transport rotorcraft (FTR)." http://www.globalsecurity.org/military/systems/aircraft/jtr.htm. Accessed 6 February 2015.

[64] GlobalSecurity, "Heavy lift vertical takeoff and landing (HVLTOL)." http://www.globalsecurity.org/military/systems/aircraft/hlvtol.htm. Accessed 6 February 2015.

[65] Gohardani, A. S., "A synergistic glance at the prospects of distributed propulsion technology and the electric aircraft concept for future unmanned air vehicles and commercial/military aviation," *Progress in Aerospace Sciences*, vol. 57, pp. 25–70, 2013.

[66] Gohardani, A. S., Doulgeris, G., and Singh, R., "Challenges of future aircraft propulsion: A review of distributed propulsion technology and its potential application for the all electric commercial aircraft," *Progress in Aerospace Sciences*, vol. 47, no. 5, pp. 369–391, 2011.

[67] Gottimukkala, S. S. V., *Design of Circularly Towed Cable-Body Systems*. PhD thesis, Pennsylvania State University, University Park, PA, Aug. 2011.

[68] Griffiths, D. A. and Leishman, J. G., "A study of dual-rotor interference and ground effect using a free-vortex wake model," in *58th Annual Forum and Technology Display of the American Helicopter Society International*, (Montréal, Canada), June 2002.

[69] Guy, C. R., Williams, M. J., and Gilbert, N. E., "Sea King Mk. 50 helicopter sonar dynamics study. A simplified control systems mathematical model," Tech. Rep. ARL/AERO-152, DTIC Document, Melbourne, Australia, 1979.

[70] Hansen, J. G. R. and Crist, S. A., "Dynamics of cables towed from aircraft," Tech. Rep. AD-753 909, Air Force Academy, Air Force Academy, CO, Oct. 1972.

[71] Heatley, M., *The illustrated history of helicopters*. London, UK: Brompton Books Corp., 1985.

[72] Henderson, J., Potjewyd, J., and Ireland, B., "The dynamics of an airborne towed target system with active control," *Institution of Mechanical Engineers, Part G: Journal of Aerospace Engineering*, vol. 213, no. 5, pp. 305–319, 1999.

[73] Hess, J., "Panel methods in computational fluid dynamics," *Annual Review of Fluid Mechanics*, vol. 22, no. 1, pp. 255–274, 1990.

[74] Hirschberg, M., "Project zero, the exclusive story of AgustaWestland's all-electric "technology incubator."," *Vertiflite*, vol. May/June 2013, pp. 10–14, June 2013.

[75] Hodges, D. H. and Pierce, G. A., *Introduction to structural dynamics and aeroelasticity*, vol. 15. Cambridge, UK: Cambridge University Press, 2nd ed., 2011.

[76] Hoerner, S. F., *Fluid-dynamic drag: practical information on aerodynamic drag and hydrodynamic resistance.* Bakersfield, CA: Hoerner Fluid Dynamics, 1992.

[77] Holzäpfel, F., "Probabilistic two-phase wake vortex decay and transport model," *Journal of Aircraft*, vol. 40, no. 2, pp. 323–331, 2003.

[78] Holzäpfel, F., "Probabilistic two-phase aircraft wake-vortex model: further development and assessment," *Journal of Aircraft*, vol. 43, no. 3, pp. 700–708, 2006.

[79] Horstmann, K. H., *Ein Mehrfach-Traglinienverfahren und seine Verwendung für Entwurf und Nachrechnung nichtplanarer Flügelanordnungen.* DFVLR-FB 87-51, Braunschweig Techn. Univ., Braunschweig, Germany, 1986.

[80] Huang, S. L., "Mathematical model for long cable towed by orbiting aircraft," Tech. Rep. AD0856221, Naval Air Development Center, Warminster, PA, June 1969.

[81] Hurren, B. J., *Helicopters of Tomorrow.* New York, NY: Staples Press Limited, 1947.

[82] Huston, R. L. and Kamman, J. W., "Validation of finite segment cable models," *Computers & Structures*, vol. 15, no. 6, pp. 653–660, 1982.

[83] IATA, "IATA technology roadmap 2013," Tech. Rep. 4th edition, International Air Transport Association, June 2013.

[84] Jackson, P. A., *Jane's all the world's aircraft 2010-2011*. London, England: Jane's Information Group, IHS Inc, 2010.

[85] Joby Motors, "JM1s motor datasheet." http://www.jobymotors.com/public/views/pages/jm1s.php. Accessed 12 March 2015.

[86] Johnson, D. and Brown, G., "NASA research & technology 2004," Tech. Rep. TM-2005-213419, NASA, 2004.

[87] Johnson, W., "CAMRAD II, Comprehensive Analytucal Model of Rotorcraft Aerodynamics and Dynamics," 1992-1997. User guide.

[88] Johnson, W., *Helicopter theory*. Mineola, NY: Dover Publications, 1994.

[89] Johnson, W., "Influence of Wake Models on Calculated Tiltrotor Aerodynamics," in *American Helicopter Society Aerodynamics, Acoustics, and Test and Evaluation Technical Specialists Meeting*, (San Francisco, CA), American Helicopter Society International, Jan. 2002.

[90] Johnson, W., *Rotorcraft aeromechanics*. Cambridge aerospace series, Cambridge, UK: Cambridge University Press, 2013.

[91] Jordan, P. F., "Structure of Betz vortex cores," *Journal of Aircraft*, vol. 10, no. 11, pp. 691–693, 1973.

[92] Kamman, J. W. and Huston, R. L., "Modeling of variable length towed and tethered cable systems," *Journal of Guidance, Control, and Dynamics*, vol. 22, no. 4, pp. 602–608, 1999.

[93] Katz, J. and Plotkin, A., *Low speed aerodynamics*. Cambridge, UK: Cambridge University Press, 2001.

[94] Khoury, G. A. and Gillett, J. D., *Airship Technology*. New York, NY: Cambridge University Press, 2004.

[95] Kolla, P. C., *Modeling Simulation and Preliminary Experimentation on Towed Tether System*. Masters Thesis, Auburn University, Auburn, AL, Dec. 2007.

[96] Kolodner, I. I., "Heavy rotating string – a nonlinear eigenvalue problem," *Communications on Pure and Applied Mathematics*, vol. 8, pp. 395–408, Aug. 1955.

[97] Lanchester, F. W., *Aerodynamics*. London, UK: Archibald Constable & CO. LTD, 1907.

[98] Langelaan, J. W., Chakrabarty, A., Deng, A., Miles, K., Plevnik, V., Tomazic, J., Tomazic, T., and Veble, G., "Green flight challenge: aircraft design and flight planning for extreme fuel efficiency," *Journal of Aircraft*, vol. 50, no. 3, pp. 832–846, 2013.

[99] Leishman, J. G., *Principles of helicopter aerodynamics with CD extra*. Cambridge university press, 2006.

[100] Leishman, J. G., Baker, A., and Coyne, A., "Measurements of rotor tip vortices using three-component laser doppler velocimetry," *Journal of the American Helicopter Society*, vol. 41, no. 4, pp. 342–353, 1996.

[101] Leishman, J. G., Bhagwat, M. J., and Bagai, A., "Free-vortex filament methods for the analysis of helicopter rotor wakes," *Journal of aircraft*, vol. 39, no. 5, pp. 759–775, 2002.

[102] Leonard, J. W. and Nath, J. H., "Comparison of finite element and lumped parameter methods for oceanic cables," *Engineering Structures*, vol. 3, no. 3, pp. 153–167, 1981.

[103] Long, L. N. and Fritz, T. E., "Object-oriented unsteady vortex lattice method for flapping flight," *Journal of Aircraft*, vol. 41, no. 6, pp. 1275–1290, 2004.

[104] Macha, J. M., "Drag of circular cylinders at transonic mach numbers," *Journal of Aircraft*, vol. 14, no. 6, pp. 605–607, 1977.

[105] Makani Power Inc., "Response to the Federal Aviation Authority, Notification or Airbone Wind Energy Systems (AWES)," Tech. Rep. FAA-2011-1279, Makani Power, Alameda, CA, 2011.

[106] Makani Power Inc., "The technology," 2014. www.google.com/makani/technology/. Accessed 15 February 2015.

[107] Margason, R., Kjelgaard, S., Sellers III, W., Morris Jr, C., Walkey, K., and Shields, E., "Subsonic panel methods – a comparison of several production codes," in *AIAA 23rd Aerospace Sciences Meeting*, (Reno, NV), Jan. 1985.

[108] Masson, P. J., Breschi, M., Tixador, P., and Luongo, C. A., "Design of HTS axial flux motor for aircraft propulsion," *IEEE Transactions on Applied Superconductivity*, vol. 17, no. 2, pp. 1533–1536, 2007.

[109] Masson, P. J. and Luongo, C. A., "High power density superconducting motor for all-electric aircraft propulsion," *IEEE Transactions on Applied Superconductivity*, vol. 15, no. 2, pp. 2226–2229, 2005.

[110] McGowen, S. S., *Helicopters: an illustrated history of their impact*. Weapons and warfare series, Santa Barbara, CA: ABC-CLIO, 2005.

[111] Melin, T., *A vortex lattice MATLAB implementation for linear aerodynamic wing applications*. Masters Thesis, Royal Institute of Technology, Stockholm, Sweden, 2000.

[112] Mook, D. T. and Nayfeh, A. H., "Application of the Vortex-Lattice Method to high-angle-of-attack subsonic aerodynamics," Tech. Rep. 851817, SAE Technical Paper, 1985.

[113] Moore, M., "NASA puffin electric tailsitter VTOL concept," in *10th AIAA Aviation Technology, Integration, and Operations (ATIO) Conference*, no. AIAA-2010-9345, (Forth Worth, TX), Sept. 2010.

[114] Moore, M. D., "Electric propulsion enabled advanced air vehicles." Oral presentation, Apr. 2008.

[115] Moore, M. D., "The joby S2 VTOL concept," *Vertiflite*, vol. 60, pp. 22–24, Dec. 2014.

[116] Moore, M. D. and Fredericks, B., "Misconceptions of electric propulsion aircraft and their emergent aviation markets," in *the 52nd Aerospace Sciences Meeting AIAA*, no. AIAA-2014-0535, (National Harbord, MD), Jan. 2014.

[117] Murray, J. E., Bowers, A. H., Lokos, W. A., Peters, T. L., and Gera, J., "An Overview of an Experimental Demonstration Aerotow Program," Tech. Rep. NASA/TM-1998-206566, NASA, Edwards, CA, 1998.

[118] Murray, R. M., "Trajectory generation for a towed cable system using differential flatness," in *IFAC world congress*, (San Francisco, CA), pp. 395–400, July 1996.

[119] NASA, "NASA Electric Research Plane Get X Number, New Name." http://www.nasa.gov/press-release/nasa-electric-research-plane-gets-x-number-new-name. Accessed 21 July 2016.

[120] NASA, "Testing electric propulsion," 2014. http://www.nasa.gov/aero/testing-electric-propulsion.html#.VNTbMy5ciER. Accessed 6 February 2015.

[121] Ning, A., Flanzer, T. C., and Kroo, I. M., "Aerodynamic performance of extended formation flight," *Journal of Aircraft*, vol. 48, no. 3, pp. 855–865, 2011.

[122] Norris, S. R. and Andrisani, D., "Longitudinal equilibrium solutions for a towed aircraft and tow cable," in *AIAA Atmospheric Flight Mechanics Conference and Exhibit*, no. AIAA-2001-4254, (Montréal, Canada), Aug. 2001.

[123] Okulov, V. L., Sørensen, J. N., and Wood, D. H., "The rotor theories by professor joukowsky: Vortex theories," *Progress in Aerospace Sciences*, vol. 73, pp. 19–46, 2015.

[124] Olson, G., "System and method for transporting cargo utilizing an air towing system that can achieve vertical take-off and vertical landing." US Patent # 8,308,142 B1, Nov. 2012.

[125] Patterson, M. D., Daskilewicz, M. J., and German, B. J., "Conceptual design of electric aircraft with distributed propellers: Multidisciplinary analysis needs and aerodynamic modeling development," in *52nd Aerospace Sciences Meeting*, no. AIAA-2014-0534, (National Harbor, MD), Jan. 2014.

[126] Patterson, M. D., German, B. J., and Moore, M. D., "Performance analysis and design of on-demand electric aircraft concepts," in *12th AIAA Aviation Technology, Integration, and Operations (ATIO) Conference and 14th AIAA/ISSM*, no. AIAA-2012-5474, (Indianapolis, IN), Sept. 2012.

[127] Picard, M., Rancourt, D., Plante, J.-S., and Brouillette, M., "Rim-rotor rotary ramjet engine, part 2: Quasi-one-dimensional aerothermodynamic design," *Journal of Propulsion and Power*, vol. 28, no. 6, pp. 1304–1314, 2012.

[128] Prouty, R. W., *Helicopter Performance, Stability, and Control*. Malabar, FL: Krieger Pub Co, 2002.

[129] Rancourt, D., Frchette, L., Landry, C., and Mavris, D. N., "Design Space Exploration of Centimeter-Scale Wind Turbines using a Physics-Modified Optimization Formulation," *Journal of Mechanics*, vol. 30, pp. 537–548, Oct. 2014.

[130] Rancourt, D., Bolduc-Teasdale, F., Bouchard, E. D., Anderson, M. J., and Mavris, D. N., "Design space exploration of gyrocopter-type airborne wind turbines," *Wind Energy*, vol. 19, no. 5, pp. 895–909, 2015.

[131] Rancourt, D., Demers Bouchard, E., and Mavris, D. N., "Optimal Flight Path of the Tethered Airplanes in the EPR2 VTOL Concept During Moderate Flight Velocity," in *AHS Technical Meeting on Aeromechanics Design for Vertical Lift*, (San Francisco, CA), Jan. 2016.

[132] Rancourt, D., Picard, M., Denninger, M., Plante, J.-S., Chen, J., and Yousefpour, A., "Rim-rotor rotary ramjet engine, part 1: Structural design and experimental validation," *Journal of Propulsion and Power*, vol. 28, no. 6, pp. 1293–1303, 2012.

[133] Raymer, D. P., *Aircraft design: a conceptual approach*. AIAA education series, Reston, VA: American Institute of Aeronautics and Astronautics, 4th ed., 2006.

[134] Reichert, T., *Kinematic Optimization in Birds, Bats and Ornithopters*. PhD thesis, University of Toronto, Toronto, Canada, 2011.

[135] Robertson, C. D. and Reichert, T. M., "Design and development of the atlas human-powered helicopter," *AIAA Journal*, vol. 53, no. 1, pp. 20–32, 2014.

[136] Rossow, V. J., "On the inviscid rolled-up structure of lift-generated vortices," *Journal of Aircraft*, vol. 10, no. 11, pp. 647–650, 1973.

[137] Rothhaar, P. M., Murphy, P. C., Bacon Barton, J., Gregory, I. M., Grauer, J. A., Busan, R. C., and Croom, M. A., "NASA langley distributed propulsion VTOL tilt-wing aircraft testing, modeling, simulation, control, and flight test development," in *14th AIAA Aviation Technology, Integration, and Operations Conference*, no. AIAA-2014-2999, (Atlanta, GA), June 2014.

[138] Russell, J., *Equilibrium and Stability of a Whirling Cable*. PhD thesis, The University of Michigan, Ann Arbor, MI, 1974.

[139] Russell, J. and Anderson, W., "Equilibrium and stability of a circularly-towed cable subject to aerodynamic drag," *Journal of Aircraft*, vol. 14, no. 7, pp. 680–686, 1977.

[140] Russell, J. and Anderson, W., "Equilibrium and stability of a whirling rod-mass system," *International Journal of Non-Linear Mechanics*, vol. 12, pp. 91–101, Jan. 1977.

[141] Schodek, D. L., *Structures*. Upper Saddle River, NJ: Pearson/Prentice Hall, 5th ed., 2004.

[142] Sgarioto, D. E., *Non-linear dynamic modelling and optimal control of aerial tethers for remote delivery and capture of payloads*. PhD thesis, RMIT University, 2006.

[143] Sheehy, T. W., "A method for predicting helicopter hub drag," Tech. Rep. USAAMRDL-TR-75-43, United Technologies Corporation, Fort Eustis, VA, 1976.

[144] Sikorsky, "Firefly technology demonstrator." http://www.sikorsky.com/Pages/Innovation/Technologies/FireflyTechnology.aspx. Accessed 10 February 2015.

[145] Sivasubramaniam, K., Zhang, T., Lokhandwalla, M., Laskaris, E., Bray, J., Gerstler, B., Shah, M., and Alexander, J., "Development of a high speed HTS generator for airborne applications," *IEEE Transactions on Applied Superconductivity*, vol. 19, no. 3, pp. 1656–1661, 2009.

[146] Skop, R. A. and Choo, Y.-I., "The configuration of a cable towed in a circular path.," *Journal of Aircraft*, vol. 8, no. 11, pp. 856–862, 1971.

[147] Smith, B. B., "Method and apparatus for cargo loading and discharging in flight." US Patent # 2,151,395, Mar. 1939.

[148] Smoot, S., *Conceptual Design and Passive Stability of Tethered Platforms*. PhD thesis, Stanford University, Palo Alto, CA, 2012.

[149] Spalart, P. R., "Airplane trailing vortices," *Annual Review of Fluid Mechanics*, vol. 30, no. 1, pp. 107–138, 1998.

[150] Stoll, A. M., Bevirt, J., Moore, M. D., Fredericks, W. J., and Borer, N. K., "Drag reduction through distributed electric propulsion," in *14th AIAA Aviation Technology, Integration, and Operations Conference*, no. AIAA-2014-2851, (Atlanta, GA), June 2014.

[151] Stoll, A. M., Bevirt, J., Pei, P. P., and Stilson, E. V., "Conceptual design of the joby S2 electric VTOL PAV," in *14th AIAA Aviation Technology, Integration, and Operations Conference*, no. AIAA-2014-2407, (Atlanta, GA), June 2014.

[152] Sun, L., *Dynamic Modeling, Trajectory Generation and Tracking for Towed Cable Systems*. PhD thesis, Brigham Young University, Provo, UT, 2012.

[153] Sun, L. and Beard, R. W., "Towed-body trajectory tracking in aerial recovery of micro air vehicle in the presence of wind," in *American Control Conference (ACC), 2011*, pp. 3209–3214, IEEE, 2011.

[154] Sun, L., Hedengren, J. D., and Beard, R. W., "Optimal trajectory generation using model predictive control for aerially towed cable systems," *Journal of Guidance, Control, and Dynamics*, vol. 37, no. 2, pp. 525–539, 2014.

[155] Wang, Z. and Mook, D. T., "Numerical aerodynamic analysis of formation flight," in *41st Aerospace Sciences Meeting and Exhibit*, no. AIAA-2003-610, (Reno, NV), Jan. 2003.

[156] Weissinger, J., "The Lift Distribution of Swept-Back Wings," Tech. Rep. Technical Memorandum 1120, NACA, Washington, DC, Mar. 1947.

[157] White, F. M., *Fluid mechanics*. New York, NY: McGraw-Hill Education, 8th ed., 2016.

[158] Widnall, S. E., "The structure and dynamics of vortex filaments," *Annual Review of Fluid Mechanics*, vol. 7, no. 1, pp. 141–165, 1975.

[159] Williams, P., "Optimal wind power extraction with a tethered kite," in *AIAA Guidance, Navigation, and Control Conference*, no. AIAA-2006-6193, (Keystone, CO), Aug. 2006.

[160] Williams, P., "Optimization of circularly towed cable system in crosswind," *Journal of guidance, control, and dynamics*, vol. 33, no. 4, pp. 1251–1263, 2010.

[161] Williams, P., Lansdorp, B., and Ockesl, W., "Optimal crosswind towing and power generation with tethered kites," *Journal of guidance, control, and dynamics*, vol. 31, no. 1, pp. 81–93, 2008.

[162] Williams, P., Lapthorne, P., and Trivailo, P., "Circularly-towed lumped mass cable model validation from experimental data," in *AIAA Modeling and Simulation Technologies Conference and Exhibit*, no. AIAA-2006-6817, (Keystone, CO), Aug. 2006.

[163] Williams, P. and Ockels, W., "Dynamics of towed payload system using multiple fixed-wing aircraft," *Journal of guidance, control, and dynamics*, vol. 32, no. 6, pp. 1766–1780, 2009.

[164] Williams, P. and Trivailo, P., "Cable-supported sliding payload deployment from a circling fixed-wing aircraft," *Journal of aircraft*, vol. 43, no. 5, pp. 1567–1570, 2006.

[165] Williams, P. and Trivailo, P., "Dynamics of circularly towed aerial cable systems, part 1: optimal configurations and their stability," *Journal of guidance, control, and dynamics*, vol. 30, no. 3, pp. 753–765, 2007.

[166] Williams, P. and Trivailo, P., "Dynamics of circularly towed aerial cable systems, part 2: Transitional flight and deployment control," *Journal of guidance, control, and dynamics*, vol. 30, no. 3, pp. 766–779, 2007.

[167] Wilson Jr., F. M., "Aerial transport of payloads with vertical pick up and delivery." US Patent # 4,416,436, Nov. 1983.

[168] Winget, J. and Huston, R., "Cable dynamics – a finite segment approach," *Computers & Structures*, vol. 6, no. 6, pp. 475–480, 1976.

[169] Woodward, F. A., "Analysis and design of wing-body combinations at subsonic and supersonic speeds.," *Journal of Aircraft*, vol. 5, no. 6, pp. 528–534, 1968.

[170] Wu, C.-H., "Whirling of a string at large angular speeds-a nonlinear eigenvalue problem with moving boundary layers," *SIAM Journal on Applied Mathematics*, vol. 22, no. 1, pp. 1–13, 1972.

[171] Yates, J. E., "Calculation of initial vortex roll-up in aircraft wakes," *Journal of Aircraft*, vol. 11, no. 7, pp. 397–400, 1974.

[172] Zanon, M., Gros, S., Andersson, J., and Diehl, M., "Airborne wind energy based on dual airfoils," *IEEE Transactions on Control Systems Technology*, vol. 21, no. 4, pp. 1215–1222, 2013.

[173] Zhu, F. and Rahn, C., "Stability analysis of a circularly towed cable–body system," *Journal of Sound and Vibration*, vol. 217, no. 3, pp. 435–452, 1998.